Springer ThesesRecognizing Outstanding Ph.D. Research

Kiran Joshi

QCD Radiation in Top-Antitop and Z+Jets Final States

Precision Measurements at ATLAS



Springer Theses

Recognizing Outstanding Ph.D. Research

Aims and Scope

The series "Springer Theses" brings together a selection of the very best Ph.D. theses from around the world and across the physical sciences. Nominated and endorsed by two recognized specialists, each published volume has been selected for its scientific excellence and the high impact of its contents for the pertinent field of research. For greater accessibility to non-specialists, the published versions include an extended introduction, as well as a foreword by the student's supervisor explaining the special relevance of the work for the field. As a whole, the series will provide a valuable resource both for newcomers to the research fields described, and for other scientists seeking detailed background information on special questions. Finally, it provides an accredited documentation of the valuable contributions made by today's younger generation of scientists.

Theses are accepted into the series by invited nomination only and must fulfill all of the following criteria

- They must be written in good English.
- The topic should fall within the confines of Chemistry, Physics, Earth Sciences, Engineering and related interdisciplinary fields such as Materials, Nanoscience, Chemical Engineering, Complex Systems and Biophysics.
- The work reported in the thesis must represent a significant scientific advance.
- If the thesis includes previously published material, permission to reproduce this must be gained from the respective copyright holder.
- They must have been examined and passed during the 12 months prior to nomination.
- Each thesis should include a foreword by the supervisor outlining the significance of its content.
- The theses should have a clearly defined structure including an introduction accessible to scientists not expert in that particular field.

More information about this series at http://www.springer.com/series/8790

Kiran Joshi

QCD Radiation in Top-Antitop and Z+Jets Final States

Precision Measurements at ATLAS

Doctoral Thesis accepted by the University of Manchester, UK



Author
Dr. Kiran Joshi
Christie Medical Physics and Engineering
The Christie NHS Foundation Trust
Manchester
UK

Supervisor
Prof. Michael Seymour
School of Physics and Astronomy
The University of Manchester
Manchester
UK

ISSN 2190-5053 IS Springer Theses ISBN 978-3-319-19652-7 IS DOI 10.1007/978-3-319-19653-4

ISSN 2190-5061 (electronic)

ISBN 978-3-319-19653-4 (eBook)

Library of Congress Control Number: 2015941339

Springer Cham Heidelberg New York Dordrecht London © Springer International Publishing Switzerland 2015

This work is subject to copyright. All rights are reserved by the Publisher, whether the whole or part of the material is concerned, specifically the rights of translation, reprinting, reuse of illustrations, recitation, broadcasting, reproduction on microfilms or in any other physical way, and transmission or information storage and retrieval, electronic adaptation, computer software, or by similar or dissimilar methodology now known or hereafter developed.

The use of general descriptive names, registered names, trademarks, service marks, etc. in this publication does not imply, even in the absence of a specific statement, that such names are exempt from the relevant protective laws and regulations and therefore free for general use.

The publisher, the authors and the editors are safe to assume that the advice and information in this book are believed to be true and accurate at the date of publication. Neither the publisher nor the authors or the editors give a warranty, express or implied, with respect to the material contained herein or for any errors or omissions that may have been made.

Printed on acid-free paper

Springer International Publishing AG Switzerland is part of Springer Science+Business Media (www.springer.com)

Supervisor's Foreword

Manchester has developed a strong tradition of joint Ph.Ds in theoretical and experimental particle physics. This Ph.D. thesis contains new research in both areas, making important contributions in each. Two analyses of collision data from the ATLAS experiment at the LHC are presented, as well as two phenomenological studies of heavy-coloured resonances that could be produced at the LHC.

The first data analysis was the measurement of top quark-antiquark production with a veto on additional jet activity [1]. Not only is this an important measurement for understanding properties of top quarks and the events they are produced in, but as the first detector-corrected measurement of jet activity in top-antitop events it played an important role in constraining the theoretical modelling. This ultimately reduced the modelling uncertainties for ATLAS's other top quark measurements by a factor of two. The detector-corrected data were published for open-access future analysis.

The second data analysis was the measurement of Z+2 jet production and the observation of the electroweak vector boson fusion (VBF) component [2]. The VBF process has long been proposed as an important channel for studying the Higgs boson quantum numbers and couplings. As the first observation of VBF at a hadron collider, this measurement demonstrated new techniques to reliably extract VBF processes and paved the way for these future Higgs measurements. The detector-corrected data were again published for open-access future analysis.

The first phenomenological study [3] developed a new technique for identifying the colour of heavy resonances produced in proton-proton collisions. As a by-product of this study, an unexpected and previously unnoticed correlation was discovered between the probability of correctly identifying a high-energy top quark (using so-called boosted jet tagging algorithms) and the colour structure of the event it was produced in. The second phenomenological study [4] explored this relationship in more detail, and could have important consequences for the identification of new particles that decay to top quarks, if any hints are found in the next run of the LHC.

The thesis also describes the author's work on the ATLAS isolated muon event filter trigger, an important contribution to the detector operation, which qualified him as an ATLAS author.

I write this foreword as Dr. Joshi's theory supervisor, but I would like to record my gratitude to his experimental supervisor, Dr. Andy Pilkington, as well as to Kiran himself, for making this such a successful project and a pleasure to cosupervise.

Manchester April 2015 Prof. Michael Seymour

References

- 1. ATLAS Collaboration (2011). Measurement of dijet production with a veto on additional central jet activity in pp collisions at $\sqrt{s} = 7$ TeV using the ATLAS detector. *JHEP*, 1109(053).
- 2. ATLAS Collaboration (2014). Measurement of the electroweak production of dijets in association with a Z-boson and distributions sensitive to vector boson fusion in proton-proton collisions at $\sqrt{s} = 8$ TeV using the ATLAS detector. *JHEP*, 1404(031).
- Ask, S., Collins, J., Forshaw, J. R., Joshi, K. & Pilkington, A. D. (2012). Identifying the colour of TeV-scale resonances. *JHEP*, 1201(018).
- 4. Joshi, K., Pilkington, A. D. & Spannowsky, M. (2012). The dependency of boosted tagging algorithms on the event colour structure. *Physical Review, D86*(114016).

Abstract

This thesis presents precision measurements and phenomenological studies of quark and gluon radiation in $t\bar{t}$ and $t\bar{t}$ + jets final states. A measurement of $t\bar{t}$ production with a veto on additional jet activity is performed using 2.1 fb⁻¹ of proton–proton collision data with a centre of mass energy of 7 TeV, collected by the ATLAS detector. Jet veto efficiency measurements are performed in several regions of rapidity and corrected for the effects of finite detector resolution and efficiency. A total experimental uncertainty of less than 5 % is achieved in all distributions.

Two phenomenological studies are performed on the additional quark and gluon radiation produced in association with boosted $t\bar{t}$ systems. In the first study, it is shown how a measurement of the jet veto efficiency can be used to identify the colour of a TeV-scale resonance decaying to $t\bar{t}$. The second follow-up study describes how the performance of several top-tagging algorithms is affected by the colour structure of an event.

Measurements of the electroweak production of dijets in association with a Z-boson and distributions sensitive to vector boson fusion are performed using 20.3 fb $^{-1}$ of proton–proton collision data collected by ATLAS at 8 TeV. Detector-corrected differential cross-sections, and distributions sensitive to radiation produced in addition to the Z_{ij} system, are measured in five fiducial regions with varying sensitivity to the electroweak component of the Z_{ij} cross-section. Data are compared to MC predictions and are in reasonable agreement in the majority of cases. The electroweak Z_{ij} cross-section is extracted and found to be in good agreement with theory predictions. Limits are also placed on anomalous triple gauge couplings. The commissioning of an event filter isolated muon trigger is also presented. The trigger became one of the primary muon triggers used during the 2012 data taking.

Preface

Every measurement and search for new physics performed at the Large Hadron Collider is affected by aspects of Quantum Chromodynamics (QCD) in some way. The uncertainty associated with the modelling of quark and gluon emissions can be large, and it is therefore crucial to perform precision measurements in a variety of final states that are sensitive to these emissions. Such measurements assist the particle physics theory and phenomenology communities in understanding the properties and features of QCD. They also allow the uncertainties associated with the QCD modelling to be constrained, which ensures that experimental measurements can be made with as much precision as possible.

The work presented in this thesis focusses on the quark and gluon radiation produced in association with $t\bar{t}$ and Z + jets final states using proton–proton collision data collected by the ATLAS experiment at both \sqrt{s} = 7 TeV and \sqrt{s} = 8 TeV. Phenomenological studies were also performed that demonstrate how quark and gluon radiation can be exploited to discriminate between the production of differently coloured heavy resonances, and also how some aspects of QCD can disrupt such attempts.

This thesis is organised as follows. In Chap. 1, a brief review of the Standard Model is given and the concept of jet vetoing is introduced, which is a recurring theme in the analyses and phenomenological studies presented. Chapter 2 introduces the Large Hadron Collider and the ATLAS detector, and Chap. 3 details how the physics objects required to perform an experimental analysis are reconstructed from the output of the various tracking detectors and calorimeters. The commissioning of an event filter isolated muon trigger is presented in Chap. 4. In Chap. 5 the analysis of tt production with a veto on additional central jet activity is documented, which is a precision measurement of the hadronic jet activity produced in association with a tt system. Additional quark and gluon emission in tt systems is again the subject of the phenomenological studies presented in Chap. 6. A jet veto is shown to be a useful tool in determining the colour of a new heavy resonance, and in a follow-up study the efficiency of tagging top-jets produced in the decay of

x Preface

such a resonance is shown to depend strongly on the event colour structure. In Chap. 7, measurements of the quark and gluon emission produced in association with a boson are made, and the extraction of the electroweak component of the Z+2 jet production cross-section is presented. Finally, Chap. 8 provides a summary of the work presented.

Acknowledgments

Biggest thanks have to go to Andy Pilkington, for inspiring me during the summer project 4 years ago, and for the endless encouragement, support, motivation and advice he has given me since then. Without him this thesis would look very different; probably much shorter(!), and certainly much less interesting. Huge thanks also to Mike Seymour for introducing me to the wonderful world of Monte Carlo event generators, for lots of support and advice and for trying, often in vain, to make sure I did not fall too far behind on my eProg forms.

Thanks to everyone in the Manchester Particle Physics Group, both at Manchester and CERN. In particular to Mark, with whom it has been a pleasure to work with over the years, to Tom for putting up with me in the Manchester and CERN offices and for being my first port of call with any stupid questions, and of course to Fred for offering me the Ph.D. position in the first place, for always being there to provide support and advice, and for never giving up on trying to get me to come to coffee breaks.

Outside of Particle Physics, I want to thank everyone who has made living in Manchester for the past 8 years a joy. To Rach, for making the last 15 months some of the best of my life; to Leo, Emily, Christina, Amanda and of course Phil, for offering me places to stay when visiting from CERN and for providing countless hours of entertainment.

Finally, special thanks to Mum, Dad and Rose, for their constant encouragement and support, for always encouraging me to do whatever I thought was interesting and for always being there if ever I need any help. I would not be where I am today without all of you, and I will be forever grateful.

Contents

Intro	oduction to the Standard Model and Jet Vetoing
1.1	History
1.2	Quantum Electro- and Chromodynamics
	1.2.1 QCD
1.3	Electroweak and Higgs Sectors
	1.3.1 The Standard Model Higgs
1.4	The Physics of Hadron Colliders
	1.4.1 Next-to-Leading Order Corrections
1.5	Monte Carlo Event Generators
	1.5.1 Matrix Elements
	1.5.2 Parton Showers
	1.5.3 Hadronisation and Underlying Event
	1.5.4 Event Generators
	1.5.5 Theoretical Uncertainties
	1.5.6 Jets
1.6	Jet vetoing
Refe	rences
Expe	erimental Apparatus
2.1	The Large Hadron Collider
	2.1.1 Design
	2.1.2 Performance
2.2	The ATLAS Detector
	2.2.1 The Inner Detector
	2.2.2 The Calorimeters
	2.2.3 The Muon Spectrometer
	2.2.4 Trigger and Data Acquisition
Refe	rences

xiv Contents

3	Reco	nstructing Physics Objects	45				
	3.1	Charged Particle Tracks	45				
	3.2	Primary Vertices	46				
	3.3	Electrons	46				
		3.3.1 Reconstruction	46				
		3.3.2 Identification	47				
	3.4	Muons	48				
		3.4.1 Reconstruction	48				
		3.4.2 Identification	48				
	3.5	Jets	49				
		3.5.1 <i>b</i> -tagging	51				
	3.6	Missing Transverse Energy	51				
	Refe	ences	53				
	10	A TOTAL DATA TO A LAC	~ ~				
4		t-Filter Muon Isolation	55 55				
	4.1	Introduction	55				
	4.2	The Need for Isolated Triggers	55				
	4.3	Implementation and Performance	56				
	4.4	4.3.1 Pile-up Dependence	60				
	4.4	Summary	62				
	Refe	rence	62				
5	Jet V	etoing in Top-Antitop Events	63				
	5.1	Introduction and Motivation	63				
		5.1.1 Variable Definition	64				
	5.2	Data and Monte Carlo Samples	65				
	5.3	Object and Event Selection	68				
		5.3.1 Muons	68				
		5.3.2 Electrons	68				
		5.3.3 Jets	69				
		5.3.4 Missing Transverse Energy	69				
		5.3.5 Event Selection Requirements	69				
	5.4	Backgrounds	71				
		5.4.1 Fake Lepton Background	71				
		5.4.2 Other Backgrounds	71				
	5.5	Corrections to the Simulation	71				
	5.6	Detector-Level Data and MC Comparisons	73				
	5.7	Correction for Detector Effects	75				
	5.8						
		5.8.1 Jet Energy Scale	78 79				
		5.8.2 Uncertainties Due to Additional pp Interactions	80				
		5.8.3 Uncertainty in the <i>b</i> -Tagging	81				
		5.8.4 Uncertainty Due to Unfolding to Particle Level	82				
		5.8.5 Uncertainty Due to Background Contamination	86				

Contents xv

		5.8.6	Uncertainty Due to Lepton Efficiencies	
			and Resolutions	88
		5.8.7	Uncertainty Due to Jet Resolution and Efficiency	88
		5.8.8	Summary of Systematic Uncertainties	90
	5.9	Results		91
	5.10	Impact.		94
	Refer	rences		99
6	Studi		applications of Jet Vetoing in Boosted Topologies	103
	6.1	Identify	ing the Colour of TeV-Scale Resonances	103
		6.1.1	Introduction	103
		6.1.2	Simulation and Event Selection	105
		6.1.3	Definition of the Jet Veto Region and the Jet Veto	
			Efficiency	107
		6.1.4	Extracting the Signal from Background	109
		6.1.5	Extracting the Colour	112
		6.1.6	Effect of Experimental and Theoretical	
			Uncertainties	113
	6.2	Depend	ency of Tagging Algorithms on the Event	
		Colour	Structure	116
		6.2.1	Introduction	116
		6.2.2	Boosted Top Reconstruction	116
		6.2.3	Basic Kinematic Features of the Signal Events	118
		6.2.4	Dependence of Top-Tagging Efficiency	
			on Event Colour Structure	118
		6.2.5	Impact on Experimental Analyses	125
	Refer	ences		126
7			s of Electroweak Z Boson + Dijet Production	129
	7.1		ction	129
	7.2		nd Object Reconstruction and Selection	130
		7.2.1	Muons	131
		7.2.2	Electrons	131
		7.2.3	Jets	131
	7.3	Theoret	ical Predictions	132
		7.3.1	Electroweak Signal Composition	133
	7.4	Monte (Carlo Simulation	134
		7.4.1	Combination of QCD Z Samples	134
	7.5	Differer	ntial Cross Section Measurements	136
		7.5.1	Phase Space Definitions	136
		7.5.2	Distributions of Interest	138
		7.5.3	Detector-Level Data and MC Comparisons	139
		7.5.4	Introduction to Bayesian Unfolding	139
		7.5.5	Bayesian Unfolding in This Analysis	141

xvi Contents

	7.5.6	Extending the EWUnfolding Package to 2D	143
	7.5.7	Selected Control Plots	144
	7.5.8	Statistical Uncertainties and Correlations	146
	7.5.9	Luminosity, Trigger and Lepton-Based Systematics	148
	7.5.10	Jet Energy-Based Systematic Uncertainties	150
	7.5.11	Pile-up and JVF Modelling Uncertainty	151
	7.5.12	Modelling Uncertainties and Unfolding Closure	153
	7.5.13	Summaries of Systematic and Statistical	
		Uncertainties	153
	7.5.14	Unfolded Differential Cross Sections	157
7.6	Electro	weak Z _{ij} Signal Extraction and Cross Section	165
	7.6.1	Extraction Technique	166
	7.6.2	Experimental Systematic Uncertainties	167
	7.6.3	Theoretical Modelling of the Signal	
		and Background	167
	7.6.4	Uncertainty Due to Signal and Background	
		Interference	169
	7.6.5	Electroweak Fiducial Cross Section Results	170
7.7	Limits	on Anomalous Triple Gauge Couplings	171
D 0			174

Chapter 1 Introduction to the Standard Model and Jet Vetoing

1.1 History

It is often said that modern elementary particle physics was born in 1897, with J. J. Thompson's discovery of the electron. Although correctly assuming that the electrons were an essential part of what made up atoms, it wasn't until 1911 that Rutherford discredited Thompson's "plum pudding" model by proposing his own, now-famous, model of the atom after analysing the results of the Geiger-Marsden experiment performed at the University of Manchester two years earlier. The mass concentrated in the nucleus of the hydrogen atom was given the name *proton* by Rutherford, and was used by Bohr in 1914 in his remarkably successful model of hydrogen, consisting simply of a single electron orbiting the proton. The final discovery within this so-called classical period of particle physics was made by Chadwick in 1932 when his discovery of the neutron gave a satisfying description of the helium atom.

For a brief period elementary particle physicists would have been forgiven for thinking that their work was done. In 1932 the answer to the question "What is everything made of" could simply have been: electrons, protons and neutrons. However, questions were already being asked whose answers would complicate this clean and simple picture. The question entering the forefront of people's minds was one of Rutherford's nucleus itself, and how it manages to hold itself together. How was it that the electric repulsion between the positively charged protons, packed so closely together, wasn't forcing the nuclei to simply break apart?

Before answering that question it is worth taking a step back to 1905, and to Einstein. His proposed solution to explain the photoelectric effect was to suggest that the electromagnetic field itself was quantised, and the little packets of light proposed by Planck in 1900 were excitations of the field. Although initially met with scepticism, the particle-nature of light became much more widely accepted after Compton's experiment of 1923 described how light scattered from particles at rest. The particles of light became known as *photons*, and were eventually incorporated into quantum field theory. Photons are now recognised to be mediators of the electromagnetic

1

force, or gauge bosons, and it is the exchange of photons that is responsible for the attraction or repulsion between two electrically charged particles.

Returning now to the question regarding the nucleus, the imaginatively named strong force was proposed as a solution; a force strong enough to bind protons together but sufficiently short-ranged that we do not experience its effects in our every-day life. It was Yukawa, in 1934, who proposed the first convincing theory for the strong interaction. Yukawa proposed that the proton and neutron are attracted to each other by some sort of field, and that the particle mediating this force, given that the force was so short-ranged, must be rather heavy. He named this new particle the meson. Yukawa himself knew no particle such as this had been observed before, however by 1937 two separate groups had seen particles which seemed to match Yukawa's description. Unfortunately, further investigation of the cosmic ray particles originally identified as Yukawa's mesons revealed that some of the particles had the wrong mass. It was not until 1947 that the mystery was resolved when it was discovered that there were two particles present in the cosmic rays—Yukawa's meson, which was named the pion (π) by the Bristol researchers who discovered it, and an unexpected addition which was completely unrelated to the strong interaction, the muon (μ) .

Taking another brief step backwards, it was in 1927 that Paul Dirac made the first major progress in tackling the problem of relativistic quantum mechanics. The Dirac equation, as it is now known, was supposed to describe free spin-1/2 particles but had a troubling feature that it allowed solutions corresponding to particles with negative energy. Dirac's original interpretation was that all of the negative energy states are filled by an infinite *sea* of electrons, which prevent any further electrons running-away into increasingly negative states. In the 1940s Stuckelberg and Feynman proposed an interpretation that physicists were more comfortable with. They suggested that solutions of the Dirac equation with negative energy can be re-expressed as positive-energy states of a different particle—the anti-electron, or positron, which had been discovered back in 1930. This interpretation came with the implication that for not just the electron, but for every particle there must exist an anti-particle with the same mass but opposite charge. The negatively charged anti-proton was discovered in 1955, and the (neutral) anti-neutron the following year.

Returning to 1930 again, the problem of radioactive beta decay was prompting Niels Bohr to consider abandoning the law of conservation of energy. The neutrino, which carries away the missing energy in the case where a neutron decays to a proton, was finally proposed by Pauli in 1930 as a solution to the problem. We now know that it is the so-called weak nuclear force that is responsible for this decay, with a down quark being transformed into an up quark accompanied by the emission of an electron and its associated electron neutrino. We will return to the weak interaction shortly, but suffice it to say that the weakly interacting anti-neutrino was finally discovered in 1955 with the observation of the inverse beta decay reaction.

With the discovery of the existence of anti-particles and neutrinos, the collection of fundamental particles was looking increasingly complicated. It was made more so in the 1950s, when a whole host of slowly-decaying particles known as baryons, as well as additional mesons known as kaons, were discovered. To explain their

1.1 History 3

production and decays a new property was assigned to each particle. Proposed by Gell-Mann [1] and Nishijima [2] the *strangeness* of a particle was defined to be conserved in the strong interaction, but not conserved in the weak interaction.

The abundance of strongly-interacting particles was now divided into two groups—baryons and mesons—and each of the particles in the group distinguished by their charge, mass and now strangeness. It was Gell-Mann [3] once again, in 1961, who restored some order when he arranged the particles into an equivalent of chemists' periodic table, known as the Eightfold Way. In doing so he boldly predicted the existence of a particle which fit his pattern but had not yet been observed, and sure enough the omega-minus [4] particle was discovered shortly after in 1964. An understanding of the Eightfold Way was to follow when Gell-Mann and Zweig proposed, independently, that all hadrons are in fact made up of even smaller, and more elementary particles which Gell-Mann called quarks. The quarks came in three flavours: up, down and strange, had fractional units of charge (+2/3, -1/3 and -1/3)respectively) and integer units of strangeness (0, 0, -1 respectively) which enabled them to be combined to form the various baryons and mesons observed so far. The composition rules proposed were that (1) every baryon is made up of three quarks (and every anti-baryon made up of three anti-quarks) and (2) that every meson is made up of two quarks.

Despite explaining Gell-Mann's Eightfold Way and the multitude of observed baryons and mesons, by the 1960s and 1970s the particle physics community was growing sceptical of the quark model. The main objections were that nobody had seen an individual quark, and that some combinations of quarks appeared to violate Pauli's exclusion principle—the Δ^{++} particle is supposed to consist of three up quarks in the same state. A solution was proposed by Greenberg in 1964 [5]. He suggested that not only do quarks come in three flavours (u, d, s) but each also comes in three colours (red, green and blue). This means that each of the up quarks comprising the Δ^{++} come in one of the three colours, and the Pauli principle is safe; the total wavefunction of the particle is antisymmetric under exchange of the quark indices. This idea of colour can also be used to explain the property of colour confinement, or why we don't see quarks anywhere other than bound up inside hadrons. The proposal is that all physical, observable particles are colour neutral. The colourless combinations that make up the hadrons of the Standard Model are three quarks qqq (the baryons), three anti-quarks $\bar{q}\bar{q}\bar{q}$ (the anti-baryons) and one quark with one anti-quark $q\bar{q}$ (the mesons). Particles made up of larger numbers of quarks are in principle allowed, with recent measurements hinting at the first observation of a tetraquark [6, 7].

It wasn't until 1974 that the particle physics community really began to accept the quark model. The J/ψ meson, which was extremely heavy and had an incredibly long lifetime (compared to any of the other known particles), was discovered to be a bound state of a new quark—the charm quark $(J/\psi=c\bar{c})$. Between 1975 and 1977 a series of new baryons and mesons were discovered with varying amount of *charmness*, providing strength to both the interpretation of the J/ψ as a $c\bar{c}$ state and the quark model as a whole.

1975 also brought the discovery of another lepton—the tau (τ) , and the inference of its associated neutrino. Shortly followed by the discovery of a new meson, the

upsilon, which implied the existence of yet another quark, the bottom (b). The first bottom baryon $(\Lambda_b^0 = udb)$ and meson (\bar{B}^0) were observed in the 1980s.

The existence of a sixth quark was predicted by many, to restore the symmetry between the number of quarks and leptons (e, μ and τ plus their neutrinos). The top (t) quark was eventually discovered in 1995 by the experiments at the Tevatron collider at Fermilab, and turned out to be exceptionally heavy (over 40 times heavier than the b quark).

We return again now to nuclear beta decay. It was widely considered that the original theory, which assumed that the interaction occurred at a single point, was incomplete and would need to be reformulated with the inclusion of a new particle to mediate this weak force. It took until Glashow, Weinberg and Salam's unification of the electromagnetic and weak forces before precise predictions of the masses of the intermediate vector bosons, as they became known, were obtained. The predicted masses of the two charged (W^{\pm}) and one neutral (Z) bosons were:

$$M_W = 82 \pm 2 \text{ GeV}$$
 $M_Z = 92 \pm 2 \text{ GeV}$.

Then in 1983 the UA1 and UA2 experiments, analysing data from proton-antiproton collisions produced by the SPS at CERN, announced their discoveries of the W [8, 9] and Z [10, 11] bosons with (combined) measured masses of:

$$M_W = 82.1 \pm 1.7 \text{ GeV}$$
 $M_Z = 93.0 \pm 1.7 \text{ GeV}$.

The particle mediating the strong force is called the gluon. Given that they carry colour charge (in fact gluons carry both colour *and* anti-colour—a gluon could be of colour red anti-green $(r\bar{g})$) they cannot be detected directly, but there is substantial indirect evidence that gluons exist.

The remaining piece of the puzzle that we must consider is the Higgs mechanism and the associated force carrier—the Higgs boson. In his paper submitted in 1964 [12], Peter Higgs proposed the idea of a new field with which the fundamental particles would interact to acquire their mass. Related papers were published by Englert and Brout [13], and Guralnik, Hagan and Kibble [14] the same year. Glashow, Weinberg and Salam included Higgs' ideas in their formulation of the electroweak theory a few years later (cf. Sect. 1.3), and so once the *W* and *Z* bosons had been discovered the Higgs boson became the next particle in the sights of the particle physics community. The discovery finally came in July 2012, when the ATLAS [15] and CMS [16] experiments at the LHC announced that they had observed a new particle consistent with a Standard Model Higgs Boson, with a mass of around 125 GeV. Higgs, Englert and Brout were awarded the Nobel Prize for their work in October 2013 [17].

The Standard Model, then, is the name given to the theory describing the properties of and interactions between the three types of elementary particle discussed so far: the quarks, leptons, and force-carrying bosons, whose basic properties are summarised in Tables 1.1, 1.2 and 1.3 respectively.

1.1 History 5

Particle		Generation	Charge	Mass	
Up quark	и	1	+2/3	2.3 ^{+0.7} _{-0.5} MeV	
Down quark	d	1	-1/3	4.8 ^{+0.5} _{-0.3} MeV	
Charm quark	С	2	+2/3	$1.275 \pm 0.025 \text{GeV}$	
Strange quark	S	2	-1/3	95 ± 5 MeV	
Top quark	t	3	+2/3	$173.1 \pm 0.977 \text{ GeV}$	
Bottom quark	b	3	-2/3	$4.18 \pm 0.03 \text{ GeV}$	

Table 1.1 Ouarks of the Standard Model [18]

The u-, d-, and s-quark masses are estimates of the so-called 'current masses' in the \overline{MS} scheme, at a scale $\mu \approx 2$ GeV. The c- and b-quark masses are also the "running" masses in the \overline{MS} scheme, at scales equal to their own masses. The top quark mass is based on direct measurements using data from the Tevatron Run-I and Run-II and the LHC at $\sqrt{s} = 7$ TeV

Table 1.2 Leptons of the Standard Model [18]

Particle		Generation	Charge	Mass
Electron	e ⁻	1	-1	511.0 keV
Electron neutrino	ν_e	1	0	<2 eV
Muon	μ^-	2	-1	107.5 MeV
Muon neutrino	ν_{μ}	2	0	<2 eV
Tau	τ-	3	-1	1.777 GeV
Tau neutrino	ν_{τ}	3	0	<2 eV

Table 1.3 Force-mediating bosons of the Standard Model [18]

e				
Particle		Force	Charge	Mass
Photon	γ	Electromagnetic	0	$<1 \times 10^{-18} \text{ eV}$
W-boson	W^{\pm}	Weak	±1	$80.385 \pm 0.015 \text{GeV}$
Z-boson	Z	Weak	0	91.188 ± 0.002 GeV
Gluon	g	Strong	0	0

While undeniably a triumph of modern physics, providing countless predictions that have been validated by experimental measurements, the Standard Model is not a complete answer to the questions of understanding the universe around us. The Standard Model does not incorporate gravitation as described by Einstein's general relativity, nor does it contain a particle which could be a candidate for making up the large proportion of dark matter known to exist in the universe. Many solutions have been proposed that address some or all of the problems (supersymmetry being one of the more popular), but thus far no physics beyond the Standard Model has been observed by the experiments operating at the LHC. Searches will continue once the LHC begins operating once more at its design energy of around 14 TeV.

1.2 Quantum Electro- and Chromodynamics

The mathematical basis of the Standard Model is founded on the principles of symmetry. The Lorentz symmetry, which implies that the laws of physics look the same to any observer regardless of their frame of reference, is believed to be an exact symmetry of nature. For example in special relativity the Lorentz symmetry implies that the scalar product between two space-time four-vectors,

$$x^{\mu}y_{\mu} = \eta_{\mu\nu}x^{\mu}y^{\nu},$$

where $\eta_{\mu\nu} = \text{diag}(1, -1, -1, -1)$ is the Minkowski metric, is invariant when transforming to a new coordinate system x'^{μ} ,

$$x^{\mu} \rightarrow x'^{\mu} = \Lambda^{\mu}_{\nu} x^{\nu}$$

where Λ^{μ}_{ν} represent a Lorentz transformation along some direction.

A transformation such as this is said to be *global*. If we were to perform some simple measurement and then move our entire laboratory and all of the experimental equipment it contained 500 m along the road, we would expect to obtain the same result when repeating our measurement.

Alternatively, we find that the Lagrangian (which summarizes the complete dynamics of a system) for non-interacting spin-1/2 fields (for example a free electron),

$$\mathcal{L}_{dirac} = i\overline{\psi}\gamma^{\mu}\partial_{\mu}\psi - m\overline{\psi}\psi, \qquad (1.1)$$

is invariant when making the global phase transformation

$$\psi \rightarrow \psi' = e^{i\theta} \psi,$$

where θ is any real number, and we have $\overline{\psi} \to \overline{\psi}' = \overline{\psi} e^{-i\theta}$ which causes the exponentials to simply cancel out in each half of the equation.

However, if we now require that the phase transformation is *local*, and takes a different value at each point in space-time

$$\psi \to \psi' = e^{iq\lambda(x)}\psi, \tag{1.2}$$

we find that, on substituting into the Eq. (1.1), the Lagrangian no longer remains invariant and gains an extra term from the derivative of $\lambda(x)$

$$\partial_{\mu}(e^{iq\lambda(x)}) = iq(\partial_{\mu}\lambda(x))e^{iq\lambda(x)}\psi + e^{iq\lambda(x)}\partial_{\mu}\psi$$

$$\therefore \mathcal{L}_{dirac} \to i\overline{\psi}\gamma^{\mu}\partial_{\mu}\psi - m\overline{\psi}\psi - q(\partial_{\mu}\lambda)\overline{\psi}\gamma^{\mu}\psi$$

$$= \mathcal{L}_{dirac} - q(\partial_{\mu}\lambda)\overline{\psi}\gamma^{\mu}\psi. \tag{1.3}$$

In order to restore the invariance of the Lagrangian under local phase transformations another term must be added to cancel the extra piece present in Eq. (1.3). Specifically, the Lagrangian must become

$$\mathcal{L} = \mathcal{L}_{dirac} - (q\overline{\psi}\gamma^{\mu}\psi)A_{\mu}, \tag{1.4}$$

where A_{μ} is some new field which, under the local phase transformation, must become

$$A_{\mu} \to A_{\mu} - \partial_{\mu}\lambda.$$
 (1.5)

However we must now also include an additional 'free' term to account for the A_{μ} field itself. It turns out that the only term it is possible to add is the so-called kinetic term

$$-\frac{1}{4}F_{\mu\nu}F^{\mu\nu}, \qquad F_{\mu\nu} = \partial_{\mu}A_{\nu} - \partial_{\nu}A_{\mu}, \tag{1.6}$$

where $F_{\mu\nu}$ is the so-called field strength tensor and is also invariant under the local phase transformation given in Eq. (1.5).

The field A_{μ} is in fact the electromagnetic potential. So by starting with the free Dirac Lagrangian and requiring that it remains invariant under local phase transformations, we have ended up with a Lagrangian that permits interactions between the spin-1/2 fields ψ and the massless vector field A_{μ} . The field A_{μ} is forced to be massless by the invariance requirement. A mass term such as

$$\frac{m^2}{2}A^{\nu}A_{\nu}$$

is *not* invariant under the transformation given in Eq. (1.5), and so we must have m = 0.

An alternative method of producing the locally invariant Lagrangian in Eq. (1.4) is to introduce the covariant derivative,

$$\mathcal{D}_{\mu} \equiv \partial_{\mu} + iqA_{\mu}.$$

then by making the replacement $\partial_{\mu} \to \mathcal{D}_{\mu}$ in Eq. (1.1) we recover the crucial piece which keeps the Lagrangian invariant after performing the local transformations in Eqs. (1.2) and (1.5).

Jumping back again to the phase transformation in Eq. (1.2), we can consider this instead as a multiplication by a 1×1 unitary matrix

$$\psi \to U \psi$$
 where $U U^{\dagger} = 1$ and $U = e^{i\theta}$ in this case. (1.7)

The group of all unitary 1×1 matrices is called U(1) and the symmetry involved is U(1) gauge invariance (the transformations in Eqs. (1.2) and (1.5) are often referred to

as gauge transformations). Given that a 1×1 matrix is just a number it seems trivial to introduce this additional terminology. However similar ideas can be applied to other symmetry groups. Indeed once the idea is extended to colour and the group SU(3) we can produce quantum chromodynamics (QCD)—the theory describing the strong interaction.

1.2.1 QCD

Similar methods can be used to construct a Lagrangian for QCD that also obeys the principle of invariance under local gauge transformations. In this case however it is the symmetry group SU(3) that must be used, and the transformations analogous to those in Eq. (1.7) are now represented by 3×3 unitary matrices with unit determinant. In general a 3×3 matrix can be specified in terms of 9 complex numbers, or eighteen real parameters. The condition of unitarity imposes 9 constraints on the parameters and the requirement of unit determinant imposes another. The eight remaining parameters correspond to eight directions about which rotations can be made and the eight rotation matrices can be expressed in terms of the generators, T^a , which define the gauge transformations for SU(3)

$$\psi \to e^{-i\omega^a(x)\mathbf{T}^{\mathbf{a}}}\psi,\tag{1.8}$$

where the repeated index a is summed-over and the generators $\mathbf{T}^{\mathbf{a}}$ can be written in terms of the eight Gell-Mann matrices λ^{a} , $\mathbf{T}^{\mathbf{a}} = \frac{1}{2}\lambda^{a}$.

The objects being transformed in the case of QCD are three-component vectors representing the quark fields in colour space. I.e. $\psi = (\psi_r, \psi_b, \psi_g)^T$.

The generators obey the commutation relation

$$[\mathbf{T}^{\mathbf{a}}, \mathbf{T}^{\mathbf{b}}] = i f^{abc} \mathbf{T}^{\mathbf{c}},$$

which defines the Lie algebra of the group. The f^{abc} are called the structure constants of the group. The Lie algebra and structure constants contain the information required to completely reconstruct the entire group, in a similar way that DNA encodes the genetic information used to develop an organism.

Following a similar procedure to the U(1) case above, we can introduce a covariant derivative that contains necessary pieces to ensure that the QCD Lagrangian remains invariant after applying the local transformation in Eq. (1.8). The covariant derivative for the case of QCD is

$$\mathcal{D}_{\mu} = \partial_{\mu} + i g_{s} \mathbf{T}^{\mathbf{a}} G_{\mu}^{a},$$

where g_s is the coupling strength and the G^a_μ are eight fields associated with the eight gluons, the mediators of the strong force.

The final piece we need is the equivalent of the kinetic term in Eq. (1.6). Since QCD is a non-Abelian (not commutative) theory, the field strength tensor contains an additional term,

$$F_{\mu\nu}^a = \partial_\mu G_\nu^a - \partial_\nu G_\mu^a - g_s f^{abc} G_\mu^b G_\nu^c,$$

which produces important differences for QCD compared to QED—when the kinetic term in the Lagrangian is evaluated with the QCD field strength tensor we find terms that correspond to gluon self-interactions at three and four-point vertices. It is these self-interactions that give rise to the properties of asymptotic freedom—the observation that at high energies quarks behave as if they were free particles—and colour confinement—that individual free quarks are never observed, and can only be detected experimentally when bound inside hadrons.

The coupling parameter g_s is often replaced by defining the strong coupling,

$$\alpha_s = \frac{g_s^2}{4\pi} \ .$$

To first order QCD is scale invariant. That is, the strong coupling α_S is constant and used to describe the strength of the quark-gluon vertex at all energies. However at higher orders of perturbation theory the presence of loop diagrams spoil this simple picture.

Integrating over the momentum of particles in the loops leads to ultraviolet divergences, which must be cancelled using renormalisation techniques. Renormalisation involves replacing the *bare* parameters—some of which have already been introduced such as the QED and QCD couplings, the electric charge and mass etc.—with renormalised versions that take into account loop corrections to the physical parameters themselves. The renormalisation scale, μ_R , is introduced as a way of truncating calculations at some finite scale, though this also introduces an uncertainty in the calculations due to higher order terms that are being omitted. There is no correct choice for the scale μ_R though sensible choices can be made, related to the some physical scale of the process under investigation, in order to keep the higher order uncertainties to a minimum. μ_R is often varied in calculations to estimate the size of these uncertainties.

Using the strong coupling as an example; the way in which α_S varies with energy scale Q^2 can be calculated (in the one-loop approximation) to be:

$$\alpha_S(Q^2) = \frac{\alpha_S(\mu_R^2)}{1 + \alpha_S(\mu_R^2)\beta_0 \ln \frac{Q^2}{\mu_R^2}}$$
 (1.9)

where $\beta_0 = \frac{33-2N_f}{12\pi}$, and N_f is the number of quark flavours that can appear in the loop diagrams. We can see from Eq. (1.9) that as Q^2 increases, α_S decreases, which is exactly the property of asymptotic freedom mentioned above.

1.3 Electroweak and Higgs Sectors

We now turn to the electroweak interactions that give rise to the nuclear beta decay reaction and processes in which quarks can be converted from one flavour to another. Our previous approach of constructing a Lagrangian that is invariant under local gauge transformations worked well for the cases of U(1) and SU(3), theories that both include *massless* gauge bosons—the photon and gluon respectively. We already know, however, that the carriers of the weak force—the W^{\pm} and Z boson—are definitely *not* massless.

The solution to this problem was provided by Glashow, Weinberg and Salam (GWS) [19–21]. Their theory was a unification of the electromagnetic and weak forces. It incorporates the Higgs mechanism and marries the concept of *spontaneous symmetry breaking* with local gauge invariance.

Beginning with the SU(2) symmetry group and following the same procedure as we did for QED and QCD, we say that our Lagrangian must be invariant under the gauge transformation

$$\psi \to e^{ig_W \omega(x) \cdot \mathbf{T}} \psi.$$
 (1.10)

The T are the three generators of the SU(2) group which can be expressed in terms of the Pauli spin matrices,

$$\mathbf{T} = \frac{1}{2}\boldsymbol{\sigma},$$

and obey the commutation relation

$$[\mathbf{T}^i, \mathbf{T}^j] = \epsilon^{ijk} \mathbf{T}^k, \tag{1.11}$$

with the structure constants of the group being given by the totally anti-symmetric tensor ϵ^{ijk} .

Before introducing the fields that are being transformed in this case, it is important to introduce the concept of handedness, since only left-handed fermions couple to the charged weak bosons. The *helicity* of a particle is defined as the projection of its spin along the direction of its momentum,

$$h \equiv \frac{\mathbf{S} \cdot \mathbf{p}}{p} = \frac{1}{2p} \begin{pmatrix} \boldsymbol{\sigma} \cdot \mathbf{p} & 0 \\ 0 & \boldsymbol{\sigma} \cdot \mathbf{p} \end{pmatrix}.$$

For spin-half particles, the component of spin along any axis is quantised to be $\pm 1/2$, therefore the eigenvalues of helicity are $\pm 1/2$. Fermions with helicity +1/2 are called right-handed, while those with helicity -1/2 are left-handed.

Helicity is only an intrinsic property for *massless* particles. For particles with mass it is always possible to transform to an alternative frame of reference in which the momentum is in the opposite direction, reversing the sign of the helicity. The *chirality* of a particle is a more general concept which is identical to the helicity for massless particles. The left- or right-handed components of a fermion spinor can be

obtained using the corresponding projection operator,

$$\gamma_{R,L} = \frac{1}{2} (1 \pm \gamma^5). \tag{1.12}$$

Since the W^{\pm} bosons couple fermions with different flavour, the fields are written as doublets in weak isospin space, e.g.

$$\psi(x) = \begin{pmatrix} v_e(x) \\ e^-(x) \end{pmatrix}.$$

In weak isospin space the ν_e and e^- have total weak isospin $I_W=1/2$ and third component of weak isospin $I_{W,3}(\nu_e)=+\frac{1}{2}$ and $I_{W,3}(e^-)=-\frac{1}{2}$. The weak isospin is related to the electric charge Q and so-called weak hypercharge Y by:

$$Y = 2(Q - I_{W3}).$$

The experimental observation that the charged weak current only couples to left-handed particles is achieved in the theory by assigning the right-handed particles to a singlet with total weak isospin $I_W = 0$, thus being unaffected by the SU(2)_L gauge transformation.

The covariant derivative required to keep the Lagrangian invariant under the transformation in Eq. (1.10) is

$$\mathcal{D}_{\mu} = \partial_{\mu} + i g_{W} \mathbf{T} \cdot \mathbf{W}_{\mu}(x) = \left(\partial_{\mu} \mathbf{I} + \begin{pmatrix} W_{\mu}^{3} & W_{\mu}^{1} + i W_{\mu}^{2} \\ W_{\mu}^{1} - i W_{\mu}^{2} & -W_{\mu}^{3} \end{pmatrix} \right)$$
$$= \left(\partial_{\mu} \mathbf{I} + \begin{pmatrix} W_{\mu}^{3} & \sqrt{2} W_{\mu}^{-} \\ \sqrt{2} W_{\mu}^{+} & -W_{\mu}^{3} \end{pmatrix} \right), \tag{1.13}$$

where we define

$$W_{\mu}^{\pm} = \frac{1}{\sqrt{2}} (W_{\mu}^{1} \mp i W_{\mu}^{2}). \tag{1.14}$$

The $W^a_\mu(x)$ are the three gauge fields required to keep the Lagrangian invariant. As we have alluded to in the final line of Eq. (1.13), the $W^\pm(x)$ will eventually be associated with the physical W-bosons. As we will see after introducing the Higgs mechanism below, the Z-boson will manifest itself as a mixture of fields associated with the U(1) $_Y$ and SU(2) $_L$ local gauge symmetries.

The crucial pieces which we are still missing are terms that provide masses to the bosons associated with the weak force. As we saw in the case of QED, a mass term of the type

$$\frac{1}{2}m_W^2A_\mu A^\mu$$

transforming according to Eq. (1.5) would become

$$\frac{1}{2}m_W^2(A_\mu + \partial_\mu \chi)(A^\mu - \partial^\mu \chi) \neq \frac{1}{2}m_W^2A_\mu A^\mu.$$

We therefore turn to the Higgs mechanism to help us solve this problem of a massless Standard Model.

1.3.1 The Standard Model Higgs

The minimal Higgs model consists of two complex scalar fields placed in a weak isospin doublet:

$$\phi = \begin{pmatrix} \phi^+ \\ \phi^0 \end{pmatrix} = \frac{1}{\sqrt{2}} \begin{pmatrix} \phi_1 + i\phi_2 \\ \phi_3 + i\phi_4 \end{pmatrix}. \tag{1.15}$$

Since we are aiming to generate masses for the electroweak gauge bosons, one of the scalar fields, labelled ϕ^0 must be neutral while the other must be charged.

The corresponding Lagrangian can be written as

$$\mathcal{L}_{\mathrm{Higgs}} = (\mathcal{D}_{\mu}\phi)^{\dagger}(\mathcal{D}^{\mu}\phi) - V(\phi)$$
,

with the necessary covariant derivative

$$\mathcal{D}_{\mu} = \partial_{\mu} + i g_{W} \mathbf{T} \cdot \mathbf{W}_{\mu} + i g' \frac{Y}{2} B_{\mu}$$

where the W_{μ} and B_{μ} are the 3+1 fields needed to keep the Lagrangian invariant under the now combined $SU(2)_L \times U(1)_Y$ gauge transformations.

The Higgs potential,

$$V(\phi) = \mu^2 \phi^{\dagger} \phi + \lambda (\phi^{\dagger} \phi)^2, \tag{1.16}$$

is shown in Fig. 1.1 and defined by the choice of parameters μ^2 and λ . The vacuum state is the lowest energy state of a field, and in the Higgs case corresponds to the minimum of the potential in Eq. (1.16). The parameter λ must be greater than zero to ensure that $V(\phi) \to \infty$ as $\phi \to \infty$, otherwise the theory would be unstable. μ^2 however could be positive or negative. When $\mu^2 > 0$, as in Fig. 1.1a, the potential has a minimum only at the origin. However when $\mu^2 < 0$ (Fig. 1.1b) the potential has an infinite set of degenerate minima described by a circle of radius

$$v = \sqrt{\frac{\mu^2}{\lambda}}.$$

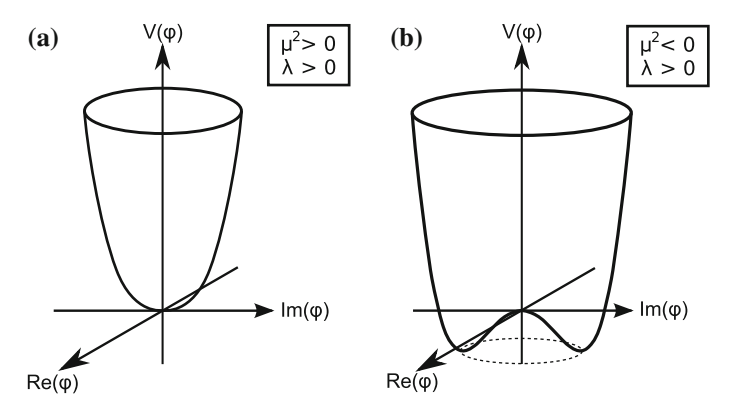


Fig. 1.1 The Higgs potential for $\mathbf{a} \ \mu^2 > 0$ and $\mathbf{b} \ \mu^2 < 0$

The physical vacuum corresponds to choosing a particular point on this circle. This non-zero vacuum expectation value is said to have spontaneously broken the gauge symmetry. We can now re-express the field in terms of excitations about the vacuum. We choose to work in the unitary gauge, which corresponds to choosing the complex scalar field $\phi(x)$ in Eq. (1.15) to be completely real,

$$\phi(x) = \frac{1}{\sqrt{2}} \begin{pmatrix} 0\\ v + h(x) \end{pmatrix}. \tag{1.17}$$

The h(x) is the Higgs field, and is the physical field in the unitary gauge.

It is the $(\mathcal{D}_{\mu}\phi)^{\dagger}(\mathcal{D}_{\mu}\phi)$ term in the Lagrangian that generates the masses of the gauge bosons:

$$(\mathcal{D}_{\mu}\phi)^{\dagger}(\mathcal{D}_{\mu}\phi) = \frac{1}{2}(\partial_{\mu}h)(\partial^{\mu}h) + \frac{1}{8}g_{W}^{2}(W_{\mu}^{(1)} + iW_{\mu}^{(2)})(W^{(1)\mu} - iW^{(2)\mu})(v+h)^{2} + \frac{1}{8}(g_{W}W_{\mu}^{(3)} - g'B_{\mu})(g_{W}W^{(3)\mu} - g'B^{\mu})(v+h)^{2}$$

$$(1.18)$$

and in particular the terms that are *quadratic* in the gauge boson fields determine their mass. The corresponding term for the *W*-boson ultimately appears as

$$\frac{1}{4}g_W^2 v^2 W_\mu^- W^{+\mu} \ ,$$

where we have used the definition of W^{\pm} from Eq. (1.14), and identify the mass of the W-boson as

$$m_W = \frac{1}{2}g_W v,$$

which is determined from the strength of the coupling to the Higgs field, g_W , and the vacuum expectation value of the Higgs field, ν .

The photon and Z_0 gauge bosons are identified as mixings of the neutral $W^{(3)}$ and B fields,

$$A_{\mu} = \frac{g'W_{\mu}^{(3)} + g_W B_{\mu}}{\sqrt{g_W^2 + g'^2}}$$
 with $m_A = 0$,

$$Z_{\mu} = \frac{g_W W_{\mu}^{(3)} - g' B_{\mu}}{\sqrt{g_W^2 + g'^2}}$$
 with $m_Z = \frac{1}{2} v \sqrt{g_W^2 + g'^2}$.

Interactions between the electroweak gauge bosons are described by the kinetic term of the Lagrangian,

$$\mathcal{L}_{\rm int,bosons} = -\frac{1}{4} W^i_{\mu\nu} W^{i\mu\nu} - \frac{1}{4} B_{\mu\nu} B^{\mu\nu}$$

where the field strength tensors can be written as

$$X_{\mu\nu}^{i} = \partial_{\mu}X_{\nu}^{i} - \partial_{\nu}X_{\mu}^{i} - gf^{ijk}X_{\mu}^{j}X_{\nu}^{k}. \tag{1.19}$$

X stands for W or B, g is the relevant coupling strength and f^{ijk} are the relevant structure constants of the group (i.e. the ϵ^{ijk} of Eq. 1.11).

The Lagrangian requires that interaction vertices exist that involve three and four electroweak bosons. We focus here just on the interaction between three bosons, the so-called triple gauge coupling (TGC) (such as the vector boson fusion process studied in Chap. 7). The interaction must conserve charge, and the Abelian nature of the U(1) group means that the photon cannot interact with itself. Interactions such as ZZZ or $ZZ\gamma$ are forbidden by the structure of the field strength tensor in Eq. (1.19). The term ϵ^{ijk} will only allow a TGC vertex of the form $W^1W^2W^3$ (or cyclic permutations) where W^1 and W^2 form the W^\pm bosons and W^3 contributes to forming the Z-boson and photon. Therefore the only allowed TGCs in the Standard Model are of the form W^+W^-Z and $W^+W^-\gamma$.

Masses for the fundamental fermions can be included in a similar manner. It is not possible to simply add a fermion mass term to the Dirac Lagrangian, since the different transformation properties of the left- and right-handed chiral states violate the required gauge invariance of the $SU(2)_L \times U(1)_Y$ symmetry group. However, a term in the Lagrangian of the form

$$-g_f(\overline{L}\phi R + \overline{R}\phi^{\dagger}L) \tag{1.20}$$

can be constructed, which does satisfy the $SU(2)_L \times U(1)_Y$ gauge symmetry.

For the case of the electron, this corresponds to

$$\mathcal{L}_{e} = -g_{e} \left[\left(\overline{\nu}_{e} \ \overline{e} \right)_{L} \begin{pmatrix} \phi^{+} \\ \phi^{0} \end{pmatrix} e_{R} + \overline{e}_{R} \left(\phi^{+*} \ \phi^{0*} \right) \begin{pmatrix} \nu_{e} \\ e \end{pmatrix}_{L} \right]$$
(1.21)

where g_e is known as the Yukawa coupling of the electron to the Higgs field. After applying the spontaneous symmetry breaking prescription and setting $\phi(x)$ as in Eqs. (1.17), (1.21) can be written

$$\mathcal{L}_e = -m_e \overline{e}e - \frac{m_e}{v} \overline{e},$$

where the first term gives us the electron mass, $m_e = \frac{g_e v}{\sqrt{2}}$, and the second term gives rise to the coupling between the electron and Higgs boson.

Yukawa interactions can also be included that introduce mass terms for the other fermion fields. Analogously to the doublets created for the leptons, quark doublets can be written,

$$\begin{pmatrix} u \\ d' \end{pmatrix}, \begin{pmatrix} c \\ s' \end{pmatrix}, \begin{pmatrix} t \\ b' \end{pmatrix}.$$
 (1.22)

In order to provide mass terms to the up-type quarks, the conjugate doublet must first be formed from the fields in Eq. (1.15),

$$\phi_C = -i\sigma_2\phi^* = \begin{pmatrix} -\phi^{0*} \\ \phi^- \end{pmatrix} = \frac{1}{\sqrt{2}} \begin{pmatrix} -\phi_3 + \phi^4 \\ \phi_1 - i\phi_2 \end{pmatrix}$$

then, in general, gauge invariant mass terms can be constructed from either Eq. (1.20) or

$$\mathcal{L} = g_f \left[\overline{L} \phi_C R + (\overline{L} \phi_c R)^{\dagger} \right]$$

and as before the Yukawa couplings of the fermions to the Higgs boson are related to the fermion masses by

$$g_f = \sqrt{2} \frac{m_f}{v}.$$

The down-type quarks in Eq. (1.22) were denoted with primes because they refer to the weak eigenstates of the quarks, which differ from the mass eigenstates (i.e. the physical d, s, b quarks). The idea of weak eigenstates was introduced by Cabbibo to explain the difference between the strength of the u-d and u-s weak vertices. The weak eigenstates are related to the mass eigenstates via the Cabbibo-Kobayashi-Maskawa (CKM) matrix

$$\begin{pmatrix} d' \\ s' \\ b' \end{pmatrix} = V_{CKM} \begin{pmatrix} d \\ s \\ b \end{pmatrix} = \begin{pmatrix} V_{ud} & V_{us} & V_{ub} \\ V_{cd} & V_{cs} & V_{cb} \\ V_{td} & V_{ts} & V_{tb} \end{pmatrix} \begin{pmatrix} d \\ s \\ b \end{pmatrix},$$

and the current values of the real parts of the elements of the CKM matrix are [18]:

$$V_{CKM} = \begin{pmatrix} 0.97427 \pm 0.00015 & 0.22534 \pm 0.00065 & 0.00351^{+0.00015}_{-0.00014} \\ 0.22520 \pm 0.00065 & 0.97344 \pm 0.00016 & 0.0412^{+0.0011}_{-0.0005} \\ 0.00867 \pm^{+0.00029}_{-0.00031} & 0.0404^{+0.0011}_{-0.0005} & 0.999146^{+0.00021}_{-0.000046} \end{pmatrix}.$$

By requiring invariance under local gauge transformations, which provides the necessary fields, and by including a spontaneously broken symmetry to provide masses to the gauge bosons, we have arrived at the Standard Model of particle physics. The symmetry group transformation which our theory—or theories, those of QED, QCD and the Electroweak theory—is invariant under can be summarised as $SU(3) \times SU(2)_L \times U(1)_Y$. We turn now to some of the practicalities of performing calculations and producing theoretical predictions for use at a hadron collider such as the LHC.

1.4 The Physics of Hadron Colliders

In particle physics at hadron colliders one of the most important quantities for testing the validity of the Standard Model is the *cross section* for a particular set of final-state particles to be produced from a given initial state. The cross section is an expression of the quantum-mechanical probability for a particular interaction to take place. Often it is the differential cross section that is measured. This describes the variation of the cross section as a function of kinematic properties of final-state particles. The cross section for the process where two initial-state particles interact to produce N final-state particles is given by:

$$d\sigma = \frac{1}{2s} \overline{\Sigma} |M_{fi}|^2 d\Phi_N,$$

where M_{fi} is the Lorentz invariant matrix element, or amplitude, for producing the final state f from initial state i, and the $\overline{\Sigma}$ implies a sum over all unobserved quantum numbers in the final state and an average over quantum numbers in the initial state. The variable s is the centre-of-mass energy, defined as

$$s = (p_1 + p_2)^2,$$

where p_1 and p_2 are the 4-momentum of the two incoming particles. The Lorentz invariant phase space for the final state, $d\Phi_N$ is given by

$$d\Phi_N = (2\pi^4)\delta^4(p_1 + p_2 - \sum_i^N p_i) \prod_i^N \frac{d^4 p_i}{2\pi^4} (2\pi)\delta(p_i^2 - m_i^2) ,$$

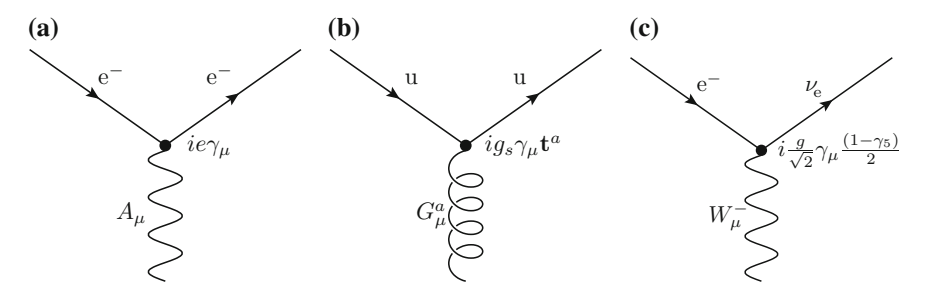


Fig. 1.2 Examples of Feynman diagrams for some of the fundamental interaction vertices in the Standard Model. **a** Shows an electron interacting with a photon, **b** shows an up quark interacting with a gluon and **c** shows an electron interacting with a W^- -boson and changing into an electron neutrino. In all diagrams time runs from *left-to-right*

where p_i is the 4-momentum of each outgoing particle and m_i is its mass. The δ -functions ensure that all final-state particles are on mass-shell and that energy and momentum are conserved in the interaction.

The matrix element can be calculated using Feynman diagrams. Examples of the Feynman diagrams corresponding to the fundamental QED and QCD interaction vertices are given in Fig. 1.2. Each piece of the Feynman diagram represents a mathematical object relevant to the theory describing the interaction. Each external (i.e. only attached to one vertex) initial- or final-state (anti-)fermion line represents a plane wave Dirac spinor. External vector boson lines represent a polarisation vector, e.g. ϵ_{μ} , and internal lines, which are connected at two vertices and neither enter or leave the diagrams, represent so-called propagator terms. Anti-particles are typically drawn as lines with arrows pointing backwards in time, from right-to-left.

Feynman diagrams can also be helpful in elucidating the *colour structure* of a scattering process. At leading order we can draw colour lines to represent the flow of colour through a diagram, as shown in the examples in Fig. 1.3. In the example on the left the quarks in the final state are *colour connected* to each other, since the colour singlet photon carries no colour charge. In contrast, in the example on the

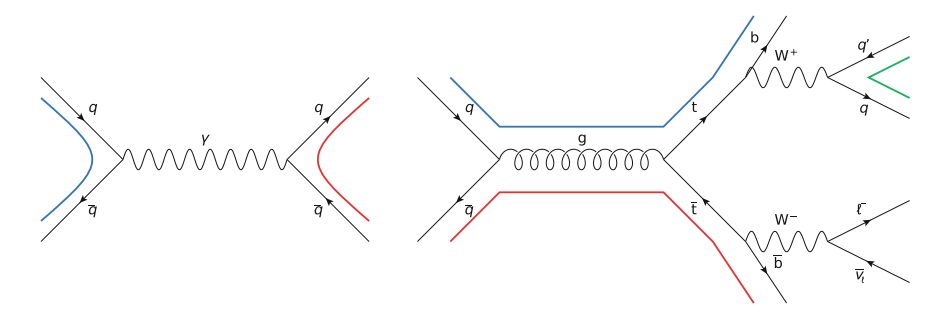


Fig. 1.3 Examples illustrating processes with different colour structure

right hand side the colour carried by the initial-state quarks flows through the gluon and into the final-state *b*-quarks. The W-boson, being a colour singlet, produces a pair of quarks which are colour connected to each other. The colour structure of a process affects the way in which additional radiation is produced. Typically more QCD radiation is produced in the region between two colour connected partons. It is possible to exploit this property by requiring or vetoing additional radiation in specific regions of phase space in an attempt to distinguish between processes with different colour flow (cf. Sect. 1.6 and Chaps. 5, 6 and 7).

A scattering process may proceed through multiple Feynman diagrams. The complete matrix element for a process is therefore the sum of the individual diagrams. For example if two Feynman diagrams can be drawn for a scattering process then after squaring the total matrix element,

$$M_{\text{tot}} = |M_1 + M_2|^2 = |M_1|^2 + |M_2|^2 + M_1^* M_2 + M_1 M_2^*,$$
 (1.23)

interference between the diagrams, as in the final two terms of Eq. (1.23), will result and should be carefully considered (cf. Sect. 7.1).

Life at the LHC is complicated by the fact that it is protons that are brought to collision. The protons are composite particles made up of quarks and gluons, collectively referred to as partons, and at high-enough energies (and therefore shortenough distances) the partons interact as if they were free particles. The interaction represented by the matrix element is assumed to take place between the partons. Fortunately it is possible to separate, or *factorise* the calculation of the cross section into a hard-scattering process which occurs on short time scales, and a long-range part which takes into account the interaction of the partons inside the hadrons and other lower energy ('softer') non-perturbative physics which occurs on time scales much longer than the hard scatter. The cross section for a scattering process initiated by two hadrons P_1 and P_2 and producing some final-state X, $d\sigma_{P_1,P_2\to X}$, is given by [22]:

$$d\sigma_{P_1,P_2\to X} = \sum_{i,j} \int dx_1 dx_2 f_{i/P_1}(x_1,\mu_F^2) f_{j/P_2}(x_2,\mu_F^2) d\hat{\sigma}_{i,j\to X}.$$

 $\hat{\sigma}_{p_i,p_j \to X}$ is the partonic cross section for the interaction $p_i, p_j \to X$, calculable using perturbation theory and the Feynman diagram techniques presented above. The $f_{a/b}(x,\mu_F)$ are the so-called parton distribution functions (PDFs) and give the probability of obtaining a parton a from hadron b entering the hard scatter with momentum fraction x (i.e. parton p_1 carries momentum x_1P_1). The PDFs are defined at a factorisation scale μ_F^2 . The factorisation scale is just an arbitrary parameter and can be thought of as a scale that separates the high- and low-energy (short- and long-distance) physics. For example a parton emitted with a small transverse momentum, less than the scale μ_F^2 , can be considered part of the structure of the hadron and is absorbed into the PDFs. A high transverse momentum parton is part of the short-distance cross section. The more terms included in the perturbative expansion, the

weaker the dependence on the scale μ_F will be. In practice, as was the case for the renormalisation scale mentioned in Sect. 1.2.1, the factorisation scale is varied when producing theoretical predictions, to estimate the uncertainty introduced by ignoring higher-order corrections.

1.4.1 Next-to-Leading Order Corrections

We have been assuming so far that we are working with leading order (LO) matrix elements and taking just the first relevant term of the perturbative expansion. By including higher-order terms we can greatly improve the accuracy of predictions and reduce the effects of scale uncertainties. However with improved accuracy comes greatly increased difficulty in performing the calculations. In recent years much effort has been focussed on evaluating matrix elements at next-to-leading—or higher—orders (NLO, NNLO, N³LO etc.)

An NLO cross section is made up of three parts. The LO, or Born-level, part and two corrections—the virtual and real-emission parts. Example diagrams for the LO, virtual and real emission parts for the case of tt production are shown in Fig. 1.4. Schematically, the differential cross section is given by [23]:

$$d\sigma^{NLO} = d\widetilde{\Phi}_n \left[\mathcal{B}(\widetilde{\Phi}_n) + \alpha_s \mathcal{V}(\widetilde{\Phi}_n) \right] + d\widetilde{\Phi}_{n+1} \alpha_s \mathcal{R}(\widetilde{\Phi}_{n+1}) , \qquad (1.24)$$

where \mathcal{B} , \mathcal{V} and \mathcal{R} are the Born, virtual and real emission parts, and $d\widetilde{\Phi}_n$ stands for integrals over the n-particle final state and incoming partons. The main difficulty in working at NLO is dealing with the divergences that appear in the calculations. Divergences are encountered in both the low-energy and collinear (infrared), and high-energy (ultraviolet) limits of the calculation. The ultraviolet divergences are taken care of by regularisation and renormalisation procedures. The infrared divergences appear in both the virtual and real-emission parts of the calculation, which involve integrals over an n- and n + 1-particle final-state, respectively. In order to make sure that these divergences cancel and produce sensible results so-called infrared subtraction algorithms [24–31] are used. This involves subtracting terms

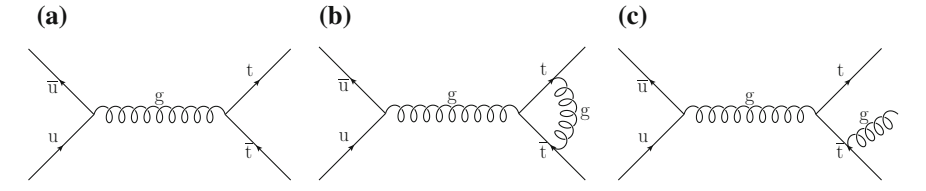


Fig. 1.4 Example Born-level, virtual correction and real-emission Feynman diagrams for the production of $t\bar{t}$. a Born-level, **b** virtual correction, **c** real emission

from the real-emission part of the calculation such that it becomes finite and can be integrated over the full n + 1-particle phase-space. The integrated subtraction terms are then added back in and combined with the virtual correction term.

1.5 Monte Carlo Event Generators

Performing calculations of cross sections by hand is a difficult and time-consuming business, and the prospect of automating the procedure is a highly attractive one. Once the relevant matrix elements have been calculated for a process of interest, the problem remains of dealing with the divergences that arise, before integrating them and ultimately producing a final-state that is typically made up of hundreds of physically observable particles.

General-purpose Monte Carlo event generators are an integral part of modern particle physics. Describing the complex final states of the high-energy proton-proton collisions at the LHC is a problem that is ideally suited to computer simulation using Monte Carlo techniques. The accuracy of Monte Carlo integration improves as $1/\sqrt{N}$, where N is the number of phase-space points, or events, generated, regardless of the dimension of the integral. Given that the dimension of the integrals that must be evaluated is proportional to the number of particles in the final state, an integration technique whose accuracy does not depend on dimension is obviously a perfect candidate.

1.5.1 Matrix Elements

The generation of an event by Monte Carlo (MC) methods is split up into several steps. First is the evaluation of the matrix elements, calculated to some fixed order in perturbative QCD, typically LO or NLO in α_S . As discussed earlier, all Feynman diagrams that contribute to the process of interest must be calculated and summed coherently. Modern MC generators have had for some time the ability to automatically calculate all relevant leading order Feynman diagrams contributing to a specific process. NLO calculations are typically performed by hand, before putting the results into MC programs for general use.

1.5.2 Parton Showers

Figure 1.5 shows a comparison between a Feynman diagram that would contribute to the matrix element calculation for a dijet event at the LHC, and an actual dijet event detected by ATLAS. The differences are clear: we do not detected isolated, high-energy partons, but sprays of low-energy *hadrons* which align themselves along the

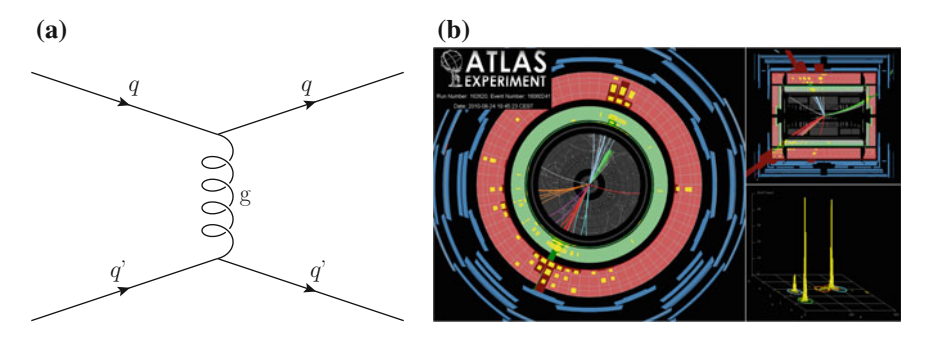


Fig. 1.5 From [32]. a Shows an example of a leading-order Feynman diagram contributing to the production of dijet events. b Shows an actual dijet event recorded by the ATLAS detector

approximate directions of the original partons. We also see the presence of additional jets of particles, emerging from real-emission corrections to the diagram in Fig. 1.5a and changing the topology of the event compared to what we might expect from our naïve 2-to-2 picture.

The parton shower is a process-independent tool that can help to transform the simple partonic picture of an event into a more realistic one, and accounts for both real and virtual corrections that are encountered in next-to-leading order calculations. Rather than calculating the NLO pieces exactly, approximations are used that take into account only the dominant contributions at each order. The real-emission corrections are formulated as series of $1\rightarrow 2$ (or $2\rightarrow 3$ in the case of so-called dipole showers) splittings. The partons resulting from the splitting are each split again, and the process is iterated to produce a cascade of partons with successively lower energies. Strictly speaking the parton shower takes care of the soft and collinear emissions. These emissions are logarithmically enhanced, i.e., if a given term in the perturbative expansion contributes at order α_s^n , a logarithmically-enhanced term may contribute with α_s \ln^{2n} . Therefore even though α_s may be small, if the logarithms are sufficiently large they may prevent the perturbative series from converging. The parton shower overcomes this problem by including such logarithmically-enhanced terms to all orders in αs using so-called resummation techniques.

The virtual corrections encountered at higher orders are taken into account in the parton shower by estimating the probability of *not* splitting during the evolution, given by the so-called Sudakov form factor.

We now have a mechanism through which the hard partons appearing in Feynman diagrams can evolve down in scale until a point at which α_S becomes large and perturbative QCD is no longer applicable (~1 GeV). Parton showering is used to evolve

 $^{^1}$ Other logarithms are also encountered, for example $\alpha_s^n \ln^{2n-1}$, $\alpha_s^n \ln^{2n-2}$ etc. In so-called leading-logarithmic parton showers it is typically the case that the $\alpha_s \ln^{2n}$ and $\alpha_s^n \ln^{2n-1}$ terms are included correctly. The notation used here, of a logarithm without an argument, represents general logarithmic functions. In practice the logarithms have arguments involving ratios of scales relevant to the physical process being calculated. See for example Sect. 1.6, where logs of the form $\ln(Q/Q_0)$ are encountered.

the hard matrix elements both forwards and backwards in time. In the case of the forward, or time-like, shower the initial energies of the final-state partons are known, and partons with a range of momenta can result as the event generation proceeds. The partons entering the initial state of the hard process, however, could be the results of the *n*th splittings of the unknown partons that originally emerged from the proton. A space-like parton shower evolution therefore also takes place (backwards in time) from the known final energies of the initial-state partons. Partons resulting from the time-like shower are referred to as making up the final-state radiation (FSR) and those from the space-like shower as initial-state radiation (ISR). However the split is purely for ease of implementation. The separation between radiation arising from the initial and final state is gauge dependent and therefore scheme dependent, and therefore in principle the two are not separable.

1.5.2.1 Matching Matrix Elements to Parton Showers

Fixed-order matrix element calculations provide accurate descriptions for final states involving hard and well-separated partons. Nowadays they are also relatively easily automated, and leading order calculations can be performed with several additional partons in the final state. (e.g. $t\bar{t}+3$ partons). Including NLO contributions further improves the accuracy of predictions and reduces dependencies on non-physical scales. Parton showers are exact in the soft and collinear limits—where the fixed-order calculations diverge—and so in recent years a lot of effort has been put into methods of combining these techniques to enable the generation of events with as much precision as possible.

The main problem one encounters when attempting to match fixed-order calculations to parton showers is one of double counting. Following the same example given in [33]; suppose we want to generate events containing a Z-boson and one additional parton (Z+1j). We could get a good estimate of the cross-section by asking for Z+1j events as the initial hard process in our MC generator. The Z+2j rate, however, would be poorly estimated. A naïve solution would be to generate Z+2j events with our LO generator, pass the matrix elements to our parton showering algorithm and then combine the resulting events. Proceeding like this however, would lead us to the problem depicted in Fig. 1.6. In some events (left,middle) applying the parton shower to the matrix element partons leads to just soft and collinear emissions. However, since it is probabilistic in nature, it is possible for the parton shower to produce hard, wide-angle emissions (right). These events are in the same region of phase space as the showered Z+2j events. Therefore if we simply added the showered Z+1j and Z+2j events we would end up with twice the number of events shown in the middle and right panels that we would expect to find in reality.

Several techniques exist to match LO matrix elements with parton showers while accounting for this double counting. So-called MEPs (Matrix Element plus Parton Shower) events are produced. Currently the two most commonly used methods fall into the category of slicing techniques. The CKKW [34] and MLM [35] matching schemes proceed by separating the phase space into two regions—one that is meant

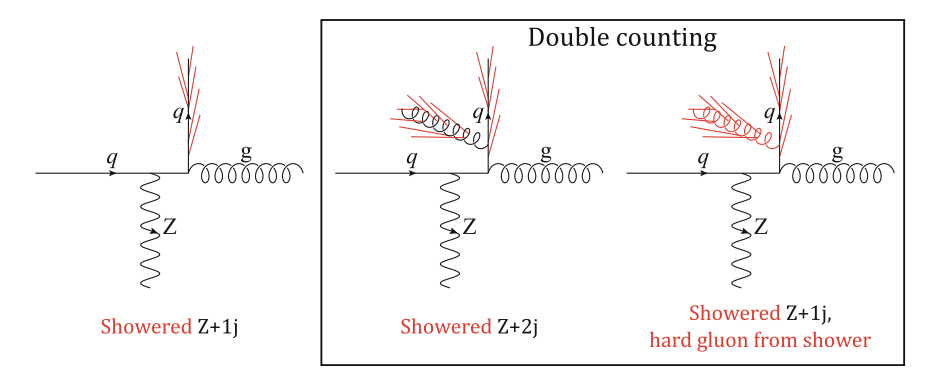


Fig. 1.6 Adapted from [33]. Cartoon showing the double counting problems that can arise when naïvely attempting to combine events after parton showering

to be well described by the hard matrix elements and the other by the parton shower. The separation between the two regions is adjusted via a *matching scale*. Physics at energies well above the matching scale should be independent of the scale chosen, and distributions at scales around the matching scale should be reasonably smooth, providing the matching scale has been chosen sensibly and the parton shower can be expected to give a reasonable description of the emissions.

Matching NLO calculations to parton showers results in double counting of a similar kind, this time between the real emission pieces of the NLO calculation and hard emissions produced by the shower. Two matching techniques have been developed—the MC@NLO [36] and POWHEG [37] methods—both can be thought of as subtraction techniques.

The MC@NLO (Monte Carlo at Next-to-Leading Order) method involves analytically calculating how the first branching in a parton shower starting from an n-particle final-state would populate an n+1-particle phase space. These terms are an approximation of the actual NLO corrections. The parton shower expression is then subtracted from the n+1-body NLO matrix element. The two pieces agree with each other in the soft and collinear limits and the singularities there cancel, leaving finite cross sections for the n and n+1-particle final states. Drawbacks of the MC@NLO method are that it requires a deep understanding of the parton shower used. NLO matrix elements calculated with the MC@NLO technique can only be interfaced to one parton shower since the relevant terms of the parton shower expansion must be calculated in advance. MC@NLO also produces events with negative weights, since there is no guarantee that the parton shower terms will be smaller in magnitude than the NLO ones.

Avoiding the negative weighted events produced by MC@NLO was one of the motivations for developing the POWHEG (**PO**sitive **W**eight **H**ardest **E**mission **G**enerator) formalism for matching NLO MEs with parton showers. The basic idea of POWHEG is to calculate the hardest real emission in the event in such a way to be sufficient to give the correct NLO result. It does this by introducing a modified

Sudakov form factor which essentially gives the probability of no real emissions with transverse momentum, p_T , above some scale k_t . Subsequent emissions are left to the parton shower algorithm, with some additional vetoing implemented to ensure that the shower does not produce any radiation harder than the POWHEG emission. The POWHEG method, as the name implies, is able to generate event with no negative weights (although in practice a tiny percentage of events with negative weights can result). It also allows matrix elements to be interfaced to any shower MC.

Both MC@NLO and POWHEG are formally equivalent at NLO, but not beyond. Any differences in predictions made using the different techniques would be interesting probes of higher-order corrections.

1.5.3 Hadronisation and Underlying Event

Once the partons have reached an energy of (\sim 1 GeV) the value of α_S is too large to produce a quickly-converging perturbative expansion. At this point we must turn to models, rather than calculations from first principles, to attempt to describe features of the underlying physical processes. Although perturbative QCD can no longer be used, we still have the general principles of Lorentz invariance and unitarity to help guide the solutions. Several models exist that attempt to confine the post-shower partons into physically observable hadrons. The two most popular are the Lund string model [38, 39] and the cluster model [40].

The underlying event, or multiple parton interactions (MPI) are typically soft collisions between additional partons that were not involved in the hard scatter. MPI is usually modelled as low-p_T QCD 2 \rightarrow 2 scatters. Although the fraction of multiple interactions resulting in reconstructible jets is quite small, they can give significant corrections to the overall colour flow of the event. This can produce major changes to quantities like the overall particle multiplicity of the final state.

1.5.4 Event Generators

General purpose Monte Carlo event generators make use of the full suite of technologies listed above to produce events containing stable final-state particles that can be analysed in the same way as events recorded by a detector. The most well-used MC event generators are PYTHIA [41, 42], HERWIG [43, 44] and SHERPA [45]. These generators automatically calculate all relevant leading-order Feynman diagrams for a user-requested process. The required phase-space integrations are then performed, before applying parton shower algorithms and models of hadronisation and the underlying event. It is also possible to take matrix elements generated using external programs and interface them with the parton shower, hadronisation and underlying event models of these so-called shower Monte Carlos (SMCs). Indeed it is often required to perform this step. The events produced by the NLO event generators

MC@NLO and POWHEG and the multi-leg leading order generators MADGRAPH [46] and ALPGEN [47] contain partons in the final state of their event records. These events cannot be compared to experimental data until the partons have been showered and hadronised into physically observable particles.

Recent developments include the automatic generation of NLO matrix elements and matching to parton showers in aMC@NLO + MADGRAPH5 [48], SHERPA [49], and MatchBox in HERWIG++ [50]; and the merging of NLO predictions for the production of multi-jet final states with parton showers, with the MEPs@NLO [51] technique in SHERPA.

1.5.5 Theoretical Uncertainties

Uncertainties in the theoretical predictions arise due to scales introduced to truncate or separate parts of the calculation. The factorisation scale, μ_F , for example was introduced as an arbitrary parameter that separated the short and long-distance physics. However, although it is in principle arbitrary, a sensible parameter value should be chosen in order to minimize the truncation error.

For example [32], for processes like Drell-Yan production $(q\bar{q} \to Z/\gamma^* \to \ell^+\ell^-)$ which are characterised by a single well-defined energy scale—the dilepton invariant mass in this case—the choice of μ_F is easy to make, and choosing μ_F too far from this scale would lead to large missing higher-order terms. In processes in which multiple objects are produced (e.g. Z+jets) there are several equally-valid choices of scale that can be made by combining the various final-state objects, then taking either the highest or lowest QCD scale involved.

Similar arguments apply to the renormalisation scale, μ_R , and it is often the case that μ_R and μ_F are set to the same value. Conventionally the uncertainty in the choice of μ_R and μ_F is estimated by varying the scales individually up and down by a factor of two.

Uncertainties associated with the matching of matrix elements with the parton shower are often estimated by varying the corresponding matching scales, and uncertainties in the modelling of MPI are also assessed by varying relevant parameters. An example of a comprehensive evaluation of the uncertainties associated with event generation and comparisons of the uncertainties to experimental data can be found in [52].

1.5.6 Jets

The term *jet* has already been used without giving a definition of what we mean by such an object. An equally valid interpretation of the dijet event in Fig. 1.5b, if we were to slightly change our definition of what we mean by a jet, could be a tri-jet event with the third jet being made up of the particles colour-coded in light

blue. Deciding between these interpretations means deciding exactly how hard and separated in angle an emission must be for it to be considered a unique jet.

A jet, then, is something that *we* define, rather than some pre-existing object that we attempt to find. The aim is to choose a definition that gives us jets that as closely as possible resemble the underlying partons that took part in the hard scatter. Hadronisation and the underlying event should therefore not have a large effect on the definition of our jets. Indeed for us to have any confidence in the jets we define the application of the jet definition to the partons produced at the end of the matrix element calculation, the hadrons we're left with at the end of the event generation, or the tracks and calorimeter hits we obtain after a simulation of the detector, should all yield the same set of jets. A crucial property of the jet algorithm is that it should be soft and collinear safe. That is, if we add an infinitely soft parton to our event it should not affect the jets we produce at all. Similarly, our jet algorithm should be capable of producing the same set of jets in an event where a hard parton splits collinearly, with the resulting partons taking approximately equal shares of the energy.

These properties were not satisfied in early cone-based jet-finding algorithms [53]. Nowadays so-called cluster algorithms are used almost exclusively for theoretical and experimental studies alike, the k_t [54] and anti- k_t [55] being two of the most popular. The cluster algorithms work by iteratively combining constituents—be they partons, hadrons, calorimeters cells—into jets based on two distance measures:

$$d_{ij} = \min(k_{Ti}^{2p}, k_{Tj}^{2p}) \frac{\Delta R_{ij}^2}{R^2}$$
$$d_{iB} = k_{Ti}^{2p},$$

where $\Delta R_{ij}^2 = (y_i - y_j)^2 + (\phi_i - \phi_j)^2$, y_i is the rapidity and ϕ_i is the azimuthal angle of object i. d_{ij} gives the distance between two objects, and d_{iB} the distance between the object and the beam. The two measures are calculated for all pairs of objects, if the smallest value is a d_{ij} then objects i and j are combined, otherwise the object i is removed from the list and considered as a complete jet. The process is repeated until all objects in the event are called jets. R defines the approximate size of the jet. If R is large then the d_{ij} will be smaller and more objects are combined before the jet is complete.

The difference between the types of cluster algorithm comes from the choice of p. For the k_t algorithm p=1. Softer particles are merged first, leaving any hard structure in the jet until the last combination. In the anti- k_t algorithm p=-1; harder objects are merged first, and the jets are built up starting from a hard core.

An attractive feature of anti- k_t jets is that they tend to be much more regular in shape. However information about any hard structure within the jet is lost. Techniques that aim to explore this sub-jet structure usually proceed by reversing the order of the clustering of the jet constituents. Performing this task with a jet produced using the k_t algorithm is like separating a pair of chopsticks—we can immediately see whether any structure is present inside the jet. The decay of a boosted W-boson to two quarks might produce this chopstick-like or two-pronged topology. Attempting

to look inside an anti- k_t jet, however, would be more like peeling a vegetable. In reversing the clustering sequence we would just be removing soft partons from the edge of the jet and learn nothing about any substructure hidden within.

A third alternative is the Cambridge-Aachen algorithm in which p=0 and the jet constituents are clustered according only to their spatial separation. Cambridge-Aachen jets also provide useful substrucure information, and are used extensively in the studies presented in Chap. 6.

1.6 Jet vetoing

The proton-proton collisions produced by the LHC provide a fantastic test bed for a wide range of aspects of QCD. The cross section for inclusive production of QCD jets and dijets is huge. Predictions of these quantities from perturbative QCD have been compared to experimental data and found to be in remarkable agreement [56, 57].

A direct probe of the colour structure of a hard process is the probability that it does not emit any *additional* radiation into some well-defined region of phase space. For example a widely-studied process is that of dijet production with a veto on the emission of additional QCD activity in the rapidity interval between the two jets. The process has been studied at HERA [58–60], the Tevatron [61] and also more recently at the LHC [62].

The quantity that is often measured is the jet veto efficiency, or gap fraction and can be written as a ratio of cross sections,

$$f^{gap} = \frac{\sigma_{\text{fid.}}^{\text{gap}}}{\sigma_{\text{fid.}}}$$

where $\sigma_{\rm fid.}$ is the fiducial cross section for the production of the system of interest (e.g. dijets with average p_T greater than some value Q, or a $t\bar{t}$ system), and $\sigma_{\rm fid.}^{\rm gap}$ is the fiducial cross section for the production of the same system with the requirement that there be no additional jets with p_T greater than some scale Q_0 , in a chosen region of rapidity.

Using the property of unitarity, we can write

$$\sigma_{\text{fid.}} = \sigma_{\text{fid.}}^{\text{gap}} + \sigma_{\text{fid.}}^{\overline{\text{gap}}}$$

$$f^{gap} = 1 - \frac{\sigma_{\text{fid.}}^{\overline{\text{gap}}}}{\sigma_{\text{fid.}}}$$
(1.25)

where $\sigma_{\rm fid.}^{\rm \overline{gap}}$ is the fiducial cross section for the production of the system of interest *with* at least one additional jet in the defined region of rapidity. Equation 1.25 is more tractable theoretically and is often used when studying the properties of the gap fraction analytically [63].

By studying the gap fraction it is possible to gain insight into a wide range of perturbative QCD phenomena. For example, as the separation in rapidity between the two jets defining the dijet system becomes large BFKL-like dynamics are expected to become increasingly important [64–70].

Although it is possible to measure the gap fraction with high precision due to many experimental uncertainties cancelling when taking the ratio of cross-sections, the gap fraction is prone to quite large theoretical uncertainties. The restriction of the additional emission to a corner of phase space when computing the 'gap' cross section leads to a miscancellation between the real and virtual corrections in the calculation. This in turn leads to logarithms of the form $\left[\alpha_s \ln(\frac{Q}{Q_0})\right]^n$ (cf. Sect. 1.5.2). If Q is significantly larger than Q_0 then these logarithms will be large, and the perturbative series will no longer converge. Therefore these large logarithms must be resummed to all orders. This is not a straightforward task, and much work has been invested in it. Developments include the discovery of non-global logarithms [71, 72], which can appear when gluons emitted outside of the gap region then radiate back into it, and super-leading logarithms [73] of the form $\alpha_s^n \ln^{n+1}(\frac{Q}{Q_0})$ which appear at higher orders $(n \ge 4)$ but are formally more important than the leading logarithms. Theoretical predictions of the gap fraction and other non-global observables are an active and challenging area of research, and indeed with precise experimental measurements having already been performed, it is clear that "the accuracy of the experimental data already demands better theoretical calculations" [63].

References

- 1. Gell-Mann, M. (1982). Strangeness. Journal of Physics (France), 43, 395-408.
- Nishijima, K. (1955). Charge independence theory of V particles. Progress of Theoretical Physics, 13, 285–304.
- 3. Gell-Mann, M. (1961). The Eightfold way: A theory of the strong interaction symmetry. doi:10. 2172/4008239.
- 4. Barnes, V. E. (1964). Observation of a hyperon with strangeness minus three. *Physical Review Letter*, 12(8), 204–206.
- 5. Greenberg, O. W. (1964). Spin and unitary-spin independence in a Paraquark model of baryons and mesons. *Physical Review Letter*, 13(20), 598–602.
- 6. Ablikim, M. (2013). Observation of a charged Charmoniumlike structure in $e^+e^- \rightarrow \pi^+\pi^-J/\psi$ at $\sqrt{s} = 4.26$ GeV. *Physical Review Letter*, 110, 252001.
- 7. Liu, Z. Q. (2013). Study of $e^+e^- \to \pi^+\pi^- J/\psi$ and observation of a charged charmonium-like state at belle. *Physical Review Letter*, 110(25), 252–002.
- Arnison, G. (1983). Experimental observation of isolated large transverse energy electrons with associated missing energy at s=540 GeV. *Physics Letters B*, 122, 103–116. ISSN: 0370-2693.
- Banner, M., et al. (1983). Observation of single isolated electrons of high transverse momentum in events with missing transverse energy at the CERN pp collider. *Physics Letters B*, 122, 476– 485. ISSN: 0370-2693.
- 10. Arnison, G., et al. (1983). Experimental observation of lepton pairs of invariant mass around 95 GeV/c2 at the CERN SPS collider. *Physics Letters B*, 126, 398–410. ISSN: 0370-2693.
- 11. Bagnaia, P., et al. (1983). Evidence for $Z0 \rightarrow e^+e^-$ at the CERN pp collider. *Physics Letters B*, 129, 130–140. ISSN: 0370-2693.

References 29

12. Higgs, P. W. (1964). Broken symmetries and the masses of gauge bosons. *Physical Review Letter*, 13(16), 508-509.

- 13. Englert, F., & Brout, R. (1964). Broken symmetry and the mass of gauge vector mesons. *Physical Review Letter*, *13*(9), 321–323.
- 14. Guralnik, G. S., Hagen, C. R., & Kibble, T. W. B. (1964) Global conservation laws and massless particles. *Physical Review Letter*, *13*(20), 585–587.
- 15. Aad, G., et al. (2012). Observation of a new particle in the search for the standard model Higgs boson with the ATLAS detector at the LHC. *Physics Letter B*, 716, 1–29.
- 16. Chatrchyan, S., et al. (2012). Observation of a new boson at a mass of 125 GeV with the CMS experiment at the LHC. *Physics Letter B*, 716, 30–61.
- 17. The Nobel prize in physics (2013). Retrieved October 25, 2014, from http://www.nobelprize.org/nobel_prizes/physics/laureates/2013/.
- 18. Beringer, J., et al. (2012). Review of particle physics. *Physics Review D*, 86(1), 010001.
- Glashow, S. L. (1961). Partial-symmetries of weak interactions. *Nuclear Physics*, 22, 579–588.
 ISSN: 0029-5582.
- Salam, A., & Ward, J. (1964). Electromagnetic and weak interactions. *Physics Letters*, 13, 168–171. ISSN: 0031-9163.
- 21. Weinberg, S. A. (1967). Model of leptons. Physical Review Letter, 19(21), 1264-1266.
- 22. Ellis, R. K., Stirling, W. J., & Webber, B. R. (1996). *QCD and Collider Physics* (pp. 1–435). Cambridge: Cambridge University Press.
- 23. Buckley, A., Butterworth, J., Gieseke, S., Grellscheid, D., Hoche, S., et al. (2011). General-purpose event generators for LHC physics. *Physics Report*, 504, 145–233.
- 24. Catani, S., & Seymour, M. (1997). A general algorithm for calculating jet cross-sections in NLO QCD. *Nuclear Physics*, *B485*, 291–419.
- 25. Catani, S., Dittmaier, S., Seymour, M. H., & Trocsanyi, Z. (2002). The Dipole formalism for next-to-leading order QCD calculations with massive partons. *Nuclear Physics B*, 627, 189–265.
- Kosower, D. A. (1998). Antenna factorization of gauge theory amplitudes. *Physical Review D*, 57, 5410–5416.
- Kosower, D. A. (2005). Antenna factorization in strongly ordered limits. *Physical Review D*, 71, 045016.
- 28. Gehrmann-De Ridder, A., Gehrmann, T. & Glover, E. N. (2005). Antenna subtraction at NNLO. *JHEP*, 0509, 056.
- 29. Daleo, A., Gehrmann, T., & Maitre, D. (2007). Antenna subtraction with hadronic initial states. *JHEP*, 0704, 016.
- 30. Frixione, S., Kunszt, Z., & Signer, A. (1996). Three jet cross-sections to next-to-leading order. *Nuclear Physics B*, 467, 399–442.
- 31. Frixione, S. (1997). A General approach to jet cross-sections in QCD. *Nuclear Physics B*, 507, 29–314.
- 32. Skands, P. Z. (2011). QCD for Collider Physics. arXiv: 1104.2863 [hep-ph].
- 33. Salam, G. P. (2010). Elements of QCD for hadron colliders. arXiv: 1011.5131 [hep-ph].
- 34. Catani, S., Krauss, F., Kuhn, R., & Webber, B. (2001). QCD matrix elements + parton showers. *JHEP*, 0111, 063.
- 35. Mangano, M. L., Moretti, M., Piccinini, F., & Treccani, M. (2007). Matching matrix elements and shower evolution for top-quark production in hadronic collisions. *JHEP*, 0701, 013.
- Frixione, S., & Webber, B. R. (2002). Matching NLO QCD computations and parton shower simulations. JHEP, 0206, 029.
- Nason, P. (2004). A New method for combining NLO QCD with shower Monte Carlo algorithms. JHEP, 0411, 040.
- 38. Sjostrand, T. (1984). Jet fragmentation of nearby partons. Nuclear Physics B, 248, 469.
- 39. Andersson, B., Gustafson, G., Ingelman, G. & Sjöstrand, T. (1983). Parton fragmentation and string dynamics. *Physics Reports*, 97, 3–145. ISSN: 0370-1573.
- 40. Webber, B. (1984). A QCD model for jet fragmentation including soft gluon interference. *Nuclear Physics B*, 238, 492.

- Sjostrand, T., Mrenna, S. & Skands, P. Z. (2006). PYTHIA 6.4 physics and manual. *JHEP*, 0605, 026.
- 42. Sjostrand, T., Mrenna, S., & Skands, P. Z. (2008). A brief Introduction to PYTHIA 8.1. Computer Physics Communication, 178, 852–867.
- 43. Corcella, G., Knowles, I., Marchesini, G., Moretti, S., Odagiri, K., et al. (2001). HERWIG 6: An Event generator for hadron emission reactions with interfering gluons (including supersymmetric processes). *JHEP*, 0101, 010.
- 44. Bahr, M., Gieseke, S., Gigg, M., Grellscheid, D., Hamilton, K., et al. (2008). Herwig++ physics and manual. *The European Physical Journal C*, 58, 639–707.
- 45. Gleisberg, T., Hoeche, S., Krauss, F., Schonherr, M., Schumann, S., et al. (2009). Event generation with SHERPA 1.1. *JHEP*, 0902, 007.
- 46. Alwall, J., Herquet, M., Maltoni, F., Mattelaer, O., & Stelzer, T. (2011). MadGraph 5: going beyond. *JHEP*, 1106, 128.
- 47. Mangano, M. L., Moretti, M., Piccinini, F., Pittau, R., & Polosa, A. D. (2003). ALPGEN, a generator for hard multiparton processes in hadronic collisions. *JHEP*, 0307, 001.
- 48. Frederix, R., & Frixione, S. (2012). Merging meets matching in MC@NLO. JHEP, 1212, 061.
- 49. Hoche, S., Krauss, F., Schonherr, M., & Siegert, F. (2011). Automating the POWHEG method in Sherpa. *JHEP*, 1104, 024.
- 50. Platzer, S., & Gieseke, S. (2012). Dipole showers and automated NLO matching in Herwig++. *The European Physical Journal C*, 72, 2187.
- 51. Hoeche, S., Krauss, F., Schonherr, M., & Siegert, F. (2013). QCD matrix elements + parton showers: the NLO case. *JHEP*, *1304*, 027.
- 52. Hoeche, S., & Schonherr, M. (2012). Uncertainties in next-to-leading order plus parton shower matched simulations of inclusive jet and dijet production. *Physical Review D*, 86, 094042.
- 53. Seymour, M. (1998). Jet shapes in hadron collisions: higher orders, resummation and hadronization. *Nuclear Physics B*, 513, 26–300.
- Catani, S., Dokshitzer, Y. L., Seymour, M., & Webber, B. (1993). Longitudinally invariant K_t clustering algorithms for hadron collisions. *Nuclear Physics B*, 406, 187–224.
- 55. Cacciari, M., Salam, G. P., & Soyez, G. (2008). The Anti-k(t) jet clustering algorithm. *JHEP*, 0804, 063.
- ATLAS Collaboration. (2011). Measurement of inclusive jet and dijet cross sections in protonproton collisions at 7 TeV centre-of-mass energy with the ATLAS detector. *The European Physical Journal*, C71, 1512.
- 57. ATLAS Collaboration. (2012). Measurement of inclusive jet and dijet production in pp collisions at $\sqrt{s} = 7$ TeV using the ATLAS detector. Physics Review, D86, 014022.
- 58. Derrick, M., et al. (1996). Rapidity gaps between jets in photoproduction at HERA. *Physical Letter B*, 369, 55–68.
- 59. Chekanov, S., et al. (2007). Photoproduction of events with rapidity gaps between jets at HERA. *The European Physical Journal C*, 50, 283–297.
- 60. Adloff, C., et al. (2002). Energy flow and rapidity gaps between jets in photoproduction at HERA. *The European Physical Journal C*, 24, 517–527.
- 61. Abbott, B., et al. (1998). Probing hard color-singlet exchange in $p\bar{p}$ collisions at $\sqrt{s}=630$ GeV and 1800 GeV. *Physics Letter B*, 440, 189–202.
- 62. ATLAS Collaboration. (2011). Measurement of dijet production with a veto on additional central jet activity in pp collisions at $\sqrt{s} = 7$ TeV using the ATLAS detector. *JHEP*, 1109, 053.
- 63. Delgado, R. M. D., Forshaw, J. R., Marzani, S., & Seymour, M. H. (2011). The dijet cross section with a jet veto. English. *Journal of High Energy Physics*, 2011, 1–18.
- 64. Fadin, V., Kuraev, E. & Lipatov, L. (1975). On the pomeranchuk singularity in asymptotically free theories. *Physics Letters B*, 60, 50–52. ISSN: 0370-2693.
- Kuraev, E. A., Lipatov, L. N. & Fadin, V. S. (1976). Multi-Reggeon processes in the Yang-Mills theory. Soviet Physics JETP, 44, 443–450.
- 66. Kuraev, E., Lipatov, L. & Fadin, V. S. (1977). The Pomeranchuk singularity in nonabelian gauge theories. *Soviet Physics JETP*, 45, 199–204.

References 31

67. Balitsky, I., & Lipatov, L. (1978). The Pomeranchuk singularity in quantum chromodynamics. *Soviet Journal of Nuclear Physics*, 28, 822–829.

- 68. Andersen, J. R., & Smillie, J. M. (2010). Constructing all-order corrections to multi-jet rates. *JHEP*, 1001, 039.
- 69. Andersen, J. R., & Smillie, J. M. (2010). High energy description of processes with multiple hard jets. *Nuclear Physics B Proceedings Supplements*, 205–206, 205–210.
- 70. Forshaw, J. R., Kyrieleis, A., & Seymour, M. (2005). Gaps between jets in the high energy limit. *JHEP*, 0506, 034.
- 71. Dasgupta, M., & Salam, G. (2001). Resummation of nonglobal QCD observables. *Physical Letter B*, 512, 323–330.
- 72. Dasgupta, M., & Salam, G. P. (2002). Accounting for coherence in interjet E(t) flow: a case study. *JHEP*, 0203, 017.
- 73. Forshaw, J. R., Kyrieleis, A., & Seymour, M. (2006). Super-leading logarithms in non-global observables in QCD. *JHEP*, 0608, 059.

Chapter 2 **Experimental Apparatus**

2.1 The Large Hadron Collider

2.1.1 Design

The Large Hadron Collider (LHC) [1] was constructed between 1998–2008 at CERN, the European Centre for Nuclear Research. It occupies the same 27 km circumference tunnel, 100 m below ground, that originally housed the Large Electron-Positron (LEP) [2–4] collider. It accelerates counter-rotating beams of protons to speeds much greater than 0.999c before bringing them to collision at one of four main interaction points (IPs) positioned around the ring. The LHC is the largest, highest energy and highest luminosity particle accelerator ever constructed.

There are four main experiments operating at the LHC. ATLAS (cf Sect. 2.2) and CMS [5] (Compact Muon Solenoid) are general-purpose detectors designed with a broad physics programme in mind. From performing precision measurements that test and constrain the Standard Model, to discovering the long-sought Higgs boson and searching for new physics such as Supersymmetry and new heavy particles, these detectors are able to observe a wide range of particles and physical phenomena. The LHCb [6] (LHC beauty) experiment is a single arm forward spectrometer whose main goal is to study heavy flavour physics and the parameters of CP-violation. These studies aim to help explain the matter-antimatter asymmetry in the universe. ALICE [7] (A Large Ion Collider Experiment) is focussed mainly on the study of heavy-ion (lead-lead and proton-lead) collisions. The quark-gluon plasma produced in the extremely high density conditions is of great interest. The main experiments are situated in four of the eight octants that make up the LHC. ATLAS and CMS are located in newly excavated caverns at IP 1 and IP 5. LHCb and ALICE can be found in caverns at IP 2 and IP 8 respectively.

Before entering the LHC itself, beams of protons pass through a series of accelerators in the CERN complex (cf. Fig. 2.1) Once the protons have been accelerated to an energy of 450 GeV they are injected into the LHC ring, and over the course of around 20 minutes are accelerated further until they reach an energy sufficient for

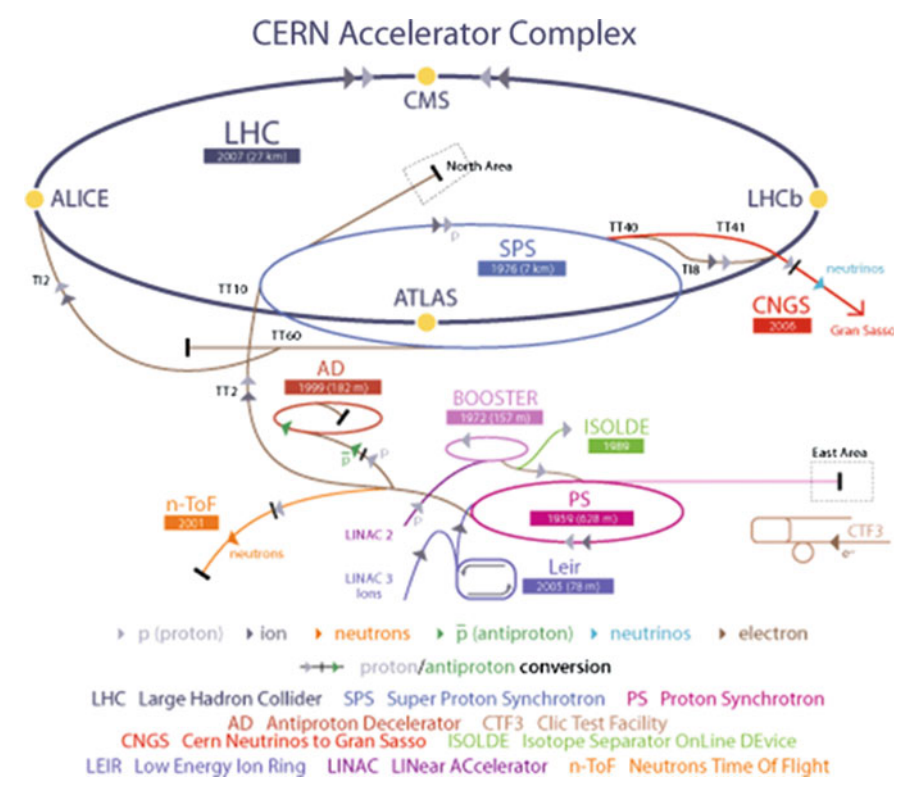


Fig. 2.1 A schematic layout of the accelerator complex and some of the detectors operating at CERN

collisions. The LHC is designed to be capable of colliding proton beams each with energies of 7 GeV.

Protons in each beam are arranged in bunches. One bunch consists of around 1×10^{11} protons, with each LHC ring capable of holding 2808 bunches. The bunches travel in trains, with bunch trains being brought to collision with a design frequency of 40 MHz. The luminosity, \mathcal{L} , of a pp collider can be expressed as [8]

$$\mathcal{L} = \frac{n_b f_r n_1 n_2}{\pi \Sigma_x \Sigma_y} \,, \tag{2.1}$$

where n_b is the number of colliding bunches, f_r is the LHC revolution frequency (11245.5 Hz), n_1 and n_2 are the number of protons per bunch in colliding beams 1 and 2, and Σ_x and Σ_y characterise the horizontal and vertical beam widths.

2.1.2 Performance

The LHC was designed to operate with a centre-of-mass energy of 14 TeV. However after a very brief nine-day commissioning period in 2008 a faulty electrical connection led to a ruptured liquid helium tank and caused around 6 tonnes of liquid helium to escape into the vacuum pipe. This caused damage to over fifty of the LHC's superconducting magnets and delaying the start of the detectors' data-taking programme by fourteen months.

After the repairs, a short run of collisions with centre-of-mass energy 900 GeV began in November 2009. Following this, high-energy data-taking started again on 30th March 2010 at a centre-of-mass energy of 7 TeV. The LHC continued operating with 3.5 TeV beams throughout 2011 and by the end of its initial data-taking period the LHC had delivered 5.61 fb $^{-1}$ of data, which ATLAS collected with $\approx 94\,\%$ efficiency. A brief shutdown took place at the start of 2012, before collisions were started again with a centre-of-mass energy of 8 TeV. Throughout 2012 the LHC again exceeded expectations and delivered 23.3 fb $^{-1}$ by the end of the year. Starting in February 2013 the LHC was shut down for repairs and upgrades to be made to the machine. Proton-proton collisions will take place again in early 2015, with beam energies close to the design energy of around 7 TeV (Fig. 2.2).

The bunch spacing was decreased steadily during 2011 to a peak value of 50 ns, corresponding to a maximum of colliding 1380 bunches within the machine at one time. Peak instantaneous luminosity was reached in 2012 at a value of around $7\times10^{33}~\rm cm^{-2}~s^{-1}$. Such a high instantaneous luminosity led to great challenges in dealing with pile-up. In-time pile-up refers to multiple proton-proton collisions taking place within one bunch crossing, and can be quantified by considering the average number of interactions per bunch crossing, $\langle\mu\rangle$. The peak values for the 7 and 8 TeV data-taking periods were 9.1 and 20.0 respectively, as shown in Fig. 2.3. Out-of-time

Fig. 2.2 Cumulative luminosity versus time delivered to (*green*), and recorded by (*yellow*) ATLAS during stable beams and for pp collisions at 7 and 8 TeV centre-of-mass energy in 2011 and 2012 [9]

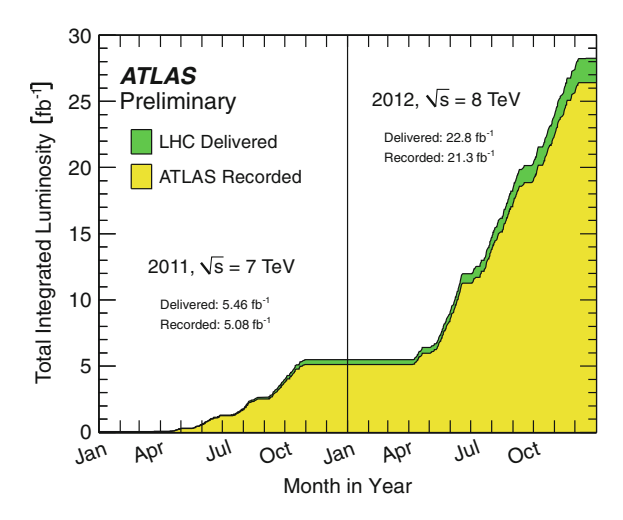
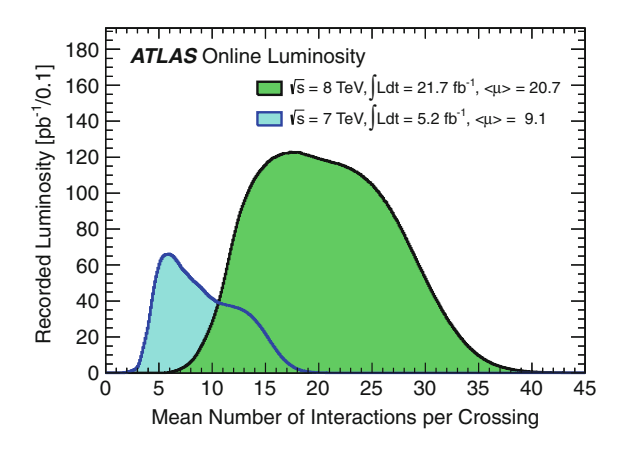


Fig. 2.3 The average number of interactions per bunch crossing during the 7 and 8 TeV data-taking periods [10]



pile-up occurs due to the read-out time of the detector, when particles produced in successive bunch crossings overlap and are read out as part of the same event. Pile-up affects much of the physics being performed at the LHC, from reconstructing vertices and tracks to measuring the energy of hadronic jets. Understanding and limiting the effects of pile-up on the reconstruction of physics objects has been, and will continue to be, crucial to the success of physics analyses.

2.2 The ATLAS Detector

The ATLAS detector was constructed by institutes in 34 countries, and assembled in the cavern at IP 1 around the LHC ring between 2003 and 2008. With a volume of over 1000 m³ and weighing in at around 7000 tonnes it is the largest of the four main detectors.

The coordinate system employed by ATLAS is right-handed, with the z-axis aligned along the beam line and the x-axis pointing towards the centre of the LHC ring. Pseudorapidity, η , is defined as

$$\eta = -\ln \tan \left(\frac{\theta}{2}\right) \tag{2.2}$$

where θ is the angle with respect to the z-axis. Transverse energy, E_T , and transverse momentum, p_T , are also defined with respect to the z-axis as:

$$E_T = E \sin(\theta)$$
 and $p_T = \vec{p} \sin(\theta)$ (2.3)

¹Pseudorapidity is preferred to θ because differences in η are invariant under boosts along the z-axis. Pseudorapidity is equivalent to the more general quantity rapidity, $y = \frac{1}{2} \ln \left(\frac{E + p_z}{E - p_z} \right)$, when the mass of the particle can be neglected.

where E and \vec{p} are the energy and momentum of the relevant object. The azimuthal angle in the transverse plane, ϕ , is defined to be zero along the x-axis.

The detector itself is split into three sections. A cylindrical barrel surrounding the interaction point which provides coverage out to approximately $|\eta| < 1.4$ and two end-caps at either end of the barrel, covering $\sim 1.4 < |\eta| < 4.9$.

Each of the regions are split further into several sub-detectors. At the heart of ATLAS is the Inner Detector (ID) that enables measurements of the momentum of charged particles and accurate reconstruction of vertices produced by primary proton-proton collisions, as well as those that arise from the decay of long-lived particles. Surrounding the ID are the electromagnetic and hadronic calorimeters used to determine the energy of all charged and neutral particles. The outermost sub-detector is the Muon Spectrometer (MS), which enables precision measurements of the momentum of muons.

ATLAS contains both solenoidal (in the barrel) and toroidal (in barrel and end caps) magnet systems. The solenoid is aligned along the beam axis and provides a 2 T magnetic field. It completely surrounds the ID but has been designed to ensure that the material thickness in front of the calorimeters is as low as possible. Charged particles travelling through the solenoid have their trajectory curved in the ϕ -direction. The barrel and end-cap toroids produce 0.5 and 1 T magnetic fields, respectively. The toroid magnets enable measurements of the momentum of muons and cause the tracks produced by them to be curved in the η -direction. Measurements of the momentum of all charged particles are performed by measuring the curvature of the tracks produced by the particles as they traverse the detector subject to these magnetic fields.

2.2.1 The Inner Detector

The ATLAS Inner Detector (ID) is made up of three independent sub-detectors and in total is contained within a cylindrical region of length ± 3512 mm and radius 1150 mm. Closest to the beam is the pixel detector, followed by the semi-conductor tracker (SCT) and transition radiation tracker (TRT). The combination of the three complementary sub-detectors allows precision reconstruction of collision vertices, robust pattern recognition, and precision measurements of the momentum of charged particles produced with $|\eta| < 2.5$. It can also provide electron identification over $|\eta| < 2.0$ and a wide range of energies (0.5–150 GeV).

2.2.1.1 Pixel Sensors and Semi-conductor Trackers

Both the pixel and SCT sensors are made from silicon. A charged particle passing through the silicon creates electron-hole pairs and a potential difference applied across the silicon causes the charges to drift towards the readouts.

Each pixel module is 250 μ m thick and allows double-sided processing. The module measures $19 \times 63 \text{ mm}^2$ and contains ~47,000 pixels, each of which measures $50 \times 400 \ \mu\text{m}^2$. In total the pixel detector is made up of 1744 modules split between three barrel layers and two sets of three end-cap disks. The barrel layers have radii of 50.5, 88.5 and 122.5 mm and provide coverage out to $|\eta| < 1.7$ and complete azimuthal coverage. End-cap disks have |z| = 495, 580 and 650 mm and cover the range $1.7 < |\eta| < 2.5$. The spatial resolution of pixel modules varies with the incident angle of the particle from 12 μ m at normal incidence, to an optimal resolution of 4.7 μ m for incident angles of $10-15^\circ$.

The SCT sensors are made up of a series of single-sided p-in-n silicon microstrips of thickness $285\pm15\,\mu m$. In the barrel, strips are created by joining two rectangular sensors with dimensions $6.39\times6.36\,cm^2$. Each sensor has 768 strips with an $80\,\mu m$ pitch, with four sensors making up one module, mounted back-to-back in pairs. There are 2112 modules in the barrel of the SCT, arranged in four layers and aligned such that the strips lie along the direction of the beam and offer precise measurements of the ϕ coordinate. The 1976 SCT modules making up the two end-caps are arranged in nine layers of disks. Each of the sensors in the end-caps are trapezoidal in shape and come in three sizes for separate construction of inner, middle and outer regions of the disk. The sensors are aligned with their microstrips in the radial direction, again allowing precise measurements of the ϕ coordinate. The spatial resolution of sensors in both the barrel and end-caps is ~16 μ m for normally-incident particles.

2.2.1.2 The Transition Radiation Tracker

The basic TRT detector elements are drift tubes (straws) of diameter 4 mm and length 144 cm (37 cm) in the barrel (end-caps). The straws are filled with a gas mixture of 70 % Xe, 27 % $\rm CO_2$ and 3 % $\rm O_2$. Charged particles passing through the straws cause ionisation of the gas, and the electrons that are produced drift towards a tungsten anode mounted at the centre of each tube. As in the pixel and SCT detectors, if the total charge collected is above some threshold it is defined as a particle hit. In the barrel the TRT contains ~52500 straws arranged in 73 layers and aligned in the z-direction, while each end-cap is made up of 160 planes of radially-aligned straws—over 120,000 straws per end-cap. Any charged particle with $\rm p_T > 0.5~GeV$ will traverse at least 36 layers of straws, except in the transition region between the barrel and end-cap, where the number is reduced to a minimum of 22 crossed straws. Radiator material is placed between each of the straws. Highly relativistic particles crossing the boundary between radiator and straw emit transition radiation photons, which cause additional ionisation. Higher thresholds are defined to determine whether a hit contains transition radiation in addition to the particle itself.

2.2.2 The Calorimeters

ATLAS contains a number of calorimeters that measure the energy of incident particles through absorption. Alternating layers of absorber and sampling material cause particles entering the calorimeter to shower into secondary particles, the energy of which are collected and measured. The number of layers of material and the geometry of the calorimeter modules is such that the probability of particles 'punching-through' the calorimeters and escaping with some unmeasured energy is kept to a minimum.

2.2.2.1 Electromagnetic Calorimeters

The electromagnetic (EM) calorimeters use a combination of lead and liquid argon (LAr) layers to measure the energy of electrons and photons. On passing through the calorimeters electrons emit bremsstrahlung photons, which in turn can produce electron-positron pairs. The resulting shower of electromagnetic particles causes ionisation in the active LAr layers, with copper electrodes collecting the charge. An accordion-like geometry gives the barrel and end-cap EM calorimeters complete ϕ coverage without any cracks or gaps. In the barrel the EM calorimeter is made of two half-barrels. Each half-barrel is 3.2 m in length, weighs 57 tonnes and contains 1024 absorbers interleaved with readout electronics. Constructed in 16 separate modules, the barrel of the EM calorimeter provides between 22 and 33 radiation lengths (X_0) of material to try and keep punch-through of particles into the muon system to a minimum. In the region $|\eta|<1.8$ a liquid-argon presampler layer is used to correct for energy lost by electrons or photons before reaching the calorimeter, such as through interactions with the ID or supporting structure.

The granularity of the barrel EM calorimeter varies between the three layers that make up each module. The second layer, consisting of 16 radiation lengths of material, absorbs the majority of the energy of the particles and has a granularity of 0.025×0.025 in $\eta \times \phi$. Such a fine granularity is ideally suited for precision measurements of electrons and photons.

The layout of the end-cap calorimeters is more complex. The two wheels, one at either end of the barrel, each weigh 27 tonnes and are made up of a series of wedge-shaped modules. The granularity and thickness of the wheels varies as a function of $|\eta|$. For $|\eta| > 1.475$ the thickness is greater than $24X_0$, and in the precision regions of the end-cap the granularity matches that of the barrel, $\eta \times \phi = 0.025 \times 0.025$.

2.2.2.2 Hadronic Calorimeters

The hadronic calorimeters are used to measure the energy of baryons and mesons. The tile calorimeter is constructed in three sections, a barrel and two extended barrels, providing coverage over the region $|\eta| < 1.7$. Each section is made up of 64 wedge-shaped modules, and each module uses layers of steel as the absorber material that

causes the particles to shower, and scintillating tiles as the active medium that sample the energy of the shower particles and produce detectable signals proportional to the energy. Each scintillating tile is coupled to a photomultiplier tube and readout electronics. Tiles are grouped to form cells with dimensions $\Delta \eta \times \Delta \phi = 0.1 \times 0.1$ in the first two layers and 0.2×0.1 in the last layer.

The hadronic end-cap (HEC) calorimeters cover the region 1.5 < $|\eta|$ < 3.5 and use copper sheets to provide the hadron shower and liquid-argon gaps for the active medium. As in the end-caps of the EM calorimeter, the granularity of the HEC varies with $|\eta|$, from $\Delta\eta \times \Delta\phi = 0.1 \times 0.1$ in the region $|\eta|$ < 2.5, to 0.2 × 0.2 for larger values of η .

The forward calorimeters (FCal) extend the coverage of the calorimeters to $3.1 < |\eta| < 4.9$. Each FCal is made up of three modules: an electromagnetic module that uses copper as its main absorber material, and two hadronic modules which use tungsten. Liquid-argon is used as the active material in all three modules and they all make use of the same cryostat systems as the other end-cap calorimeters, reducing any gaps in coverage. At just 0.27 mm the liqud-argon gaps in the FCal are smaller than in the EM barrel calorimeter. This enables the FCal to provide faster signals, and deal with the large particle flux produced at low angles with respect to the beam.

2.2.3 The Muon Spectrometer

The ATLAS Muon Spectrometer (MS) has been designed to provide both triggering (See Sect. 2.2.4) and precision measurement capabilities. Both functions are performed in the barrel and end-caps, triggering on muons with $|\eta| < 2.4$ and precision tracking on muons with $|\eta| < 2.7$.

2.2.3.1 Precision Measurements

Precision measurements of muon momenta are performed by Monitored Drift Tubes (MDTs) in both the barrel and end-caps, apart from the innermost layer in the forward region $2 < |\eta| < 2.7$ where they are replaced by Cathode Strip Chambers (CSCs), for their higher rate capabilities.

Each MDT chamber is made up of two multi-layers (three or four layers, depending on the position of the chamber) of pressurised drift tubes. Muons traversing the chamber cause ionisation of the gas and the resultant electrons are collected by tungsten-rhenium wires held at the centre of each tube. The tubes have a diameter of 29.97 mm, are filled with a mixture of CO_2 and Ar and are aligned along ϕ in both the barrel and end-caps. In the barrel the MDT chambers are arranged in concentric layers around the beam axis and are mounted between and on the coils of the toroid magnets. In the two end-caps the MDTs form large wheels, and are located in front of and behind the two end-cap toroids. This configuration allows a precise measurement of the η -coordinate of the muons—the direction they are bent on passing through the

toroidal magnetic field. The resolution of a single MDT is 80 μm , or about 35 μm per chamber.

The Cathode Strip Chambers are multi-wire proportional chambers with wires aligned in the radial direction. A single chamber is made of four planes of wires. Eight small and eight larger chambers make up one end-cap disk. Within each plane, one set of cathode strips is aligned parallel to the wires, while the other is oriented perpendicularly. This allows the CSCs to determine both the η and ϕ coordinates of the tracks at once, by reading out the charged induced on each set of cathode strips. The more precise measurement, in the bending direction, has a resolution of 60 μ m while in the non-bending direction measurements are coarser with a resolution of around 5 mm.

2.2.3.2 Trigger Chambers

The trigger chambers comprise Resistive Plate Chambers (RPCs) in the barrel region $|\eta| < 1.05$ and Thin Gap Chambers (TGCs) in the end-cap $1.05 < |\eta| < 2.4$. Muon hit information is produced within a few tens of nanoseconds of the passage of the particle.

Contrary to the other technologies employed within the muon spectrometers, the RPCs contain no wires. Each is made up of two parallel resistive plates, with perpendicular sets of metallic strips mounted on the outer faces providing the signal readout, and gas filling the 2 mm gap in between. Charged particles passing through the RPCs ionise the gas, and a uniform 4.9 kV/mm electric field between the plates allows avalanches of electrons to form along the ionising tracks.

Most RPC chambers are made up of two rectangular detectors, or units, each of which consists of two independent gas volumes. The RPCs are arranged in three concentric cylinders around the beam axis, requiring in total 544 RPC chambers and 962 separate units. They are mounted above and below their MDT counterparts.

The TGCs are multi-wire proportional chambers with a gas gap of 2.8 mm filled with a mixture of CO_2 and $n-C_5H_{12}$ (n-pentane). They perform two main functions: triggering capabilities for muons with $1.05 < |\eta| < 2.4$ and measurements of the azimuthal coordinate of the muons, to complement the precise measurement of the coordinate in the bending direction performed by the MDTs. One chamber is made up of a gas volume, containing a wire plane, and two cathodes. Chambers are arranged in doublets or triplets to form each TGC unit. The cathode planes are coated on one side with graphite and on the other with copper. The copper layers are segmented into readout strips and are used to perform the measurement of the azimuthal coordinate.

2.2.4 Trigger and Data Acquisition

It is not possible to store the output of every proton-proton collision occurring within ATLAS. A single event recorded by ATLAS requires ~1.5 MB of memory when

stored offline [11]. With a bunch cross frequency of 40 MHz at design luminosity, recording every event would therefore require data to be written to disk at a rate of ~60 TBs⁻¹. The majority of these events do not contain objects such are hard jets or high-p_T leptons which are the signatures of many rarer, lower cross-section processes such as the production of top quarks or Higgs bosons. It would be preferable to only write such events to disk for detailed analysis.

The ATLAS trigger system identifies interesting events containing high- p_T objects in three distinct levels. The Level-1 (L1) trigger is hardware-based and reduces the event rate to 75 kHz. A decision to keep an event is made within 2.5 μs . This is achieved through the use of reduced granularity information from a subset of the detectors. For example the RPC and TGC sections of the muon spectrometer are used to check whether muons with transverse momentum above specified thresholds are present in the event. All parts of the EM and hadronic calorimeters can be used to place requirements on the number and energy of electrons, photons, jets and τ -leptons, and also the amount of missing transverse energy, E_T^{miss} , and total transverse energy in each event.

If a physics object is found by the L1 trigger, its position is recorded and a region-of-interest (RoI) containing the object is passed on to the Level-2 (L2) trigger system. The L2 trigger reduces the event rate further to around 3.5 kHz, with the decision to keep the event made within 40 ms. The L2 algorithms use partial detector information from within the vicinity of the RoI to refine the objects reconstructed at L1.

The third and final level of the trigger system is the Event Filter (EF). The EF makes use of the full granularity of the detector to reduce the event rate to approximately 200 Hz. Algorithms similar to those used when reconstructing events offline are used to reconstruct the objects of interest.

Trigger nomenclature typically follows the format:

Level_Stream&Cut_Note. For example an event passing the trigger L1_MU11 must contain a muon identified at L1 with $p_T > 11$ GeV. EF_mu24i_medium requires events to contain an isolated muon with $p_T > 24$ GeV and the medium in this case refers to a specific L1 trigger that must also have fired.

Only once an event has passed an EF trigger is it written to disk for permanent storage. As data is being collected it is organised into *periods* and *runs*, which allows easy organisation and management of the huge amount of data collected by ATLAS. A run begins once the Data Acquisition (DAQ) infrastructure, detectors and other sub-systems are configured correctly, and once the conditions of the beam provided by the LHC are stable. A run is ended either cleanly when there is deemed to be sufficient data collected or is aborted when a problem occurs, for example if the LHC beams are lost. A period is defined as a succession of DAQ runs.

After data have been collected a series of further data quality checks are performed. If the data in the runs under scrutiny are of a sufficient quality, and all of the triggers and detector systems were functioning optimally, then the runs are added to a so-called *Good Runs List* (GRL). Only those runs which appear in a GRL can be used for physics analysis.

References 43

References

- 1. Evans, L., & Bryant, P. (2008). LHC Machine. In L. Evans (ed.), JINST 3 (S08001).
- 2. LEP Design Report. (1983). 1. The LEP injector chain.
- 3. LEP Design Report. (1984). Vol. 2. The LEP Main Ring.
- 4. Myers, S. (1991). The LEP collider, from design to approval and commissioning.
- 5. Chatrchyan, S., et al. (2008). The CMS experiment at the CERN LHC. JINST, 3, S08004.
- 6. Augusto Alves, A., et al. (2008). The LHCb Detector at the LHC. JINST, 3, S08005.
- 7. Aamodt, K., et al. (2008). The ALICE experiment at the CERN LHC. JINST, 3, S08002.
- 8. ATLAS Collaboration. (2013). Improved luminosity determination in pp collisions at $\sqrt{s} = 7$ TeV using the ATLAS detector at the LHC. European Physical Journal C, 73, 2518.
- 9. ATLAS Collaboration. (2014). Total integrated luminosity in 2011 and 2012. Retrieved March 12, 2014, from https://twiki.cern.ch/twiki/bin/view/AtlasPublic/LuminosityPublicResults.
- ATLAS Collaboration. (2014). Number of interactions per crossing. Retrieved March 12, 2014, from https://twiki.cern.ch/twiki/bin/view/AtlasPublic/LuminosityPublicResults.
- 11. ATLAS Collaboration. (2014). ATLAS fact sheet. Retrieved April 8, 2014, from http://www.atlas.ch/pdf/ATLAS_fact_sheets.pdf.

Chapter 3 Reconstructing Physics Objects

This section gives details of the experimental techniques used to reconstruct physics objects from the hits and energy deposits left by particles as they traverse the ATLAS detector.

3.1 Charged Particle Tracks

Tracks in the inner detector are reconstructed using information from the pixel, SCT and TRT detectors. The most commonly used track-finding strategy is the so-called *inside-out* strategy. The first step undertaken is pattern recognition. Measurements of particles in the pixel and SCT detectors are used to produce three-dimensional (3D) representations of the locations of interactions. In the pixel layers clusters of pixel hits, as well as the radial position of the silicon surface, define the *space point*. In the SCT, individual modules only provide measurements perpendicular to the direction of the SCT strip, so the back-to-back structure of the SCT modules are crucial in determining the *space point*.

At least three *space points* in the silicon detectors are required to seed track reconstruction using the *inside-out* algorithm [1]. A Kalman Filter [2] is used to combine successive *space points* and propagate a track through the silicon detectors. After resolving ambuiguities in the track candidates, tracks are extended into the TRT. The silicon tracks are used to define roads inside which TRT hits must lie. In a second stage of track reconstruction, an *outside-in* algorithm is run on any remaining TRT hits not already associated to tracks. This back-tracking aims to reconstruct secondary particles, produced by the interactions of the primaries.

3.2 Primary Vertices

Reconstruction of vertices in an event takes place in two steps. The primary vertex finding algorithm first associates reconstructed tracks to vertex candidates, before the vertex fitting algorithm reconstructs vertex positions. Tracks are used as input to the vertex reconstruction if they pass cuts on the transverse and longitudinal impact parameters, the number of pixel and SCT hits, and the track transverse momentum.

The position of vertices is determined using an Iterative Vertex Finding algorithm [3]. A vertex seed is found by looking for the global maximum in the distribution of z-coordinates of the tracks, and an iterative χ^2 fit is made using the seed and nearby tracks. If a track is displaced from the vertex by more than 7σ it is used to seed a new vertex, and the process is repeated until no further vertices can be found.

The primary vertex of an event is defined to be the vertex with the largest $\sum_{\text{tracks}} p_T^2$.

The vertex resolution improves with the number of associated tracks. The resolution in the x and y (z) directions determined using the 7 TeV [4] and 8 TeV [5] data for vertices with $\sqrt{\sum p_T^2} > 12$ GeV is $20~\mu m$ (40 μm).

3.3 Electrons

3.3.1 Reconstruction

Reconstruction of electrons in the central region of the detector ($|\eta| < 2.5$) begins with the reconstruction of EM clusters in the calorimeter. After dividing the calorimeter into a grid of cells of size $\eta \times \phi = 0.025 \times 0.025$, a sliding window algorithm with window size 3×5 is used to search for regions that contain local maxima in energy. An attempt is then made to match the calorimeter clusters to tracks in the inner detector. ID tracks with $p_T > 0.5$ GeV are extrapolated outwards to the middle layer of the EM calorimeter and are considered matched to the EM clusters if they have $|\Delta\eta| < 0.05$ and $\Delta\phi < 0.1$ —the larger window in $\Delta\phi$ accounts for bremsstrahlung. Finally the cluster sizes are optimised, and enlarged to 3×7 cells in the barrel and 5×5 cells in the end-caps. The total reconstructed electron energy is determined from the energy deposited in the cluster, as well as the energy deposited in dead material in front of the EM calorimeter and estimated energy leakage outside the cluster and beyond the calorimeter.

The reconstructed electron energies are calibrated using a series of techniques [6]. A purely MC-based calibration relates the true electron energy to detector-level quantities using a boosted decision tree (BDT) algorithm [7]. This relies heavily on an accurate description of the detector geometry and particle-matter interactions in the simulation. Preliminary corrections are applied before the MC-based calibration to take into account details in specific regions of the detector that are not included in

3.3 Electrons 47

the simulation, and afterwards the absolute energy scale is determined by comparing the difference in response in data and monte carlo using a sample of $Z\rightarrow$ ee events. The electron energy scale uncertainty is minimal for electrons with $E_T \sim 40\,\text{GeV}$. For electrons with $E_T \sim 10\,\text{GeV}$ the uncertainty ranges from 0.4 to 2% depending on the pseudorapidity of the electron.

3.3.2 Identification

For electrons to qualify for use in analysis they must pass various cuts on cluster, track and combined track-cluster quantities. Three sets of reference criteria are defined, labelled loose++, medium++ and tight++, which provide increasing background rejection with a slight decrease in identification efficiency. During the 2011 data-taking period the reference criteria were defined as follows:

- For an electron to pass the loose++ criteria it must pass cuts on variables such the EM shower shape, the amount of hadronic leakage in the second layer of the EM calorimeter and the number of hits in the pixel and SCT layers of the ID. There is also loose matching performed between the ID tracks and position of the EM cluster: $|\Delta\eta| < 0.015$. The efficiency of the loose++ criteria, estimated using Z tag-and-probe studies is around 95%.
- medium++ has tighter cuts on the shower shape variables, a tighter ID-cluster matching cut of $|\Delta \eta| < 0.005$, strict b-layer and pixel hit requirements and impact parameter cut of $d_0 < 5$ mm. The efficiency of the medium++ cuts is around 85 %.
- The tight++ criteria include shower shape cuts at least as tight as the medium++ ones, a tighter impact parameter cut of $d_0 < 1$ mm and additional cuts on the cluster energy to track momentum ratio E/p and a $\Delta \phi$ track-cluster matching requirement. The efficiency of the tight++ criteria is about 78%.

For the 2012 data-taking period the reference criteria we re-defined in order to cope with the increased luminosity and pile-up delivered by the LHC. In general cuts on pile-up-sensitive variables were loosened and replaced with tighter cuts on pile-up-robust ones. In the loose++ definition, cuts on some of the shower shape cuts were loosened to recover efficiency at high pile-up. medium++ in 2012 employed tighter cuts on pile-up-robust shower shape variables and an additional cut on the fraction of energy in the third calorimeter sampling layer. The tight++ definition was changed in the same way as medium++. In 2012 the loose++ and tight++ definitions were highly efficient, while losing some background rejection power (approximately 10-20% lower than in 2011. The changes made to the medium++ definition enabled it to make the same efficiency improvements without suffering any losses in rejection power.

3.4 Muons

3.4.1 Reconstruction

The ATLAS muon reconstruction algorithms make use of information from the ID, the calorimeter and the MS. Reconstruction begins by searching for hits in the MDT, inside regions of interested defined by the trigger chambers. Hits in each layer of the MDT are combined into track segments. Track segments from each of the layers are then combined into track candidates, and a full track fit is performed taking into account the magnetic field and material distribution of the MS. Muon tracks in the inner detector are reconstructed using the techniques described in Sect. 3.1. The goal is then to combine the tracks found in the MS with those found in the ID to produce a so-called *combined* muon. Energy loss on interaction with the calorimeters must be taken into consideration when extrapolating tracks from the MS into the ID or vice-versa. ATLAS uses two main algorithms to perform the combination of the MS and ID tracks, called MuID [8] and STACO [9]. Although employing different techniques to reconstruct tracks and combine them, the performance of the two algorithms is comparable. The STACO (STAtistical COmbination) algorithm attempts to statistically merge the two independent tracks, while the MuID (Muon IDentification) algorithm performs a complete re-fit of all hits associated with both

If full tracks in the ID and MS cannot be merged into a combined muon, segment-tagged, MS stand-alone and calorimeter-tagged muons can be defined:

- Segment-tagged: An ID track associated with at least one track segment in the MS.
 These muons are typically found by extrapolating ID tracks to the inner stations of the MS. Low-p_T (<6 GeV) muons are often identified as *segment-tagged*, since they may not have sufficient energy to penetrate all layers of the MS.
- MS stand-alone: A track identified solely in the MS and extrapolated back to the interaction point, taking into account the energy lost by the muon as it traverses the ID and calorimeters.
- Calorimeter-tagged: Muons reconstructed from ID tracks matched to calorimeter deposits of minimum ionising particles.

The muon momentum resolution depends on the η and ϕ of the muon. Momentum resolutions can be derived by translating measurements of dimuon mass resolution [10]. For muons with p_T ~40 GeV, ID (MS) measurements in the barrel, $|\eta| < 1.05$, have a resolution of 2% (4%).

3.4.2 Identification

Muons considered for use in analyses must pass cuts on the quality of tracks used to reconstruct them. For example the number of pixel hits and crossed dead pixel

3.4 Muons 49

sensors, and the presence of a successful TRT extension where expected. Specific cut values are listed in Sects. 5.3.1 and 7.2.1. Compared to the recommended cuts used in 2011, the 2012 cut values were relaxed to recover some efficiency losses. For example hits in the pixel b-layer were not required during the 2012 data taking, and TRT cuts were not applied outside the region $0.1 < |\eta| < 1.9$.

3.5 Jets

Hadronic jets are not only a crucial aspect of all analyses described in this thesis, but of the majority of analyses undertaken by ATLAS at the LHC. As discussed in Sect. 1.5.6 jets can be constructed from various kinds of object, and in ATLAS those objects are topological clusters (topo-clusters) of calorimeter cells. Topo-clusters are created from neighbouring calorimeters cells containing energy sufficiently above the noise level.

For the majority of analyses topo-clusters are formed into jets using the anti- $k_{\rm t}$ algorithm (see Sect. 1.5.6) with a radius parameter R of 0.4. A series of corrections and calibrations must be performed to correct for experimental effects that cause the reconstructed jet to have a different energy from the 'true' particle-level jet. The calibrated jets then serve as our best estimate of the particle-level jets produced in the hard scatter.

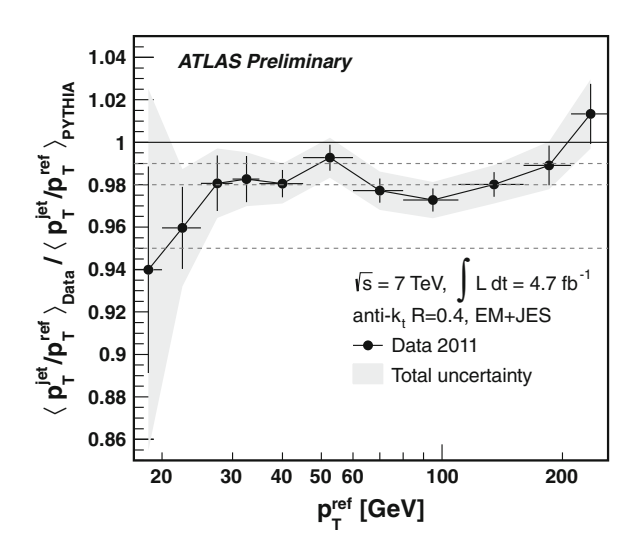
The calibration process proceeds as follows. A pile-up correction is first applied to account for energy added into the jets from other pp collisions. The general approach is to calculate how much of a given jet's transverse momentum is generated by pile-up and to subtract this offset from the reconstructed jet. For the 2011 data-taking period the pile-up offset corrections were derived by performing measurements in samples of minimum bias data as a function of the number of reconstructed vertices in the event (N_{PV}), the jet pseudorapidity, and the bunch cross frequency provided by the LHC [11]. In 2012 the offset correction was determined using MC simulations to compare the true jet transverse momentum to the reconstructed value as a function of N_{PV} and the average number of interactions per bunch crossing, $\langle \mu \rangle$ [12].

Once the pile-up offset correction has been applied, an origin correction is applied, wherein the direction of the jet is corrected to point back to the primary vertex associated with the jet, rather than the nominal interaction point. This does not affect the energy of the jets, but does improve angular resolution slightly and provides a very small improvement in p_T response (<1%).

Following the origin correction, the jet energies are corrected using p_T - and η -dependent correction factors derived from simulation. These account for effects such as partial measurements of the energy deposited by hadrons as they pass through the calorimeter, known as calorimeter non-compensation; the energy loss due to hadrons passing through un-instrumented regions of the detector; and energy deposited in the calorimeter but outside of the region which defines the jet.

Finally, a residual calibration derived using in-situ measurements is applied, which corrects for the fact that the MC may not perfectly describe the data. Several methods

Fig. 3.1 From [14]. Mean p_T -balance in data compared to MC as a function of p_T^{ref} . for anti- k_t jets with distance parameter R=0.4. The reference object is a Z-boson decaying to an e^+e^- pair



are used to determine this correction, and also to determine the uncertainty on the total jet energy scale (JES) calibration. All of the methods involve defining some experimentally well-measured reference object and choosing events in which the p_T of the reference object is balanced against the p_T of a jet. A double ratio then probes how well the data is described by the MC

$$\langle p_T^{\text{jet}}/p_T^{\text{ref}}\rangle_{\text{data}}/\langle p_T^{\text{jet}}/p_T^{\text{ref}}\rangle_{\text{MC}}$$
 (3.1)

For jets falling into the central region of the detector ($|\eta| < 1.2$), for example, the reference object is chosen to be a high-p_T photon (γ +jet) [13] or a Z-boson decaying to *ee* or $\mu\mu$ (Z+jet) [14]. An example of the data/MC ratio for the p_T-balance in Eq. 3.1 is shown in Fig. 3.1. For events containing very high-p_T jets (~1 TeV) the reference object can be chosen to be a recoil system of low-p_T jets [15] (with $|\eta| < 2.8$), providing the low-p_T jets can be well calibrated using the γ +jet or Z+jet techniques.

The original jets used as input to the sequence of calibrations and corrections are formed from topo-clusters reconstructed at the electromagnetic (EM) energy scale. This energy scale correctly reconstructs the energy deposited by particles in an electromagnetic shower in the calorimeter, and is established using test beam measurements of electrons in the barrel and end-cap calorimeters. Once the suite of calibrations have been applied to these jets they are know as the EM+JES jet collection.

In an alternative scheme called Local Cluster Weighting (LCW), topo-clusters are initially classified as either electromagnetic or hadronic by measurements of energy density and longitudinal shower depth. Dedicated corrections are applied to the topo-clusters based on single charge and neutral pion MC simulations, and the entire calibration chain (pile-up subtraction, origin correction, energy calibration,

residual in-situ calibration) is then re-derived. Once the remaining calibrations have been applied to these jets, they are known as the LCW+JES jet collection.

3.5.1 b-tagging

Accurately identifying jets originating from *b*-quarks is important for the physics program of ATLAS. It is particularly crucial in analyses involving top quarks, such as the one presented in Sect. 5. Many algorithms have been developed that attempt to identify, or tag, jets originating from *b*-quarks. The *b*-tagging algorithm used in Sect. 5 makes use of impact parameter and secondary vertex information.

The uncertainty on the transverse impact parameter d_0 is used to construct the transverse impact parameter significance d_0/σ_{d_0} . The longitudinal impact parameter significance, z_0/σ_{z_0} , is defined similarly. The IP3D [16] b-tagging algorithm uses a likelihood ratio technique in which the transverse and longitudinal impact parameter significances are compared to pre-defined distributions for both the b-jet and light-jet hypotheses, constructed from MC.

The SV1 [16] b-tagging algorithm makes use of the decay length significance L_0/σ_{L_0} of a reconstructed secondary vertex, as well as the invariant mass of all tracks associated to the vertex, the ratio of the sum of the energies of the tracks in the vertex to the sum of the energies of all tracks in the jet, and the number of two-track vertices. These variables are combined using a likelihood ratio technique.

The output of each of the IP3D and SV1 *b*-tagging algorithms is a single number, a *b*-tagging weight. The two algorithms can be combined, into the IP3D+SV1 [16] algorithm by simply summing the individual weights and then cutting on this quantity.

Various working points are defined for the taggers using MC samples. Each working point is chosen to successfully tag a certain fraction of real b-jets while rejecting a chosen fraction of light quark and gluon jets. For a b-tagging efficiency of 70 % the IP3D+SV1 algorithm has a light jet rejection rate of ~80 (i.e. 1/80 = 1.25 % of light jets are mis-tagged as b-jets) [17].

3.6 Missing Transverse Energy

The missing transverse momentum, E_T^{miss} , is defined as the momentum imbalance in the plane transverse to the beam axis. As the two incoming protons only have momentum along the direction of the beam, conservation of momentum tells us that the net momentum in the plane transverse to the beam axis should be zero after the protons have collided. Any missing transverse momentum signals the presence of weakly or non-interacting particles such as neutrinos.

The E_T^{miss} is computed using information from energy depositions in the calorimeters and muons reconstructed in the MS [18]. The missing transverse component is calculated from the missing x and y components by

$$E_T^{miss} = \sqrt{(E_x^{miss})^2 + (E_y^{miss})^2} \;, \label{eq:emiss}$$

where the x and y components are each calculated by summing the contributions from the calorimeter and MS, i.e.

$$E_{x(y)}^{\text{miss}} = E_{x(y)}^{\text{miss,calo}} + E_{x(y)}^{\text{miss},\mu} .$$

The calorimeter term is made up of several independently calibrated terms associated with all objects that deposit energy in the calorimeter,

$$\begin{split} E_{x(y)}^{miss,calo} &= E_{x(y)}^{miss,e} + E_{x(y)}^{miss,\gamma} + E_{x(y)}^{miss,\tau} \\ &+ E_{x(y)}^{miss,jets} + E_{x(y)}^{miss,softjets} + E_{x(y)}^{miss,CellOut} \;. \end{split}$$

These objects are electrons, photons and hadronically decaying taus all with $p_T > 10\,\text{GeV}$, LCW+JES jets with $p_T > 20\,\text{GeV}$, softer LCW+JES jets with $7\,\text{GeV} < p_T < 20\,\text{GeV}$, and a "CellOut" term to account for calorimeter cells not associated with any specific physics object.

Each of the terms is built by taking the negative sum of the energy deposited in all calorimeter cells associated with the object, up to $|\eta| < 4.5$,

$$E_{x}^{\text{miss,term}} = -\sum_{i=1}^{N_{\text{cell}}^{\text{term}}} E_{i} \sin \theta_{i} \cos \phi_{i} ,$$

$$\mathbf{E}_{\mathbf{y}}^{\text{miss,term}} = -\sum_{i=1}^{N_{\text{cell}}^{\text{term}}} \mathbf{E}_{i} \sin \theta_{i} \sin \phi_{i} \ .$$

The E_T^{miss} muon term is calculated from the momenta of muon tracks reconstructed with $|\eta| < 2.7$,

$$E_{\mathrm{T}}^{\mathrm{miss},\mu} = -\sum_{\mathrm{muons}} p_{x(y)}^{\mu} . \tag{3.2}$$

In the region $|\eta| < 2.5$ only *combined* muons are used, i.e. those with tracks in the MS matched to tracks in the ID. In the range $2.5 < |\eta| < 2.7$, which is beyond the coverage of the ID, stand-alone muons are used.

For non-isolated muons ($\Delta R(\mu, \text{jet}) < 0.3$) an additional term is added to the calculation of the missing E_T , $E_{x(y)}^{\text{miss,calo},\mu}$. This takes into account energy lost by muons as they traverses the calorimeters, which cannot be distinguished from energy deposits left by particles in the jet. The muon spectrometer measurement of the momentum, after energy loss, is therefore used in this case. For isolated muons the combination of the MS tracks with those found in the ID takes into account the energy lost by the muon in the calorimeter, so the extra term is not needed.

References

 ATLAS Collaboration. (2012). Performance of the ATLAS inner detector track and vertex reconstruction in the high pile-up LHC environment technical report ATLAS-CONF-2012-042. Geneva: CERN.

- 2. Kalman, R. E., et al. (1960). A new approach to linear filtering and prediction problems. *Journal of Basic Engineering*, 82, 35–45.
- ATLAS Collaboration. (2010). Performance of primary vertex reconstruction in proton-proton collisions at √s =7 TeV in the ATLAS experiment technical report. ATLAS-CONF-2010-069. Geneva: CERN.
- Meloni, F, Milov, A, Pagan-Griso, S, Prokofiev, K, & Wildauer, A. (2011). Vertexing performance data vs MC comparison for LPCC technical report ATL-COM-PHYS-2011-1312. Geneva: CERN. https://twiki.cern.ch/twiki/bin/view/AtlasPublic/InDetTrackingPerformanceApprovedPlots#Vertex_performance.
- Vertex reconstruction public plots. Retrieved May, 2014, from http://atlas.web.cern.ch/Atlas/ GROUPS/PHYSICS/IDTRACKING/PublicPlots/ATL-COM-PHYS-2012-474/.
- ATLAS Collaboration. (2013). Electron and photon calibration for the LHC Run1 tech. rep. ATL-COM-PHYS-2013-1652. Geneva: CERN.
- Hoecker, A. et al. (2007). TMVA—Toolkit for multivariate data analysis. ArXiv Physics eprints. eprint: physics/0703039.
- 8. Adams, D., et al. (2003) *Track reconstruction in the ATLAS Muon spectrometer with MOORE 007 technical report*. ATL-SOFT-2003-007. Revised version number 1 submitted on 2003–10-13 13:51:39. Geneva: CERN.
- Hassani, S., et al. (2007). A muon identification and combined reconstruction procedure for the ATLAS detector at the LHC using the MUONBOY, STACO, MuTag reconstruction packages. Nuclear Instruments and Methods in Physics Research Section A: Accelerators, Spectrometers, Detectors and Associated Equipment 572, 77–79. ISSN: 0168–9002.
- 10. ATLAS Collaboration. (2014). Muon reconstruction efficiency and momentum resolution of the ATLAS experiment in proton-proton collisions at $\sqrt{s} = 7$ TeV in 2010. arXiv: 1404.4562 [hep-ex].
- 11. ATLAS Collaboration. (2013). Jet energy measurement with the ATLAS detector in protonproton collisions at $\sqrt{s} = 7$ TeV. The European Physical Journal, C73, 2304.
- 12. ATLAS Collaboration. (2012). Pile-up corrections for jets from proton-proton collisions at $\sqrt{s} = 7$ TeV in ATLAS in 2011 technical report. ATLAS-CONF-2012-064. Geneva: CERN.
- 13. ATLAS Collaboration. (2012). Probing the measurement of jet energies with the ATLAS detector using photon+jet events in proton-proton collisions at $\sqrt{s} = 7$ TeV technical report. ATLAS-CONF-2012-063. Geneva: CERN.
- 14. ATLAS Collaboration. (2012). Probing the measurement of jet energies with the ATLAS detector using Z+jet events from proton-proton collisions at √s = 7 TeV technical report. ATLAS-CONF-2012-053. Geneva: CERN.
- ATLAS Collaboration. (2013). TeV-scale jet energy calibration using multijet events including close-by jet effects at the ATLAS experiment technical report. ATLAS-CONF-2013-003. Geneva: CERN.
- 16. ATLAS Collaboration. (2011). Commissioning of the ATLAS high-performance b-tagging algorithms in the 7 TeV collision data technical report. ATLAS-CONF-2011-102. Geneva: CERN.
- 17. ATLAS Collaboration. (2012). *Measurement of the mistag rate with 5 fb-1 of data collected by the ATLAS detector technical report*. ATLAS-CONF-2012-040. Geneva: CERN.
- ATLAS Collaboration. (2012). Performance of missing transverse momentum reconstruction in proton-proton collisions at 7 TeV with ATLAS. European Physical Journal, C72, 1844.

Chapter 4 Event-Filter Muon Isolation

4.1 Introduction

Muons can be produced in a range of physics processes. Typically those of most interest are muons that originate in the decay of a heavy boson, for example $W \to \mu \nu$. Such muons are usually isolated from hadronic activity, in contrast to muons that originate in the decays of hadrons, which are often found within jets. To give us more confidence that muons collected have come from heavy boson decays, as well as reducing the rate of collecting non-isolated and potentially "fake" muons, isolation variables are defined that quantify the amount of hadronic activity surrounding the muon. This chapter describes work performed on commissioning a new isolated muon trigger that uses track information available at the Event Filter (EF). After commissioning, the isolated trigger was used as one of the primary triggers for the 2012 data-taking period. Work in this chapter has been published in [1].

4.2 The Need for Isolated Triggers

During the 2011 data-taking period, as the luminosity of the LHC increased, the rate of muons being accepted by EF muon triggers increased steadily. Table 4.1 gives some examples of representative rates for EF muon triggers obtained during a typical run in the 2011 data taking. The final column also gives an estimate of the trigger rates that would be obtained after extrapolating to instantaneous luminosities predicted for the 2012 data taking at $\sqrt{s} = 7$ TeV.

Given that the total rate allowed at the output of the EF is 400 Hz, it is clear that a single trigger using around 50% of the total available bandwidth would not be acceptable. Potential solutions to this problem include increasing the p_T thresholds on triggers or imposing isolation requirements inside the triggers. It was predicted that increasing p_T thresholds would reduce the number of muon events available for

mu18 65 203 mu18_medium 62 193 mu20_medium 43 134 mu22_medium 31 97	Trigger	2011 rate (Hz)	Predicted 2012 rate (Hz)
mu20_medium 43 134	mu18	65	203
	mu18_medium	62	193
mu22_medium 31 97	mu20_medium	43	134
	mu22_medium	31	97

Table 4.1 Rates for EF muon triggers

2011 trigger rates were taken from a typical run with instantaneous luminosity $1.6 \times 10^{33} \, \text{cm}^{-2} \text{s}^{-1}$. Predictions for rates that might be obtained in 2012 were made by scaling the 2011 rates to an instantaneous luminosity of $5 \times 10^{33} \, \text{cm}^{-2} \text{s}^{-1}$

analysis by an unacceptable amount, however selecting only those muons that are isolated reduces the trigger rate, as required, and increases the fraction of muons collected that originate from decays such as $Z \to \mu\mu$.

4.3 Implementation and Performance

In the L2 trigger, isolation variables are defined using information from tracks reconstructed in the ID and energy deposits in the calorimeters. The track isolation variable, $\sum p_T$, is defined as the scalar-sum of the p_T of tracks with $\Delta R(\mu, \text{L2 track}) < 0.2$. The ID tracks found at L2 were required to have $p_T > 1$ GeV and have a longitudinal impact parameter close to that of the L2 muon, $\Delta z_0 = |z_0(\text{L2 track}) - z_0(\text{L2 muon})| < 15$ mm. Calorimeter isolation is also calculated at L2 by summing the energy deposited in calorimeter cells in annuli surrounding the muons. The annuli are defined as $0.07 < \Delta R < 0.2$ for the ECal and $0.1 < \Delta R < 0.2$ for the HCal. Different lower bounds are chosen due to the different granularities of the ECal and HCal.

At the EF, the efficiency of reconstructing tracks, as well as the precision with which their p_T can be measured, is higher. Therefore only information from reconstructed tracks is used to define the isolation variable. As at L2, $\sum p_T$ is defined as the scalar-sum of the p_T of tracks surrounding the muon with $\Delta R(\mu, \text{EF track}) < 0.2$. ID tracks used in the calculation of the EF track isolation variable were required to have $p_T > 1$ GeV and a longitudinal impact parameter close to that of the EF muon, $\Delta z_0 = |z_0(\text{EF track}) - z_0(\text{EF muon})| < 10$ mm. Cuts on Δz_0 were used to stop tracks from pile-up interactions entering the calculation of the isolation variable. The choice of cut value was re-evaluated to ensure it was robust against the increasingly severe pile-up conditions provided by the LHC, as described in Sect. 4.3.1.

Two samples of events, collected from the 2011 data, were needed to measure the performance of the isolation variables and define cuts to be used by the isolated trigger. Both samples contained muons that were successfully found by offline reconstruction algorithms. In the first sample, events containing muons originating in the decay of a Z-boson were selected and used to measure the efficiency of the isolation algorithms. A second sample of events were collected that were required only to

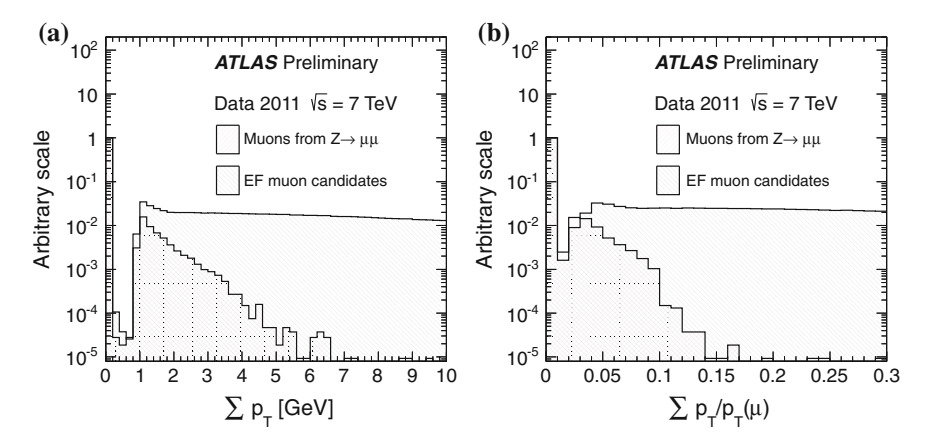


Fig. 4.1 Distribution of the isolation variables $\sum p_T a$ and $\sum p_T/p_T(\mu) b$ for muons originating from the decay of a Z-boson (*pink* hatching) and a sample of muons passing a non-isolated trigger with $p_T > 22 \text{ GeV}$ (*black* hatching)

pass a single muon trigger with no isolation requirements. Muons in this sample originate from a mixture of background processes that produce non-isolated muons, for example $b\bar{b}$ production, as well as processes that produce high-p_T isolated muons such as the production and decay of W- and Z-bosons.

Figure 4.1a shows the distribution of the isolation variable, $\sum p_T$, obtained from each sample of events. Naïvely we would expect that the smallest non-zero value $\sum p_T$ would be 1 GeV, from events in which a muon was accompanied by a single minimum p_T track. However some entries are visible in bins between 0 and 1 GeV. The reason for this comes from the way in which the calculation of the isolation variable is performed. The ID track associated with the muon is reconstructed twice, initially during the reconstruction of the combined muon and then again during the calculation of the isolation variable. The regions of η - ϕ used when reconstructing the tracks are slightly different in each case, and therefore the subtraction of the ID track associated with the combined muon from $\sum p_T$ can result in values between 0 and 1 GeV. Figure 4.1b shows the distribution of the relative isolation, $\sum p_T/p_T(\mu)$, where the p_T of the combined muon is used in the denominator.

The muons from Z-boson decays have much narrower $\sum p_T$ and $\sum p_T/p_T(\mu)$ distributions and are therefore good quantities to use to distinguish isolated muons.

Before an isolated trigger could be used online to accept or reject real events, the parameters and cut values had to be optimised. The efficiency for $Z \to \mu\mu$ events to pass cuts on the isolation variable had to be kept as high as possible, while ensuring that inclusive muon events from the single muon trigger were rejected at a sufficiently high rate. The efficiency and rejection rate were plotted as a function of the cut value on the isolation variable, shown for the EF track isolation variable in Fig. 4.2. The

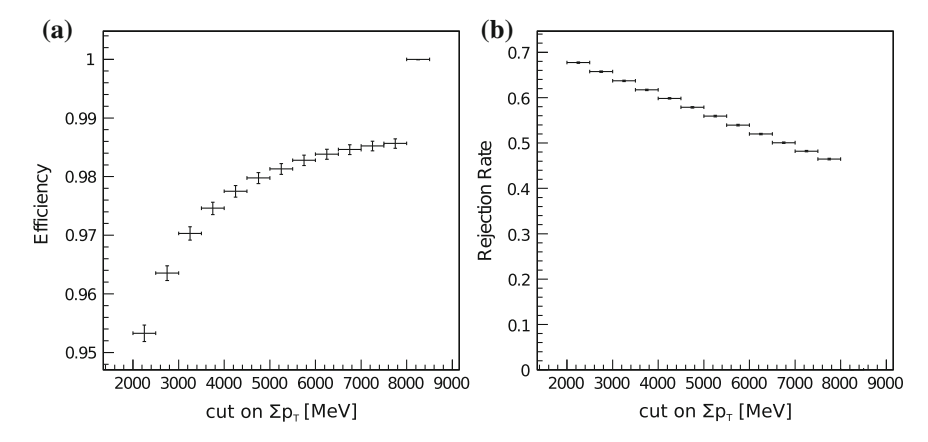
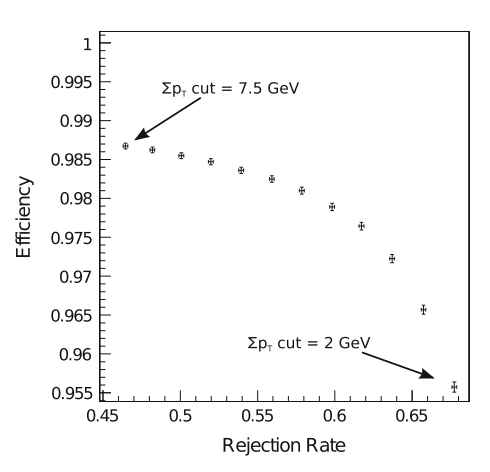


Fig. 4.2 Efficiency **a** and rejection rate **b** of various cuts on the isolation variable $\sum p_T$. The efficiency is calculated using a sample of $Z \to \mu\mu$ events, and the rejection from a sample of inclusive muon events. The right-most bins of the distributions show the efficiency and rejection rate when no cut is made and are therefore 1 and 0, respectively, by definition. The cut values used elsewhere are the values at the lower edge of the bin

Fig. 4.3 Efficiency versus rejection curve produced by varying the cut on the isolation variable $\sum p_T$ in 500 MeV increments

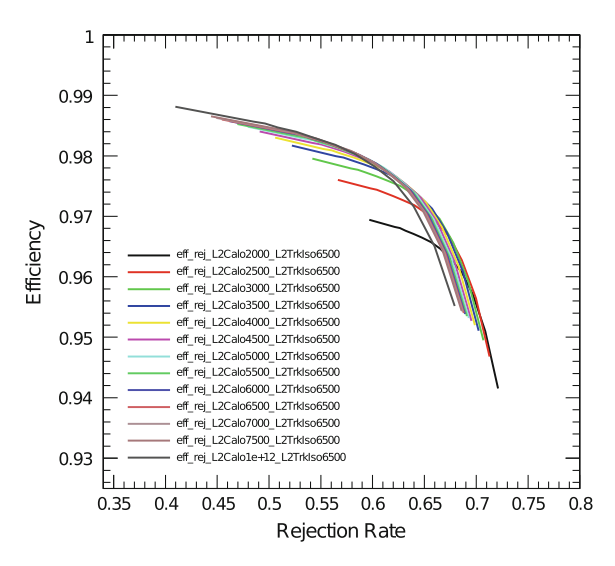


efficiency versus rejection rate can then be plotted, as shown in Fig. 4.3, to show how a target rejection rate maps to an efficiency.¹

The plots shown in Figs. 4.2 and 4.3 were produced by varying only the cut on the EF track isolation variable, with no cut on the L2 track or calorimeter isolation variables. Similar efficiency versus rejection curves can be created by imposing cuts

¹In Figs. 4.2, 4.3 and 4.4 the trigger efficiency is measured with respect to offline muons with $p_T > 20$ GeV and which pass cuts on the quality of their ID tracks. From Fig. 4.5 onwards efficiencies are measured with respect to *isolated* offline muons that satisfy the same p_T and track quality requirements and also have $\sum p_T/p_T(\mu) < 0.1$.

Fig. 4.4 Efficiency versus rejection rate curves. Each curve is produced by first choosing cuts values for the L2 isolation variables and then varying the cut on the EF track isolation variable. The cuts on the L2 isolation variables are described in the legend, "L2Calo4500" refers to a cut of 4.5 GeV on the L2 calorimeter isolation variable, "L2TrkIso6500" refers to a cut of 6.5 GeV on the L2 track isolation variable, which is kept fixed to produce the curves in this example



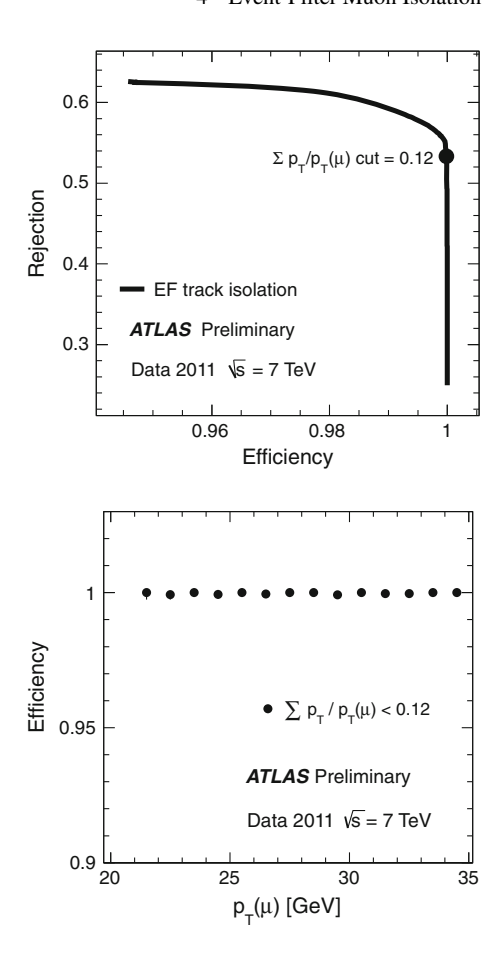
on both the L2 and EF isolation variables. An example of a family of curves produced by varying the cuts on the EF track isolation and L2 calorimeter isolation variables for a given cut on the L2 track isolation variable is shown in Fig. 4.4. Equivalent curves can be produced by varying the cut on the relative EF track isolation variable, $\sum p_T/p_T(\mu)$. It can be seen that cutting on the L2 isolation variables produces a smaller effect than imposing cuts on the EF track isolation.

Physics analysis groups required that the p_T threshold on the isolated single muon trigger was to be kept as low as possible for the 2012 data taking. Searches for rare processes such as $H \rightarrow \tau \tau$, for example, need as many potential signal events to be kept as possible. A 24 GeV p_T threshold was used and it was decided that a sufficient rejection rate could be obtained, and computation time saved, by cutting on only the EF track isolation variable. The relative isolation, $\sum p_T/p_T(\mu)$ was ultimately used, since it produces a looser isolation requirement for high- p_T muons, where isolation is less important. The cut value chosen was $\sum p_T/p_T(\mu) < 0.12$ —a looser cut than that applied by offline analyses to ensure no loss of efficiency. As shown in Fig. 4.5, this is a point at which a rejection of around 55 % is achieved without any noticeable drop in efficiency.

The efficiency of the isolated trigger with respect to offline isolated muons is shown as a function of muon p_T in Fig. 4.6. With the choice of $\sum p_T/p_T(\mu) < 0.12$ the efficiency of the isolated trigger is close to one, and does not show any noticeable dependence on the p_T of the muons.

Fig. 4.5 Rejection of muons selected by a non-isolated muon trigger with a p_T threshold of 22 GeV, as a function of efficiency for muons arising from $Z \to \mu\mu$ decays. The cut on the relative isolation variable $\sum p_T/p_T(\mu)$ is varied in order to make the *curve*

Fig. 4.6 Efficiency of the EF isolated trigger with respect to isolated offline muons from $Z \rightarrow \mu\mu$ decays, as a function of muon p_T



4.3.1 Pile-up Dependence

The pile-up dependence of the isolation was important to evaluate before deploying the trigger online. The pile-up conditions in 2011 were known to be less severe than those expected in 2012. Therefore any pile-up dependence observed in the 2011 data could render the isolated trigger unusable in 2012. In Fig. 4.7 the mean of the isolation variable $\sum p_T$ is shown as a function of the number of primary vertices reconstructed in the event. The mean increases with increasing numbers of vertices, indicating a small pileup dependency.

Figure 4.8a shows the difference in longitudinal impact parameter between muons and nearby ID tracks, for events with different numbers of reconstructed vertices. The distribution broadens slightly as the number of vertices increases, indicating that increasing numbers of tracks from pile-up are being included in the calculation of $\sum p_T$. In an attempt to reduce the pile-up dependence the Δz_0 cut was tightened to

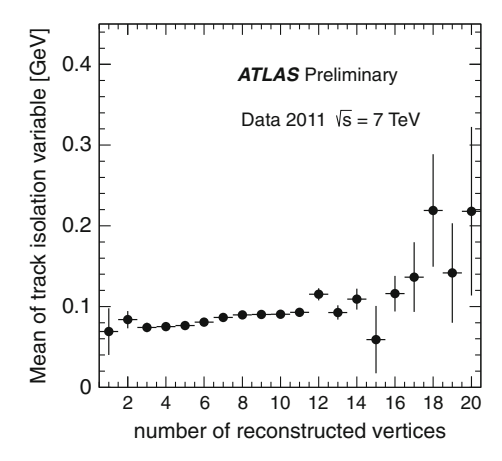


Fig. 4.7 The mean of the track isolation variable $\sum p_T$ for muons from $Z \to \mu\mu$ decays, as a function of the number of reconstructed vertices

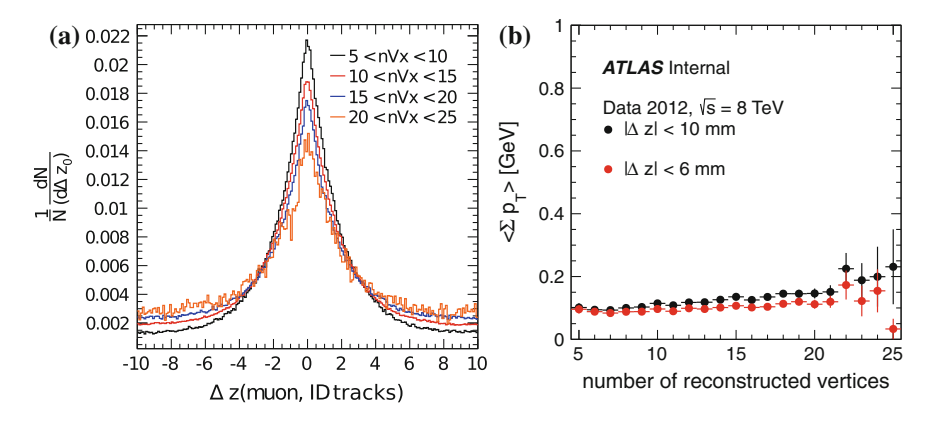
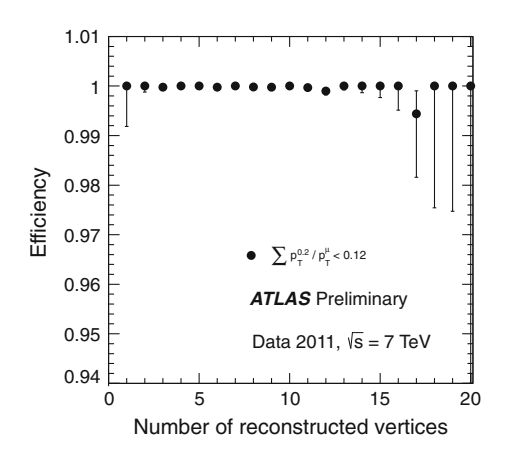


Fig. 4.8 a Distribution of Δz_0 (muon, ID tracks) for muons from $Z \to \mu\mu$ decays, shown separately for events with different numbers of reconstructed vertices. **b** Comparison of the mean of the track isolation variable $\sum p_T$ for muons from $Z \to \mu\mu$ decays, as a function of the number of reconstructed vertices, for cases where the Δz_0 cut is 10 mm (black) and 6 mm (red)

6 mm. Making a change such as this increased the isolated trigger rate; fewer tracks were being used to calculate $\sum p_T$ and so a given muon would look slightly more isolated than when the cut of $\Delta z_0 < 10$ mm was used. The muon would then pass the cut on the isolation variable where it had failed before. The change in rate was calculated by running two versions of the trigger, with the 10 and 6 mm cuts, on the same set of data and counting the number of events which passed in each case. Tightening the Δz_0 cut to 6 mm was observed to increase the trigger rate by just 2%, an amount which was deemed to be acceptable. Figure 4.8b compares the mean value of the isolation variable when the longitudinal impact parameter cut is reduced to

Fig. 4.9 The efficiency of the EF isolated trigger with respect to isolated offline muons from $Z \rightarrow \mu\mu$ decays, as a function of the number of reconstructed vertices in the event



6 mm. As expected the value of the isolation variable reduces, since there are fewer tracks being included in the summation, and the pile-up dependence is also reduced.

Figure 4.9 shows the efficiency of the isolated trigger as a function of the number of reconstructed vertices in the event. No significant dependence on the pile-up conditions is observed.

4.4 Summary

The EF isolated muon trigger was used online throughout the 2012 data-taking period. A cut of $\Delta z_0 < 6\,\mathrm{mm}$ was used on the tracks entering the calculation of the isolation variable, and a cut on the relative isolation variable of $\sum p_T/p_T(\mu) < 0.12$ was used to determine whether a given muon was isolated. The trigger became one of the primary muon triggers used in 2012 and was used in the analysis described in Chap. 7.

Reference

 ATLAS Collaboration. (2012). Performance of the ATLAS muon trigger in 2011 technical report. ATLAS-CONF-2012-099. Geneva: CERN.

Chapter 5 Jet Vetoing in Top-Antitop Events

5.1 Introduction and Motivation

Measurements of the properties of the top quark provide important tests of the Standard Model and any deviations from the SM predictions could be an indication of new physics. However, many top quark analyses suffer from large uncertainties associated with the Monte Carlo modelling of tt final states, in particular the additional quark or gluon radiation present in the events. In many cases the modelling of additional radiation is one of the dominant uncertainties limiting the precision of ATLAS measurements. Table 5.1 gives some examples. Given the large number of analyses in which the uncertainty associated with the modelling of additional radiation produced in association with a tt system was dominant, it was clear that measurements sensitive to this radiation were needed. The Monte Carlo modelling could then be constrained and uncertainties in subsequent measurements could be reduced.

This chapter will describe how a jet veto was used to quantify the amount of additional jet activity in tt events and constrain the uncertainty associated with modelling the additional quark and gluon radiation. As discussed in Sect. 1.6, jet vetoes have been studied for many years, typically in events containing a dijet system. One of the first measurements of such quantities at the LHC was the ATLAS measurement of dijet production with a veto additional central jet activity [5]. The measurements presented in this chapter were not only the first measurements of jet vetoes in tt events, but also the first detector corrected measurements of tt final states at the LHC. All measurements were performed using data from proton-proton collisions at $\sqrt{s} = 7\,\text{TeV}$ collected by the ATLAS detector during 2011. The integrated luminosity of the data sample was $2.05\pm0.08\,\text{fb}^{-1}$.

Work in this chapter has been published in [6, 7].

Measurement	Uncertainty	% of total (%)
tt spin-correlations [1]	ISR/FSR	10
tt cross section [2]	Generator	40
top mass [3]	ISR/FSR	22
tt charge asymmetry [4]	ISR/FSR	17

Table 5.1 Measurements performed using the 2011 data collected by ATLAS in which the dominant source of systematic uncertainty was the MC modelling of the tr system

ISR/FSR refers to an uncertainty associated with the amount of initial and final-state radiation produced (cf. Sect. 5.2). Generator refers to the combined uncertainty obtained after comparing the description of the tt system provided by different MC generators, varying the amount of ISR and FSR, and assessing PDF uncertainties. The dominant contribution in the Generator category is the modelling of ISR and FSR

5.1.1 Variable Definition

The variable of interest is the jet veto efficiency, or gap fraction, defined as

$$f(Q_0) = \frac{n(Q_0)}{N} \tag{5.1}$$

where N is the number of selected $t\bar{t}$ events, and $n(Q_0)$ is the subset of these events which do not contain any additional jets with transverse momentum above a threshold Q_0 , in a central rapidity interval. The jet veto efficiency can then be expressed as

$$f(Q_0) = \frac{\sigma(Q_0)}{\sigma} \tag{5.2}$$

where σ is the fiducial cross section for inclusive $t\bar{t}$ production, and $\sigma(Q_0)$ is the fiducial cross section for $t\bar{t}$ events not containing any additional jets with $p_T > Q_0$ in the rapidity interval. The jet veto efficiency is measured for four jet rapidity intervals: $|y| < 0.8, \, 0.8 \le |y| < 1.5, \, 1.5 \le |y| < 2.1, \, \text{and} \, |y| < 2.1.$ The jet veto efficiency presented in this way as a function of Q_0 is sensitive to the highest- p_T emission into each rapidity interval, but does not account for multiple emissions into each region. The veto criterion was also extended to probe radiation beyond the leading additional jet,

$$f(Q_{\text{sum}}) = \frac{n(Q_{\text{sum}})}{N} \equiv \frac{\sigma(Q_{\text{sum}})}{\sigma},$$
 (5.3)

where $n(Q_{\text{sum}})$ is the number of $t\bar{t}$ events, and $\sigma(Q_{\text{sum}})$ the fiducial cross section in which the scalar sum of the transverse momentum of all additional jets in the rapidity interval is less than Q_{sum} . Note here that there is still a minimum jet p_T requirement, which introduces an additional scale dependence to this variable.

5.2 Data and Monte Carlo Samples

The data used in this analysis were collected between March and August 2011. All events in data were required to pass data quality requirements, as defined by Top_GRL_K (cf. Sect. 2.2.4), which ensure that all sub-detectors crucial to the detection and reconstruction of electrons, muons, jets and missing transverse energy were fully functional. Events were also required to have fired either the single electron trigger (EF_e20_medium until period K and EF_e22_medium in periods J and Ef_mu18_medium in periods J and K). The e20 and e22 refer to single electron triggers with p_T thresholds of 20 and 22 GeV, respectively. The mu18 refers to a single muon trigger with a p_T threshold of 18 GeV, and $_medium$ in this case is shorthand for the requirement that a specific L1 trigger must also have fired.

Monte Carlo events were produced using a variety of generators, capable of producing tt events with differing levels of theoretical accuracy. MC@NLO [8] and POWHEG [9] were used to generate inclusive tt events with next-to-leading order accuracy. A cartoon schematic of the accuracy to which these events can be produced is shown in Fig. 5.1. As the inclusive tt events are produced with

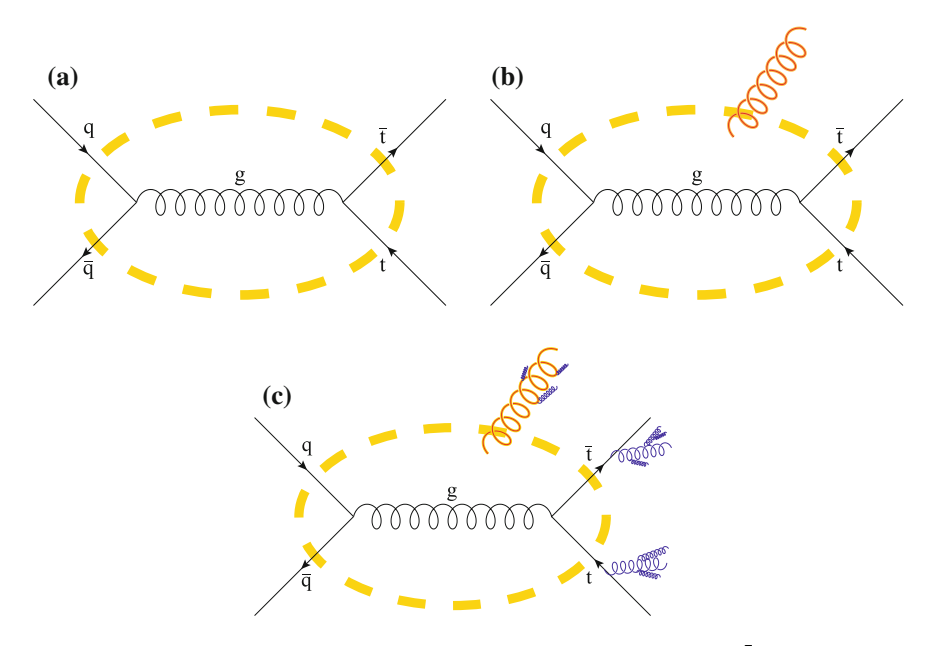


Fig. 5.1 Cartoons giving a schematic description of the physics included in $t\bar{t}$ events generated with the next-to-leading order MCs MC@NLO and POWHEG. The dashed oval in a represents all virtual corrections to the leading order $t\bar{t}$ diagram. The external gluon shown in b represents the real emission corrections, which could be attached to any leg of the diagram enclosed by the loop. The cartoon in c shows the additional QCD radiation produced by the parton shower, which is typically softer than that produced by the matrix element

next-to-leading order accuracy (Fig. 5.1a), the first *additional* jet, originating from the real emission piece of the NLO calculation, has only leading order accuracy in QCD. This is depicted in Fig. 5.1b. The parton-level events are then interfaced to Monte Carlo programs to provide the parton shower, hadronisation and underlying event models. Jets originating from the parton shower are often quoted as having leading logarithmic accuracy, as described previously in Sect. 1.5.2. However, due to the presence of the non-global and super-leading logarithms discussed in Sect. 1.6, when estimating a jet veto efficiency the leading-logarithmic accuracy is not guaranteed.

The MC@NLO events were generated using the CTEQ6.6 [10] PDF, and interfaced to HERWIG [11] v6.510 and JIMMY [12] for parton showering, hadronisation and underlying event. The event generator tune used was AUET1 [13]. POWHEG events were also generated using the CTEQ6.6 PDF. Parton shower, hadronisation and underlying event were included by interfacing the POWHEG events to PYTHIA [14] with tune AMBT1 [15], or to HERWIG+JIMMY with tune AUET1.

ALPGEN and SHERPA were used to produce tt+jets events with leading order accuracy. Figure 5.2 shows a cartoon depicting the theoretical accuracy to which the events were generated. Contrary to the NLO generators, the inclusive tt system is produced with just leading order accuracy (Fig. 5.2a). However, the matrix elements for tt production with multiple additional partons in the final state are also included with leading-order accuracy (Fig. 5.2b). Parton showers are then applied as before (Fig. 5.2c), along with the usual hadronisation and underlying event models.

ALPGEN [16] was used to generate matrix elements with up to three additional partons in the final state, using the CTEQ6L1 [10] PDF. HERWIG+JIMMY was used to provide parton showering, hadronisation and underlying event (tune AUET1). The MLM [17] matching prescription was used to remove the double-counting between partons produced by the matrix elements and those coming from the parton shower.

SHERPA was also used to generate tt events with up to three additional partons in the final state using the CTEQ6L1 PDF. The CKKW [18] matching scheme was used when combining matrix elements with the parton shower. Events were generated with the authors' default underlying event tune.

The generator ACERMC [19], which essentially acts as an interface between MADGRAPH matrix element calculations and the PYTHIA6 parton shower, was used to produces $t\bar{t}$ events with leading order accuracy, using the MRST2007LO* [20] PDF and AMBT1 underlying event tune. The ACERMC events have the poorest theoretical accuracy as the jets are produced only by the parton shower. However the generator allows easy access to parameters that control the amount of parton shower activity. Samples of events are generated with increased and decreased amounts of initial-state radiation, and are typically used to assess ISR-related modelling uncertainties in ATLAS measurements of $t\bar{t}$. In the sample of events generated with decreased amounts of ISR the following parton shower parameters were set, PARP [67] = 0.5, PARP [64] = 4. The sample with increased ISR was generated with parameter values PARP [67] = 6, PARP [64] = 0.25.

The main expected backgrounds to the tt process consist of diboson production, single top production and Z+jets events. Diboson events were generated with HERWIG and single top events were generated with MC@NLO interfaced to HERWIG. Z+jets

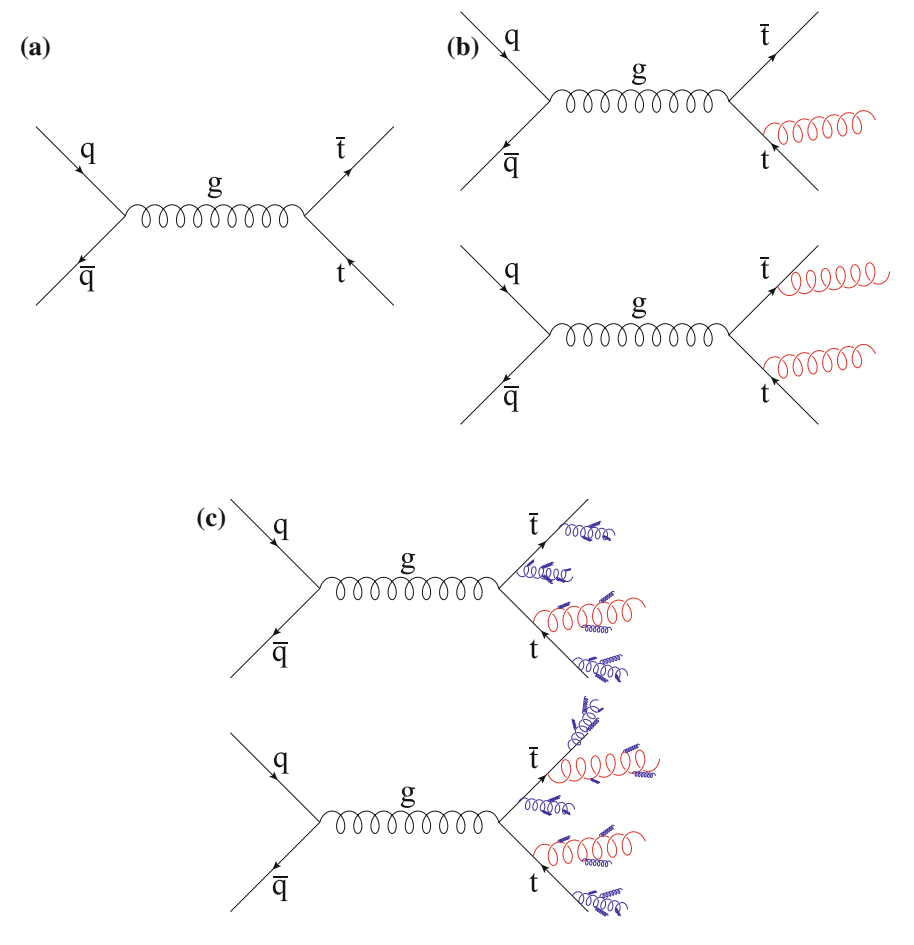


Fig. 5.2 Cartoons giving a schematic description of the physics included in tt events generated with the multi-leg leading-order MCs Sherpa and Alpgen

events were generated using ALPGEN interfaced to HERWIG and contained up to five additional partons in the final state. Separate samples were generated for Z production in association with $b\bar{b}$ production, and overlap removal was performed to remove the double-counting of the heavy quark events. Further backgrounds were expected from W+jets and QCD multijet events, where one or more leptons do not originate from a W or Z decay. These backgrounds are difficult to accurately model and so they were estimated using the data in Sect. 5.4.

All MC samples are passed through the full GEANT4 [21, 22] simulation of the ATLAS detector. Additional minimum bias events generated with PYTHIA are overlaid on the signal and background samples and used to simulate the effect of multiple proton-proton interactions. The simulated events are then reweighted to

ensure that the average number of proton-proton interactions per bunch crossing, $\langle \mu \rangle$, is the same in MC as in data. $\langle \mu \rangle$ varied between data-taking periods and for the data used in this analysis was in the range $4 < \langle \mu \rangle < 8$.

5.3 Object and Event Selection

5.3.1 Muons

The muons used in this analysis were identified as *combined*, as described in Sect. 3.4. Cuts were applied to the inner detector tracks used to construct the combined muons. These cuts are defined by the Muon Combined Performance (MCP) group, to ensure that all muons used in analyses are of sufficient quality. At the time of this analysis the cut requirements were:

- Muons must produce at least one hit in the pixel b-layer, at least two hits across all pixel layers and at least six hits in the SCT.
- There must be fewer than 3 holes across all silicon layers.
- If the muon has $|\eta| < 1.9$, the number of TRT hits + TRT outliers must be greater than five and the outlier fraction, $N_{\text{outliers}} / (N_{\text{outliers}} + N_{\text{hits}})$, must be less than 0.9.
- For muons with $|\eta| \ge 1.9$, if the number of hits + outliers is greater than five the outlier fraction must be less than 0.9.

The muons must be isolated in the calorimeter, by requiring that the sum of energy deposits in a cone of $\Delta R=0.3$ around the muon is less than 4 GeV. The muons must also be isolated in the inner detector by requiring that the scalar sum of the p_T of tracks within a cone of $\Delta R=0.3$ around the muon is less than 4 GeV. Finally a muon-jet overlap removal cut is applied; any muons with $\Delta R(\text{muon, jet})<0.4$ are rejected.

5.3.2 Electrons

Electrons with a so-called author of 1 or 3 are used in the analysis. These make up the standard electron collection, and must satisfy the tight++ electron identification requirements as described in Sect. 3.3. To ensure well-measured electrons, the electromagnetic shower produced by electrons traversing the detector must be contained completely within the barrel or end-cap calorimeters. Therefore electrons with $1.37 < |\eta| < 1.52$, which fall into the transition region between the barrel and end-caps, are rejected. All electrons must also pass calorimeter isolation requirements. The total transverse energy in a cone of $\Delta R = 0.3$ around the electron candidate—without including the electron candidate itself—must be less than 3.5 GeV.

5.3.3 Jets

Jets are reconstructed using the anti- k_t algorithm [23, 24] with radius parameter R set to 0.4. The inputs to the jet-finding algorithm are clusters of adjacent calorimeter cells calibrated at the electromagnetic (EM) scale. These jets are corrected for calorimeter response and other detector effects as described in Sect. 3.5.

Jets originating from b-quarks are identified using the IP3D+SV1 algorithm at the 70% efficiency working-point, described in Sect. 3.5.1, and are referred to as b-tagged jets.

To remove jets originating from additional proton-proton (pile-up) interactions the jet vertex fraction (JVF) is required to be greater than 0.75. The JVF variable is constructed by first associating tracks to jets by checking that ΔR (jet, track) < 0.4. The scalar-summed transverse momentum of tracks originating at the primary vertex is then divided by the scalar-summed transverse momentum of tracks from all vertices,

$$JVF = \frac{\sum_{i}^{tracks from primary vertex} p_{T}^{i}}{\sum_{j}^{all tracks} p_{T}^{j}}.$$
 (5.4)

If a jet is located outside the acceptance of the inner detector (|y| > 2.4) and therefore has no associated tracks it receives a JVF value of -1.

5.3.4 Missing Transverse Energy

The missing transverse energy (E_T^{miss}) in an event is calculated using the MET_RefFinal_em_tight definition [25]. The inputs to the algorithm are topological clusters calibrated at the EM scale, and corrected according to the energy scale of the associated jet or electron. The momentum of muons is not primarily measured using the calorimeters. They are included in the E_T^{miss} calculation using measurements from the tracking and muon spectrometer systems. Topological clusters are associated with electrons, high-p_T jets and low-p_T jets. Any clusters not associated to one of these objects are included in the E_T^{miss} calculation in the so-called CellOut term.

All energy corrections and uncertainties applied to reconstructed electron, muons and jets are also consistently propagated to the calculation of the missing transverse energy. For example if the energy of a jet is increased when applying the uncertainty, the missing transverse energy is updated to ensure overall conservation of energy.

5.3.5 Event Selection Requirements

Electrons selected for use in further analysis are required to have large transverse energy, $E_T > 25\,\text{GeV}$ and $|\eta| < 2.47$. Electrons in the transition region between

the barrel and end-cap calorimeters, with 1.37 $< |\eta| < 1.52$ are not used. Muons are required to have $p_T > 20\,\text{GeV}$ and $|\eta| < 2.5$. All jets, after calibration, are required to have $p_T > 25\,\text{GeV}$ and |y| < 2.4. Jets must also be well-separated from all selected leptons, ℓ , by $\Delta R(j,\ell) > 0.4$.

In order to create a highly enriched $t\bar{t}$ sample, events are required to contain two high-p_T leptons—either two isolated muons $(\mu\mu)$, two isolated electrons (ee) or one isolated muon and one isolated electron $(e\mu)$. The analysis is then divided according to the three dilepton decay channels. In all channels events are required to have two *b*-tagged jets with p_T > 25 GeV and |y| < 2.4. In the ee and $\mu\mu$ channels, the background from $Z\rightarrow ee/\mu\mu$ events is reduced by requiring that the dilepton invariant mass is not close to the Z-boson mass, i.e. $|m_{II}-91\,\text{GeV}|>10\,\text{GeV}$. The dilepton invariant mass must also be larger than 15 GeV to reject backgrounds from vector-meson decays. Finally the E_T^{miss} is required to be greater than 40 GeV to help ensure the presence of two neutrinos. In the $e\mu$ channel the backgrounds are significantly smaller, mainly coming from $Z\rightarrow \tau\tau$ and diboson events, and are suppressed by requiring that H_T (the scalar sum of the transverse momentum of all reconstructed leptons and jets satisfying the selection criteria) is greater than 130 GeV. A summary of the event selection criteria is shown in Table 5.2.

The event selection described here provides an ideal environment to probe any additional radiation present in $t\bar{t}$ events. By requiring two b-tagged jets we gain confidence in the assumption that any additional (non-pileup) jets that are observed have come from some QCD emission. The requirement that both W-bosons must decay to leptons removes complications that arise from jet combinatorics present when considering hadronically-decaying W's and gives us further confidence that the additional jet(s) we select originated from QCD radiation produced in association with a $t\bar{t}$ system.

Table 5.2	Selection requirements	applied to the t	three analysis channels
-----------	------------------------	------------------	-------------------------

	Channel	Channel			
Selection	ee	$\mu\mu$	$e\mu$		
Electrons	$\begin{array}{c} \text{2 with } E_T > 25 \text{ GeV}, \\ \eta < 2.47, \\ 1.37 < \eta < 1.52 \\ \text{excluded} \end{array}$	_	1 with $E_{\rm T} > 25$ GeV, η < 2.47, 1.37 < η < 1.52 excluded		
Muons	_	$ \begin{array}{l} 2 \text{ with } p_T > 20 \text{ GeV}, \\ \eta < 2.5 \end{array} $	$ \begin{array}{l} 1 \text{ with } p_T > 20 \text{ GeV}, \\ \eta < 2.5 \end{array} $		
E _T miss	>40 GeV	>40 GeV	_		
H_T	_	_	>130 GeV		
$m_{\ell\ell}$	>15 GeV $ m_{\ell\ell} - 91 \text{GeV} > 10 \text{GeV}$	>15 GeV $ m_{\ell\ell}-91$ GeV $ >$ 10 GeV	_		
b-tagged jets	At least 2 with $p_T > 2$	At least 2 with $p_T > 25$ GeV, $ y < 2.4$, $\Delta R(j, \ell) > 0.4$			

5.4 Backgrounds 71

5.4 Backgrounds

5.4.1 Fake Lepton Background

The background resulting from events in which objects are mis-identified as leptons—the fake background—was estimated by another member of the analysis team using the matrix method [26]. The technique was also used in the $t\bar{t}$ cross section [2] and spin correlation [1] analyses, and makes used of a sample of events in which leptons are identified using criteria less stringent than those used in the main analysis. The numbers of events containing one or more fake leptons can be related to the number of events containing loose, or combinations of tight and loose leptons. The matrix method predicted a total fake background of 42 ± 21 events, which was much smaller than the uncertainty on the expected number of $t\bar{t}$ events.

5.4.2 Other Backgrounds

Backgrounds from Z+jets, diboson and single-top processes are estimated using the MC samples described in Sect. 5.2, after scaling the number of expected events to the NLO (or NNLO where available) cross sections. Cross sections and k-factors applied to each sample are documented in [27]. Expected numbers of events for the dominant background sources are shown in Table 5.3. The largest physics background comes from single-top production and contributes approximately 2% to the final event yield. All other backgrounds are negligible. The total background contamination is estimated to be smaller than the uncertainty on the theoretical calculation of the $t\bar{t}$ cross section of around 5% [28–30]. Therefore backgrounds are neglected in the extraction of the jet veto efficiencies. The systematic uncertainty associated with neglecting the backgrounds is discussed in Sect. 5.8.5.

5.5 Corrections to the Simulation

Various sets of corrections were applied to the simulated events to ensure that the MC matches the performance observed in data. The corrections applied were those recommended by the top group [31] and combined performance groups for the dataset used in the analysis.

• The MC events are reweighted to produce the same experimental conditions as observed in the data. The reweighting ensures that (i) the fraction of events affected

Sample	Events expected (observed) at 2 fb ⁻¹				
	ee	$\mu\mu$	еμ	Total	
Data	242	436	1095	1773	
MC@NLO tī	256.9	363.3	924.0	1544.2	
Single top	6.0	12.3	19.7	37.9	
$Z \rightarrow \mu\mu$	0.0	1.1	0.0	1.1	
$Z\rightarrow \mu\mu$ +bb	0.0	2.1	0.0	2.1	
Z→ee	0.5	0.0	0.0	0.5	
Z→ee+bb	1.8	0.0	0.0	1.8	
WW	0.0	0.1	0.3	0.4	
ZZ	0.0	0.1	0.1	0.2	
WZ	0.0	0.2	0.0	0.2	

Table 5.3 Number of events observed in 2 fb⁻¹ of data, as well as numbers of events expected from the signal and dominant background processes

by the LAr hole¹ is the same in data and MC, and (ii) the average number of interactions per bunch crossing, $\langle \mu \rangle$, was the same in MC and data.

- The muon momentum resolution in the MC was corrected to match the data by applying additional Gaussian smearing.
- The muon reconstruction efficiency in the MC was corrected to match the performance found in Z data events, by applying scale factors.
- The L2 muon trigger was incorrectly configured in the MC simulation and lost efficiency at high p_T. The MC trigger information is therefore not used, but the trigger efficiency measured in Z data events was applied to the reconstructed offline muons.
- The efficiency of the muon isolation cuts in the MC was corrected to match the performance found in Z data events.
- The efficiency of the electron identification and reconstruction in the MC was corrected to match the performance in Z data events.
- The efficiency and mis-identification rates of the *b*-tagging algorithm in the MC were corrected to match those in data.
- The jet energy resolution in the MC was corrected to match the data by applying additional Gaussian smearing.

The correction factors associated with muons, electrons and jets were provided with associated uncertainties. The effects of these uncertainties is discussed in Sects. 5.8.6 and 5.8.7.

¹During part of the 2011 data-taking period six front-end boards of the Liquid Argon calorimeter failed.

5.6 Detector-Level Data and MC Comparisons

The MC samples used in the analysis were compared to data to ensure that the relevant kinematic properties were modelled sufficiently well. The uncertainty on the expected number of $t\bar{t}$ events was quite large—approximately 20 % uncertainty associated with b-tagging and ~9 % uncertainty from the NNLO cross section. However because the jet veto efficiency is not sensitive to the overall event normalisation, the $t\bar{t}$ simulation was normalised to the number of events observed in data to allow a comparison of the shapes of distributions. Some example distributions are shown in Fig. 5.3 (lepton

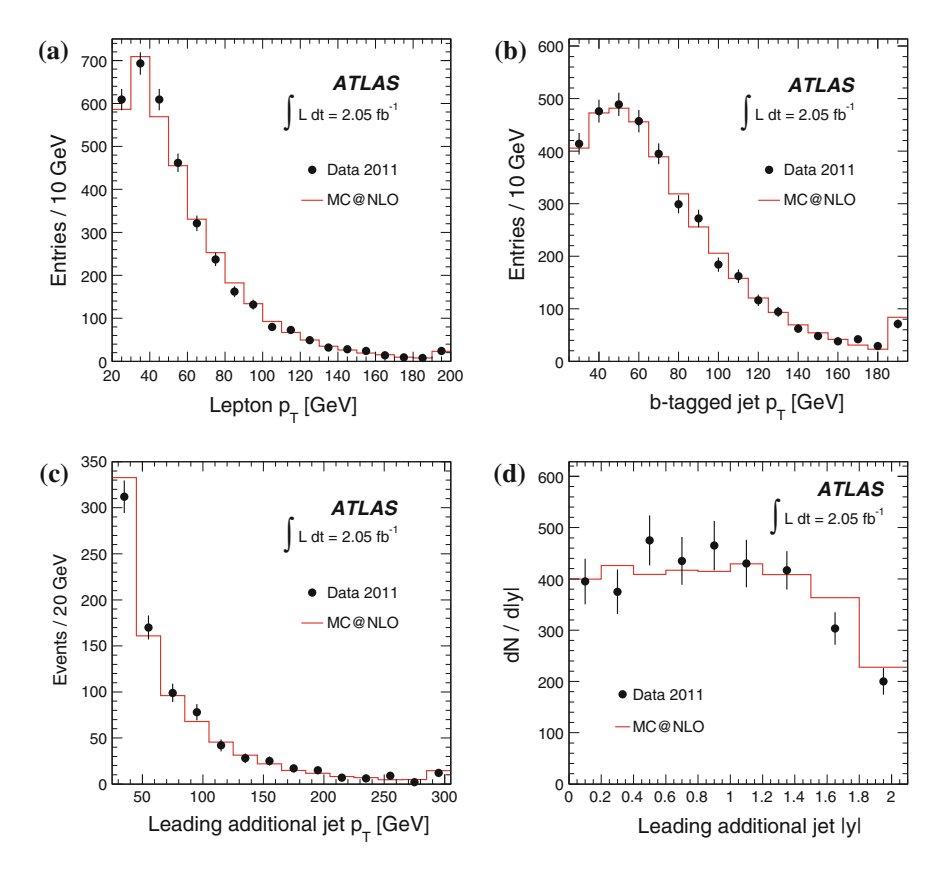


Fig. 5.3 Distributions of **a** lepton p_T , **b** b-tagged jet p_T , **c** leading additional jet p_T and **d** leading additional jet rapidity for the selected data events compared to the MC@NLO prediction. The data are shown as *closed black circles* with the statistical uncertainty. The MC@NLO prediction is normalised to the number of events observed in data and is shown as a *solid red line*. The overflow events at high p_T are included in the final bin of each histogram

p_T, b-tagged jet p_T, leading additional jet p_T and leading additional jet rapidity) and the agreement between data and MC was good in all such distributions.

The jet veto efficiency as a function of Q_0 in the uncorrected data is compared to MC@NLO and POWHEG+PYTHIA6 in Fig. 5.4. The data are seen to be in slightly better agreement with POWHEG+PYTHIA6. The jet veto efficiency as a function of $Q_{\rm sum}$ is compared to the detector-level MC@NLO and POWHEG+PYTHIA6 predictions in Fig. 5.5.

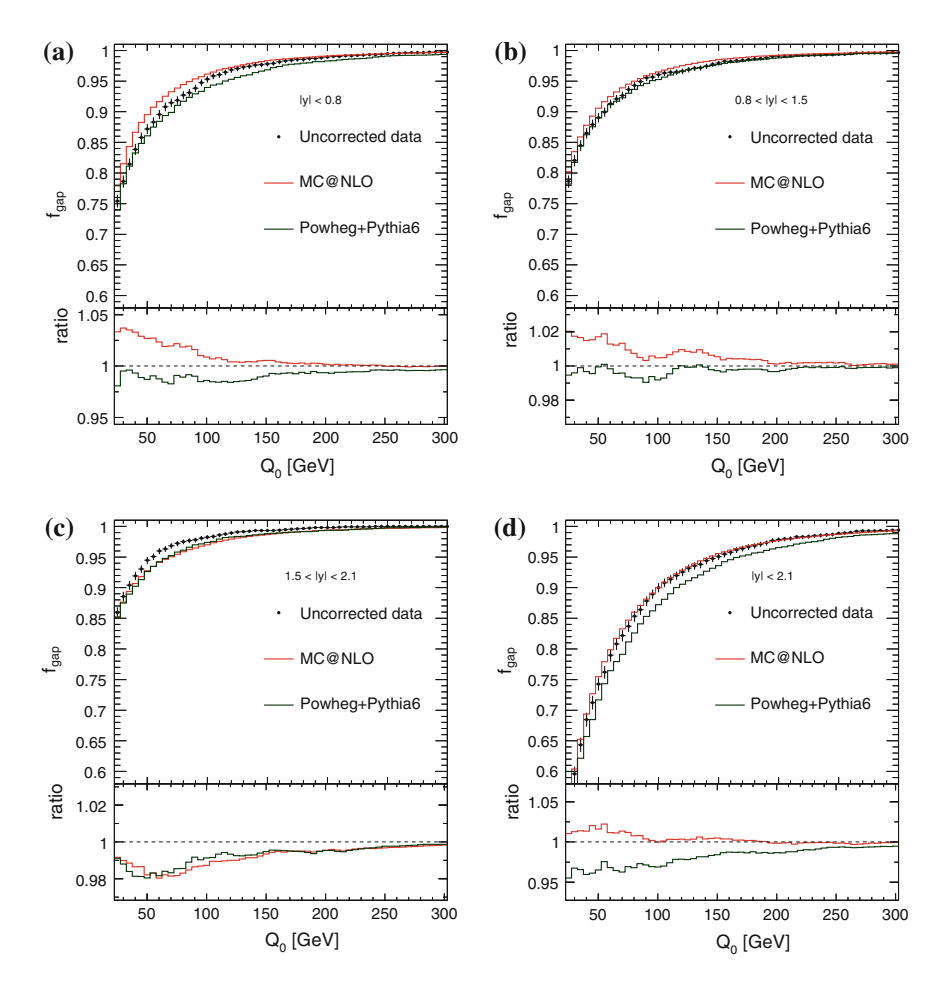


Fig. 5.4 Distribution of the jet veto efficiency as a function of Q_0 in the uncorrected data compared to detector-level predictions from MC@NLO and POWHEG+PYTHIA6 for $\mathbf{a} \ |y| < 0.8, \mathbf{b} \ 0.8 \le |y| < 1.5, \mathbf{c} \ 1.5 \le |y| < 2.1$ and $\mathbf{d} \ |y| < 2.1$

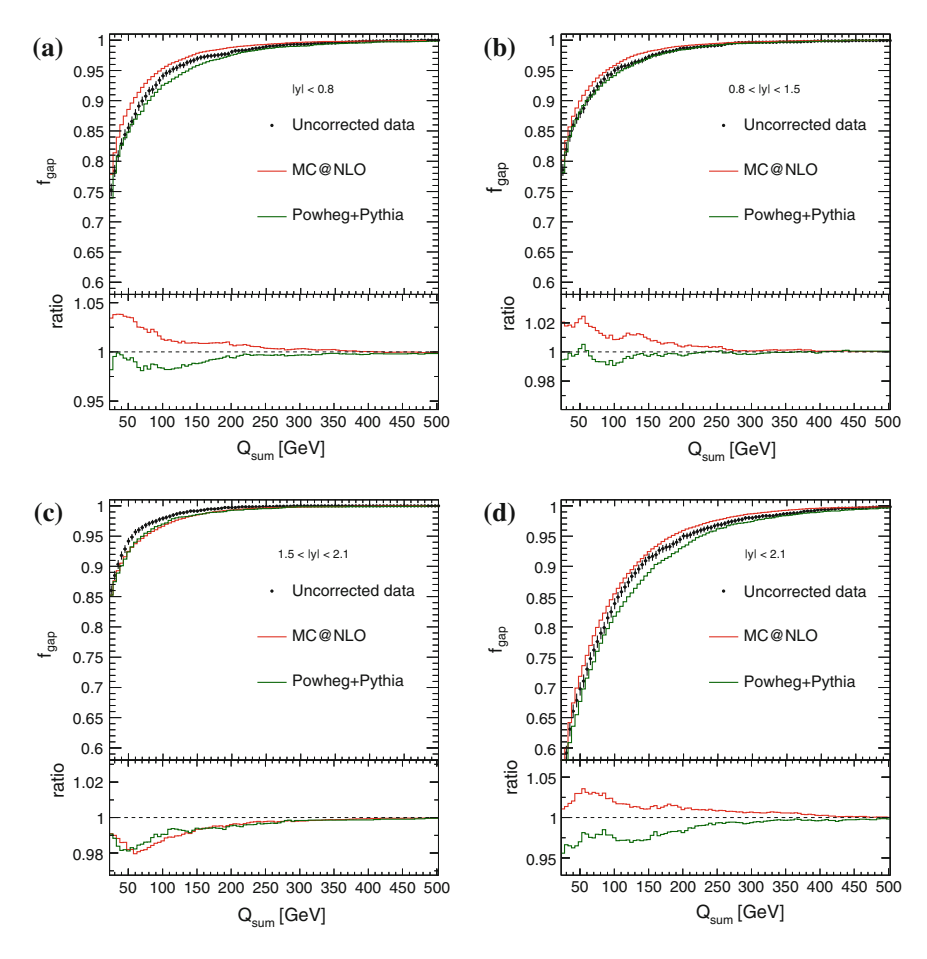


Fig. 5.5 Distributions of the jet veto efficiency as a function of Q_{sum} in the uncorrected data compared to detector-level predictions from MC@NLO and POWHEG+PYTHIA6 for $\mathbf{a} \ |y| < 0.8$, $\mathbf{b} \ 0.8 \le |y| < 1.5$, $\mathbf{c} \ 1.5 \le |y| < 2.1$ and $\mathbf{d} \ |y| < 2.1$

5.7 Correction for Detector Effects

It is now common practice that LHC experimental results are unfolded, and presented after all efficiency and resolution effects have been accounted for. The most important benefit of undertaking this effort is that it enables detector-independent comparisons of data from different experiments, as well as comparisons of data to any theoretical prediction available currently or in the future.

The jet veto efficiencies measured in this analysis were corrected to particle level by defining correction factors which were applied to each data point. The correction factor, C, for the jet veto efficiency at a specific value of $x = Q_0$ or Q_{sum} is defined as

$$C(x) = \frac{f_{\text{MC}}^{\text{particle}}(x)}{f_{\text{MC}}^{\text{reco}}(x)}$$
 (5.5)

where $f^{\text{reco}}(x)$ is the reconstructed jet veto efficiency and $f^{\text{particle}}(x)$ is the particle-level jet veto efficiency. To correct the data, each point in the measured jet veto efficiency in data is multiplied by the corresponding correction factor to obtain an estimate at particle-level, i.e.

$$f_{\text{data}}^{\text{corrected}}(x) = C(x) \cdot f_{\text{data}}^{\text{uncorrected}}(x)$$

The cuts applied on particle-level events are chosen to be as similar as possible to those imposed at detector-level. All particle-level cuts on leptons are identical to the detector-level cuts listed in Table 5.2, except for the pseudorapidity requirement; electrons falling into the transition region between the barrel and end-cap calorimeters are included at particle-level to produce symmetric pseudorapidity requirements between electrons and muons.

Particle-level jets are also produced using the anti- k_t algorithm with R=0.4; the input objects to the jet finding algorithm are the final-state interacting particles (excluding muons and neutrinos) with mean lifetime greater than 10 ps. B-jets at particle-level are identified by requiring that the jets have a nearby b-hadron i.e. $\Delta R(\text{jet}, b\text{-hadron}) < 0.3$. The E_T^{miss} at particle-level is defined by taking the vector sum of all neutrinos in the final state.

Although being conceptually simple and computationally easy to implement, the use of bin-by-bin correction factors has one important drawback. If the distribution being unfolded exhibits large bin-to-bin migrations between particle and reconstructed level then the unfolded results can be highly biased by the MC sample used to construct the correction factors. The correction factors obtained from MC@NLO, POWHEG+PYTHIA6 and POWHEG+HERWIG are shown as a function of Q_0 in Fig. 5.6 and as a function of $Q_{\rm sum}$ in Fig. 5.7. The difference in the correction factors obtained from the different generators is taken as a systematic uncertainty, as described in Sect. 5.8.4.

The correction factor method of unfolding in this analysis is justified in Fig. 5.8 by checking the purity, P, and efficiency, E of the selected events. At each point in the distribution, the purity and efficiency are defined as

$$P(Q_0) = \frac{n_{\text{gap}}^{\text{particle & reco}}(Q_0)}{n_{\text{gap}}^{\text{reco}}(Q_0)} \qquad E(Q_0) = \frac{n_{\text{gap}}^{\text{particle & reco}}(Q_0)}{n_{\text{gap}}^{\text{particle}}(Q_0)}$$
(5.6)

where $n_{\rm gap}^{\rm particle~\&~reco}(Q_0)$ is the number of events that pass the particle and reconstruction level event selection and have no additional jets with $p_T>Q_0$, $n_{\rm gap}^{\rm reco}(Q_0)$ is the number of events that pass the reconstruction level event selection and have no additional jets with $p_T>Q_0$, and $n_{\rm gap}^{\rm particle}(Q_0)$ is the number of events that pass the particle level event selection and have no additional jets with $p_T>Q_0$.

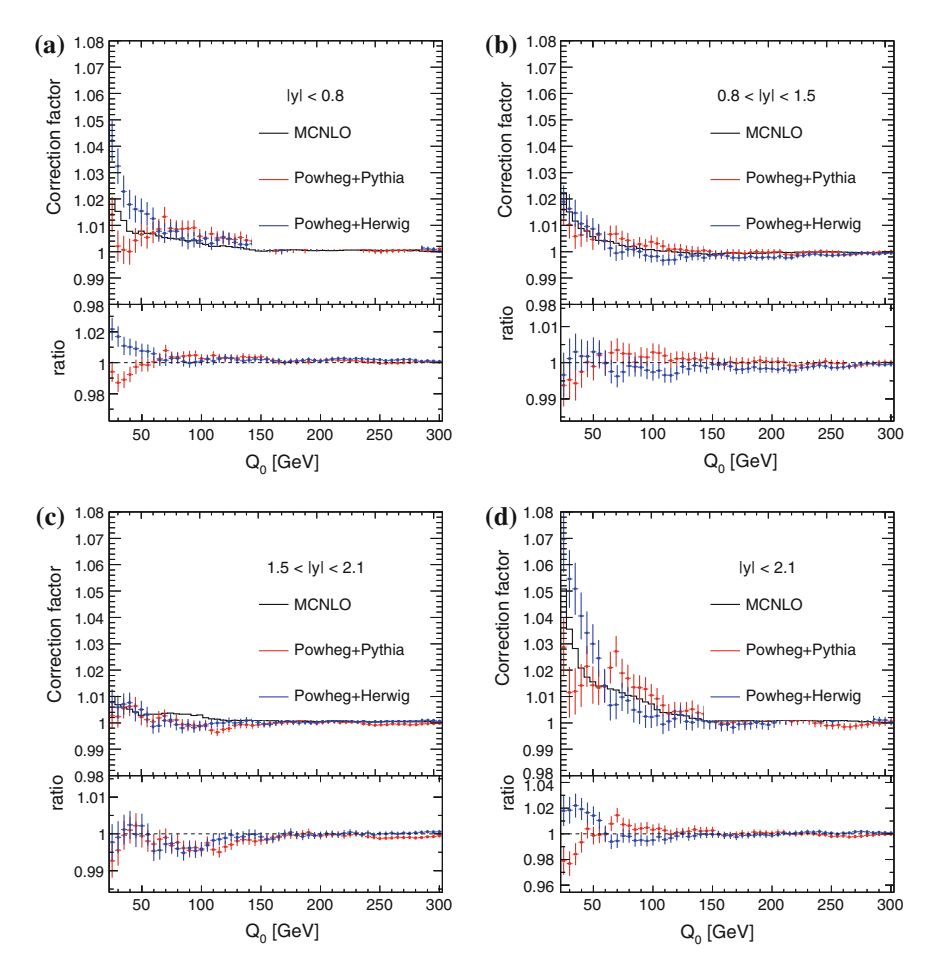


Fig. 5.6 Correction factors for the jet veto efficiency as a function of Q_0 for $\mathbf{a} |y| < 0.8$, $\mathbf{b} 0.8 \le |y| < 1.5$, $\mathbf{c} 1.5 \le |y| < 2.1$ and $\mathbf{d} |y| < 2.1$

The purity is designed to probe the effects of lepton and jet energy/momentum resolution on the number of events entering into the numerator of the jet veto efficiency ("gap" events), while the efficiency shows the effect of reconstruction efficiency on the events. The low efficiency reflects the efficiencies of the lepton triggers and lepton reconstruction. These effects affect both the numerator and denominator of the jet veto efficiency and do not have to be explicitly corrected for in the analysis. The high purity reflects the small effect of lepton and jet resolutions across the selection boundaries which define the number of gap events.

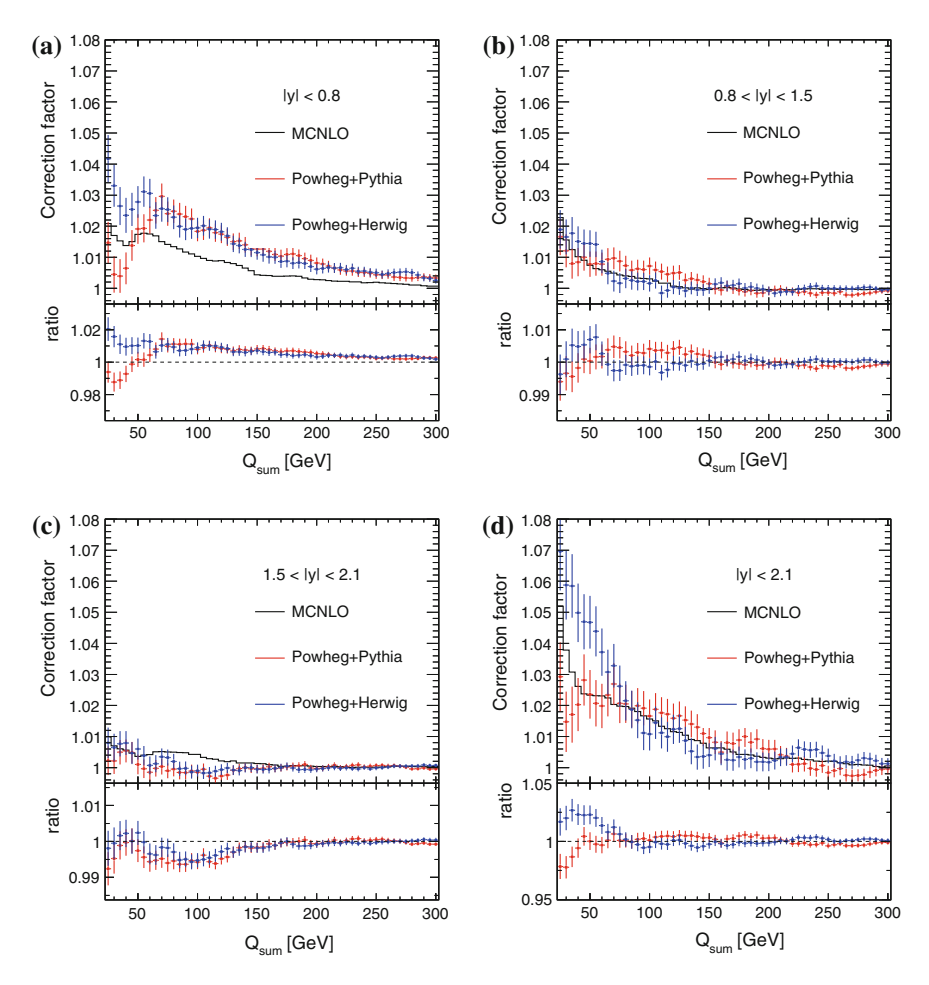


Fig. 5.7 Correction factors for the jet veto efficiency as a function of Q_{sum} for $\mathbf{a} |y| < 0.8$, $\mathbf{b} 0.8 \le |y| < 1.5$, $\mathbf{c} 1.5 \le |y| < 2.1$ and $\mathbf{d} |y| < 2.1$

5.8 Systematic Uncertainties

Since the jet veto efficiency is defined as a ratio of events, systematic uncertainties affecting the inclusive event selection are expected to cancel. This includes uncertainties on the top cross section, the luminosity, lepton trigger and reconstruction efficiencies and b-tagging efficiency, which are otherwise significant uncertainties in many $t\bar{t}$ analyses. Uncertainties that affect the jets, and in particular the additional jets that define whether or not an event passes the jet veto, will not cancel and must be evaluated in detail. The systematic uncertainties expected to dominate are the jet energy scale (JES), jet energy resolution (JER), jet reconstruction efficiency

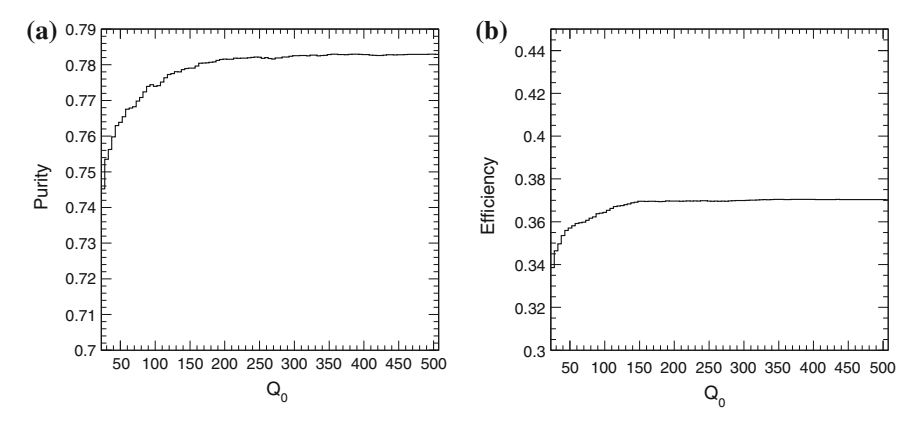


Fig. 5.8 Purity (a) and efficiency (b) of selected "gap" events, as defined in the text

and the uncertainty associated with estimating the number of additional (pile-up) interactions.

The effects of systematic uncertainties on the jet veto efficiency as a function of Q_0 are presented individually in the following sections. The systematic uncertainties on the jet veto efficiency as a function of Q_{sum} are qualitatively very similar and are therefore not presented separately here.

5.8.1 Jet Energy Scale

The uncertainty due to the jet energy scale has been evaluated by the combined performance group [32] and is provided in the MultijetJESUncertainty Provider [33] package. The package provides a per-jet energy uncertainty and includes the uncertainty in the calibration method, uncertainties from close-by jets, an uncertainty due to the different response of quark or gluon-initiated jets and the uncertainty due to soft activity from additional proton-proton interactions. To evaluate the effect of each source of JES uncertainty, the energy of each jet in the MC sample is shifted up or down by one standard deviation. The event selections are then re-applied and the jet veto efficiencies are re-calculated. The fractional difference between the nominal jet veto efficiency and the shifted one is taken to be the uncertainty due to the jet energy scale. Figure 5.9 shows the resulting systematic uncertainty due to the JES. At low values of Q_0 the uncertainty is, at worst, 3% for the veto region |y| < 2.1, falling to 1% by $Q_0 = 70$ GeV. In the other veto regions the uncertainty is around 1% at low Q_0 .

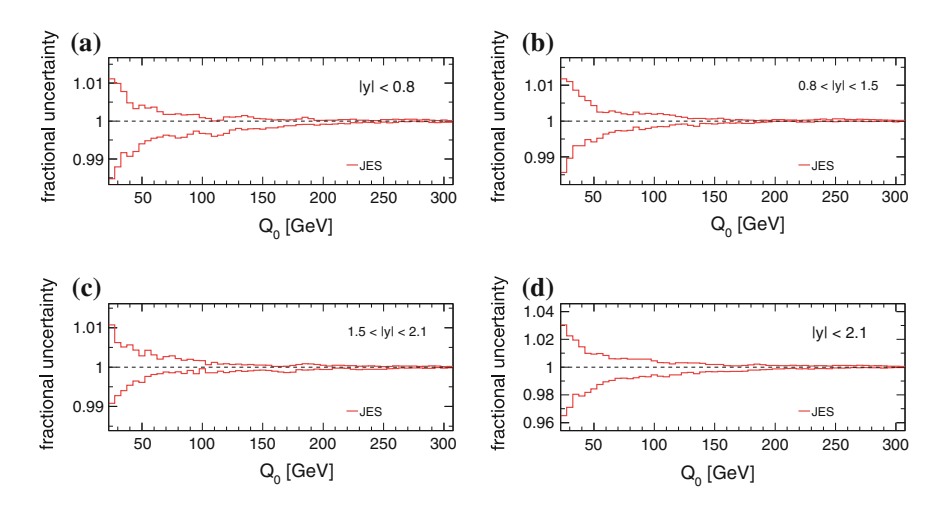


Fig. 5.9 Uncertainty due to the jet energy scale on the jet veto efficiency as a function of Q_0 , for $\mathbf{a} |y| < 0.8$, $\mathbf{b} 0.8 \le |y| < 1.5$, $\mathbf{c} 1.5 \le |y| < 2.1$ and $\mathbf{d} |y| < 2.1$

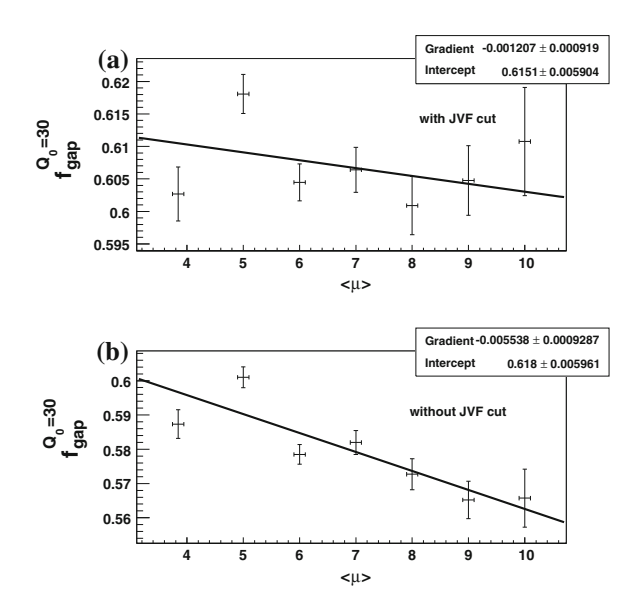
5.8.2 Uncertainties Due to Additional pp Interactions

The presence of additional proton-proton interactions can affect the measured jet veto efficiency in two ways. Firstly, soft energy can be added into the jets originating from the $t\bar{t}$ interaction. This source of uncertainty is included in the overall jet energy scale uncertainty described in Sect. 5.8.1. Secondly, jets can be reconstructed entirely from energy produced in the pile-up collisions. The effect of these pile-up jets is greatly reduced by the application of the jet vertex fraction requirement, described in Sect. 5.3.3. Figure 5.10 shows the reconstructed jet veto efficiency predicted by MC@NLO at $Q_0 = 30\,\text{GeV}$, as a function of the average number of interactions $\langle\mu\rangle$, with and without the application of the JVF cut. The effect of the JVF cut significantly reduces the $\langle\mu\rangle$ -dependence. However, the JVF cut is not guaranteed to remove all pile-up jets, and the uncertainty due to this residual pile-up must be estimated.

The effect of residual pile-up is estimated using the MC events by matching the reconstructed jets to particle-level jets that originate from the hard scatter. Figure 5.11a shows the ΔR between reconstructed jets and their nearest particle-level jet. The reconstructed jets are required to have $25 < p_T < 30$ GeV and the particle-level jets allowed to have p_T as low as 7 GeV to avoid resolution issues when performing the matching. The ΔR distribution was constructed using three requirements on the jet vertex fraction: (i) no JVF cut, (ii) JVF > 0.1 and (iii) JVF > 0.75. Figure 5.11b shows the JVF cut efficiency as a function of ΔR .

Jets that have a large ΔR with respect to the nearest particle-level jet are likely to have originated from a pile-up interaction. Therefore the uncertainty due to residual pile-up jets is estimated by removing jets from the analysis if they have $\Delta R > 0.3$. Figure 5.12 shows the ratio of the jet veto efficiency obtained after the ΔR -matching

Fig. 5.10 Reconstructed jet veto efficiency predicted by MC@NLO at $Q_0 = 30$ GeV, as a function of the average number of interactions with a JVF > 0.75 and **b** without JVF cut



to that obtained in the standard analysis. The effect of residual pile-up is estimated from this comparison to be less than 1 %.

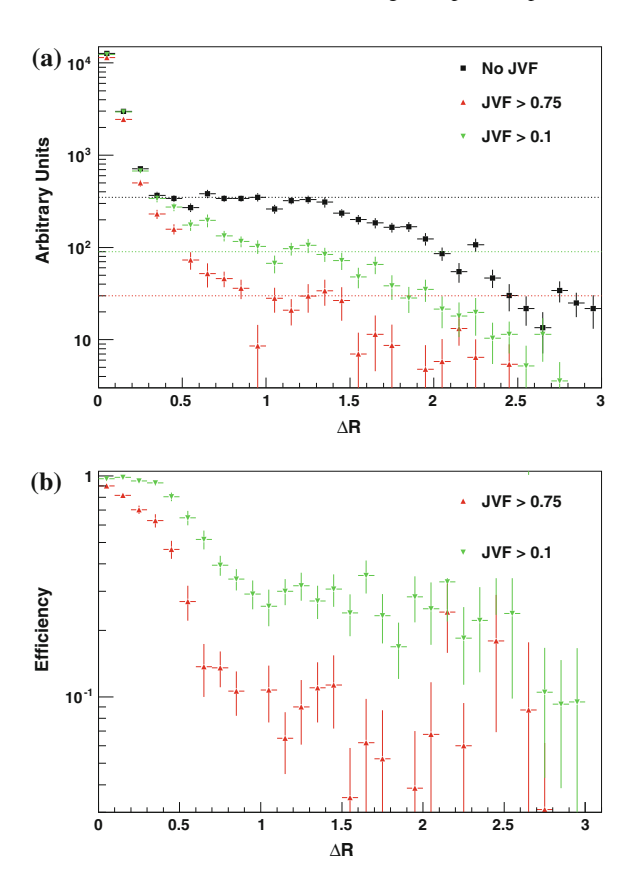
The use of the JVF requirement also introduces a potential source of systematic uncertainty in the measurement; the efficiency of the JVF algorithm in the data may not be correctly reproduced in the MC samples. In order to estimate this uncertainty the entire analysis chain is repeated with different values of the JVF cut. The unfolding corrections are re-derived and the data are corrected back to particle level. The resulting unfolded jet veto efficiencies are then compared to the standard result. Any relevant differences between the performance of the JVF algorithm in data and MC are expected to manifest themselves as differences in the unfolded jet veto efficiencies, and so any observed differences are taken as the systematic uncertainty due to the JVF algorithm.

Figure 5.13 shows the shift in the unfolded data obtained after (i) changing the JVF cut to 0.1 and (ii) dropping the JVF cut entirely, as a function of Q_0 . In both cases the shift in the unfolded jet veto efficiency is about 2% at the smallest values of Q_0 . The data obtained with a JVF cut of 0.1 was chosen to estimate the uncertainty to reduce any effects from the mismodelling of pile-up jets, the majority of which are observed to lie in the range 0 < JVF < 0.1.

5.8.3 Uncertainty in the b-Tagging

The performance of the *b*-tagging algorithm has been measured in the data [34, 35] and the uncertainty on the calibration was propagated to the analysis. The uncertainty

Fig. 5.11 ΔR is the distance between a reconstructed jet and the nearest particle-level jet originating from the pp interaction that produced the $t\bar{t}$ system. **a** Shows the ΔR distribution for reconstructed jets with 25 < p_T < 30 GeV. **b** Shows the JVF efficiency as a function of ΔR



on the identification of b-jets is expected to cancel in the jet veto efficiency. However there is a small class of events where one b-jet from the top decay falls outside the detector acceptance and a jet from additional radiation is identified as a b-jet. The effect of the uncertainty on the b-tagging algorithm in this class of events will not fully cancel in the ratio when the jet veto efficiency is constructed. Figure 5.14 shows the effect of the b-tagging uncertainty on the jet veto efficiency as a function of Q_0 and is found to be $<1\,\%$ across the full range.

5.8.4 Uncertainty Due to Unfolding to Particle Level

The point-by-point unfolding outlined in Sect. 5.7 is sensitive to the physics modelling in the event generator used to obtain the correction factors. The MC@NLO MC samples were used as the default. To estimate an uncertainty due to physics modelling the correction factors were re-derived using both POWHEG+PYTHIA6 and POWHEG+HERWIG, as illustrated in Fig. 5.6.

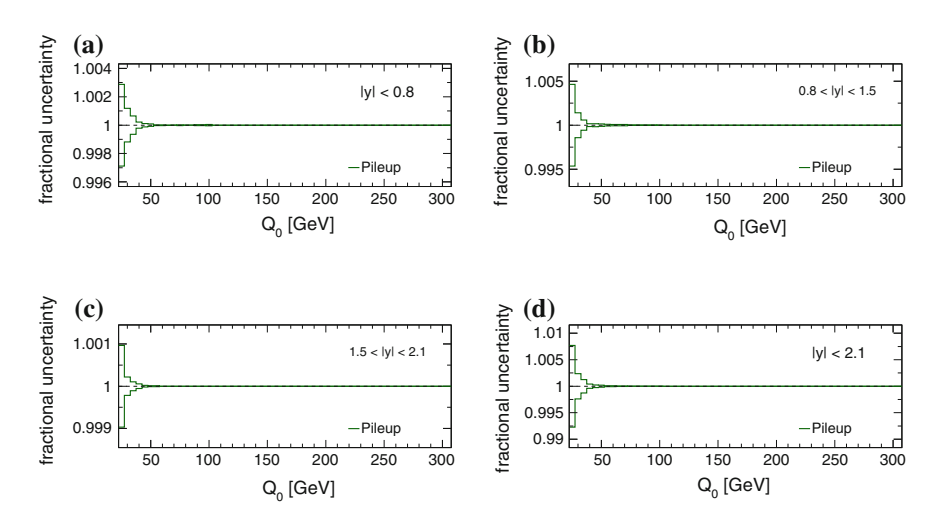


Fig. 5.12 Uncertainty associated with residual pile-up on the jet veto efficiency as a function of Q_0 for $\mathbf{a} | \mathbf{y} | < 0.8$, $\mathbf{b} 0.8 \le | \mathbf{y} | < 1.5$, $\mathbf{c} 1.5 \le | \mathbf{y} | < 2.1$ and $\mathbf{d} | \mathbf{y} | < 2.1$

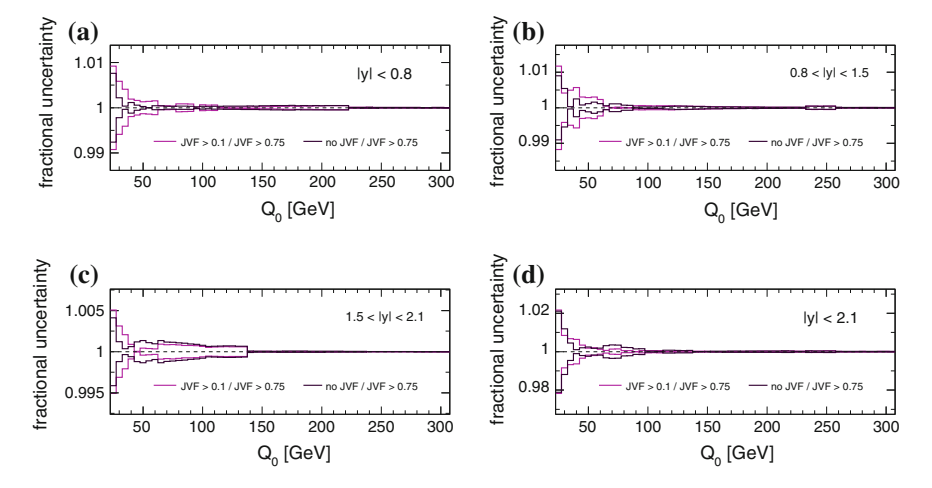


Fig. 5.13 Uncertainty due to potential mismodelling of the performance of the jet vertex fraction algorithm on the jet veto efficiency as a function of Q_0 for $\mathbf{a} |y| < 0.8$, $\mathbf{b} 0.8 \le |y| < 1.5$, $\mathbf{c} 1.5 \le |y| < 2.1$ and $\mathbf{d} |y| < 2.1$

The systematic uncertainty in each bin of the distribution was defined to be the largest difference between either of the POWHEG predictions and the MC@NLO default. However, if this difference was smaller than the statistical uncertainty present in the MC samples, then the statistical uncertainty in the POWHEG+HERWIG sample—which had the poorest statistics—was taken to be the systematic uncertainty in that particular bin. The final systematic uncertainty on the unfolding procedure was symmetrised and is shown in Fig. 5.15.

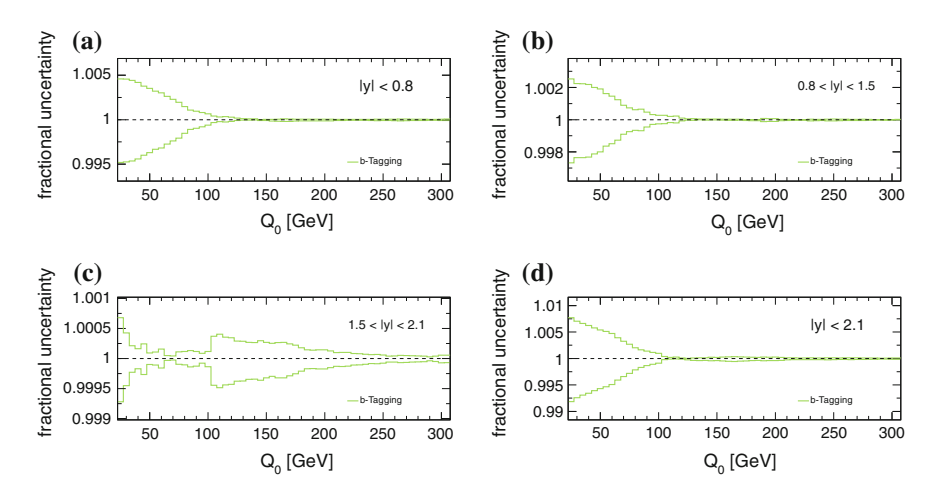


Fig. 5.14 Uncertainty due to the performance of the *b*-tagging algorithm on the jet veto efficiency as a function of Q_0 for $\mathbf{a} |y| < 0.8$, $\mathbf{b} 0.8 \le |y| < 1.5$, $\mathbf{c} 1.5 \le |y| < 2.1$ and $\mathbf{d} |y| < 2.1$

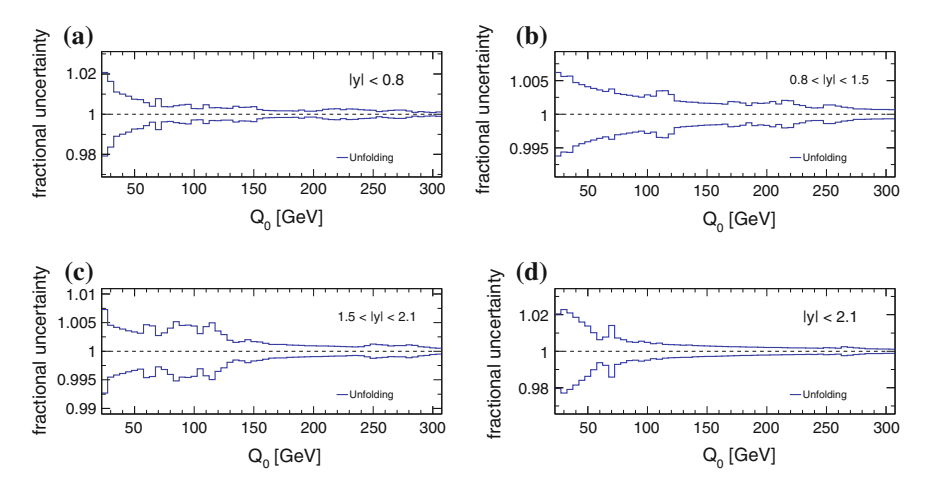


Fig. 5.15 Uncertainty due to unfolding to particle level on the jet veto efficiency as a function of Q_0 for $\mathbf{a} |y| < 0.8$, $\mathbf{b} 0.8 \le |y| < 1.5$, $\mathbf{c} 1.5 \le |y| < 2.1$ and $\mathbf{d} |y| < 2.1$

As an additional cross-check of the physics modelling uncertainty in the unfolding, a reweighting procedure was used to alter the shape of the p_T spectrum of the leading additional jet. The MC@NLO events were reweighted such that the leading additional jet p_T distribution was given a change in shape equal to the maximum allowed by the jet energy scale uncertainty bands. Figure 5.16 shows the effect of these variations on the jet veto efficiency and the corresponding change in the correction factors. This effect was found to be smaller than the variations between the correction factors

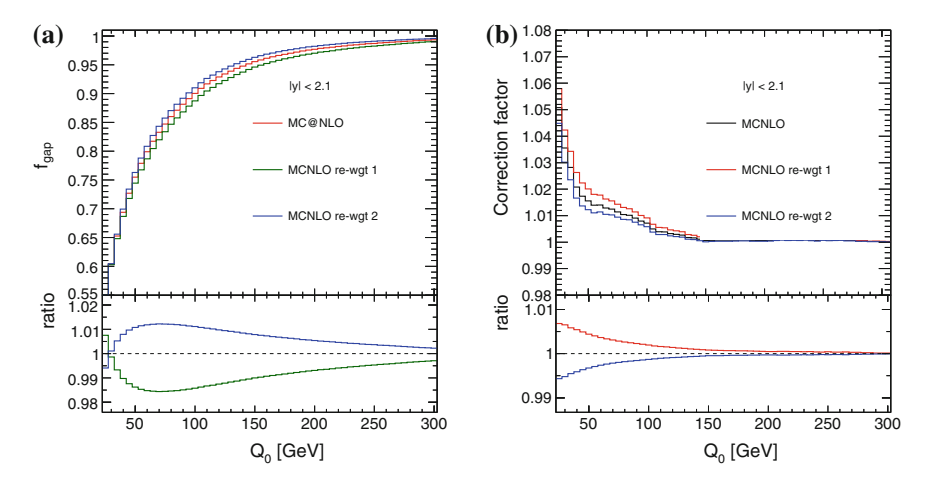


Fig. 5.16 a The effect on the reconstructed jet veto efficiency of reweighting the leading additional jet p_T . b The corresponding change in the unfolding correction factors

obtained with different NLO generators, and was not used as an additional uncertainty in the final measurement.

The particle-level definition used in this measurement was chosen to closely match the acceptance of the ATLAS detector, resulting in different fiducial regions in the electron and muon channel. The effect of changing the lepton fiducial region was investigated by decreasing the electron p_T cut to 20 GeV, thereby mimicking the cuts used to select muons. The effect was observed to be negligible, and it is therefore concluded that the effect of small changes in the lepton kinematics cancel in the ratio when constructing the jet veto efficiency.

The effect of using dressed or bare leptons was also investigated. Leptons were dressed by combining them with *all* photons with $\Delta R(\gamma, \ell) < 0.2$. Figure 5.17 shows the effect of using dressed or bare electrons on the jet veto efficiency. The difference is negligible, which is expected given that the acceptance due to lepton definition should cancel in the ratio when constructing the jet veto efficiency.

Finally the definition of the particle-level jets was also examined. It has been common in previous jet-based analyses to construct particle-level jets using all final-state particles including muons and neutrinos. In the default analysis here, muons and neutrinos were not included in the input to the jet finding algorithm. In principle it is preferable to include these particles, to capture the energy of the jet carried by muons and neutrinos originating from in-flights decays. However, including neutrinos would lead to neutrino-jets being produced from the high-p_T neutrinos originating in the hard scatter. These neutrino-jets have no analogue at reconstruction level and would need to be carefully removed from the particle-level events. Therefore the simpler definition—no muons or neutrinos included—was used. The effect on the jet veto efficiency of using a different jet definition was tested by comparing the default choice to a definition in which all final-state particles *except* muons, electrons or neutrinos

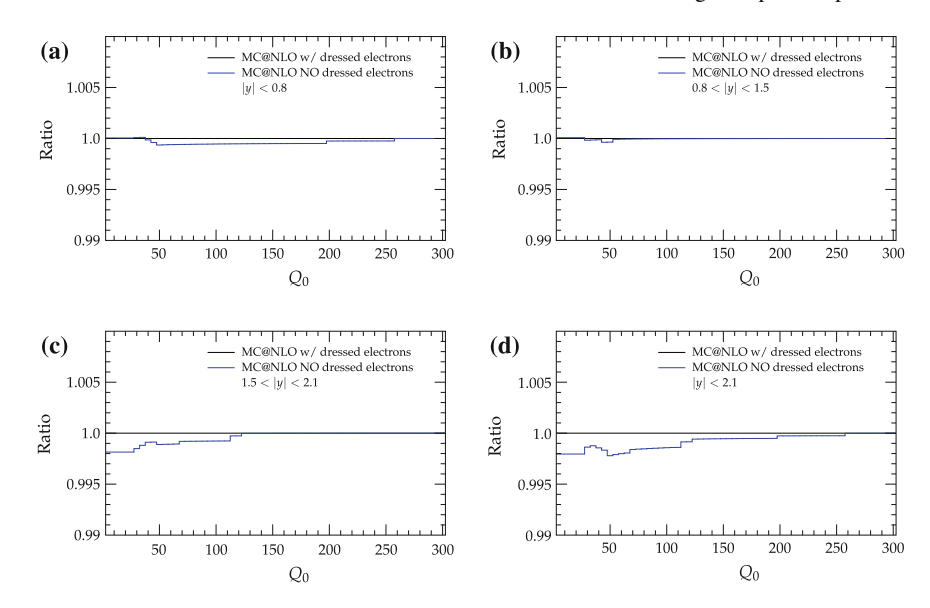


Fig. 5.17 Change in the particle level jet veto efficiency as a function of Q_0 when using dressed electrons for $\mathbf{a} | \mathbf{y} | < 0.8$, $\mathbf{b} | 0.8 \le | \mathbf{y} | < 1.5$, $\mathbf{c} | 1.5 \le | \mathbf{y} | < 2.1$ and $\mathbf{d} | \mathbf{y} | < 2.1$

all with $p_T > 20\,\text{GeV}$ are used to build the jets. With this selection any soft leptons from processes such as in-flight decays are preserved. The change in the jet veto efficiency was $0.4\,\%$ at $Q_0 = 25\,\text{GeV}$, falling to less than $0.1\,\%$ by $Q_0 = 60\,\text{GeV}$.

5.8.5 Uncertainty Due to Background Contamination

As discussed in Sect. 5.4 the contribution from background processes is small, and so this contribution is not explicitly subtracted from the data before unfolding to particle level. The possible bias from this choice is evaluated here for the two largest backgrounds—single top and fake events. The key issue is to estimate the difference between the jet veto efficiency for each background sample and the jet veto efficiency in data. In the limit that the two distributions have the same shape then the background will cause no bias in the measurement.

The single top background is estimated using MC@NLO MC events. The jet veto efficiency obtained using these events is shown in Fig. 5.18a. The events expected from the single top process are subtracted from the data and the jet veto efficiency re-calculated. The difference between this new distribution and the default result is taken to be the systematic uncertainty and is shown in Fig. 5.19.

The matrix method used to estimate the contribution from fake events has a large statistical uncertainty. An estimate of the jet veto efficiency produced using fake events is shown in Fig. 5.18b. Because the statistical uncertainty is significant, two

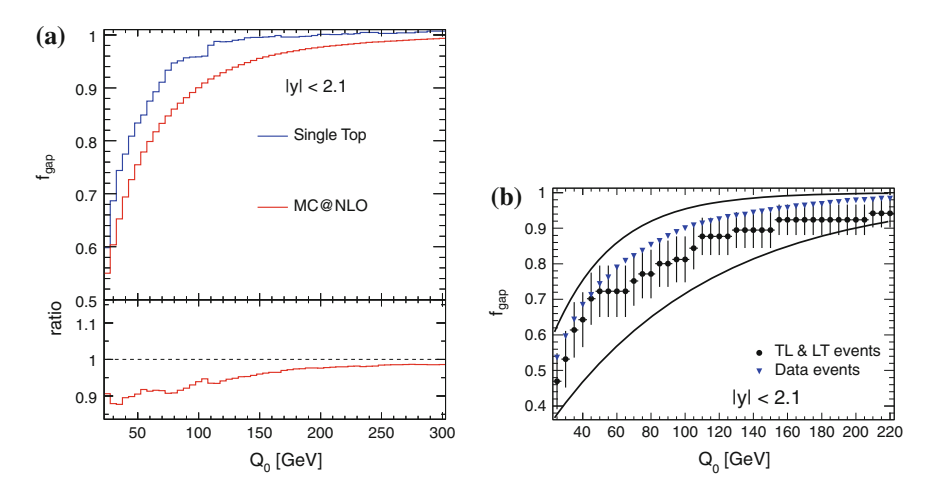


Fig. 5.18 a The jet veto efficiency distribution for single top events is compared to the prediction from tt events. Both samples of events were generated with MC@NLO. b The jet veto efficiency for the fake background is compared to the observed jet veto efficiency in the data. TL and LT refers to events in which one of the leptons was identified as tight and the other as loose. The way in which these events are used to estimated the fake background is described in [26]

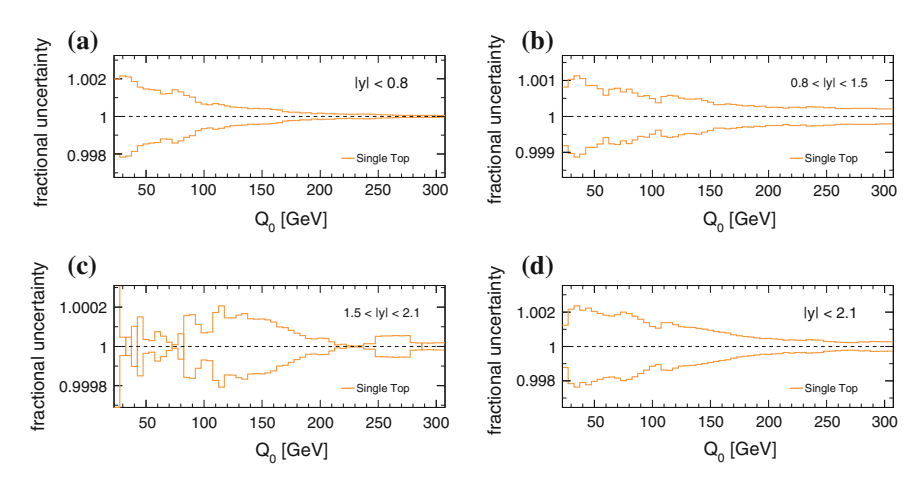


Fig. 5.19 Uncertainty from the single top background on the jet veto efficiency as a function of Q_0 for $\mathbf{a} |y| < 0.8$, $\mathbf{b} 0.8 \le |y| < 1.5$, $\mathbf{c} 1.5 \le |y| < 2.1$ and $\mathbf{d} |y| < 2.1$

smooth curves are used to band the distribution. From these curves two alternate shapes of the leading jet p_T distribution can be inferred. These distributions are then subtracted from the leading jet p_T distribution observed in data, and the resulting distribution is used to produce two new jet veto efficiencies. The fractional difference between these distributions and the default jet veto efficiency is taken as the

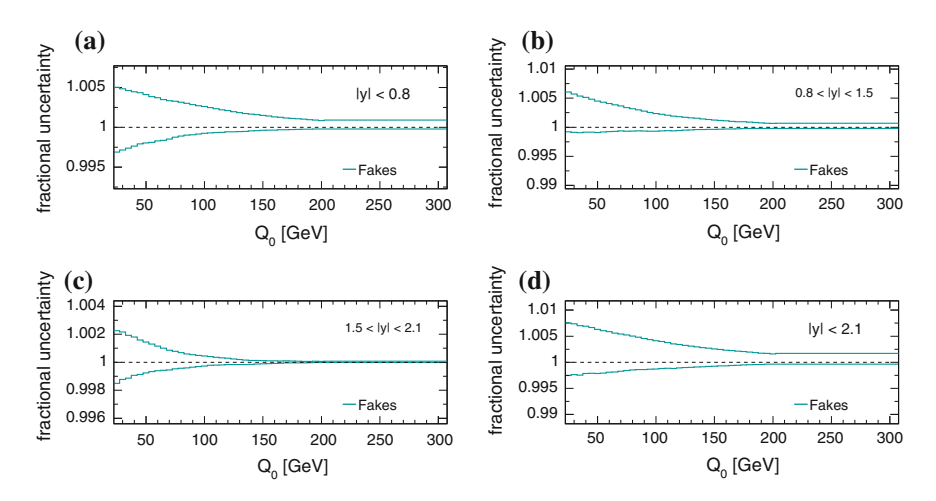


Fig. 5.20 Uncertainty from the fake backgrounds on the jet veto efficiency as a function of Q_0 for $\mathbf{a} |y| < 0.8$, $\mathbf{b} 0.8 \le |y| < 1.5$, $\mathbf{c} 1.5 \le |y| < 2.1$ and $\mathbf{d} |y| < 2.1$

systematic uncertainty due to the fake background, and is shown in Fig. 5.20. A maximum uncertainty of 0.5% was estimated for the smallest values of Q_0 .

5.8.6 Uncertainty Due to Lepton Efficiencies and Resolutions

The efficiency to select and trigger on muons and electrons has an associated uncertainty. This uncertainty is propagated to the $t\bar{t}$ MC samples, using the official tools provided by the combined performance groups, and the gap fraction is recalculated. As expected the uncertainties are found to cancel in the ratio when constructing the jet veto efficiency and the residual uncertainty on the jet veto efficiency is found to be less than $0.1\,\%$.

5.8.7 Uncertainty Due to Jet Resolution and Efficiency

The uncertainty due to the modelling of the jet energy resolution has been evaluated in [36] and is assessed using the JetResolution-00-00-09 package. Additional Gaussian smearing corresponding the to the uncertainty on the data measurement of the jet energy resolution [36] is applied to all jets in the MC, and the jet veto efficiency curves are recalculated. The systematic uncertainty due to the jet energy resolution is obtained by comparing the default jet veto efficiency curve to those calculated after applying the jet energy resolution uncertainty, and is shown in Fig. 5.21.

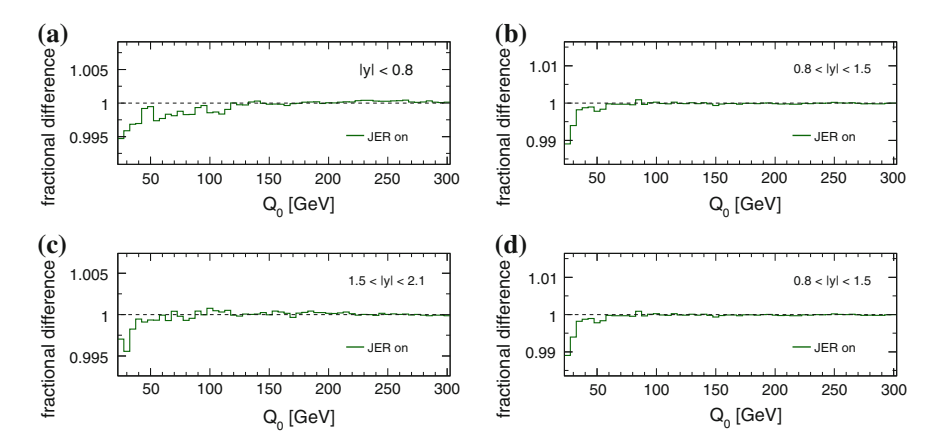


Fig. 5.21 Uncertainty due to the jet energy resolution on the jet veto efficiency as a function of Q_0 for $\mathbf{a} |y| < 0.8$, $\mathbf{b} 0.8 \le |y| < 1.5$, $\mathbf{c} 1.5 \le |y| < 2.1$ and $\mathbf{d} |y| < 2.1$

The reconstruction efficiency for jets is assessed using the <code>JetEffiProvider-00-02</code> package. Jets are removed from the MC according to the uncertainty in the jet reconstruction efficiency [36], which is 98 % at $p_T=25$ GeV, for example. The analysis is re-run using the updated jet collection and the jet veto efficiency is recalculated. The resulting uncertainty is shown in Fig. 5.22.

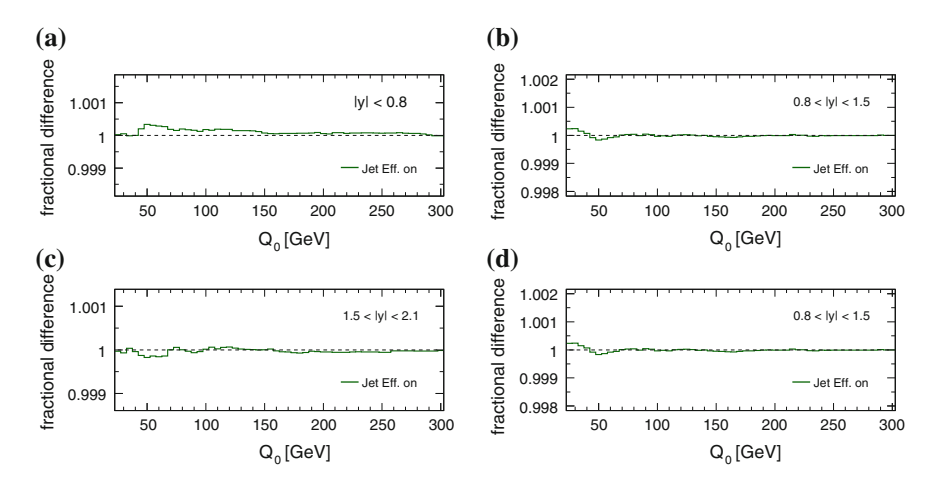


Fig. 5.22 Uncertainty due to the jet reconstruction efficiency on the jet veto efficiency as a function of Q_0 for $\mathbf{a} |y| < 0.8$, $\mathbf{b} 0.8 \le |y| < 1.5$, $\mathbf{c} 1.5 \le |y| < 2.1$ and $\mathbf{d} |y| < 2.1$

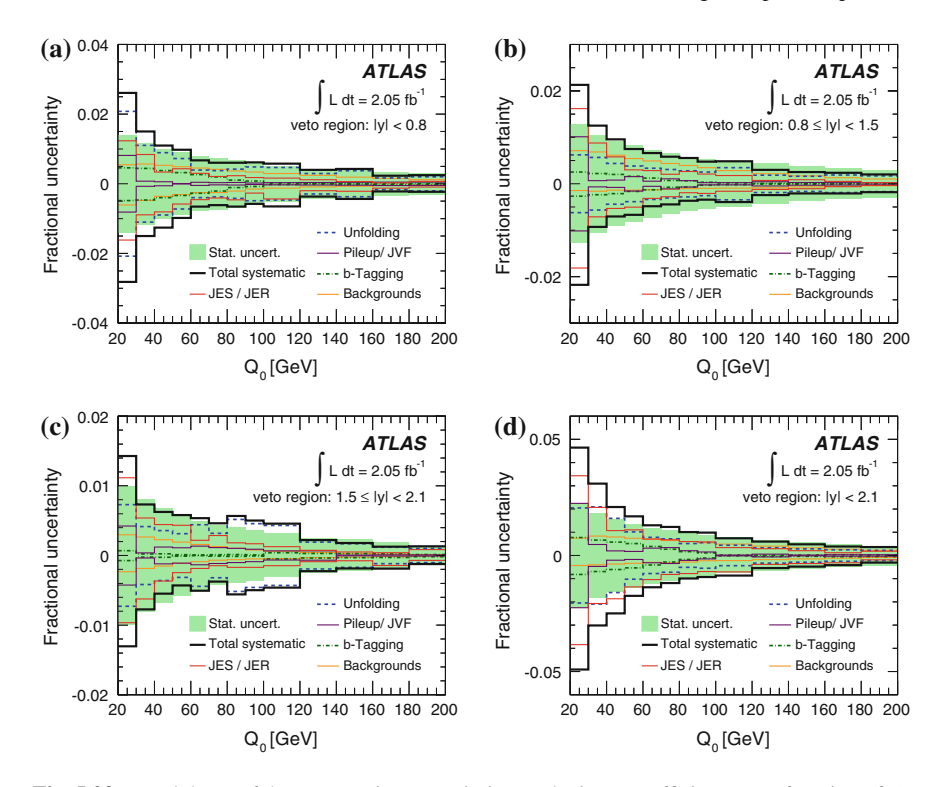


Fig. 5.23 Breakdown of the systematic uncertainties on the jet veto efficiency as a function of Q_0 for $\mathbf{a} \ |y| < 0.8$, $\mathbf{b} \ 0.8 \le |y| < 1.5$, $\mathbf{c} \ 1.5 \le |y| < 2.1$ and $\mathbf{d} \ |y| < 2.1$. The step size in Q_0 was chosen to be commensurate with the jet energy resolution. The individual systematic uncertainties are shown as labelled lines of different styles and the total systematic uncertainty is shown as the outer black solid line. The statistical uncertainty on the data is shown as the shaded area. The systematic uncertainties are only shown up to $Q_0 = 200$ GeV. The results above this value are consistent with the results at 200 GeV

5.8.8 Summary of Systematic Uncertainties

Figure 5.23 shows a breakdown of the fractional systematic uncertainties on the jet veto efficiency as a function of Q_0 . Also shown as a green band is the relative statistical uncertainty on the data. The dominant uncertainties come from the jet energy scale, pileup modelling and unfolding to particle level. The final systematic uncertainties are smaller than 4% in the veto region |y| < 2.1 and smaller than 2% for the veto region |y| < 0.8.

Figure 5.24 shows a breakdown of the systematic uncertainties on the jet veto efficiency as a function of Q_{sum} . Each systematic uncertainty is slightly larger than the associated uncertainty in the Q_0 distribution, due to the impact of low-p_T jets across the full spectrum.

5.9 Results 91

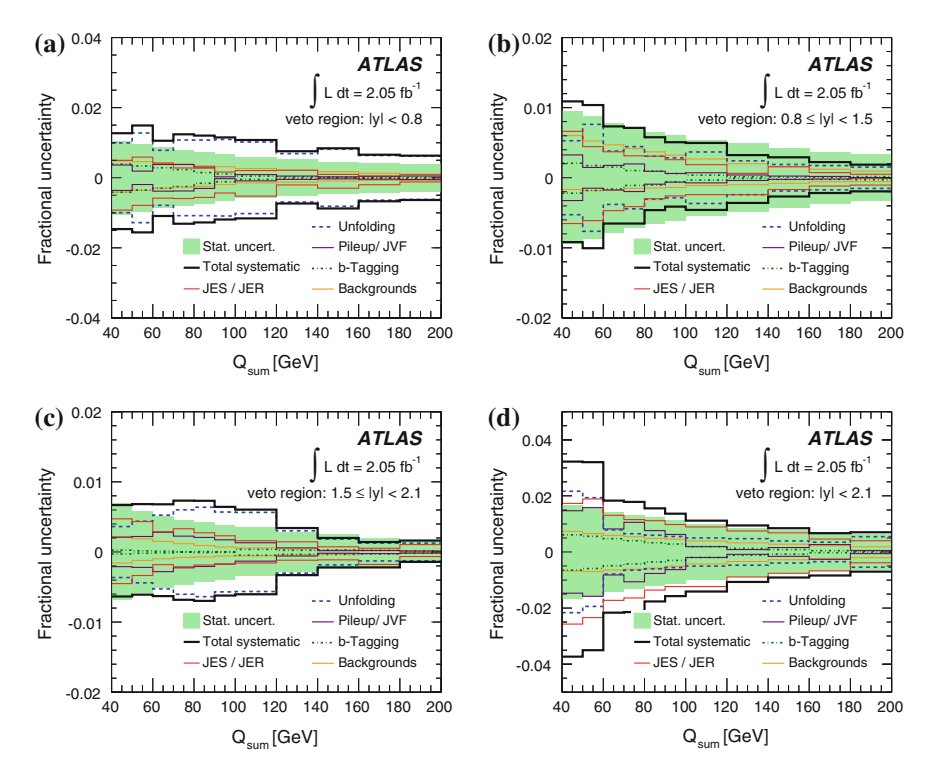


Fig. 5.24 Breakdown of the systematic uncertainties on the jet veto efficiency as a function of Q_{sum} for $\mathbf{a} | y | < 0.8$, $\mathbf{b} | 0.8 \le | y | < 1.5$, $\mathbf{c} | 1.5 \le | y | < 2.1$ and $\mathbf{d} | y | < 2.1$. The step size in Q_{sum} was chosen to be commensurate with the jet energy resolution. The individual systematic uncertainties are shown as *labelled lines* of different styles and the total systematic uncertainty is shown as the *outer black solid line*. The statistical uncertainty on the data is shown as the *shaded area*. The systematic uncertainties are only shown up to $Q_{\text{sum}} = 200$ GeV. The results above this value are consistent with the results at 200 GeV

5.9 Results

The jet veto efficiency as a function of Q_0 is compared to the predictions from the NLO and multi-leg LO generators in Fig. 5.25. In general all of the generators are found to give a reasonable description of the data. The difference between the predictions from MC@NLO and POWHEG is approximately the same size as the total experimental uncertainty, and therefore the measurement is beginning to probe the differences between the alternative methods of merging next-to-leading order matrix element calculations with parton showers.

When investigating the additional jet activity produced in a very central region of the detector, |y| < 0.8 (Fig. 5.25a), it is found that the jet veto efficiency produced by MC@NLO slightly over-shoots the data. A jet veto efficiency that is too large implies that too little additional radiation is being produced in this very central region

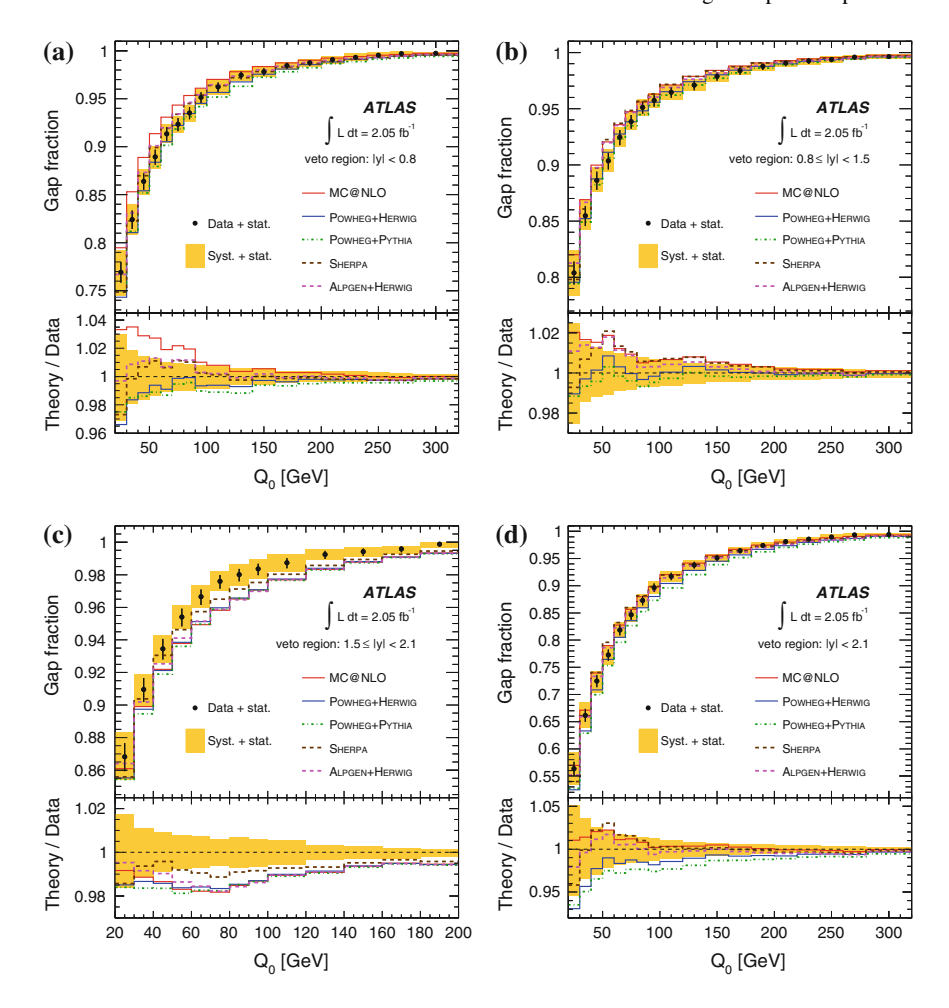


Fig. 5.25 The measured jet veto efficiency as a function of Q_0 is compared to the predictions from the NLO and multi-leg LO MC generators in the rapidity regions $\mathbf{a} \ |y| < 0.8$, $\mathbf{b} \ 0.8 \le |y| < 1.5$, $\mathbf{c} \ 1.5 \le |y| < 2.1$ and $\mathbf{d} \ |y| < 2.1$. The data are shown as closed *black circles* with statistical uncertainties. The *yellow band* is the total experimental uncertainty on the measurement (statistical and systematic). The theoretical predictions are shown as *solid* and *dashed coloured lines*

of rapidity. The observation that MC@NLO produces fewer jets than ALPGEN has been previously discussed in the literature [37], and recent measurements of the jet multiplicity in $t\bar{t}$ events [38] have also found that MC@NLO produces fewer additional jets than that predicted by other MC generators and that found in data.

In the most forward rapidity interval, $1.5 \le |y| < 2.1$ (Fig. 5.25c), none of the predictions from the NLO or multi-leg LO generators completely described the jet veto efficiency measured in data. Although the predictions from MC@NLO, POWHEG,

5.9 Results 93

ALPGEN and SHERPA are similar to each other the predicted jet veto efficiencies are all slightly too low, which implies that all of the generators are producing slightly too much additional radiation in the forward region of rapidity. One potential reason for this discrepancy could be the lack of BFKL physics (cf. Sect. 1.6) present in these generators.

In general, when the veto is applied to jets falling in the full rapidity range, |y| < 2.1, it is found that all of the generators give a good description of the jet veto efficiency measured in data.

The jet veto efficiency as a function of Q_0 is compared to the predictions from ACERMC in Fig. 5.26. The difference between the default sample and the ISR-varied samples was commonly used in top physics analyses to estimate a systematic uncertainty associated with the parton shower and the modelling of additional quark and gluon emissions. The ISR-varied samples are found to be poor models of the data, and the spread of predictions is much larger than the total experimental uncertainty. This indicates that the size of the variations used to assess the uncertainty could be significantly reduced. Further discussion on the impact of this measurement and updated prescriptions for estimating QCD modelling uncertainties can be found in Sect. 5.10.

In Fig. 5.27 the jet veto efficiency as a function of $Q_{\rm sum}$ is compared to the predictions produced by the multi-leg LO and NLO MC generators. The jet veto efficiency at given values of $Q_{\rm sum}$ are lower than for the Q_0 , indicating that the measurement is sensitive to the quark and gluon radiation beyond the first emission. As expected, the largest difference between the jet veto efficiency as a function of $Q_{\rm sum}$ compared to Q_0 occurs when jets are vetoed in the full rapidity interval |y| < 2.1. However, the agreement between the data and MC predictions is similar to the Q_0 case. This implies that the leading emission is typically the most important, and the leading logarithmic approximations used for jets beyond the first emission, produced by the PYTHIA and HERWIG parton showers, are performing as well as the leading order predictions produced by ALPGEN and SHERPA.

Since the jet veto efficiency can be expressed as a ratio of cross sections (c.f. Eq. 5.2) which is calculated at each value of $Q_{\rm sum}$ and Q_0 using all selected events, there exist significant statistical correlations between the jet veto efficiency at different values of Q_0 or $Q_{\rm sum}$. The statistical correlation matrices for the jet veto efficiency at different values of Q_0 and $Q_{\rm sum}$ are shown in Figs. 5.28 and 5.29 respectively. Neighbouring points are strongly correlated, while well-separated points are less correlated.

All detector-corrected data are available in the HepData database [39], and a Rivet [40] routine was prepared [41] to allow access to the data points and the easy comparison of data and MC predictions.

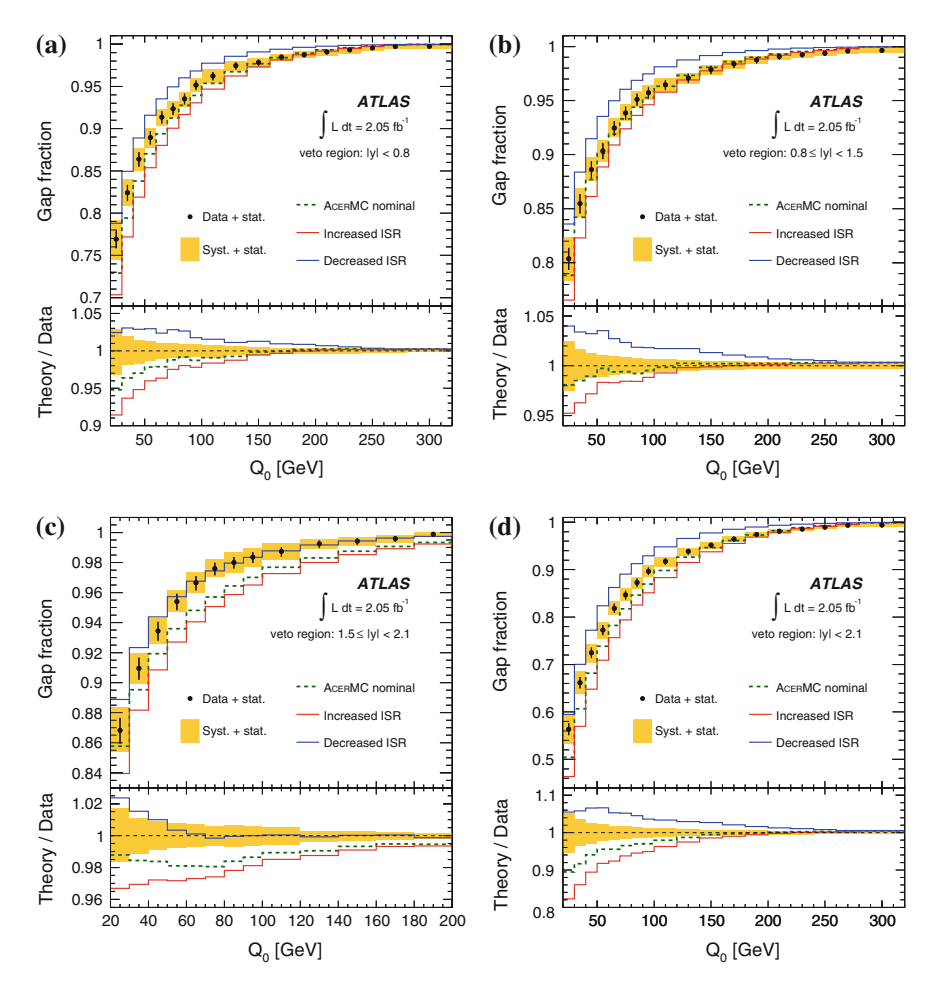


Fig. 5.26 The measured jet veto efficiency as a function of Q_0 for $\mathbf{a} \ |y| < 0.8$, $\mathbf{b} \ 0.8 \le |y| < 1.5$, $\mathbf{c} \ 1.5 \le |y| < 2.1$ and $\mathbf{d} \ |y| < 2.1$ is compared to predictions from the ACERMC generator, where different PYTHIA parton shower parameters are used to produce samples of events with nominal, increases and decreased initial state radiation (ISR). The data are shown as closed *black circles* with statistical uncertainties. The *yellow band* is the total experimental uncertainty on the measurement (statistical and systematic). The theoretical predictions are shown as *solid* and *dashed coloured lines*

5.10 Impact

The ISR variations produced with ACERMC (Fig. 5.26) had been used in previous tt measurements [1–4] to estimate an uncertainty due to the parton shower and QCD modelling. After finding that the variations were much larger than the total experimental uncertainty on the data, the parameters used to alter the amount of

5.10 Impact 95

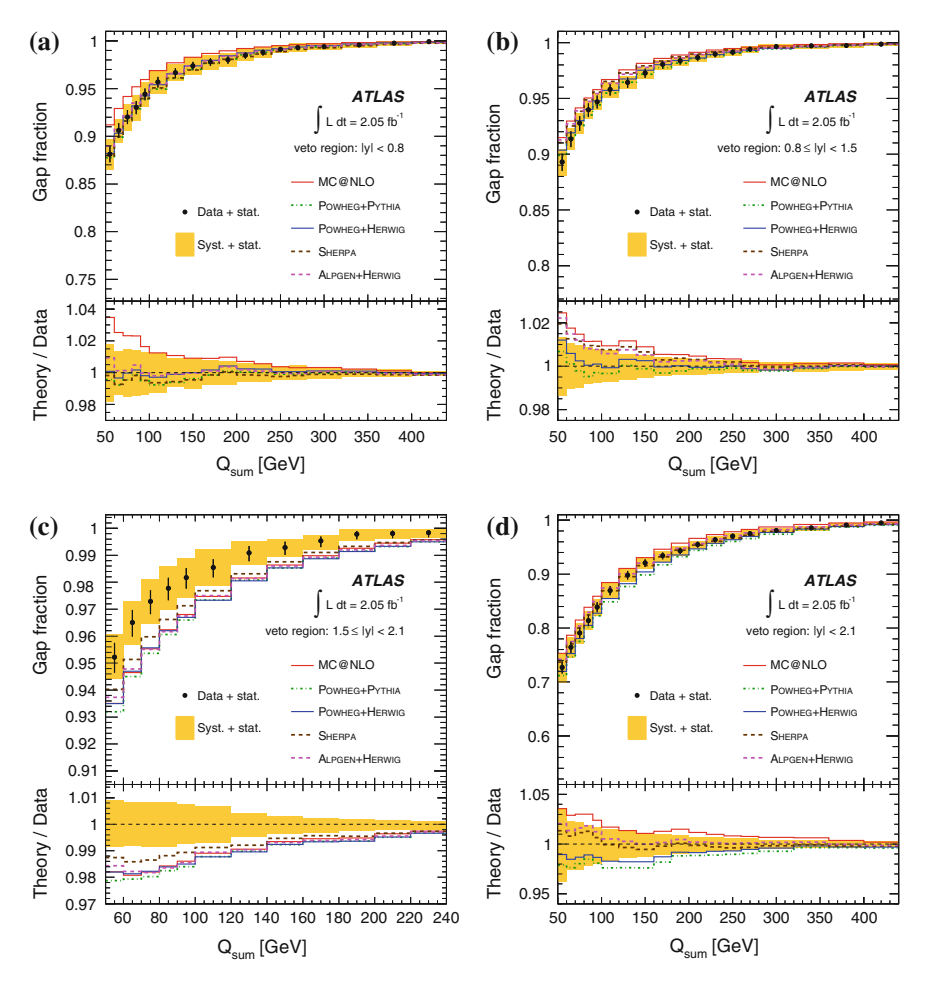


Fig. 5.27 The measured jet veto efficiency as a function of Q_{sum} is compared to predictions from the NLO and multi-leg LO MC generators in the rapidity regions $\mathbf{a} \ |y| < 0.8$, $\mathbf{b} \ 0.8 \le |y| < 1.5$, $\mathbf{c} \ 1.5 \le |y| < 2.1$ and $\mathbf{d} \ |y| < 2.1$. The data are shown as closed *black circles* with statistical uncertainties. The *yellow band* is the total experimental uncertainty on the measurement (statistical and systematic). The theoretical predictions are shown as *solid* and *dashed coloured lines*

parton shower activity were re-tuned to be more consistent with the size of the total experimental uncertainty. The updated ACERMC curves used to estimate this uncertainty are constructed using combinations of the parameters that control the amount of initial and final-state radiation. They are now labelled simply 'MorePS' and 'LessPS' which produce more ISR/FSR and less ISR/FSR respectively, and are shown as a function of Q_0 in Fig. 5.30. The use of the new samples resulted in a reduced parton shower-related uncertainty for $t\bar{t}$ measurements by around a factor of

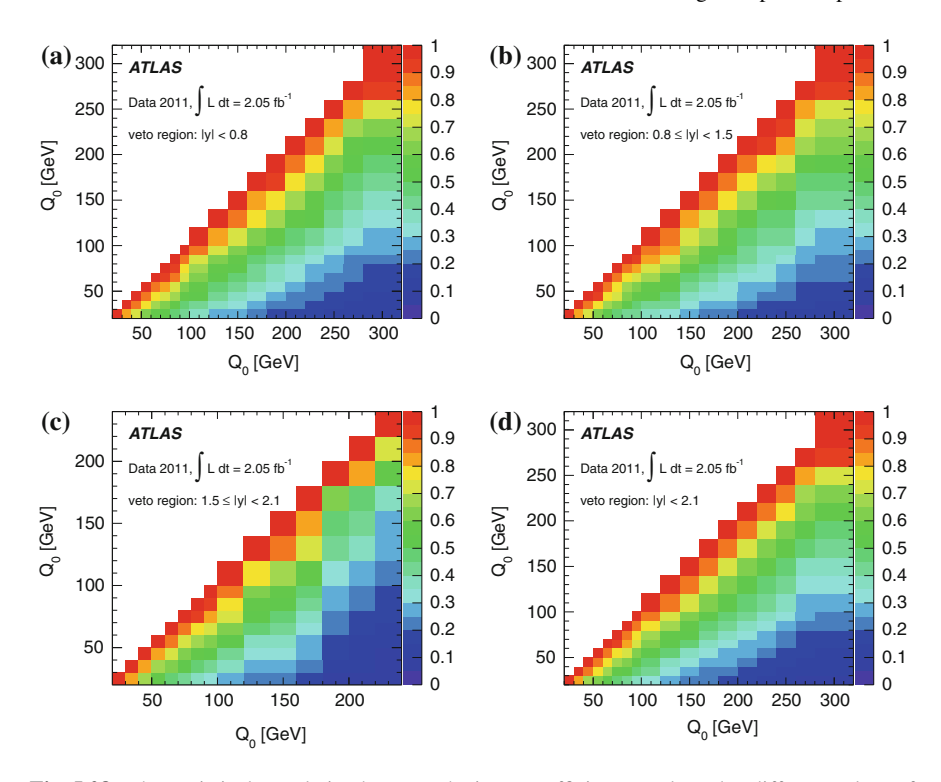


Fig. 5.28 The statistical correlation between the jet veto efficiency evaluated at different values of Q_0 , shown for $\mathbf{a} \ |y| < 0.8$, $\mathbf{b} \ 0.8 \le |y| < 1.5$, $\mathbf{c} \ 1.5 \le |y| < 2.1$ and $\mathbf{d} \ |y| < 2.1$

two. As this was often a dominant systematic uncertainty, the results of the jet veto analysis have made possible even more precise measurements of $t\bar{t}$ final states.

Given that multi-leg generators can produce leading order predictions for tt+ up to 4 jets, the idea of using a leading order generator, which produces tt events containing additional jets with just leading logarithmic accuracy, to estimate a QCD modelling uncertainty must be questioned. Indeed, the uncertainty being assessed using the ACERMC samples is widely regarded as being poorly motivated and unnecessary, and much work has been started on using alternative generators to estimate the impact of unknowns in QCD modelling. A theoretically more robust approach to estimating such an uncertainty would be to vary renormalisation and factorisation scales in the MC generators.

After the publication of the jet veto analysis, work began on exploring the effects of scale variations in the MADGRAPH and ALPGEN generators. The Rivet routine associated with the analysis, allowing easy access the unfolded data and analysis results, proved to be invaluable. It was used extensively to compare the published data to samples of MC events generated with different sets of scale variations. Preliminary results of studies were presented at top-LHC working group meetings—attended by analysers from the CMS collaboration and members of the theory community—and

5.10 Impact 97

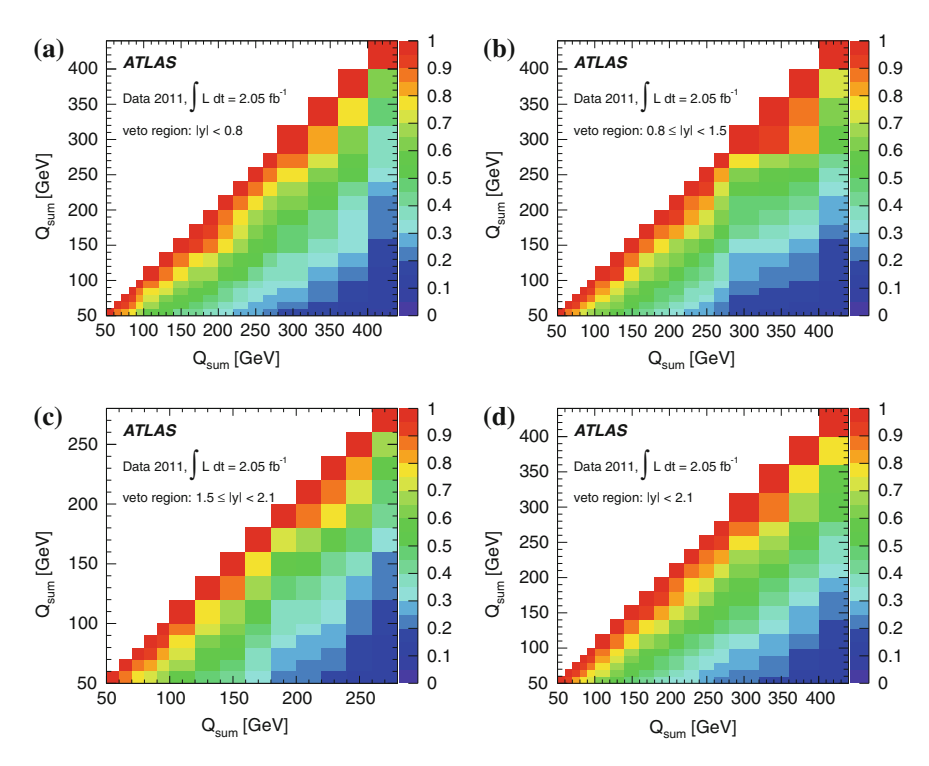


Fig. 5.29 The statistical correlation between the jet veto efficiency evaluated at different values of Q_{sum} , shown for $\mathbf{a} |y| < 0.8$, $\mathbf{b} 0.8 \le |y| < 1.5$, $\mathbf{c} 1.5 \le |y| < 2.1$ and $\mathbf{d} |y| < 2.1$

discussions have been started with the goal of standardising the way in which ATLAS and CMS evaluate QCD-modelling uncertainties in $t\bar{t}$ events.

Some example results are shown in Fig. 5.31, taken from [7]. Figure 5.31a shows a comparison of the published jet veto efficiency data to the 'standard' ATLAS MC generators used for $t\bar{t}$, as well as a sample of MADGRAPH events obtained from CMS. Figure 5.31b shows some examples of ALPGEN events in which the renormalisation scale has been varied. Events were also generated with increased (radHi) and decreased (radLo) amounts of parton shower activity. This is as suggested in [42], where it was found that it is important to treat α_S consistently in both the matrix element and parton shower parts of the MC prediction, to ensure that uncertainties are not overestimated.

The samples generated with the nominal scale choice, ALPGEN +PYTHIA (central), were consistent with the data to within the experimental uncertainty. However, a better description of the data was given after increasing the scale of α_S (and thereby reducing the value of α_S) used in both the matrix element calculation and parton shower ALPGEN +PYTHIA (α_S _down, radLo).

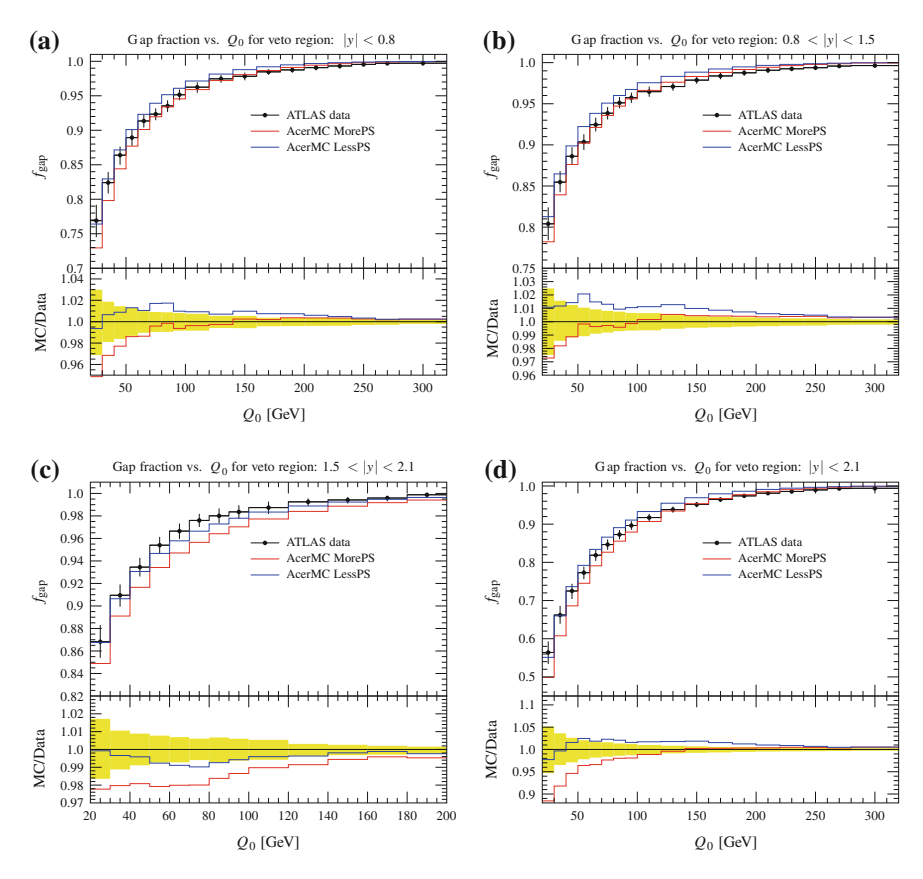


Fig. 5.30 Updated ACERMC parton shower variations compared to the published jet veto efficiency data as a function of Q_0 for $\mathbf{a} \mid y \mid < 0.8$, $\mathbf{b} \mid 0.8 \leq \mid y \mid < 1.5$, $\mathbf{c} \mid 1.5 \leq \mid y \mid < 2.1$ and $\mathbf{d} \mid y \mid < 2.1$. The total experimental uncertainty is shown as *black* uncertainty bars in the *upper panel* and a *yellow* uncertainty band in the *lower panel*. The spread between the MorePS and LessPS samples is now approximately the same size as the total experimental uncertainty

References 99

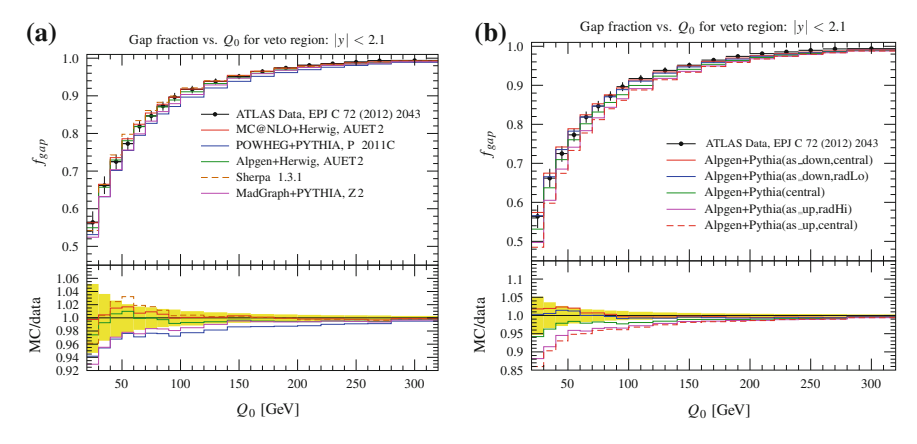


Fig. 5.31 Comparisons of the published jet veto efficiency data in *black points* and *yellow error bands* to predictions from different generators. In **a** the standard ATLAS generators, as well as a sample of MADGRAPH events obtained from CMS are compared. **b** Shows comparisons of various sets of ALPGEN events in which the renormalisation scale and other generator parameters have been varied. α_S up/down refer to increasing or decreasing of the renormalisation scale, *radHi* and *radLo* refer to events generated with increased and decreased amounts of parton shower activity

References

- 1. ATLAS Collaboration. (2012). Observation of spin correlation in $t\bar{t}$ events from pp collisions at sqrt(s) = 7 TeV using the ATLAS detector. *Physical Review Letters*, 108, 212001d.
- 2. ATLAS Collaboration. (2012). Measurement of the cross section for top-quark pair production in pp collisions at $\sqrt{s} = 7$ TeV with the ATLAS detector using final states with two high-pt leptons. *JHEP*, 1205, 059.
- 3. ATLAS Collaboration. (2012). Measurement of the top quark mass with the template method in the $t\bar{t} \rightarrow$ lepton + jets channel using ATLAS data. *European Physical Journal*, C72, 2046.
- 4. ATLAS Collaboration. (2012). Measurement of the charge asymmetry in top quark pair production in pp collisions at $\sqrt{s} = 7$ TeV using the ATLAS detector. *European Physical Journal*, C72, 2039.
- 5. ATLAS Collaboration. (2011). Measurement of dijet production with a veto on additional central jet activity in pp collisions at $\sqrt{s} = 7$ TeV using the ATLAS detector. *JHEP*, 1109, 053
- 6. ATLAS Collaboration. (2012). Measurement of $t\bar{t}$ production with a veto on additional central jet activity in pp collisions at sqrt(s) = 7 TeV using the ATLAS detector. European Physical Journal, C72, 2043.
- ATLAS Collaboration. (2013). Monte Carlo generator comparisons to ATLAS measurements constraining QCD radiation in top anti-top final states technical report. ATL-PHYS-PUB-2013-005. Geneva: CERN.
- 8. Frixione, S., & Webber, B. R. (2002). Matching NLO QCD computations and parton shower simulations. *JHEP*, 0206, 029.
- Nason, P. (2004). A new method for combining NLO QCD with shower Monte Carlo algorithms. JHEP, 0411, 040.
- Pumplin, J., Stump, D., Huston, J., Lai, H., Nadolsky, P. M., et al. (2002). New generation of parton distributions with uncertainties from global QCD analysis. *JHEP*, 0207, 012.

- 11. Corcella, G., Knowles, I., Marchesini, G., Moretti, S., Odagiri, K., et al. (2001). HERWIG 6: An event generator for hadron emission reactions with interfering gluons (including supersymmetric processes). *JHEP*, 0101, 010.
- 12. Butterworth, J., Forshaw, J. R., & Seymour, M. (1996). Multiparton interactions in photoproduction at HERA. *Zeitschrift fur Physik*, *C72*, 637–646.
- 13. ATLAS Collaboration. (2010). First tuning of HERWIG/JIMMY to ATLAS data technical report. ATL-PHYS-PUB-2010-014. Geneva: CERN.
- Sjostrand, T., Mrenna, S., & Skands, P. Z. (2006). PYTHIA 6.4 physics and manual. *JHEP*, 0605, 026.
- 15. ATLAS Collaboration. (2010). Charged particle multiplicities in p p interactions at $\sqrt{s} = 0.9$ and 7 TeV in a diffractive limited phase-space measured with the ATLAS detector at the LHC and new PYTHIA6 tune technical report. ATLAS-CONF-2010-031. Geneva: CERN.
- Mangano, M. L., Moretti, M., Piccinini, F., Pittau, R., & Polosa, A. D. (2003). ALPGEN, a generator for hard multiparton processes in hadronic collisions. *JHEP*, 0307, 001.
- 17. Mangano, M. L., Moretti, M., Piccinini, F., & Treccani, M. (2007). Matching matrix elements and shower evolution for top-quark production in hadronic collisions. *JHEP*, 0701, 013.
- 18. Catani, S., Krauss, F., Kuhn, R., & Webber, B. (2001). QCD matrix elements + parton showers. *JHEP*, 0111, 063.
- 19. Kersevan, B. P., & Richter-Was, E. (2013). The Monte Carlo event generator AcerMC versions 2.0 to 3.8 with interfaces to PYTHIA 6.4, HERWIG 6.5 and ARIADNE 4.1. *Computer Physics Communications*, 184, 919–985.
- Sherstnev, A., & Thorne, R. (2008). Parton distributions for LO generators. European Physical Journal C, 55, 553–575.
- Agostinelli, S., et al. (2003). Geant4-a simulation toolkit. Nuclear Instruments and Methods in Physics Research Section A: Accelerators, Spectrometers, Detectors and Associated Equipment, 506, 250–303. ISSN: 0168–9002.
- Allison, J., et al. (2006). Geant4 developments and applications. *IEEE Transactions on Nuclear Science*, 53, 270–278. ISSN: 0018–9499.
- Cacciari, M., Salam, G. P., & Soyez, G. (2008). The anti-kt jet clustering algorithm. JHEP, 04, 063. arXiv:0802.1189
- 24. Cacciari, M., & Salam, G. P. (2006). Dispelling the N³ myth for the kt jet-finder. *Physics Letters*, *B641*, 57–61. ISSN: 0370–2693. arXiv:hep-ph/0512210
- 25. ATLAS EtMiss Recommendations. (2014). Retrieved August 27, 2014, from https://twiki.cern. ch/twiki/bin/view/AtlasProtected/EtmissRecommendations2012.
- 26. Becker, K., et al. (2011). Mis-identified lepton backgrounds in top quark pair production studies for EPS 2011 analyses. ATL-COM-PHYS-2011-768.
- ATLAS Top Group MC common conventions (2014). Retrieved August 27, 2014, from https://twiki.cern.ch/twiki/bin/view/AtlasProtected/TopMC11.
- 28. Moch, S., & Uwer, P. (2008). Theoretical status and prospects for top-quark pair production at hadron colliders. *Physical Review D*, 78, 034003.
- 29. Langenfeld, U., Moch, S., & Uwer, P. (2009). New results for t anti-t production at hadron colliders. arXiv: 0907.2527 [hep-ph].
- 30. Beneke, M., et al. (2010). Threshold expansion of the gg(qq-bar) ->; QQ-bar + X cross section at O(alpha(s)**4). *Physical Letters*, *B690*, 483–490.
- ATLAS Top group scale factors for use in release 16 2011 analyses. https://twiki.cern.ch/twiki/ bin/view/AtlasProtected/TopCommonScales?rev=54
- 32. ATLAS Collaboration. (2011). Jet energy measurement with the ATLAS detector in proton-proton collisions at $\sqrt{s} = 7$ TeV. *European Physical Journal*, *C 73* [Comments: 100 pages plus author list (111 pages total), 93 figures, 17 tables, submitted to European Physical Journal C, 2304. 111 p (2011)].
- ATLAS Jet uncertainties package—JetUncertainties-00-03-05-01. https://twiki.cern.ch/twiki/bin/viewauth/AtlasProtected/JetUncertainties
- 34. ATLAS Collaboration. (2011). Commissioning of the ATLAS high-performance b-tagging algorithms in the 7 TeV collision data technical report. ATLAS-CONF-2011-102. Geneva: CERN.

References 101

35. ATLAS Collaboration. (2011). Calibrating the b-Tag Efficiency and Mistag Rate in 35 pb⁻¹ of data with the ATLAS Detector technical report. ATLAS-CONF-2011-089. Geneva: CERN.

- 36. ATLAS Collaboration. (2013). Jet energy resolution in proton-proton collisions at $\sqrt{s} = 7$ TeV recorded in 2010 with the ATLAS detector. *European Physical Journal*, *C73*, 2306.
- 37. Mangano, M. L., et al. (2007). Matching matrix elements and shower evolution for top-quark production in hadronic collisions. *JHEP*, 0701, 013. arXiv:hep-ph/0611129
- 38. ATLAS Collaboration. (2014). Measurement of the $t\bar{t}$ production cross-section as a function of jet multiplicity and jet transverse momentum in 7 TeV proton-proton collisions with the ATLAS detector. arXiv: 1407.0891 [hep-ex].
- HepData—ins1094568. Retrieved May 05, 2014, from http://hepdata.cedar.ac.uk/view/ins1094568.
- 40. Buckley, A., Butterworth, J., Lonnblad, L., Grellscheid, D., Hoeth, H., et al. (2013). Rivet user manual. *Computer Physics Communications*, 184, 2803–2819.
- 41. Rivet analysis ATLAS_2012_I1094568. Retrieved May 5, 2014, from https://rivet.hepforge.org/analyses#ATLAS_2012_I1094568.
- 42. Cooper, B., Katzy, J., Mangano, M., Messina, A., Mijovic, L., et al. (2012). Importance of a consistent choice of alpha(s) in the matching of AlpGen and Pythia. *European Physical Journal C*, 72, 2078.

Chapter 6 Studies and Applications of Jet Vetoing in Boosted Topologies

Event topologies in which objects with large momentum decay such that all of their decay products are captured within one large jet were originally recognised for heavy Higgs bosons decaying to boosted W's [1]. Similar studies were performed for WW scattering at high energies [2], the analysis of SUSY decay chains [3] and high-p_T Higgs bosons decaying to *b*-quarks [4]. All of these studies proposed tagging algorithms in order to separate the signal from the large backgrounds.

In this chapter the identification and utility of boosted top quarks is studied. Firstly, in Sect. 6.1, it is shown that a jet veto can be used to identify the colour of a heavy resonance decaying to t̄. In Sect. 6.2 the efficiency of boosted top-tagging algorithms is studied and the extent to which the efficiency depends on the colour structure of the event explored. Work presented in this chapter has been published in [5] and [6].

6.1 Identifying the Colour of TeV-Scale Resonances

6.1.1 Introduction

The work presented in this Section illustrates how the additional quark and gluon radiation that accompanies the production of a new heavy resonance can be exploited to yield information about the colour structure of the resonance.

Differently coloured resonances will in general produce different patterns of accompanying QCD radiation and this difference can be exploited to establish the colour structure of the resonance. For example in the case of the leading-order production of colour singlet and colour octet *s*-channel resonances, the flow of colour across the respective diagrams is very different, as illustrated in Fig. 6.1. These ideas have been explored in recent papers [7–10], and the purpose here is to present a feasibility study that quantifies the prospects for such a measurement to be made at the LHC.

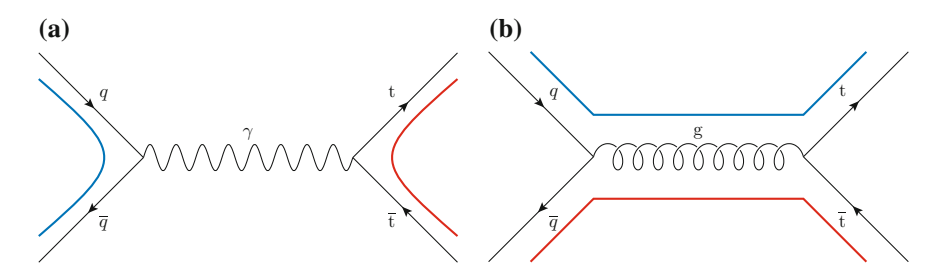


Fig. 6.1 Examples of the difference in colour flow between the exchange of \mathbf{a} an s-channel photon and \mathbf{b} an s-channel gluon. Since the gluon is a colour octet there is a flow of colour between the initial and final-state partons

The associated radiation is explored by studying the efficiency of a jet veto (cf. Eq. 5.1). The use of jet vetoes to probe colour structure has already been shown to have other important applications. For example in [11] it was shown that it is possible to extract the contributions from vector boson fusion and gluon fusion production of a Higgs boson in Higgs plus dijet events.

The jet veto efficiency has many properties that make it well-suited for an experimental measurement. As shown in Sect. 5.8, any experimental systematic uncertainties associated with overall event selection cancel in the ratio when calculating the jet veto efficiency. The jet veto efficiency is also an observable that is robust against pile-up, since it is calculated using all selected events and can easily be corrected for backgrounds and pile-up, providing the contributions can be subtracted statistically. Observables that are measured on an event-by-event basis however, such as the 'jet pull' [8] which uses the structure of jets to probe the colour flow in an event, would suffer from event-by-event background contamination and events dominated by pileup.

The production of a new heavy resonance is a primary signal of new physics in several extensions to the Standard Model. One popular scenario is the Randall-Sundrum (RS) model [12–14], which proposes that Kaluza-Klein gauge bosons exist, can be produced at the LHC and decay primarily to tt. The RS framework is attractive because it solves a number of issues with the Standard Model, e.g. the gauge hierarchy problem [12], the fermion mass hierarchy problem [15–17] and it provides a dark matter candidate [18, 19]. Furthermore, at the time of publication, results from the CDF [20] and DØ [21, 22] experiments on the forward-backward charge asymmetry in tt events indicated a potential deviation from the SM expectation, which could have been caused by a colour octet resonance with mass of 2 TeV [23]. Therefore it was decided to investigate if the jet veto efficiency could be used to distinguish between the production of colour octet and singlet resonances of mass 2 TeV and spin-1.

6.1.2 Simulation and Event Selection

A heavy gluon (colour octet) resonance has been implemented within the PYTHIA8 event generator. Details of the implementation can be found in [5]. The implementation was validated against results found in the literature and was used to investigate some characteristics of the resonance.

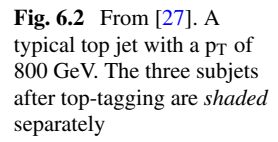
Events were generated at $\sqrt{s}=14$ TeV. The cross section times branching-ratio for the gluon resonance was 1.1 pb and the resonance mass was set to 2 TeV and its width to 400 GeV. Events containing a heavy photon (colour singlet) resonance were generated by changing the colour flow; colour factors were replaced and $\alpha_s \to e_q^2 \alpha_{em}$ where e_q is the electric charge. The coupling of the heavy photon resonance to light quarks was adjusted to reproduce the production rate of the heavy gluon, and the coupling of the heavy photon to top quarks was adjusted to match the decay width of the heavy gluon. The CTEQ5L [24] parton distribution functions were used with the PYTHIA8 authors' default tune to the underlying event (Tune1) [25]. The main backgrounds to the heavy production are due to SM tt and QCD 2 \rightarrow 2 scattering. Both sets of background events were generated with PYTHIA8.

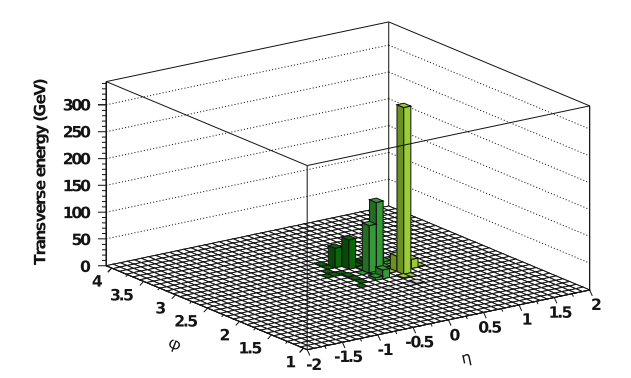
The sensitivity to the non-perturbative physics was investigated using a very conservative approach—repeating the analysis with hadronisation and multiple parton interactions turned off. The observed change in the jet veto efficiencies was less than 2%, indicating that the modelling of non-perturbative physics does not play an important role in the measurement.

Given the large masses of the heavy gluon and photon, the top quarks produced in the decay are highly boosted. The decay products of the top quarks tend to be collimated and confined to a small area of the detector. In such a situation all of the radiation from the decay products can typically be collected inside one 'fat' jet. Jet substructure techniques, which examine the energy distribution of the constituents of the fat jets, can then be used to distinguish between jets originating from the decays of boosted top quarks and the light quark and gluon jets originating in backgroud QCD-induced processes. Top-jet candidates are identified using the FASTJET [26] library and the JOHNS-HOPKINS top-tagging algorithm [27].

The JOHNS-HOPKINS algorithm attempts to identify jets originating from the decays of boosted top quarks to a *b*-quark and W-boson, with subsequent decay of the W to two light jets. When the top quark is highly boosted the three jets can end up lying very close together, as shown in Fig. 6.2. Although falling entirely within one fat jet, the three subjets would still be distinguishable from each other with the granuality of the ATLAS calorimeter. In contrast, QCD jets typically start as a single hard parton, which tends to cascade into a high multiplicty of soft and collinear particles. In order for a QCD jet to mimic a decayed top quark it would need to have undergone at least two large-angle splittings, with energy being shared somewhat equally. This is a relatively rare occurrence.

¹I.e. The cross section times branching ratio for the heavy colour singlet was also set to 1.1 pb.





The JOHNS-HOPKINS algorithm proceeds as follows. Particles are first clustered into jets of size R using the Cambridge-Aachen (C-A) algorithm (cf. Sect. 1.5.6). Each C-A jet is then examined to search for subjets; the last step of the clustering is undone and the two subjets produced in the splitting $(j \rightarrow j_1 j_2)$ must satisfy the following criteria: $\min(p_T^{j1}, p_T^{j2})/p_T^j > \delta_p$ and $\Delta R(j_1, j_2) > \delta_r$. The values of the parameters δ_p and δ_r used are given in Table 6.1, and follow the choices made by the authors of the algorithm. If both cuts are passed then the declustering is applied to j_1 and j_2 , and continues until n irreducible jets remain. If n = 3 or n = 4 then the subjets are then required to pass the following kinematic constraints: the total invariant mass of the subjets should be near m_t , two subjets should reconstruct m_W and the helicity angle, $\cos(\theta_h)$ should be consistent with a top decay, which in this case is $cos(\theta_h) < 0.7$. Because more highly boosted top quarks will produce decay products that are more highly collimated, the parameters and cuts are set as a function of the total transverse energy in the event. The exact choice of kinematic cuts used in this study were as follows. For jets with p_T < 1000 GeV a top mass window of $m_t\pm 30$ GeV and a W mass window of $m_W\pm 15$ GeV was used. If the jets had p_T > 1000 GeV the upper ranges of the top and W mass windows were shifted to $p_T/20 + 155 \text{ GeV}$ and $p_T/40 + 70 \text{ GeV}$ respectively.

The inputs to the jet-finding algorithm were all stable final-state particles (excluding neutrinos) in the MC event record with $|\eta| < 4.9$ i.e. within the acceptance of the LHC detectors. Events were then required to contain two tagged top-jets (as reported by the JOHNS-HOPKINS algorithm) with $p_T > 400$ GeV. After these initial event selection requirements the cross section for heavy gluon production was 46.8 fb while the cross section for heavy photon production was 31.4 fb. This difference in cross sections demonstrates an unexpected and important difference in the efficiency to tag top quarks originating from resonances with different colour structure. It was confirmed that the difference was not due to non-perturbative physics; the difference arises after the parton shower, with hadronisation and underlying event playing a

²The helicity angle is defined as the angle, measured in the rest frame of the reconstructed W, between the direction of the reconstructed top and one of the W decay products.

(0.17)

\(\sum_{E_T}(GeV)\)	δ_p	R_{CA}	δ _r
$\sum E_T \le 1000$	0.13	0.9	0.19
$1000 < \sum E_T \le 1600$	0.10	0.8	0.19
$1600 < \sum E_T \le 2600$	0.05	0.6	0.19
$\sum E_T > 2600$	0.05	0.4	0.16
All parameters are deper	ndent on the scalar-sumn	ned E_T and defined on a	n event-by-event basis

Table 6.1 Parameters used in the top-tagging algorithms defined in the text

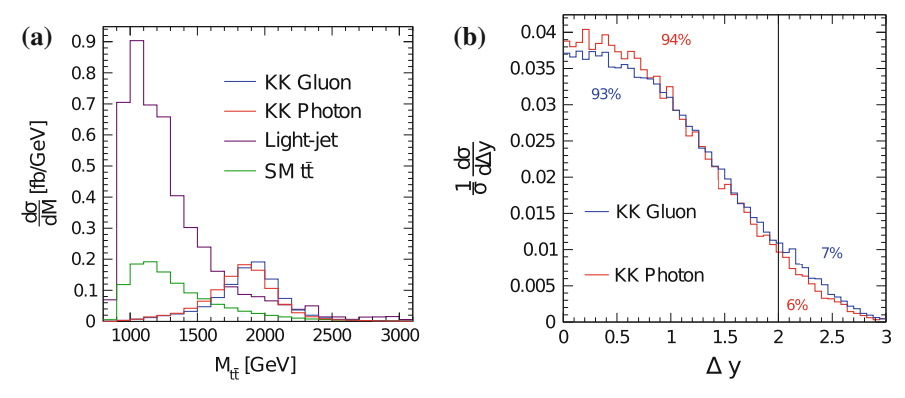


Fig. 6.3 Kinematic distributions obtained after tagging the leading two jets as originating from top quarks using the JOHNS-HOPKINS top-tagging algorithm. **a** The invariant mass of the top candidates for the signal resonances and SM background processes. **b** Difference in rapidity between the two top candidates

small role. This observed difference in tagging efficiency is investigated further in the follow-up study presented in Sect. 6.2.

For both resonances, the application of the top-tagging algorithm is sufficient to reduce backgrounds to a manageable level in a window where the invariant mass of the tagged top-jets is close to the resonance. Figure 6.3a shows invariant mass distributions for the two resonance signals as well as the light-jet and SM $t\bar{t}$ backgrounds. In order to compare the resonances, one further change was made to the heavy photon cross section when presented in the rest of the study—it was set equal to the heavy gluon cross section after top-tagging, i.e. $\sigma_{\gamma_{KK}} = \sigma_{G_{KK}} = \sigma_0 = 46.8$ fb. All final results are presented for a range of production cross section values.

6.1.3 Definition of the Jet Veto Region and the Jet Veto Efficiency

In order to identify any jets in an event that originate from additional quark or gluon emissions, the anti- k_t algorithm was used with R = 0.6. The particles used as input to this second stage of jet finding were the same as those used in the top-tagging

stage, however only those jets that were sufficiently far from the previously tagged top jets were kept,

$$\Delta R(j,t) > R_{CA},\tag{6.1}$$

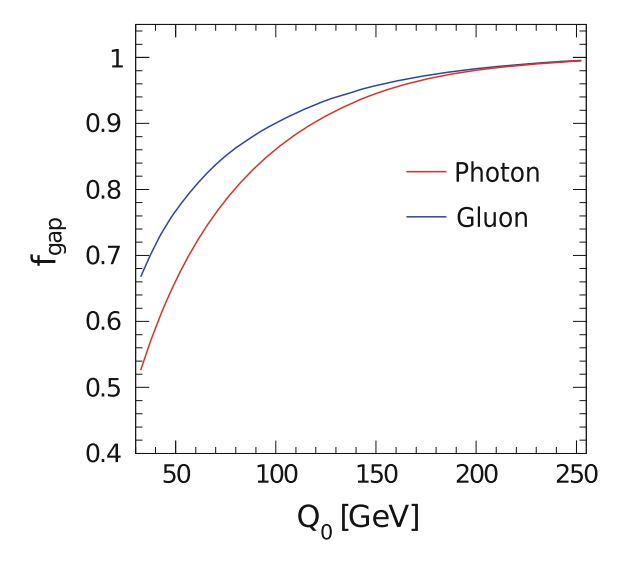
where R_{CA} is the same as in Table 6.1. A veto can then be applied to these additional jets in order to identify the colour flow in the $t\bar{t}$ system. One choice would be to veto on additional jet activity between the two top jet candidates, in order to identify a colour connected between the top and antitop quark for a colour singlet resonance decay. However this would require that the top jets are separated in rapidity by a sufficiently large amount. Figure 6.3b shows the rapidity difference between the two top candidates where it is found that less than 10% of the events would remain after applying a $|\Delta y| > 2.0$ cut. Therefore the veto is applied to jets falling in a central rapidity interval, |y| < 1.5. Vetoing on jets falling into very central regions has the added benefit that they would be entirely contained within the acceptance of the ID tracker of the ATLAS experiment.

The observable of interest is the jet veto efficiency (referred to as $f_{\rm gap}(Q_0)$, for gap fraction, in the remainder of this Section), as was also measured in the analysis in Chap. 5. In this study $f_{\rm gap}(Q_0)$ was defined to be the fraction of events that do not contain any jets in addition to the top-jet candidates with $p_T > Q_0$ GeV and |y| < 1.5. i.e.

$$f_{\rm gap} = \frac{\sigma(Q_0)}{\sigma(Q_0 = \infty)} \ . \tag{6.2}$$

Figure 6.4 shows a comparison of the jet veto efficiencies as a function of Q_0 for the case of the heavy colour octet (gluon) and heavy colour singlet (photon) reso-

Fig. 6.4 Jet veto efficiencies predicted by PYTHIA8 for a heavy gluon (*blue*) and heavy photon (*red*) resonance



nances generated using PYTHIA8. The jet veto efficiency for the photon is lower than for the gluon, indicating that more additional radiation is produced in associated with the photon. This is slightly counter-intuitive, but can be understood by considering the handwavy argument that the amount of additional radiation produced is proportional to the acceleration that the colour charge undergoes (cf. bremsstrahlung for electrically charged particles). Looking again at the colour flow of the different production mechanisms shown in Fig. 6.1, we see that for the case of the heavy photon the colour lines of the initial and final states are not connected. Therefore the colour charge must be annihilated in the initial state and ripped out of the vacuum in the final state, a process that involves larger accelerations than in the case of the heavy gluon, where the colour can flow from the initial to the final state. This is in contrast to the case of a *t*-channel exchange of a colour singlet such as the vector boson fusion processes studied in Chap. 7. The flow of colour from initial to final state does not result in the same acceleration of colour charges, and there is a lack of additional quark and gluon radiation produced in the events.

In Fig. 6.5a, b the jet veto efficiency as a function of Q_0 predicted by PYTHIA8 is compared to predictions in which MADGRAPH was used to generate the matrix elements for the heavy resonance plus up to three additional partons. Although the sets of theoretical predictions are significantly different from each other (effects of theoretical uncertainty are discussed in Sect. 6.1.6). Figure 6.5c shows that the difference between the heavy gluon and photon jet veto efficiencies is large in each case. The results presented later therefore do not depend on the choice of generator used, and so events generated using PYTHIA8 are used in the following sections.

6.1.4 Extracting the Signal from Background

Pseudo-experiments are used to assess the sensitivity of the jet veto efficiency to the colour of the heavy resonance at a given luminosity, \mathcal{L} . For a given signal or background process, i, the number of expected events is $\lambda_i = \sigma_i \mathcal{L}$ where σ_i is the process cross section. The actual number of events, n_i , that contribute to a given pseudo-experiment is chosen by sampling from a Poisson distribution with mean λ_i . The n_i events are then chosen at random from the MC events that remain after top-tagging has been applied. The invariant mass of the pair of top candidates, $m_{t\bar{t}}$, is constructed from the events remaining after vetoing those containing additional jets with $p_T > Q_0$ GeV and |y| < 1.5. This $m_{t\bar{t}}$ distribution is constructed for every value of Q_0 .

The number of signal events at each value of Q_0 is determined by fitting the combined signal+background invariant mass distribution with a skewed Breit-Wigner distribution + background template,

$$\frac{m_0^2 \Gamma^2 [a + b(m_{t\bar{t}} - m_0)]}{(m_{t\bar{t}}^2 - m_0^2)^2 - m_0^2 \Gamma^2},$$
(6.3)

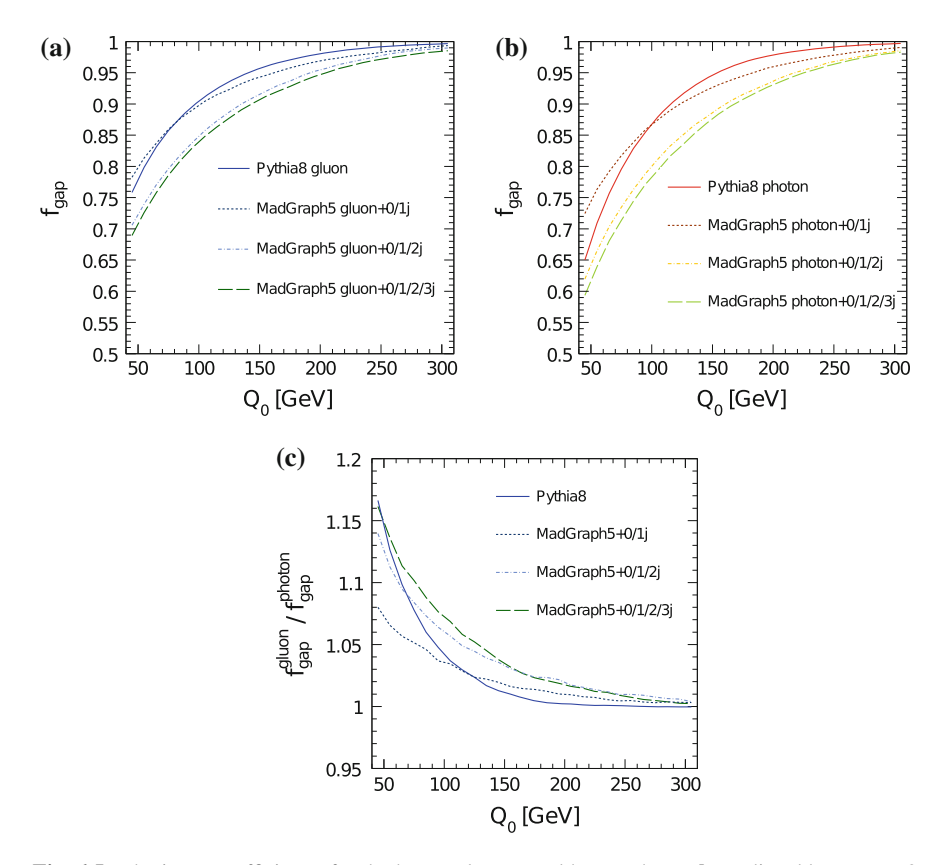


Fig. 6.5 The jet veto efficiency for the heavy gluon **a** and heavy photon **b** predicted by PYTHIA8 and MADGRAPH. The MADGRAPH predictions correspond to events generated with matrix elements including up to one, up to two or up to three additional partons in the final state. All MADGRAPH events are interfaced to PYTHIA8 for parton showering, hadronisation and underlying event modelling

where m_0 , Γ , a and b are allowed to vary in the fit. The $m_{t\bar{t}}$ distribution in the SM tt MC samples is used as a template for the background shape and only its normalisation is allowed to vary in the fit. This is a reasonable assumption to make, since the QCD-induced light-jet and $t\bar{t}$ m_{jj} distributions have very similar shapes, especially in the region of the signal at large values of m_{jj} . The sensitivity of the signal extraction to the background shape was assessed by altering the shape of the background template and repeating the fits. It was found that even quite large changes in the shape of the background have a small effect on the results.

After fitting the $m_{t\bar{t}}$ distribution the number of signal events is defined as $N_s = N_T - N_b$ where N_T is the total number of events in the pseudo-experiment that contain top pair candidates with an invariant mass in the range 1.5 TeV $< m_{t\bar{t}} < 2.5$ TeV, and N_b is the number of background events in this region as determined by the fit. The

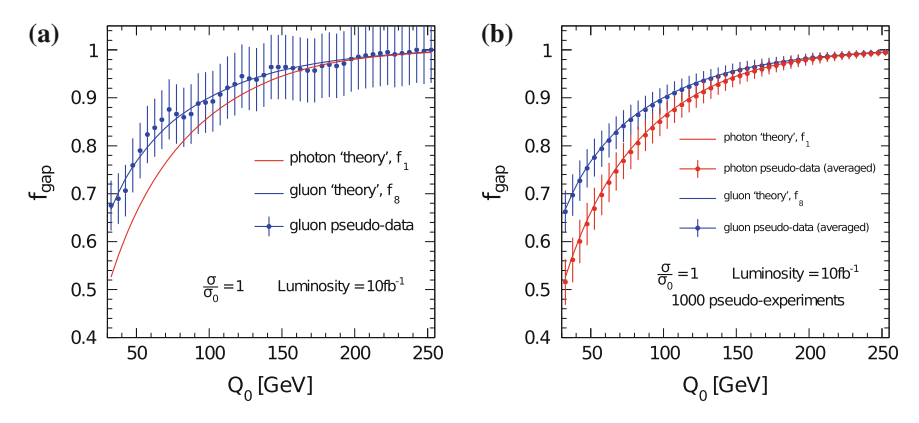


Fig. 6.6 a *Blue points* show the result of a single pseudo-experiment given that a heavy gluon signal was used as input. *Solid blue* and *red curves* show the theoretical predictions for the jet veto efficiency produced in events containing a heavy gluon and heavy photon resonance. **b** Mean jet veto efficiencies after averaging over 1000 pseudo-experiments. Uncertainty bars show the RMS spread of the jet veto efficiency values obtained in the pseudo-experiments

size of this mass window of course depends on the mass and width of the resonance and would be optimised in a real experimental analysis.

The jet veto efficiency at a particular value of Q_0 can then be constructed as,³

$$f_{\text{gap}}(Q_0) = \frac{N_s(Q_0)}{N_s(Q_0 = \infty)}$$
 (6.4)

Figure 6.6a shows the result of a typical pseudo-experiment. A heavy gluon has been used for the signal, and an integrated luminosity of 10 fb^{-1} . The pseudo-data are compared to theoretical predictions for jet veto efficiencies produced by the heavy gluon and heavy photon. Although there are quite large fluctuations in the pseudo-data⁴ it is clear that they are better described by the heavy gluon prediction, particularly at low values of Q_0 .

Figure 6.6b demonstrates the degree to which the signal can be correctly extracted. The mean of jet veto efficiencies obtained from all pseudo-experiments is calculated, and it is clear they agree well with the corresponding predictions for the signal-only heavy gluon or heavy photon resonances. The error bars are determined by taking the RMS of the jet veto efficiencies obtained in the pseudo-experiments, and show that a measurement of the jet veto efficiency would be able to distinguish between the differently coloured resonances with around 10 fb⁻¹ of data, assuming that the production cross sections are approximately the same size as those considered here.

 $^{^{3}}$ In practice Q_{0} = 300 GeV is taken as the upper bound. A point at which the jet veto efficiency is consistent with unity.

⁴For simplicity the error bars in Fig. 6.6a are calculated by assuming that the numerator and denominator of the jet veto efficiency (Eq. 6.4) are uncorrelated, Poisson, random variables.

6.1.5 Extracting the Colour

The colour of the resonance can be extracted using a fit of the form

$$f_{\text{gap}}(Q_0) = a_1 f_1(Q_0) + a_8 f_8(Q_0),$$
 (6.5)

where f_1 (f_8) is the signal-only prediction for the jet veto efficiency produced by the colour singlet (octet) resonance, and a_i are allowed to vary in the fit but are constrained to be in the range $0 \le a_i \le 1$. Figure 6.7a shows the probability of obtaining a specific value of a_8 for the case of a heavy gluon input, $P(a_8|g)$, assuming an integrated luminosity of 10 fb^{-1} . $P(a_8|g)$ is peaked strongly at one, and indicates that the heavy gluon is correctly identified in the majority of pseudo-experiments. Also shown is $P(a_1|g)$ and as expected it is strongly peaked at zero. Figure 6.7b shows the same distributions for the case that the true signal comes from a heavy photon, $P(a_1|\gamma)$ and $P(a_8|\gamma)$.

A more interesting quantity is the probability, given a fitted value of a_8 , that the true signal was a heavy gluon, i.e. $P(g|a_8)$. This can be calculated using Bayes' theorem and by making the assumption that the prior probability for the true signal to be a heavy gluon is equal to that for a heavy photon,

$$P(g|a_8) = \frac{P(a_8|g)}{P(a_8|g) + P(a_8|\gamma)}.$$
(6.6)

The curves in Fig. 6.7 can be used to construct these probability distributions, $P(g|a_8)$ and $P(\gamma|a_8)$, which are shown in Fig. 6.8a. Therefore for each pseudo-experiment a value of a_8 (a_1) can be extracted from the fit to the jet veto efficiency,

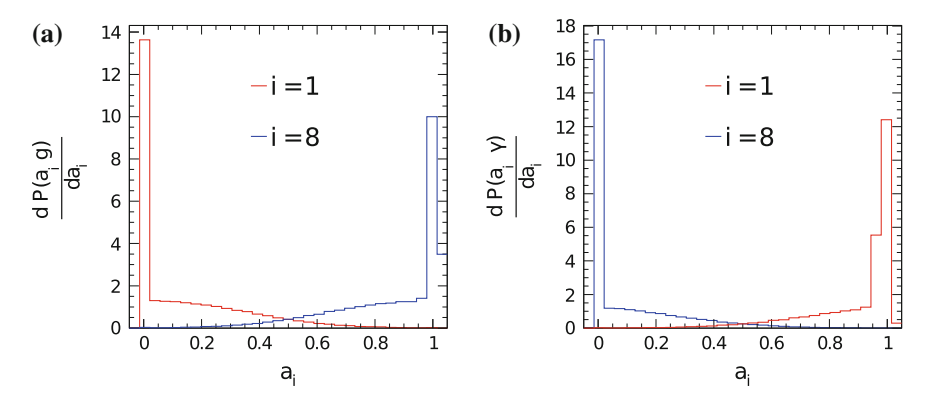


Fig. 6.7 a $P(a_1|g)$ and $P(a_8|g)$ obtained from 10^5 pseudo-experiments for the case of a heavy gluon input. **b** $P(a_1|\gamma)$ and $P(a_8|\gamma)$ distributions obtained from 10^5 pseudo-experiments for the case of the heavy photon input. Both sets of pseudoexperiments assume an integrated luminosity of 10 fb^{-1}

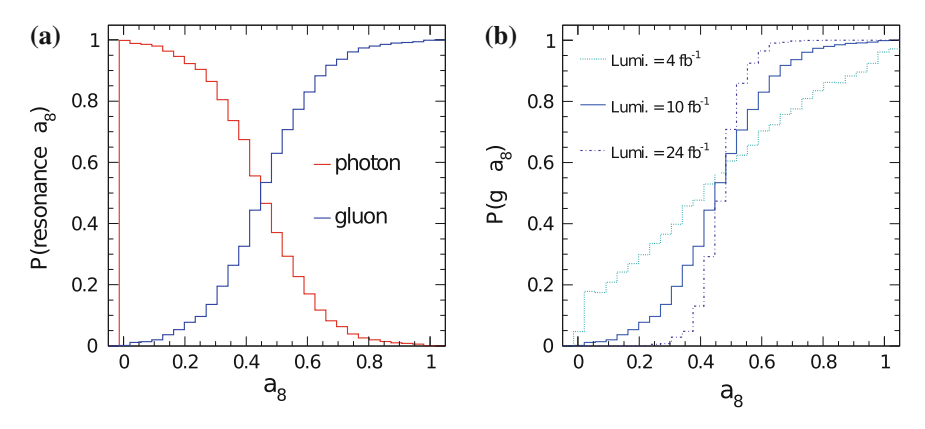


Fig. 6.8 a $P(g|a_8)$ and $P(\gamma|a_8)$ in the case of a heavy gluon resonance input as signal and assuming the baseline cross section and an integrated luminosity of $10 \, \text{fb}^{-1}$. **b** $P(g|a_8)$ for three different values of integrated luminosity

and used along with the probability distributions shown in Fig. 6.8a to calculate the probability that the true resonance was a heavy gluon (photon).

To quantify the feasibility of extracting the colour in an experimental analysis at the LHC, the quantity G_{95} is defined to be the fraction of pseudo-experiments that have $P(g|a_8)$ larger than 95 %. For example, $G_{95}=0.77$ for the baseline heavy gluon cross section and an integrated luminosity of 10 fb⁻¹. It is therefore very likely that this method could be used by the LHC experiments to identify the colour of such a resonance should it be shown to exist.

Figure 6.9a shows how G_{95} varies as the size of the signal cross section is changed, and for different integrated luminosities. For signal cross sections less than around 1/3 of the baseline value, σ_0 , an integrated luminosity in excess of 50 fb⁻¹ would be necessary to extract the colour of the resonance. Figure 6.9b shows the same set of distributions for the case of a heavy photon resonance (Γ_{95}), and Fig. 6.10 shows the corresponding plots when the probability requirements $P(a_8|g)$ and $P(a_1|\gamma)$ are increased to 99 % (G_{99} and Γ_{99}).

6.1.6 Effect of Experimental and Theoretical Uncertainties

Experimental and theoretical uncertainties will adversely affect the determination of the colour of a heavy resonance. As discussed in Sect. 5.8 the experimental uncertainties associated with extracting the signal will largely cancel in the ratio when constructing the jet veto efficiency. It is expected that uncertainties related to top-tagging efficiency, luminosity, and energy scale and resolution of top-tagged jets will not affect the measurement in a significant way. However, uncertainties associated

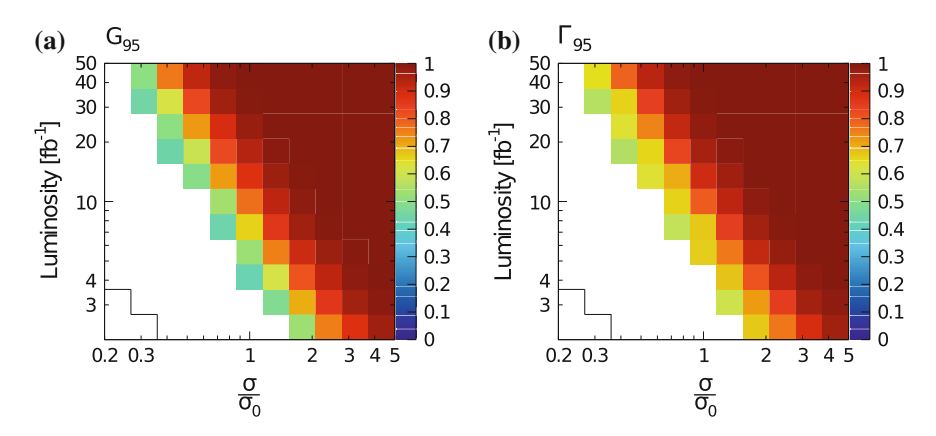


Fig. 6.9 The fraction of LHC experiments that would measure $P(g|a_8) \ge 95\%$ is denoted G_{95} , and the fraction $P(\gamma|a_1) \ge 95\%$ is denoted Γ_{95} . a G_{95} (b Γ_{95}) as a function of integrated luminosity and signal cross section size assuming a heavy gluon (heavy photon) resonance. The *solid line* in the *bottom left corner* indicates the region where the (statistical) significance of the signal extracted from the fit is less than 5σ

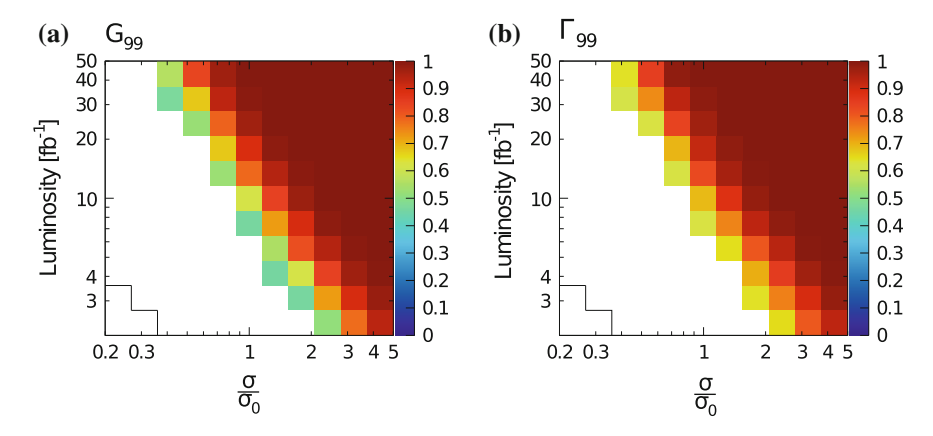


Fig. 6.10 The fraction of LHC experiments that would measure $P(g|a_8) \ge 99\%$ is denoted G_{99} , and the fraction $P(\gamma|a_1) \ge 99\%$ is denoted P_{99} , and P_{99} (brown a function of integrated luminosity and signal cross section size assuming a heavy gluon (heavy photon) resonance. The *solid line* in the *bottom left corner* indicates the region where the (statistical) significance of the signal extracted from the fit is less than P_{99} (significance) and P_{99} (significance) are the fit is less than P_{99} (significance) and P_{99} (significance) are the fit is less than P_{99} (significance) are

with the jets upon which the veto is placed, e.g. the jet energy scale, jet energy resolution and jet reconstruction efficiency will affect the measurement. The ATLAS measurement of dijet production with a veto on additional central jet activity [28] was used to estimate the likely size of the experimental systematic uncertainties.⁵ The results presented by ATLAS show that the total experimental uncertainty on the

⁵The measurement presented in Sect. 5 would have provided an equally useful feel for the size of systematic uncertainties, had it been completed before the analysis discussed here.

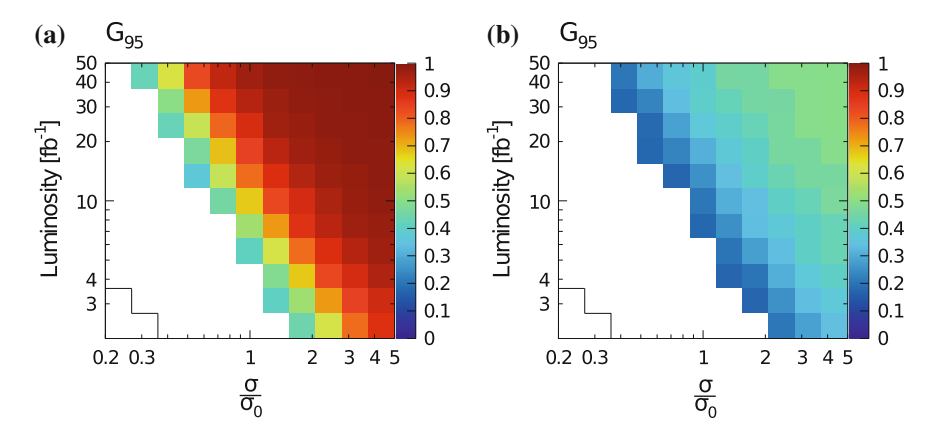


Fig. 6.11 a The impact a 10 % uncertainty on the jet veto efficiency has on the value of G_{95} . b The impact a 25 % uncertainty on the jet veto efficiency has on the value of G_{95}

 $f_{\rm gap}(Q_0)$ values was at worst 5% at $Q_0 = 20$ GeV, for dijet systems constructed from high-p_T jets falling into central rapidity regions.

The theoretical modelling uncertainties associated with the jet veto efficiency are much larger than this. The predictions used in [28] deviate from the ATLAS data by ~25 % at $Q_0 = 20$ GeV, and in [29] the uncertainty in the theoretical prediction of the jet veto efficiency in dijet events was found to approach 50 % in some regions of phase space. There is no reason to assume that jet vetoing in boosted $t\bar{t}$ events is understood more accurately than this, and so it is clear that it is the theoretical uncertainties that limit the feasibility of making a measurement such as this.

The effect of theoretical uncertainties are estimated by changing the shape of the predictions from PYTHIA8 used to fit the jet veto efficiencies in each pseudo-experiment (i.e. f_1 and f_8). Uniformly distributed random numbers in the interval [-X, +X] are chosen in each pseudo-experiment and applied as fractional shifts to f_1 and f_8 at $Q_0 = 20$ GeV. The shift of the jet veto efficiency at $Q_0 = 300$ GeV is zero by definition, and size of the shift used for intermediate values of Q_0 is obtained by linear interpolation. Figure 6.11 shows the G_{95} values for X = 10% and X = 25%. An uncertainty in the jet veto efficiency of 25% has a serious effect on the measurement. An uncertainty of 10% does not have a large effect on the final results. Therefore to ensure that the jet veto efficiency can be used as a tool to extract the colour of a heavy resonance in an analysis such as this, uncertainties in the theoretical predictions of the jet veto efficiency should be reduced to around the level of 10%.

6.2 Dependency of Tagging Algorithms on the Event Colour Structure

6.2.1 Introduction

As discussed in Sect. 6.1.2 an interesting difference was observed in the efficiency of tagging top jets that originated from either a colour singlet or octet resonance. In this section this difference is explored further and the impact of the event colour structure on the performance of the well-established JOHNS-HOPKINS [27], CMS [30], HEPTOPTAGGER [31], N-SUBJETTINESS [32] top-tagging algorithms is studied.

These top-tagging algorithms only make use of the constituents of the fat jets provided as input. However, given their large radius, it is likely that radiation from the initial state or underlying event will also enter the fat jet. Therefore the ability of these algorithms to tag a real top-jet can depend on the amount of additional radiation entering the fat jet, and therefore also on the colour structure of the events in which the top-jets were produced.

The same *s*-channel resonances as used in the previous section are used again here to probe the top-tagging efficiency differences: a colour-singlet Kaluza-Klein photon, γ_{KK} , and a colour-octet Kaluza-Klein gluon, G_{KK} , with masses of 2 TeV and that decay exclusively to top quarks. The two resonances exhibit different colour flows, as shown in Fig. 6.1, and will therefore produce different patterns of additional radiation.

6.2.2 Boosted Top Reconstruction

The JOHNS-HOPKINS algorithm is described in Sect. 6.1.2. The default parameters chosen in this study were $\delta_p = 0.12$ and $\delta_r = 0.16$ which match those of the algorithm authors.

The CMS top-tagger [30] is a modification of the JOHNS-HOPKINS algorithm, where in the first step the subjets must have an angular separation larger than some p_T-dependent criterion, $\Delta R(j_1, j_2) > \delta_r - A \cdot p_{T,j}$. This replicates the scalar-summed E_T -dependent cuts of the JOHNS-HOPKINS algorithm. The default parameter values used in this study were $\delta_r = 0.4$ and A = 0.0004, which match those used by the algorithm authors. After decomposing the two fat jets the algorithm must find three or four subjets that satisfy similar requirements as for the JOHNS-HOPKINS algorithm—the invariant mass of all subjets must be close to the top mass and the pair of subjets with the lowest invariant mass must have an invariant mass larger than 50 GeV.

The HEPTOPTAGGER algorithm [33] was developed with the aim of reconstructing and tagging moderately boosted top quarks in busy environments. After first using the C-A algorithm to cluster the hadronic activity in the event into fat jets, each fat jet is decomposed and examined for substructure. Within each fat jet, all subjets are found using a mass-drop criterion: when undoing the clustering of a jet j into two subjets

 j_1 and j_2 with $m_{j_1} > m_{j_2}$, both subjets are kept if the mass of j_1 is sufficiently small, $m_{j_1} < 0.8 m_j$, otherwise only j_1 is kept. Each subjet, j_i is then either decomposed further if $m_{j_i} > 30$ GeV or added to the list of relevant substructure. All three-subjet combinations are then filtered⁶ and the combination with invariant mass closest to the top mass, within some mass window, is kept as the top candidate. The three subjets are then required to pass one of three criteria;

$$0.2 < \arctan\left(\frac{m_{13}}{m_{12}}\right) < 1.3 \text{ and } R_{\min}. < \frac{m_{23}}{m_{123}} < R_{\max}.$$

$$R_{\min}^2 \left(1 + \left(\frac{m_{13}}{m_{12}}\right)^2\right) < 1 - \left(\frac{m_{23}}{m_{123}}\right)^2 < R_{\max}^2 \left(1 + \left(\frac{m_{13}}{m_{12}}\right)^2\right) \text{ and } \frac{m_{23}}{m_{123}} > R_{\text{soft}}.$$

$$R_{\min}^2 \left(1 + \left(\frac{m_{12}}{m_{13}}\right)^2\right) < 1 - \left(\frac{m_{23}}{m_{123}}\right)^2 < R_{\max}^2 \left(1 + \left(\frac{m_{12}}{m_{13}}\right)^2\right) \text{ and } \frac{m_{23}}{m_{123}} > R_{\text{soft}}.$$

The default values of the dimensionless mass window bounds are set to $R_{\text{min.}} = 0.85 \cdot m_W/m_t$ and $R_{\text{max.}} = 1.15 \cdot m_W/m_t$.

The N-SUBJETTINESS tagger [32] takes the ideas introduced by the N-JETTINESS [34] event shape variable and applies them to the study of jet sub-structure. The algorithm attempts to quantify the extent to which a fat jet looks like it is composed of N distinct subjets. The variable of interest, τ_N , is calculated as:

$$\tau_N = \frac{\sum_k p_{T,k} \min.(\Delta R_{1,k}, \Delta R_{2,k}, ..., \Delta R_{N,k})}{\sum_k p_{T,k} R_0} ,$$

where the summation runs over all jet constituents, $p_{T,k}$ is the transverse momentum of each fat jet constituent, $\Delta R_{J,k}$ is the η - ϕ distance between the proposed subjet axis J and the constituent k, and R_0 is the fat jet radius. Small values of τ_N indicate that there are N or fewer energy deposits within the fat jet. Larger values of τ_N suggest that more than N energy deposits are present. Rather than simply cutting on τ_N , is has been found that the ratio τ_N/τ_{N-1} provides the best discriminating power between top jets and jets originating from light quarks and gluons. The parameters used to define a top candidate are τ_N/τ_{N-1} and the mass of the fat jet.

⁶When a jet is filtered it is resolved on a finer angular scale $R_{\rm filt} < R_{\rm jet}$ and any objects found that are sufficiently soft are removed [4]. This process can help to eliminate contamination from the underlying event, for example, and will be relevant when considering the tagging efficiencies found in Sect. 6.2.4.

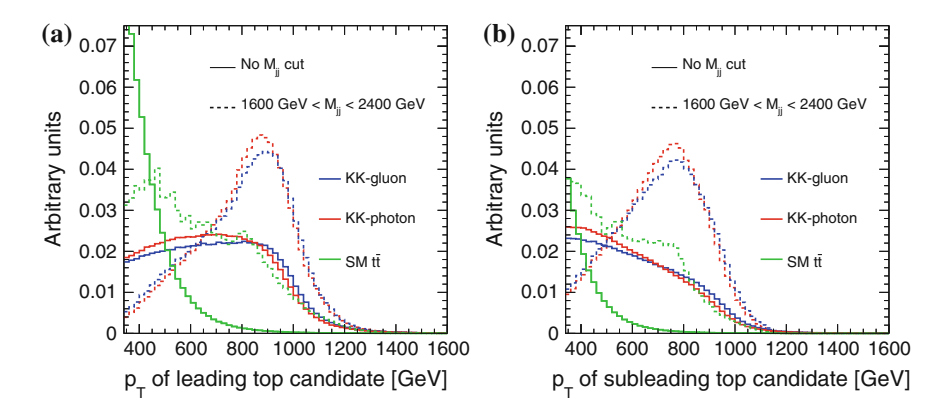


Fig. 6.12 Transverse momentum distributions of the leading **a** and sub-leading, **b** top-jet candidates as reconstructed using the C-A algorithm with R=0.8. The KK-gluon, KK-photon and SM tt events are shown in *blue*, *red* and *green* respectively. Two sets of curves are shown: before (*solid lines*) and after (*dashed lines*) a dijet invariant mass cut of 1.6 TeV $\leq m_{jj} < 2.4$ TeV

6.2.3 Basic Kinematic Features of the Signal Events

The C-A algorithm with radius parameter R=0.8 is used to reconstruct jets using all stable final-state particles (excluding neutrinos) in the MC event record with $|\eta| < 4.9$. The effect of using a different radius parameter is discussed in Sect. 6.2.4 and shown in Fig. 6.16. Jets are initially kept for further analysis, and fed into the top-tagging algorithms, if they have $p_T > 350$ GeV. The p_T distributions of the leading and sub-leading top-jet candidates are shown in Fig. 6.12a, b. After requiring that the dijet invariant mass be in the range $1.6 \, \text{TeV} \le m_{jj} < 2.4 \, \text{TeV}$ the transverse momentum of the leading and sub-leading jets originating from the KK-gluon and KK-photon are very similar. Therefore any differences in top-tagging efficiency should not be due to differences in kinematic properties of the jets.

6.2.4 Dependence of Top-Tagging Efficiency on Event Colour Structure

The performance of the top-tagging algorithms is assessed by measuring the efficiency with which they tag as top jets those which originate from top quarks, and the probability for mis-tagging jets that arise from light quarks or gluons. The single and double-tagging efficiencies, ϵ_1 and ϵ_2 , are defined as

$$\epsilon_1 = \frac{N_{1t}}{N_{2i}}$$
 and $\epsilon_2 = \frac{N_{2t}}{N_{2i}}$ (6.7)

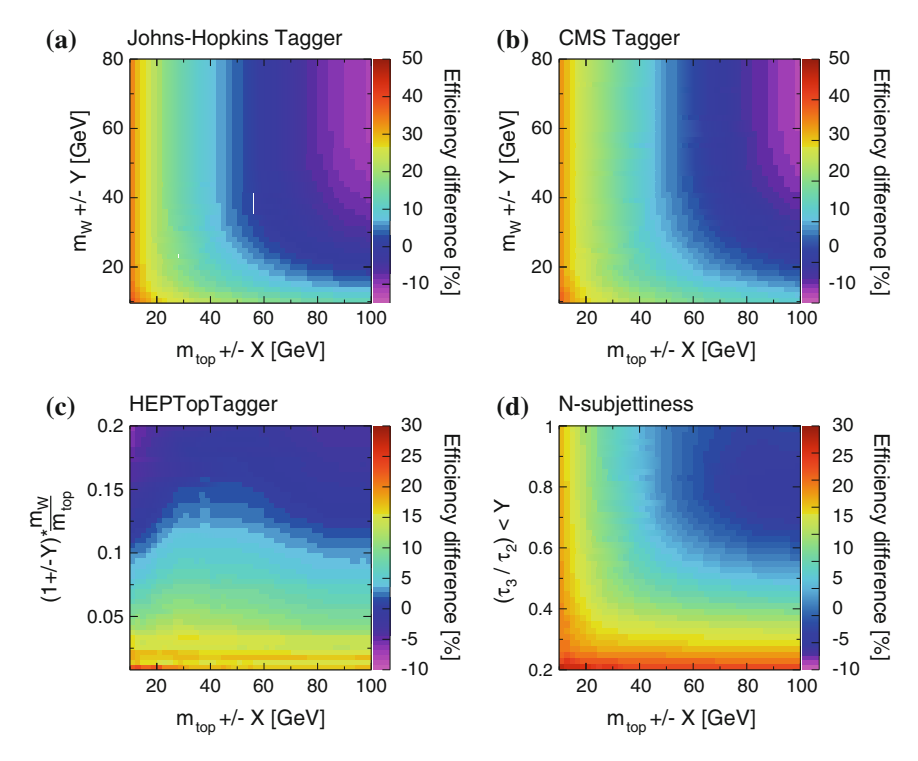


Fig. 6.13 Double-tagging efficiency differences for a JOHNS-HOPKINS, **b** CMS, **c** HEPTOPTAGGER, **d** N-SUBJETTINESS algorithms. The difference in efficiencies is presented as a function of the algorithm input parameters. For example, $m_{\text{top}} \pm X$ refers to the size of the window in which the top mass reconstructed from the jet constituents is required to lie. Details of top mass reconstruction and other algorithm parameters are given in Sect. 6.2.2

where N_{2j} is the number of events containing two C-A jets with $p_T > 500$ GeV and |y| < 2.5. N_{1t} is the subset of these events in which the leading jet was tagged as originating from a top quark, and N_{2t} is the subset of the dijet events in which both the leading *and* sub-leading jets are identified as top-jets.

Figure 6.13 shows the difference in double-tagging efficiencies obtained when attempting to tag top-jets originating from either heavy gluon or heavy photon decays, i.e. $\frac{\epsilon_2^{\text{gluon}} - \epsilon_2^{\text{photon}}}{\epsilon_2^{\text{gluon}}}$, as a function of two parameters for each algorithm. Large differences can be seen between the double-tagging efficiencies, depending on the algorithm and corresponding cut values, from 0 to 75 %. The largest differences between the double-tagging efficiencies are observed when the cut values used in the various algorithms are tightened, and the rate at which light quark and gluon jets are rejected is increased.

The differences can be explained by considering the amount of additional quark and gluon radiation produced in association with the heavy gluon and heavy photon. The study described in Sect. 6.1, as well as in other studies [7], have found that

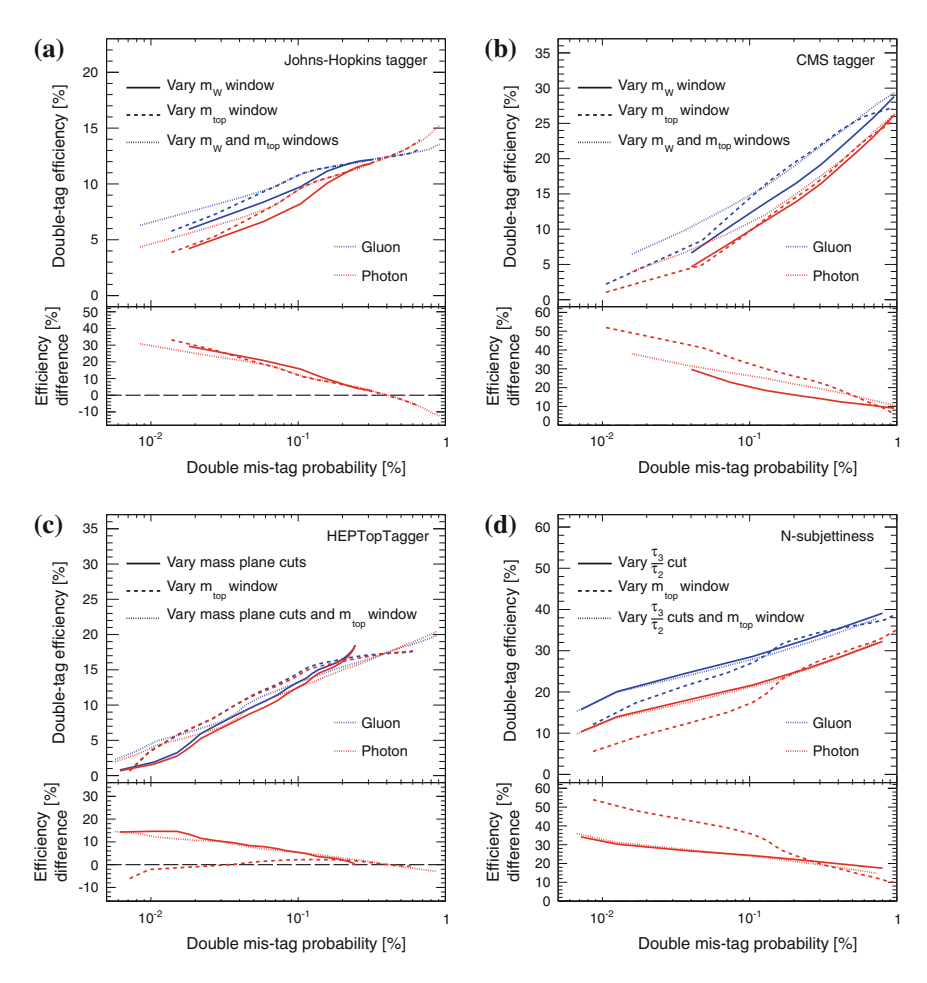


Fig. 6.14 The efficiency of correctly tagging both the leading and sub-leading jets from the decay of a heavy gluon (*blue*) and heavy photon (*red*) resonance, using **a** JOHNS-HOPKINS, **b** CMS, **c** HEPTOPTAGGER, **d** N-SUBJETTINESS algorithms. The efficiency is presented as a function of the mis-tag probability, which is the probability of incorrectly identifying two light quark or gluon jets as originating from the decay of a boosted top quark. The efficiency and mis-tag probabilities are estimated by varying the cuts on the algorithm parameters. The ratio panel shows the relative signal efficiency difference, ($\epsilon_2^{\text{gluon}}/\epsilon_2^{\text{photon}}-1$) as a function of the mis-tag probability for each algorithm and parameter variation

more radiation is produced in events containing a heavy colour singlet *s*-channel resonance. This additional radiation can contaminate the fat jets used as input to the top tagging algorithms, and can spoil the algorithms' attempts to identify the relevant subjet structure. The differences in tagging efficiencies can be minimised by carefully choosing the algorithm parameters. The choices, however, tend to correspond to very loose cuts and would therefore result in a background rejection rate that would not be optimal for use in an experimental analysis.

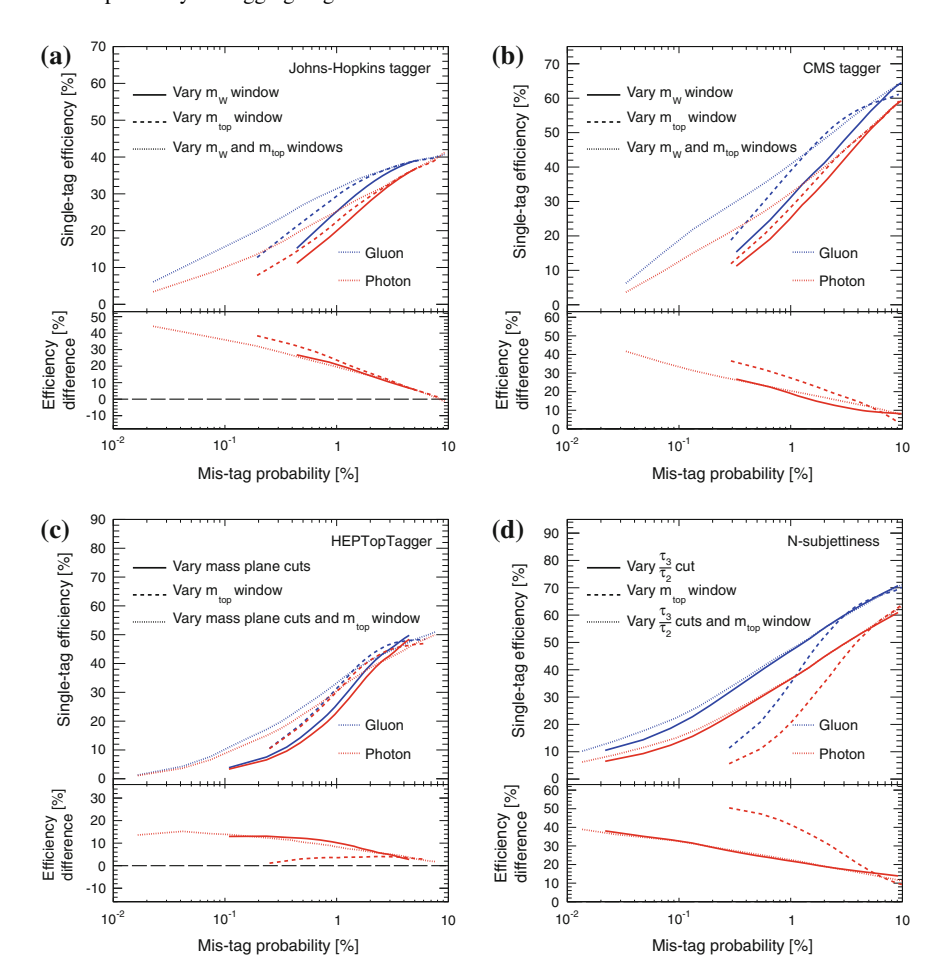


Fig. 6.15 The efficiency of correctly tagging only the leading jet from the decay of a heavy gluon (*blue*) and heavy photon (*red*) resonance, using **a** JOHNS-HOPKINS, **b** CMS, **c** HEPTOPTAGGER, **d** N-SUBJETTINESS algorithms. The efficiency is presented as a function of the mis-tag probability, which is the probability of incorrectly identifying two light quark or gluon jets as originating from the decay of a boosted top quark. The efficiency and mis-tag probabilities are estimated by varying the cuts on the algorithm parameters. The ratio panel shows the relative signal efficiency difference, $(\epsilon_1^{\text{gluon}}/\epsilon_1^{\text{photon}}-1)$, as a function of the mis-tag probability for each algorithm and parameter variation

It is typical for the performance of tagging algorithms to be evaluated at common working points at which the background rejection rates, for example, are equal. Plots showing the signal tagging efficiency vs. the background mis-tagging probability can be created by taking slices across the two-dimensional signal and background tagging efficiency distributions. Three different slices were used for each algorithm. Two correspond to horizontal or vertical slices through the distributions, where each of

the cuts are varied separately. The third slice was diagonally through the distribution and corresponds to varying both cuts simultaneously.

Specifically, for the JOHNS-HOPKINS and CMS algorithms, efficiency vs. mis-tag curves were constructed by (i) varying only the size of top mass window and keeping the W-mass windows fixed at $m_W \pm 30$ GeV, (ii) varying only the W-mass window and keeping the top-mass window fixed at $m_t \pm 50$ GeV or (c) varying both the top and W mass windows simultaneously such that the size of the W mass window is approximately 80% of the size of the top mass window For the HEPTOPTAGGER and N-SUBJETTINESS algorithms the m_W/m_t window or τ_3/τ_2 cuts are varied, rather than the W mass window. All other algorithm parameters are kept fixed at the default values discussed in Sect. 6.2.2.

In Fig. 6.14 the double-tagging efficiencies for each algorithm are shown as a function of the corresponding mis-tag probability. The JOHNS-HOPKINS (Fig. 6.14a) algorithm does not show a strong dependence on the choice of the parameter varied; when the mis-tag probability is required to be low, the efficiency difference is large regardless of the parameter that is subject to the tighter cuts. In contrast, the CMS and N-SUBJETTINESS algorithms exhibit largest efficiency differences when varying only the size of the top mass window, while the HEPTOPTAGGER algorithm shows very little sensitivity to the top mass window and significant sensitivity to the value of the mass plane cut.

A priority in experimental analyses is often to reduce background rates as much as is feasible. Therefore it is expected that top tagging algorithms such as these would be used at working points with low QCD background mis-tag probabilities. However, it is when tight cuts are applied to reduce the mis-tag probabilities that the efficiency differences between tagging the top jets arising from the differently coloured resonances is largest. Efficiency differences of over 50 % can be seen depending on the algorithm and cut values being used.

Efficiency differences of similar sizes are found when tagging only the leading jet in the events, as shown in Fig. 6.15. This implies that an analysis involving $t\bar{t}$ decaying in the lepton+jets channel would also suffer from similar problems. It also suggests that using a combination of tight and loose cuts on the leading and sub-leading jets in all-hadronic $t\bar{t}$ events would not yield significant improvements.

The radius parameter used to define the initial C-A jets is very important in any subjet analysis. Figure 6.16 shows how the double-tagging efficiency difference depends on the size of the C-A jets used as input to the top-tagging algorithms. The tagging efficiency is shown for values of R of 0.6, 0.8, 1.0, and 1.2, at three efficiency working points defined by the background mis-tag probabilities of 1, 0.1, 0.01%. The algorithm parameters that are used to obtain these mis-tag probabilities are shown in Table 6.2. The first point to notice is that for most of the tagging algorithms the double tagging efficiency decreases as the radius of the C-A jets is increased. Naïvely it would be expected that increasing the size of the original C-A jet would allow more of the top decay products to be included within it, and therefore improve the tagging efficiency. However, in the model considered here the top quarks are produced sufficiently boosted that their decay products typically fall within a C-A jet of radius 0.8. Increasing the size of the jets past this only allows additional soft

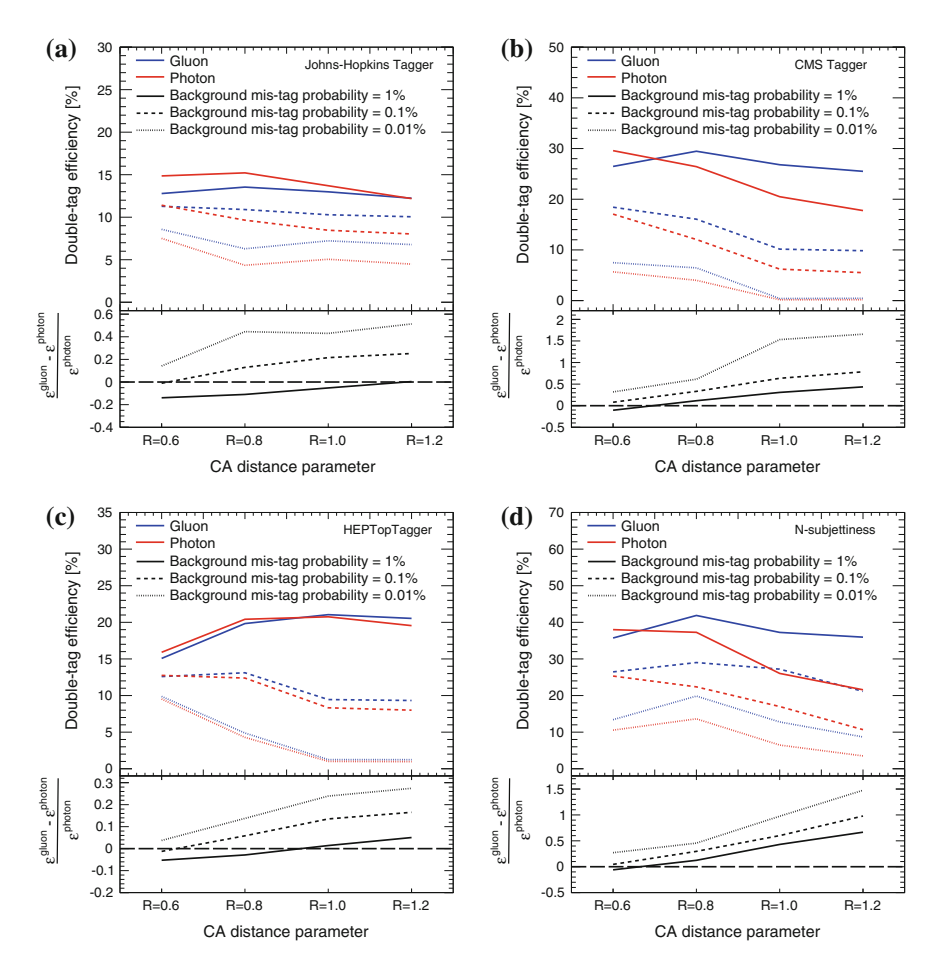


Fig. 6.16 The efficiency of correctly tagging both the leading and sub-leading jets from the decay of a heavy gluon (*blue*) and heavy photon (*red*) resonance, using **a** JOHNS-HOPKINS, **b** CMS, **c** HEPTOPTAGGER, **d** N-SUBJETTINESS algorithms. The efficiency is presented as a function of the C-A radius parameter used to reconstruct the jets. The efficiency and mis-tag probabilities are estimated by varying the cuts on the algorithm parameters. The ratio panel shows the relative signal efficiency difference, $(\epsilon_2^{\text{gluon}}/\epsilon_2^{\text{photon}}-1)$, as a function of the mis-tag probability for each algorithm and parameter variation

radiation to fall into the jet and therefore worsens the performance of the tagging algorithms.

It has previously been suggested that the jet size should be optimised as a function of the top quark transverse momentum [35]. The results of the study presented here suggest that the jets used as input to top-tagging algorithms should be defined with as small a value of R as possible. The effect of the event colour structure, and the

4
6.
Fig.
₽.
shown
d mis-tag rates
Ē.
ckground
þa
the
obtain 1
0
tagger t
each
by
required by
values
Cnt
4
9 a
Table 6.2

JOHNS-HOPKINS Tagger	R = 0.6			R = 0.8			R = 1.0			R = 1.2	.2	
Mis-tag rate (%)	1	0.1	0.01		0.1	0.01		0.1	0.01		0.1	0.01
$m_t \pm X (\text{GeV})$	97.0	41.0	21.0	97.0	33.0	15.0	97.0	37.0	17.0	97.0	39.0	19.0
$m_W \pm Y \text{ (GeV)}$	9.77	32.8	16.8	77.6	26.4	12.0	9.77	29.6	13.6	77.6	31.2	15.2
CMS Tagger	R = 0.6			R = 0.8			R = 1.0			R = 1	1.2	
Mis-tag rate (%)		0.1	0.01		0.1	0.01		0.1	0.01		0.1	0.01
$m_t \pm X \text{ (GeV)}$	85.0	37.0	17.0	47.0	21.0	0.6	39.0	17.0	5.0	39.0	15.0	5.0
$m_W \pm Y (\text{GeV})$	0.89	29.6	13.6	37.6	16.8	7.2	31.2	13.6	4.0	31.2	12.0	4.0
HEPTOPTAGGER	R = 0.6			R = 0.8			R = 1.0			R = 1	1.2	
Mis-tag rate (%)		0.1	0.01		0.1	0.01		0.1	0.01		0.1	0.01
$m_t \pm X \text{ (GeV)}$	97.0	71.0	51.0	97.0	51.0	25.0	95.0	35.0	11.0	91.0	37.0	13.0
$(1 \pm Y) * m_W/m_t$	0.19	0.14	0.10	0.19	0.10	0.05	0.19	0.07	0.02	0.18	0.07	0.03
N-SUBJETTINESS	R = 0.6			R = 0.8			R = 1.0			R = 1	1.2	
Mis-tag rate (%)		0.1	0.01		0.1	0.01		0.1	0.01		0.1	0.01
$m_t \pm X \text{ (GeV)}$	0.69	59.0	43.0	65.0	55.0	45.0	65.0	55.0	41.0	65.0	55.0	43.0
$\tau_3/\tau_2 < Y$	69.0	0.59	0.43	0.65	0.55	0.45	0.65	0.55	0.41	0.65	0.55	0.43

associated quark and gluon radiation which can reduce the performance of the toptagging algorithms, would then be kept to a minimum.

6.2.5 Impact on Experimental Analyses

The observation that the colour structure of an event can have an impact on the ability of top-tagging algorithms to tag candidate top jets has important consequences for experimental analysis, particularly those performing searches for signatures of new physics.

The various issues can be illustrated by examining a CMS analysis [36] in which limits were placed on the cross section \times branching ratio for the production of a colour singlet heavy Z' resonance and a Randall-Sundrum Kaluza-Klein gluon.

The CMS algorithm was used, with parameters as in this study, to tag candiate top jets with R=0.8 and $p_T>500$ GeV. The efficiency for tagging a single top-jet was found to be 50 %, at a working point with a background mis-tag probability of 5 %. A systematic uncertainty on the tagging efficiency was estimated by selecting a sample of standard model $t\bar{t}$ events and comparing the efficiency for tagging W-jets in data and MC. The uncertainty was estimated to be around 3 %. The same technique was also used to define an overall scale factor of 0.97, which was then applied to the signal and background MC events to ensure that the nominal values of the tagging efficiency were the same in MC and data.

The potential problem with this method is that the events used to determine the uncertainty and scale factors can exhibit very different colour flow to the signal events. It has been show in the studies presented here that there are clear differences in the efficiency of tagging top-jets, depending on the colour structure of the event. This is illustrated further in Fig. 6.17, which shows a comparison of the double tagging efficiencies obtained for standard model tt events and tt produced in the decay of the heavy gluon or photon. The efficiency difference for the CMS tagger (Fig. 6.17a) at the working point used in the CMS analysis—5% background mis-tag probability when tagging a single jet corresponds to 0.25% when tagging both jets—is around 20% (30%) for the heavy photon (gluon). Therefore applying results derived in some control region to events in a signal region would require a high degree of confidence in the description of the sets of events produced by the MC generator.

In the case of the CMS analysis it is not immediately clear how the potential mis-estimation of the uncertainty and scale factors would affect the observed limit. Typically it is the uncertainty associated with the background estimation that drives the strength of the limit, however, and the application of the derived scale factors to the standard model $t\bar{t}$ background is not unreasonable, since the colour structure of the two sets of events is similar.

It should be noted again that it is possible to reduce the difference in tagging efficiencies by optimising the choice of tagging algorithm and parameters. For example Fig. 6.17b shows that the HEPTOPTAGGER algorithm has much smaller tagging efficiency differences between the signal and control regions.

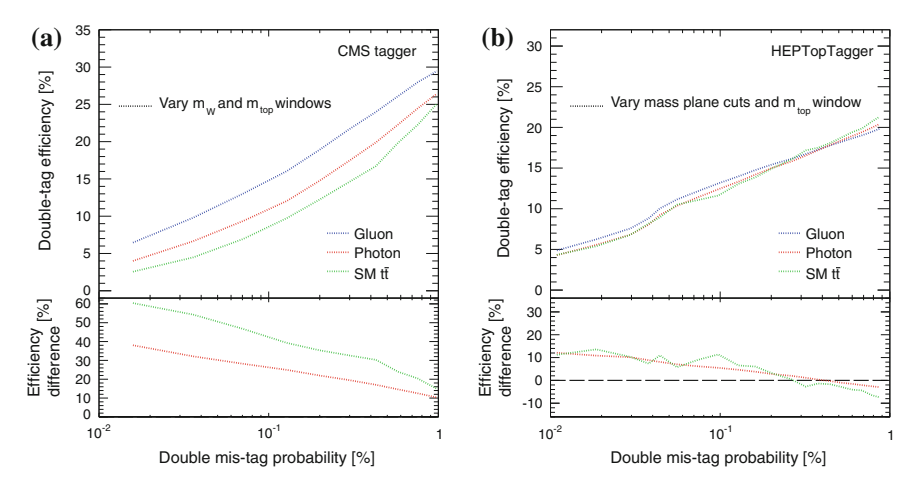


Fig. 6.17 Double-tagging efficiencies and efficiency difference for KK-gluon, KK-photon and SM $t\bar{t}$ events, using the CMS tagger and HEPTOPTAGGER

In an experimental analysis which observed a new heavy particle, identifying the colour of the new resonance using the technique described in Sect. 6.1, or others in the literature [7, 37–40], would be mandatory in order to reduce systematic uncertainties related to the tagging efficiency.

References

- Seymour, M. H. (1994). Searches for new particles using cone and cluster jet algorithms: a comparative study. Z Physics, C62, 127–138
- Butterworth, J. M., Cox, B. E. & Forshaw, J. R. (2002). WW scattering at the CERN LHC. Physical Review D, 65(9), 096014
- Butterworth, J., Ellis, J. R., & Raklev, A. (2007). Reconstructing sparticle mass spectra using hadronic decays. JHEP, 0705, 033.
- Butterworth, J. M., Davison, A. R., Rubin, M., & Salam, G. P. (2008). Jet substructure as a new Higgs search channel at the LHC. *Physical Review Letter*, 100, 242001.
- Ask, S., Collins, J., Forshaw, J. R., Joshi, K., & Pilkington, A. D. (2012). Identifying the colour of TeV-scale resonances. *JHEP*, 1201, 018.
- Joshi, K., Pilkington, A. D., & Spannowsky, M. (2012). The dependency of boosted tagging algorithms on the event colour structure. *Physical Review D*, 86, 114016.
- Sung, I. (2009). Probing the gauge content of heavy resonances with soft radiation. *Physical Review D*, 80, 094020.
- 8. Gallicchio, J., & Schwartz, M. D. (2010). Seeing in color: jet superstructure. *Physical Review Letter*, 105, 022001.
- 9. Han, T., Lewis, I., & Liu, Z. (2010). Colored resonant signals at the LHC: largest rate and simplest topology. *JHEP*, 1012, 085.
- 10. Englert, C., Plehn, T., Schichtel, P., & Schumann, S. (2011). Jets plus missing energy with an autofocus. *Physical Review D*, 83, 095009.

References 127

11. Cox, B. E., Forshaw, J. R., & Pilkington, A. D. (2011). Extracting Higgs boson couplings using a jet veto. *Physics Letter B*, 696, 87–91.

- 12. Randall, L., & Sundrum, R. (1999). A Large mass hierarchy from a small extra dimension. *Physical Review Letter*, 83, 3370–3373.
- Lillie, B., Randall, L., & Wang, L.-T. (2007). The Bulk RS KK-gluon at the LHC. JHEP, 0709, 074.
- Agashe, K., Belyaev, A., Krupovnickas, T., Perez, G., & Virzi, J. (2008). LHC signals from warped extra dimensions. *Physical Review D*, 77, 015003.
- Grossman, Y., & Neubert, M. (2000). Neutrino masses and mixings in nonfactorizable geometry. *Physics Letter B*, 474, 361–371.
- 16. Gherghetta, T., & Pomarol, A. (2000). Bulk fields and supersymmetry in a slice of AdS. *Nuclear Physics B*, 586, 141–162.
- Huber, S. J., & Shafi, Q. (2001). Fermion masses, mixings and proton decay in a Randall-Sundrum model. *Physics Letter B*, 498, 256–262.
- Agashe, K., & Servant, G. (2004). Warped unification, proton stability and dark matter. *Physical Review Letter*, 93, 231805.
- 19. Agashe, K., & Servant, G. (2005). Baryon number in warped GUTs: model building and (dark matter related) phenomenology. *JCAP*, 0502, 002.
- 20. Aaltonen, T., et al. (2008). Forward-backward asymmetry in top quark production in $p\bar{p}$ collisions at sqrts = 1.96 TeV. *Physical Review Letter*, 101, 202001.
- 21. Abazov, V., et al. (2008). First measurement of the forward-backward charge asymmetry in top quark pair production. *Physical Review Letter*, 100, 142002.
- 22. Abazov, V. M., et al. (2011). Forward-backward asymmetry in top quark-antiquark production. *Physics Review D*, 84, 112005.
- 23. Bai, Y., Hewett, J. L., Kaplan, J., & Rizzo, T. G. (2011). LHC predictions from a tevatron anomaly in the top quark forward-backward asymmetry. *JHEP*, 1103, 003.
- 24. Lai, H., et al. (2000). Global QCD analysis of parton structure of the nucleon: CTEQ5 parton distributions. *The European Physical Journal C*, 12, 375–392.
- Sjostrand, T., Mrenna, S., & Skands, P. Z. (2008). A brief introduction to PYTHIA 8.1. Computer Physics Communications, 178, 852–867.
- 26. Cacciari, M. & Salam, G. P. (2006). Dispelling the N³ myth for the kt jet-finder. *Physics Letter*, *B641*, 57–61. arXiv:hep-ph/0512210. ISSN 0370-2693
- Kaplan, D. E., Rehermann, K., Schwartz, M. D., & Tweedie, B. (2008). Top tagging: a method for identifying boosted hadronically decaying top quarks. *Physical Review Letter*, 101, 142001.
- 28. ATLAS Collaboration. (2011). Measurement of dijet production with a veto on additional central jet activity in pp collisions at $\sqrt{s} = 7$ TeV using the ATLAS detector. *JHEP*, 1109, 053
- 29. Duran Delgado, R. M., Forshaw, J. R., Marzani, S. & Seymour, M. H. (2011). The dijet cross section with a jet veto. *JHEP*, 1108, 157
- 30. (2009). A Cambridge-Aachen (C-A) based Jet Algorithm for boosted top-jet tagging tech. rep. CMS-PAS-JME-09-001. Geneva: CERN
- 31. Plehn, T., Salam, G. P., & Spannowsky, M. (2010). Fat jets for a light Higgs. *Physical Review Letter*, 104, 111801.
- 32. Thaler, J., & Van Tilburg, K. (2011). Identifying boosted objects with N-subjettiness. *JHEP*, 1103, 015.
- 33. Plehn, T., Spannowsky, M., Takeuchi, M., & Zerwas, D. (2010). Stop reconstruction with tagged tops. *JHEP*, *1010*, 078.
- 34. Stewart, I. W., Tackmann, F. J. & Waalewijn, W. J. N. (2010). Jettiness: an inclusive event shape to veto jets. *Physical Review Letter105*(9), 092002
- 35. Krohn, D., Thaler, J., & Wang, L.-T. (2009). Jets with variable R. JHEP, 0906, 059.
- 36. Chatrchyan, S., et al. (2012). Search for anomalous t t-bar production in the highly-boosted all-hadronic final state. *JHEP*, *1209*, 029.
- 37. Soper, D. E., & Spannowsky, M. (2010). Combining subjet algorithms to enhance ZH detection at the LHC. *JHEP*, 1008, 029.

- 38. Hook, A., Jankowiak, M., & Wacker, J. G. (2012). Jet dipolarity: top tagging with color flow. *JHEP*, 1204, 007.
- 39. Gallicchio, J. & Schwartz, M. D. (2010). Seeing in color: jet superstructure. *Physical Review Letter*, 105(2), 022001
- 40. Abazov, V. M., et al. (2011). Measurement of color flow in $t\bar{t}$ events from $p\bar{p}$ collisions at $\sqrt{s} = 1.96$ TeV. *Physical Review*, D83, 092002.

Chapter 7 Measurements of Electroweak Z Boson + Dijet Production

7.1 Introduction

The production of dijets in association with a Z-boson (Z_{jj} production) is dominated by the Drell-Yan process, with the additional jets arising as a result of the strong interaction. The QCD production of Z_{jj} , an example of which is shown in Fig. 7.1a, is a typical process that can produce such events. Measurements of the properties of Z_{jj} events have been performed by ATLAS [1, 2] and CMS [3, 4] using pp collision data at $\sqrt{s}=7$ TeV. In certain regions of phase space significant deviations of the data from theoretical predictions were found, in particular when the two leading jets in the events were widely separated in rapidity or had a large dijet invariant mass. It is therefore important to produce detector-corrected measurements of these event topologies, to assist the theory community in understanding and constraining the uncertainties associated with modelling them.

The production of Z_{jj} by purely electroweak processes is a much rarer occurrence. Electroweak Z_{jj} production, with the Z-boson decaying leptonically, is defined as comprising all processes which contribute to the $\ell^+\ell^-$ jj final state and contain at least one t-channel exchange of an electroweak gauge boson [5, 6], and includes the vector boson fusion (VBF) production process, as shown in Fig. 7.1b. This process is of particular interest due to the similarity it has to the VBF production of the Higgs boson. The distributions and analysis techniques used to isolate and study VBF Z_{jj} production will therefore be of interest when studying the VBF production of a Higgs boson plus 2 jets. The large background of Z_{jj} produced via the strong interaction will also be an important background to Higgs plus 2 jet production, and so strong Z_{jj} production should be studied precisely in order to understand and potentially constrain the uncertainties associated with its QCD modelling. Measurements of vector boson fusion production of Z_{jj} also allow limits to be placed on anomalous triple gauge couplings (aTGCs) between Z-bosons and W-bosons.

 Z_{jj} events produced via electroweak processes can have quite distinctive topologies, which can be exploited to distinguish between the electroweak signal events and the large background of Z_{jj} events produced via the strong interaction. Using

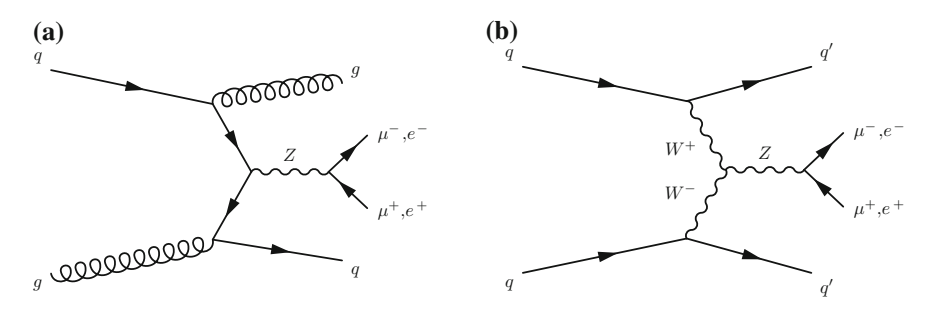


Fig. 7.1 Example leading-order Feynman diagrams for \mathbf{a} strong Z_{jj} production and \mathbf{b} production of Z_{ij} via vector boson fusion

the VBF diagram in Fig. 7.1b as an example, the two outgoing quarks which recoil against the W-bosons go on to form so-called tagging jets, that are typically produced widely separated in rapidity and with relatively large transverse momenta (the pair of jets will therefore typically also have a very large dijet invariant mass). There is also a lack of colour flow across the VBF diagram. Because the interaction proceeds via the exchange of only colourless electroweak bosons the two final-state tagging jets are not colour connected, and so it is expected that very little additional quark and gluon radiation will be produced in the rapidity interval bounded by the two tagging jets. Experimentally it is therefore likely that few jets will be detected in the this rapidity interval. Properties such as these can be used to define regions of phase space that have varying sensitivity to the electroweak component of the Z_{ij} cross section, as will be discussed in Sect. 7.5.1.

This chapter describes measurements of detector-corrected differential cross sections for the inclusive production of Z_{jj} in various phase space regions, and the extraction of the electroweak component of the production cross-section, using proton-proton collision data collected by ATLAS at $\sqrt{s}=8$ TeV. Work presented in this chapter has been published in [7].

7.2 Event and Object Reconstruction and Selection

Data used in this analysis were collected between April and December 2012 at a centre-of-mass energy of $\sqrt{s}=8$ TeV and correspond to an integrated luminosity of 20.3 fb⁻¹. Events in the muon channel are required to have passed either the isolated (cf. Chap. 4) single muon trigger EF_mu24i_tight or the non-isolated higher-p_T trigger EF_mu36_tight. Events containing a Z-candidate in the electron channel are required to have fired the dielectron trigger EF_2e12Tvh_lose1.

All events are required to have a reconstructed collision vertex, defined as a vertex with at least three inner detector tracks each with $p_T > 400$. The primary vertex is then defined as the collision vertex with the largest sum of the

squared transverse momenta of associated inner detector tracks. Events are also required to be collected during data-taking periods in which the ATLAS detector was fully operational, defined as those which make up the good runs list (cf. Sect. 2.2.4)

```
data12_8TeV.periodAllYear_DetStatus-v61-pro14-02_DQ Defects-00-01-00_PHYS_StandardGRL_All_Good.xml.
```

7.2.1 Muons

Muons produce hits in the inner detector and track segments in the muon spectrometer, and are reconstructed using the *STACO* algorithm (cf. Sect. 3.4). They are required to have $p_T > 25$ GeV and $|\eta| < 2.4$. The inner detector tracks associated with each muon must pass the quality requirements defined by the Muon Combined Performance group [8]:

- At least one pixel b-layer hit, except when the extrapolated muon track passes an un-instrumented or dead area of the b-layer.
- Number of pixel hits + number of crossed dead pixel sensors > 0.
- Number of SCT hits + number of crossed dead SCT sensors > 4.
- Number of pixel holes + number of SCT holes < 3.
- Impact parameter cuts: | trackz0pvunbiased × sin(tracktheta) | < 0.5 mm and | trackd0pvunbiased/tracksigd0pvunbiased | < 3.0
- If $0.1 < |\eta| < 1.9$, n > 5 and $n_{\text{TRT}}^{\text{outliers}} < 0.9n$, else if n > 5, require $n_{\text{TRT}}^{\text{outliers}} < 0.9n$. Where n is the sum of TRT hits and TRT outliers (cf. Sect. 5.3.1).

The muons must also be isolated, and are required to have $\sum p_T/p_T(\mu) < 0.1$, as defined in Sect. 4.3.

7.2.2 Electrons

Electron candidates must have a so-called author of 1 or 3 and must satisfy the Medium++ electron identification requirements. They must have $p_T > 25~\text{GeV}$ and $|\eta| < 2.47$, excluding the crack region between the barrel and end-cap calorimeters at $1.37 < |\eta| < 1.52$. As with the muon candidates, electrons must pass the following impact parameter cuts: $|\texttt{trackz0pvunbiased} \times \texttt{sin(tracktheta)}| < 0.5~\text{mm}$ and |trackd0pvunbiased/tracksigd0pvunbiased| < 6.0.

7.2.3 Jets

The anti- k_t algorithm with radius parameter R = 0.4 is used to define candidate jets in the events. The inputs to the algoritm are EM-scale topological clusters

of calorimeter cells. The energies of the resulting jets are subsequently corrected using the standard EMJES calibration procedure (cf. Sect. 3.5). Candidate jets are required to have $p_T > 25$ GeV and |y| < 4.4, and must be well-seperated from any of the selected leptons—jets with ΔR (jet, lepton) < 0.3 are removed from the analysis.

To remove pile-up jets originating from different pp collisions in the same bunch crossing, a jet vertex fraction (cf. Sect. 5.3.3) cut of |JVF| > 0.5 is imposed for all jets with $|\eta| < 2.4$ and $p_T < 50$ GeV.

7.3 Theoretical Predictions

Theoretical predictions for strong and electroweak Z_{jj} production were produced using the SHERPA [9] and POWHEG [10–12] MC generators.

SHERPA v1.4.3 was used to produce strong Z + n parton predictions (n = 0, 1, 2, 3, 4) at leading order in QCD. Electroweak Z + n parton predictions are also produced at leading order in QCD, with n = 2, 3.

Events contributing to the $\ell^+\ell^-$ jj final state from diboson-initiated processes such as the example given in Fig. 7.2c are generated separately using SHERPA, with up to three additional partons in the final state. Once the matrix element calculations were complete, the SHERPA built-in parton shower algorithm, hadronisation and MPI models were used to turn the parton-level final states into particle-level events which can be compared to experimental data. The CKKW [13] matching algorithm was used to match the matrix elements to the parton shower and avoid double counting.

POWHEG produces both strong [14] and electroweak [15] Z_{jj} predictions at next-to-leading order in QCD. PYTHIA6 is then used to provide parton showering, hadronisation and MPI. Strong Z_{jj} events are produced using the Multi-scale improved NLO (Minlo) [16] procedure which reduces instabilities in events with disparate scales. Z-boson plus zero and one jet events are also included using Minlo, allowing contributions to the Z_{ij} final state from MPI to be evaluated.

Theoretical scale uncertainties in the strong and electroweak predictions from SHERPA and POWHEG are estimated by varying the renormalisation and factorisation scales (separately) by a factor of 0.5 and 2.0. Additional uncertainties in the SHERPA predictions are estimated by varying the CKKW matching parameter, changing the parton shower scheme used—from the default [17] to that proposed in [18]—and varying parameters which control the amount of MPI. This potential mismodelling of the underlying event is evaluated by varying parameters in such a way that the overall amount of MPI activity is increased uniformly by 10 % [19], or by changing the shape of the MPI spectrum to force more jets from double parton scattering to be produced. The parameter variations used for the latter are SIGMA_ND_FACTOR=0.14 and SCALE_MIN=4.0. A similar set of uncertainties on the POWHEG predictions are estimated by using the Perugia 2011 [20] tunes.

7.3.1 Electroweak Signal Composition

As well as the VBF diagram shown in Fig. 7.1b, Z-boson bremsstrahlung and non-resonant $\ell^+\ell^-$ jj diagrams, examples of which are shown in Fig. 7.2a, b, also contribute to the electroweak signal. To investigate the contribution of each of the types of process to the full electroweak cross section, the SHERPA MC generator was privately modified, with help from the SHERPA authors, to set various Z-boson couplings to zero—effectively removing specific sets of Feynman diagrams. For example, the Z_{qq} coupling could be set to zero to remove the contribution from Z-boson bremsstrahlung. The following results are meant as a guide, to give a rough estimate of the size of the individual contributions and the interference between them, and should *not* be used for quantitative purposes. All diagrams must be considered when calculating a cross section in order to preserve gauge invariance.

Table 7.1 shows the fiducial cross section in the *baseline* region of phase space, defined in Sect. 7.5.1, for the full electroweak calculation and for each of the subsets of processes—VBF-only, Z-boson bremsstrahlung-only and non-resonant-only. The contribution from non-resonant production is less than 1%. The VBF- and Z-boson bremsstrahlung-only cross sections however are each a factor of four larger than the full electroweak cross section. This implies that the interference between the two is large and it is not possible to separate the two sets of processes, nor answer questions about whether specific regions of phase space are more VBF-like or more Z-boson bremsstrahlung-like.

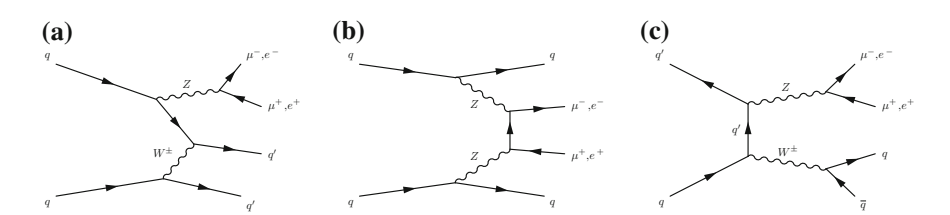


Fig. 7.2 Example Feynman diagrams for a Z-boson bremsstrahlung, b non-resonant $\ell^+\ell^-$ jj production and c diboson-initiated Z_{ij} production

Table 7.1 Cross sections calculated by SHERPA for the electroweak production of Z_{jj} after turning off specific Feynman vertices

Channel	$\sigma_{\rm baseline}$ (fb)
Full EWK	84.93
Non-resonant	0.40
VBF	333.08
Z-bremsstrahlung	329.65
VBF/EWK	3.9
Z-bremsstrahlung/EWK	3.9

 $\sigma_{baseline}$ refers to the cross section in the *baseline* region of phase space, defined in Sect. 7.5.1

7.4 Monte Carlo Simulation

Particle-level MC samples were passed through a GEANT4 [21, 22] simulation of the ATLAS detector. These reconstructed-level events can then be processed using the same analysis code as the data. Pile-up interactions were included using the same method as in Sect. 5.2; nominal reconstructed-level MC samples were overlaid with additional minimum bias event generated using PYTHIA8 with tune A2 [23] and the MSTW2008L0 [24] PDF set. The events were then reweighted such that the average number of interactions per proton-proton bunch crossing in the simulation match that in the observed data. As in Sect. 5.5, additional weights are applied to the simulated events in order to correct for data-MC discrepancies in the average number of interactions per bunch crossing ($\langle\mu\rangle$), triggering efficiencies, lepton reconstruction and identification efficiencies, and lepton energy and momentum resolutions. In the latter case the energy of electrons and momentum of muons is smeared and scaled such that the lepton energy scale and momentum resolution matched that measured in data.

Reconstructed-level strong and electroweak samples are produced using the particle-level SHERPA samples described in Sect. 7.3 and are normalised to reproduce the NLO Z_{jj} cross sections calculated by POWHEG. The NLO k-factors are 1.23 and 1.02 for the strong and electroweak samples, respectively. As a cross-check of the theoretical modelling of strong Z_{jj} production a small sample of events were generated using ALPGEN v2. 14 [25] interfaced to HERWIG and JIMMY (tune AUET2 [26]). ALPGEN matrix elements that included a Z-boson and up to five additional partons in the final state were calculated.

Background events arising from $t\bar{t}$ and single-top events were generated using MC@NLO v4.03 [27] interfaced to HERWIG and JIMMY to provide parton showering, hadronisation and MPI (tune AUET2). The $t\bar{t}$ sample was normalised to the next-to-next-to leading order (in QCD) cross section calculation, including next-to-next-to leading logarithmic soft gluon terms [28]. Background contributions from WW and W + jets events were generated using SHERPA.

7.4.1 Combination of QCD Z Samples

In addition to the nominal sample of QCD Z + jets events produced centrally by ATLAS, a sample of events was produced in which a particle-level filter was used to preferentially retain a higher proportion of events with very large dijet invariant mass than would normally be achieved. This was necessary in order to obtain sufficient statistical precision in the tails of the distributions. The filter selects and retains a fraction (f) of all events types (0-jets, 1-jet, 2+jets), while modifying the event weights by (1/f) to ensure that the original distributions can be recovered. The fraction for 0-jet and 1-jet events was set to be 1/5000 and 1/1000 respectively. The fraction for low-mass (high-mass) 2-jet events was set to 1/200 (1/1). The event

fraction for $200 \,\text{GeV} < m_{\rm jj} < 800 \,\text{GeV}$ was obtained by a power-law interpolation between the low-mass and high-mass regions. A fraction of all of the events is retained to ensure that the shape of the dijet invariant mass distribution can be correctly reproduced.

The nominal Z + jets sample contains a large number of events with low dijet invariant mass. Therefore in order to provide the best possible statistical coverage in all regions of phase space the samples were combined. Two methods were used to combined the samples of events:

- Exclusive sum: In each channel, events from the non-filtered sample are only used if they do not contain at least two particle-level jets with $p_T > 15$ GeV. Events from the filtered sample are only used if they do contain at least two particle-level jets with $p_T > 15$ GeV. In this way the two samples of events are made mutually exclusive, and the events can simply be added together.
- Weighted average: In each channel, both samples are used to independently to create distributions of interested. A given distribution, g(x), is constructed by combining the two independent distributions using a weighted average. Specifically, each bin i of the distribution is given by:

$$g_i = \frac{w_a a_i + w_b b_i}{w_a + w_b}$$

where a_i and b_i label the bin values in each of the two distributions, and the weights w_x are inversely proportional to the statistical uncertainty in each bin $w_x = 1/\sigma_{x_i}^2$.

Both methods of combining the events produce distributions that are consistent within their statistical uncertainties, as shown in the example distributions in Fig. 7.3. Since

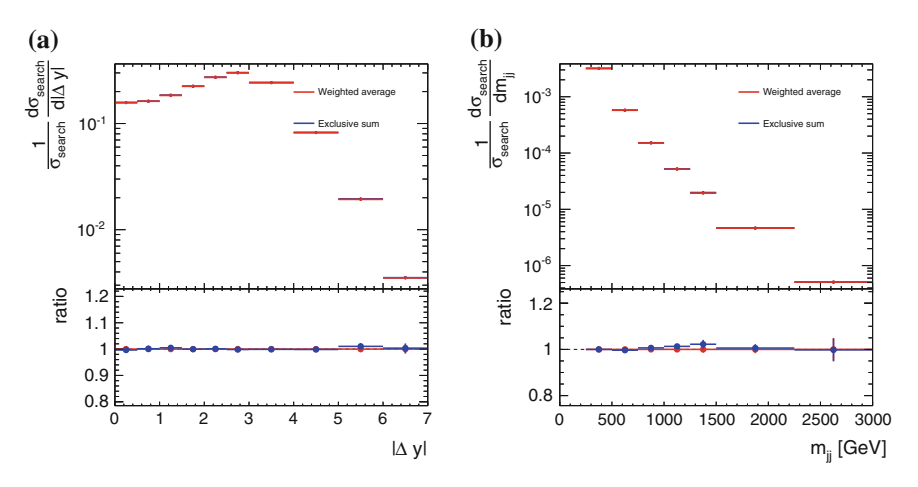


Fig. 7.3 Comparisons of the **a** differential cross section as a function of $|\Delta y|$ and **b** differential cross section as a function of m_{jj} obtained from MC samples combined using the weighted average (red) and exclusive sum (blue) techniques

the samples combined using a weighted average are slightly more statistically powerful, these samples are used when constructing distributions at both particle and detector-level which are compared to the data. They are also used in the fitting procedure used to extract the electroweak component of the Z_{jj} cross section, described in Sect. 7.6. However due to technical limitations of the unfolding software, the samples combined using a weighted average cannot be used and the exclusive summed samples are used instead.

7.5 Differential Cross Section Measurements

7.5.1 Phase Space Definitions

The measurements of the differential cross sections are performed in five regions of phase space with varying sensitivity to the strong and electroweak components of Z_{jj} production. A summary of the cuts used to define each of the fiducial regions is shown in Table 7.2.

The *baseline* region was defined to be the most inclusive, and had least sensitivity to electroweak Z_{jj} production. Comparisons between data and theory in this region of phase space provide important information about the QCD description of strong Z_{jj} production, and can be used to probe and constrain theoretical uncertainties associated with these event topologies. Events entering the *baseline* region must have an $\ell^+\ell^-$ pair with an invariant mass of 81 GeV $\leq m_{\ell\ell} < 101$ GeV which can be considered a Z-boson candidate, and two jets that are well-separated from leptons, with |y| < 4.4 and $p_T^{j_1} > 55$ GeV and $p_T^{j_2} > 45$ GeV. The remaining phase space regions are subsets of the *baseline* region. In the *high*-p_T region the jet p_T cuts are

Table 7.2 From [7], summary of the selection criteria that define the fiducial regions					
Object	Baseline	Highmass	Search	Control	High-p _T
Leptons	$ \eta^{\ell} < 2.47, p_{\mathrm{T}}^{\ell} > 25 \mathrm{GeV}$				
Dilepton pair	$81 \le m_{\ell\ell} \le 101 \text{GeV}$				
	_		$p_T^{\ell\ell} > 20 \text{ GeV}$		_
Jets	$ y^j < 4.4, \Delta R_{j,\ell} \geq 0.3$				
	$p_{T}^{j1} > 55 \text{GeV}$ $p_{T}^{j2} > 45 \text{GeV}$ $p_{T}^{j2} > 75 \text{GeV}$				$p_{\rm T}^{j1} > 85~{\rm GeV}$
					$p_{\rm T}^{j2} > 75 \mathrm{GeV}$
Dijet system	_	$m_{\rm jj} > 1{\rm TeV}$	$m_{\rm jj} > 250{\rm GeV}$	<i>I</i>	_
Interval jets	_		$N_{\rm jet} = 0$	$N_{\rm jet} \geq 1$	_
Z _{jj} system	_		p _T balance	p _T balance,3	_
			< 0.15	< 0.15	

Table 7.2 From [7], summary of the selection criteria that define the fiducial regions

^{&#}x27;Interval jets' refer to the selection criteria applied to the jets that lie in the rapidity interval bounded by the dijet system

increased to $p_T^{j_1} > 85~\text{GeV}$ and $p_T^{j_2} > 75~\text{GeV}$. This region is designed to exploit the harder jet p_T spectrum resulting from the electroweak production of Z_{jj} . Events in the *high-mass* region are the subset of those in the *baseline* region in which the invariant mass of the leading two jets is larger than 1 TeV.

The *search* region is designed to further enhance the electroweak component. The cuts defining the *search* region were optimised to maximise the expected significance of the electroweak signal when extracting the electroweak component of the Z_{jj} cross section. Events that enter the *search* region are the subset of those that enter the *baseline* region which also fulfil the following requirements.

- The invariant mass of the two leading jets must satisfy $m_{ii} > 250$ GeV.
- The normalised transverse momentum balance, ¹ p_T^{balance}, is required to be less than 0.15.
- The dilepton pair must have $p_T^{\ell\ell} > 20$ GeV.
- \bullet Events must have no additional jets with $p_T > 25$ GeV falling in the rapidity interval bounded by the two tagging jets.

The cut on the dijet invariant mass removes contributions from diboson-initiated Z_{jj} processes. The transverse momentum balance requirement removes events in which the jets were badly measured and enhances the contributions from VBF- Z_{jj} , where the lack additional radiation causes the Z-boson and dijet system to be very well balanced. Cutting on the dilepton transverse momentum removes events in which additional jets arise from pile-up, and requiring a jet veto also exploits the difference in colour flow between the electroweak signal and QCD background events.

In the *control* region the jet veto and $p_T^{balance}$ cuts are modified, compared to those in the search region, in order to reduce the contribution from electroweak Z_{jj} production and enhance the contribution from strong production. For events to enter into the control region they must satisfy the same selection criteria as those in the *search* region, except that they must contain *at least one* additional jet with $p_T > 25$ GeV falling into the rapidity interval bounded by the two leading jets, and the $p_T^{balance}$ variable is redefined to include the highest- p_T additional jet in the rapidity interval between the two leading jets. Events entering the *control* region are therefore orthogonal to those in the *search* region.

The fractions of electroweak Z_{jj} , QCD Z_{jj} and non- Z_{jj} background events (cf. Sect. 7.5.3) which compose the various fiducial regions are shown in Table 7.3. The contributions from $t\bar{t}$, WW, tW and W + jets events are estimated by applying the default analysis chain to dedicated samples of events generated as described in Sect. 7.4. The multijet background only contributes if two jets are misidentified as leptons and cannot be estimated using dedicated MC samples. Instead, a data-driven approach is taken and multijet-enhanced samples of data are obtained by selecting

$$p_{T}^{\text{balance}} = \frac{(p^{l_1} + p^{l_2} + p^{j_1} + p^{j_2})_{T}}{p_{T}^{l_1} + p_{T}^{l_2} + p_{T}^{j_1} + p_{T}^{j_2}}$$
(7.1)

where l_1 and l_2 label the two leptons which make up the Z-boson candidate.

¹ p_T^{balance} is defined as:

	Composition (%)				
Process	Baseline	High-p _T	Search	Control	High-mass
Strong Z _{jj}	95.8	94.0	94.7	96.0	85
Electroweak	1.1	2.1	4.0	1.4	12
$Z_{ m jj}$					
WZ and ZZ	1.0	1.3	0.7	1.4	1
tī	1.8	2.2	0.6	1.0	2
Single top	0.1	0.1	<0.1	<0.1	<0.1
Multijet	0.1	0.2	<0.1	0.2	<0.1
WW, W + jets	<0.1	<0.1	<0.1	<1.1	<0.1

Table 7.3 From [7], fractions of events (in %) that make up each fiducial region

events in which the leptons fail their isolation criteria. The contribution from multijet events is less than 0.5 % in all regions.

7.5.2 Distributions of Interest

The distributions measured are designed to be sensitive to various aspects of the Z_{ii} events. Those sensitive to the kinematics of the two leading jets in the event are:

- $\frac{1}{\sigma} \cdot \frac{d\sigma}{dm_{jj}}$: The normalised differential cross section as a function of the dijet invariant mass, m_{ii} .
- $\frac{1}{\sigma} \cdot \frac{d\sigma}{d|\Delta y|}$: The normalised differential cross section as a function of the rapidity difference between the two leading jets, $|\Delta y|$.

Distributions sensitive to the difference in colour flow between the strong and electroweak Z_{ii} production processes include:

- $\frac{1}{\sigma} \cdot \frac{d\sigma}{dN_{\text{ief}}}$: The normalised differential cross section as a function of the number of jets, N_{jet} , with $p_T > 25$ GeV in the rapidity interval between the two leading jets.
- $\frac{1}{\sigma} \cdot \frac{1}{dp_T^{balance}}$: The normalised differential cross section as a function of the p_Tbalancing variable.
- The fraction of events that do not contain any additional jets with $p_T > 25$ GeV in the rapidity interval bounded by the two leading jets—the jet veto efficiency—as a function of m_{ii} and $|\Delta y|$.
- The average number of jets with $p_T > 25$ GeV in the rapidity interval bounded by
- the two highest-p_T jets, $\langle N_{\rm jets} \rangle$, as a function of $m_{\rm jj}$ and $|\Delta y|$.

 The fraction of events with p_T^{balance} < 0.15—the p_T^{balance} cut efficiency—as a function of m_{ij} and $|\Delta y|$.

Finally, distributions sensitive to the azimuthal angle between the jets are:

- $\frac{1}{\sigma} \cdot \frac{d\sigma}{d|\Delta\phi(j,j)|}$: The normalised differential cross section as a function of the difference in azimuthal angle between the leading two jets, $\Delta\phi(j,j)$.
- The fraction of events with $\Delta \phi(j, j) > \pi/2$ —the $\Delta \phi(j, j)$ cut efficiency—as a function of m_{ij} and $|\Delta y|$.

7.5.3 Detector-Level Data and MC Comparisons

Figure 7.4 shows some examples of data compared to MC in the *baseline* region. The various MC predictions are summed according to their fiducial cross sections and normalised according to the integrated luminosity of the recorded dataset. The simulated events give a reasonably good description of the data. There is some degree of mismodelling in the tails of the m_{jj} and $|\Delta y|$ distributions which is consistent with what was observed in previous measurements of Z + jets.

7.5.4 Introduction to Bayesian Unfolding

As mentioned in Sect. 5.7 the goal of unfolding is to correct the measured data for effects arising from the finite efficiency and resolution of the detector. In this analysis an iterative Bayesian unfolding technique [29] was chosen to correct the data, the details of which will be given in what follows.

By treating each bin of a histogram as an element in a vector or matrix, we can write

$$\mathbf{A} \cdot \mathbf{x} = \mathbf{y} \tag{7.2}$$

where \mathbf{x} is the true distribution we are interested in, \mathbf{y} is the distribution we measure and \mathbf{A} is a matrix—often the "response", "smearing" or "transfer" matrix—which encodes information about the detector and transforms the distributions from true to measured.

After writing the problem as in Eq. (7.2), it is tempting to think that the solution is simply to invert the matrix **A** and apply it to our measured distribution **y**. However, it is argued by D'Agostini [30] that since the problem of unfolding is inherently a probabilistic one, we should use probabilistic methods to solve it.

The problem can be reformulated by writing the *probability* for finding an event in bin i of the true distribution, d'_i , as

$$d'_{i} = \sum_{j} P(T_{i}|M_{j}) d_{j} = \sum_{j} \theta_{ij} d_{j}$$
 (7.3)

where $P(T_i|M_j)$ is an element of the 'unfolding matrix' θ_{ij} and gives us the probability for finding an event in bin i of the true distribution, given that we measured one in bin j. d_j is the probability for finding an event in bin j of the measured distribution.

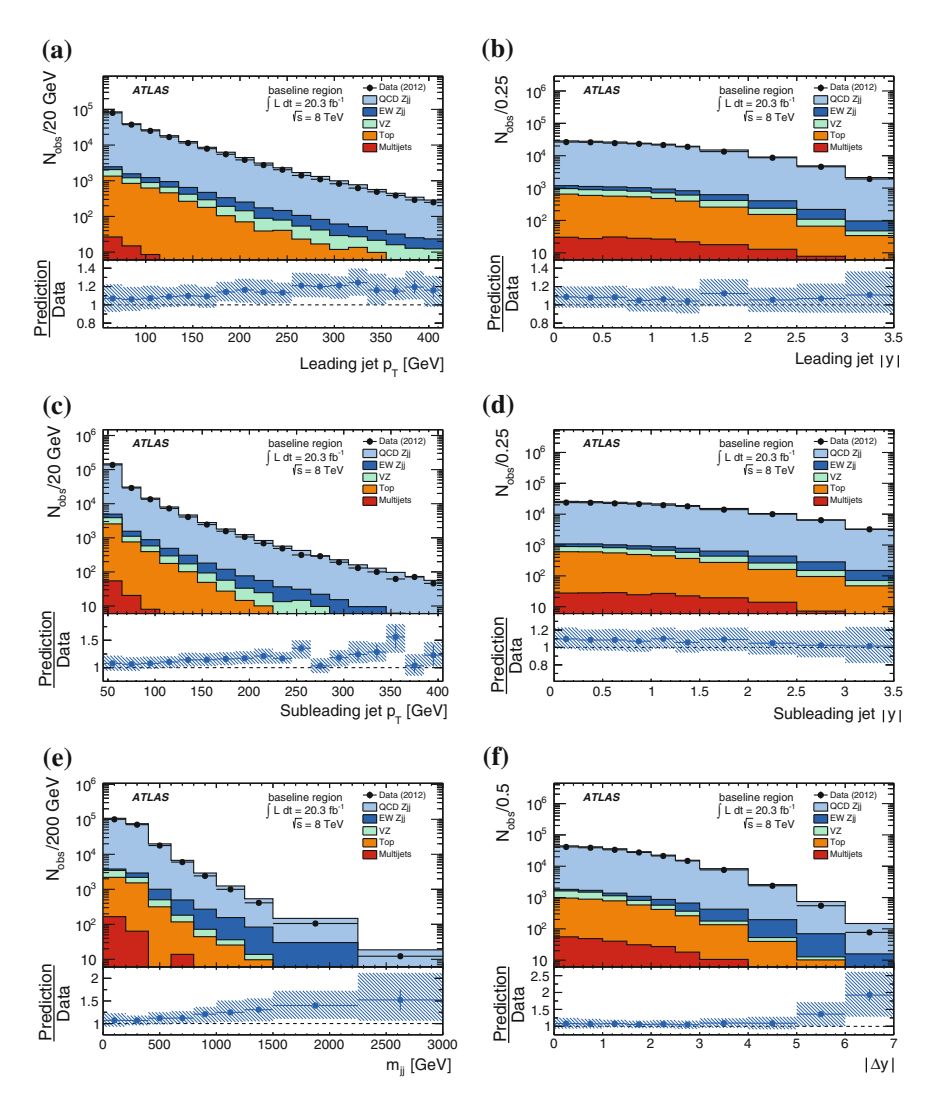


Fig. 7.4 Comparisons between data and MC for $\bf a$ the leading jet p_T , $\bf b$ the leading jet and rapidity, $\bf c$ the sub-leading jet p_T , $\bf d$ the sub-leading jet rapidity, $\bf e$ the dijet invariant mass and $\bf f$ the difference in rapidity between the two leading jets. The simulated samples are normalised to the cross sections described in Sect. 7.4

Using Bayes' theorem it is possible to rewrite the unfolding matrix as

$$\theta_{ij} = P(T_i | M_j) = \frac{P(M_j | T_i) \cdot P(T_i)}{\sum_i P(M_j | T_i) \cdot P(T_i)} = \frac{a_{ji} \cdot P(T_i)}{\sum_i a_{ji} \cdot P(T_i)},$$
(7.4)

where $P(M_j|T_i) = a_{ji}$ are elements of the response matrix introduced in Eq. (7.2), and $P(T_i)$ is the probability of finding an event in bin i of the true distribution. This is often referred to as the prior probability distribution and is typically taken to be the particle-level distribution produced by the MC.

We are now able to tackle the problem of unfolding, since we can construct the response matrix from our Monte Carlo events. If we generate a large number of events in each bin T_i we can observe which bins they fall in after being passed through a simulation of the detector. This information can then be used, with Eqs. (7.4) and (7.3), to attempt to recover the shape of the true distribution.

One potential drawback of Bayesian unfolding is the biasing of the result by the prior probability distribution. The problem can be somewhat avoided by applying the full unfolding procedure to the data distribution iteratively, and using the output of each round of unfolding as the input to the next. The elements of the unfolding matrix then become

$$\theta_{ij}^{n} = \frac{a_{ji} \cdot P(d'_{i,n-1})}{\sum_{i} a_{ji} \cdot P(d'_{i,n-1})}; \quad n \ge 1; \quad d'_{i,0} = T_{i}$$
 (7.5)

where $d'_{i,n-1}$ is the probability of finding an event in bin i of the true distribution after n-1 iterations of the unfolding, and other symbols are as defined in Eqs. (7.4) and (7.3). The initial prior distribution, $d'_{i,0}$, is taken to be the MC particle-level distribution, T_i .

The probability of finding an event in bin i of the true distribution after n iterations of unfolding, $d_{i,n}$ is then given by

$$d'_{i,n} = \sum_{j} \theta^{n}_{ij} \cdot d_{j}. \tag{7.6}$$

As the number of iterations increases, the bias from the Monte Carlo particle-level distribution decreases. However, at the same time, statistical fluctuations are amplified and the statistical uncertainty is increased. Therefore a reasonable number of iterations must be used to balance the decreasing bias against the increasing uncertainty. The number of iterations is therefore usually kept around 2–4.

7.5.5 Bayesian Unfolding in This Analysis

The particle-level predictions were constructed using final-state particles with mean lifetime $(c\tau)$ longer than 10 mm. Charged leptons were constructed from the four-momentum combination of the lepton (electron or muon) and all nearby photons in a cone of radius $\Delta R = 0.1$. Leptons are required to have $p_T > 25$ GeV and $|\eta| < 2.47$. Jets are reconstructed using the anti- k_t algorithm with a jet-radius parameter of 0.4. Jets are required to have $p_T > 25$ GeV, |y| < 4.4 and $\Delta R(j, l) \ge 0.3$, where $\Delta R(j, l)$ is the distance in η - ϕ space between the jet and the selected leptons.

The complete unfolding procedure was implemented in the EWUnfolding package. A complete discussion of the implementation of the package is given in [31] with the important details repeated here for completeness.

Unfolding begins by defining the following quantities:

- **d**—the original data distribution with n bins. The value of the distribution in bin i is labelled d_i .
- **b**—the distribution of expected background events with n bins. The value of the background distribution in bin i is b_i .
- **y**—the signal distribution with n bins. The value of the signal distribution in bin i is y_i .
- x—the unfolded distribution with n bins. The value of the unfolded distribution in bin i is x_i.

The following quantities are then also defined:

- The response matrix, **A**, is used to correct for bin-to-bin migrations between the reconstructed and particle-level distributions. It is created using *only* events that pass the event selection and fall into the required fiducial volume at particle-level *and* reconstructed level.
- and reconstructed level.

 Fiducial factors $f_i = \frac{N_i^{\text{particle \& reco}}}{N_i^{\text{reco}}}$ for each bin of the *reconstructed* distribution. $N_i^{\text{particle \& reco}}$ is the number of events entering bin i that pass both the particle and reconstructed-level cuts, while N_i^{reco} counts the number of events in bin i that pass the reconstructed-level cuts *only*. The fiducial factors correct for events that enter the fiducial region at reconstructed-level but do not fall into the fiducial region defined at particle-level. Note that bin i is defined by the *reconstructed-level* value of the variable.
- Correction factors $c_i = \frac{N_i^{\text{reco \& particle}}}{N_i^{\text{particle}}}$ for each bin of the unfolded distribution. $N_i^{\text{particle \& reco}}$ is defined above, and N_i^{particle} is the number of events in bin i that pass the particle-level but not the reconstruction-level cuts. These account for efficiency and acceptance losses on going from particle to reconstructed level. Note that bin i is defined here by the *particle-level* value of the variable.

Using these quantities the values of the signal and unfolded distributions can then be defined as

$$y_i = (d_i - b_i) \cdot f_i$$

$$x_i = (\boldsymbol{\theta} \cdot \mathbf{y})_i / c_i$$
(7.7)

where θ is the unfolding matrix, constructed from the response matrix **A** and prior probability distribution as in Eq. (7.4).

The combined SHERPA QCD and electroweak MC samples, weighted by their respective cross sections, were used as input to the unfolding. After subtracting expected numbers of background events from the data, two iterations of unfolding were used for all distributions in all phase space regions.

7.5.6 Extending the EWUnfolding Package to 2D

The version of the EWUnfolding code originally prepared by the ATLAS Standard Model Electroweak group allows one to unfold only one-dimensional distributions.

However, there is a high degree of correlation between the numerator and denominator of the jet veto efficiency, as all of the events that enter into the numerator also appear in the denominator. If the numerator and denominator distributions were unfolded separately, and then divided to obtain the fraction, this correlation information would be lost and the statistical uncertainty would not be calculated correctly.

Instead a two-dimensional distribution can be constructed such that all of the events in each bin are statistically independent. For example to construct the unfolded jet veto efficiency as a function of $|\Delta y|$ we could create a two-dimensional histogram with the $|\Delta y|$ distribution on the horizontal axis and on the vertical axis a simple two-bin distribution where events are classified according to whether they pass or fail the jet veto requirement. The distribution of the number of additional jets between the tagging jets would also be suitable to use on the vertical axis. The simpler case was chosen here in an order to keep migrations in the second dimension to a minimum. The two-dimensional distribution can be unfolded whilst keeping track of all correlations introduced by the unfolding and the jet veto efficiency can be constructed from it afterwards, thus retaining the correlation between the numerator and denominator of the efficiency.

The EWUnfolding package was extended to allow it to unfold two-dimensional distributions as well as estimate the statistical and various systematic uncertainties, described in Sect. 7.5.8, for two-dimensional input distributions. Three checks were performed to try and ensure that no bugs were introduced during the extension of the code. The first check was to run the example unfolding routine prepared by the authors of the 1D version of the code, with both the original and extended versions of the code. All outputs between the two sets of code were checked and found to be identical, and so extending the code to allow 2D unfolding did not break any of the 1D functionality.

The second check involved preparing some signal n-tuples with example MC and data events. A simple 2×2 bin distribution was unfolded with a response matrix that had no off-diagonal elements. The expected results of this simple unfolding could be calculated by-hand, and were found to be identical to the results obtained using the code.

In the third check more signal *n*-tuples were constructed, but the response matrix used to unfold the simple 2D distributions included off-diagonal elements. I.e. some bin-to-bin migrations were included. The expected result from one iteration of Bayesian unfolding was calculated by-hand, and found to be consistent with the results of the unfolding code.

7.5.7 Selected Control Plots

Figure 7.5 shows the impact of the number of iterations used in the Bayesian unfolding the on the differential cross section as a function of m_{jj} and jet veto efficiency as a function of m_{jj} . Plotted are ratios of the distributions after unfolding with three, five or ten iterations to distributions unfolded with two, the nominal. Increasing the number of iterations has minimal impact on the differential distributions. However, as can be seen in Fig. 7.5b, the effect on distributions such as the jet veto efficiency is much larger. Increasing the number of iterations used in the unfolding increased the size of fluctuations in the tails of these distributions. It was therefore decided that two iterations would be used to unfold all distributions in all phase space regions.

The purity quantifies to what extent detector resolution and smearing effects cause events to migrate from one bin at particle level into another at reconstructed level and is given by

Purity =
$$\frac{N^{\text{particle-level bin } i \text{ & reco bin } i}}{N^{\text{particle-level bin } i}} \bigg|_{\text{passed particle & reco-level cuts}}$$
, (7.8)

where $N^{\mathrm{particle-level}\,\mathrm{bin}\,i}$ & reco bin i is the number of events entering bin i of both the particle and reconstructed-level distributions and $N^{\mathrm{particle-level}\,\mathrm{bin}i}$ counts the number of events that entered bin i of the particle-level distribution. I.e. for a given bin i of a distribution, we check what fraction of the events that fell into bin i at particle-level also entered the same bin at reconstructed level. Figure 7.6 shows examples of the bin purity for the differential cross section as a function of $|\Delta y|$ and differential cross section as a function of N_{jet} .

In Fig. 7.7 the nominal Bayesian unfolding is compared to distributions obtained after applying simple bin-by-bin corrections, defined by taking the ratio of the

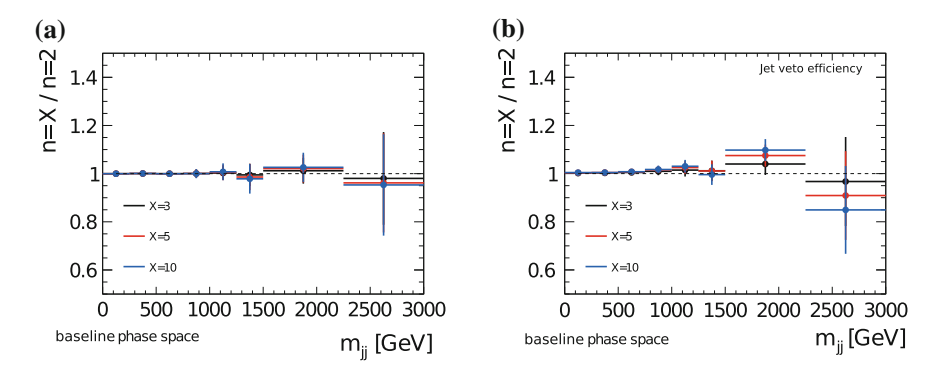


Fig. 7.5 Effect of increasing the number of iterations, X, used in the Bayesian unfolding on **a** the differential cross section as a function of m_{jj} in the *baseline* region and **b** the jet veto efficiency as a function of m_{jj} in the *baseline* region

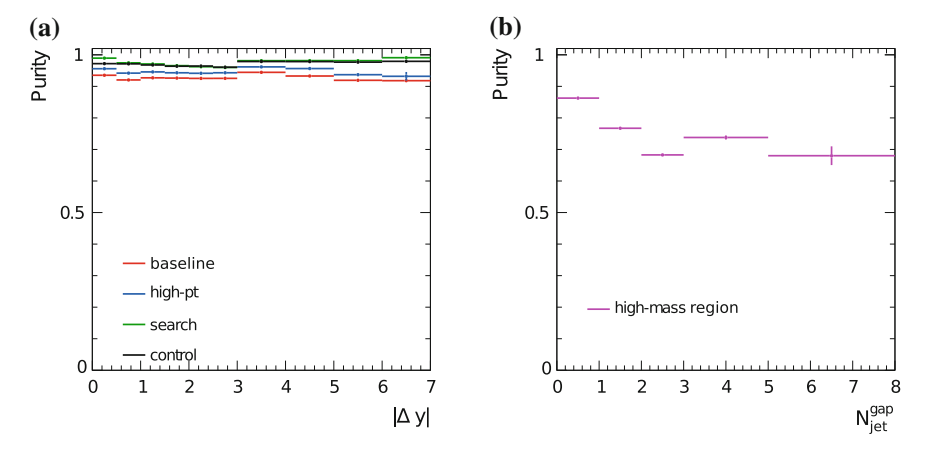


Fig. 7.6 Example distributions showing the bin purity of **a** the differential cross section as a function of $|\Delta y|$ in each of the phase space regions and **b** the differential cross section as a function of N_{jet} in the *high-mass* region

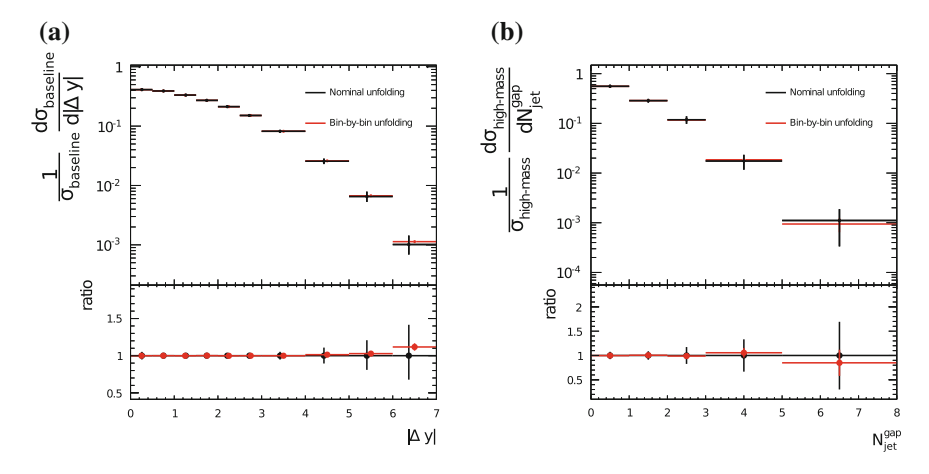


Fig. 7.7 Comparisons of the nominal Bayesian unfolding to simple bin-by-bin corrections for a the differential cross section as a function of $|\Delta y|$ in the *baseline* region and **b** the differential cross section as a function of $N_{\rm jet}$ in the *high-mass* region

particle-level and reconstructed-level distributions (cf. Sect. 5.7). Two examples are shown—the differential cross section as a function of $|\Delta y|$ in the *baseline* region and the differential cross section as a function of $N_{\rm jet}$ in the *high-mass* region. All such distributions confirm that the two methods are consistent to within the associated uncertainties.

7.5.8 Statistical Uncertainties and Correlations

7.5.8.1 Statistical Uncertainty on the Differential Cross Sections

The uncertainty on the unfolded results due to the data statistics was computed via toy Monte Carlo tests. Each bin of the data distribution, d_i , was Poisson-fluctuated and the complete unfolding procedure applied. This was repeated 2000 times and the RMS of the unfolded values in each bin was taken as the statistical uncertainty on the data.

In the original EWUnfolding package the uncertainty associated with MC statistics was estimated by repeated applications of bin-by-bin unfolding. Nominal correction factors were calculated and a bin-by-bin unfolding applied. Each correction factor was then Gaussian-fluctuated, where the width of the Gaussian was taken from the uncertainty on the correction factor² and the bin-by-bin unfolding was repeated. This procedure was repeated 2000 times and the RMS of the bin-by-bin-unfolded values in each bin was taken as the uncertainty.

As part of updating the EWUnfolding package, a new method for evaluating the uncertainty was implemented, whereby each bin of the response matrix was Gaussian-fluctuated—where the width of the Gaussian was $\sqrt{\sum_i w_i^2}$ for each bin—and the complete iterative Bayesian unfolding repeated with the new response matrix. The response matrix values were fluctuated 2000 times and the RMS of the unfolded values in each bin was taken as the uncertainty. The original method was found to underestimate the statistical uncertainty in regions of phase space with poor statistics, and an example comparison between the two methods is shown in Fig. 7.8 for the differential cross section as a function of $|\Delta y|$ in the *high-mass* region.

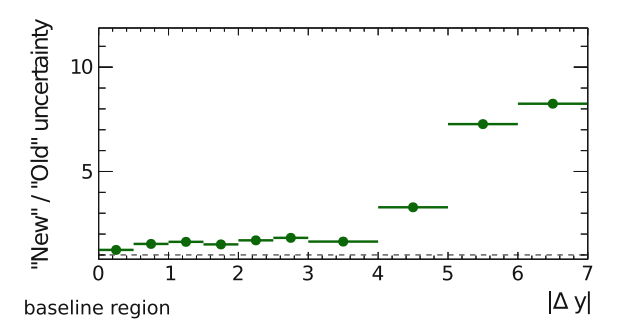


Fig. 7.8 Comparison between methods of estimating the uncertainty related to the MC statistics in the unfolding of the differential cross section as a function of $|\Delta y|$ in the *high-mass* region. In regions of phase space with low statistics the more sophisticated method of Gaussian-fluctuating each bin of the response matrix produces an uncertainty up to eight times larger than the with the simpler method

²In the EWUnfolding package the default procedure treats the correction factors like efficiencies, and the binomial uncertainty equation is used, $\sigma = \sqrt{\epsilon(1-\epsilon)/N}$. However, these correction factors are not true efficiencies and in principle could have values larger than 1.

7.5.8.2 Statistical Uncertainties and Correlations on the Efficiency-Type Distributions

The jet veto efficiency, $\Delta\phi(j,j)$ cut efficiency and $p_{T}^{balance}$ cut efficiency distributions are constructed from unfolded two-dimensional distributions. On the x-axis of these distributions are either $|\Delta y|$ or m_{jj} , and the y-axis contains just two bins labelling whether or not each event passes the cut which defines the efficiency. Before the unfolding, events in each bin of the two dimensional distribution are statistically independent. However, the nature of the Bayesian unfolding is to reshuffle events between bins, and afterwards there exist correlations between the bins of the unfolded distributions. These correlations need to be accounted for when determining the statistical uncertainty in the efficiency-type distributions.

The efficiency quantities are calculated as follows,

$$\epsilon_i = \frac{g_i}{g_i + n_i} \tag{7.9}$$

where, using the jet veto efficiency as an example, ϵ_i is the value of jet veto efficiency in bin i, g_i is the number of events which do not contain any additional jets with $p_T > 25$ GeV in the rapidity interval bounded by the two leading jets, and n_i the number of events which do contain such additional jets.

The uncertainty on the efficiency is calculated using the standard formula for propagating uncertainties with correlations,

$$\sigma_{\epsilon_{i}}^{2} = \left(\frac{\partial \epsilon_{i}}{\partial g_{i}}\right)^{2} \sigma_{g_{i}}^{2} + \left(\frac{\partial \epsilon_{i}}{\partial n_{i}}\right)^{2} \sigma_{n_{i}}^{2} + 2\frac{\partial \epsilon_{i}}{\partial g_{i}} \frac{\partial \epsilon_{i}}{\partial n_{i}} \sigma_{g_{i}} \sigma_{n_{i}} \rho(g_{i}, n_{i})$$

$$= \left[\frac{1}{g_{i} + n_{i}} - \frac{g_{i}}{(g_{i} + n_{i})^{2}}\right]^{2} \sigma_{g_{i}}^{2} + \left[\frac{g_{i}}{(g_{i} + n_{i})^{2}}\right]^{2} \sigma_{n_{i}}^{2}$$

$$-2\left[\frac{1}{g_{i} + n_{i}} - \frac{g_{i}}{(g_{i} + n_{i})^{2}}\right] \left[\frac{g_{i}}{(g_{i} + n_{i})^{2}}\right] \sigma_{g_{i}} \sigma_{n_{i}} \rho(g_{i}, n_{i}), \qquad (7.10)$$

where ϵ_i is taken from Eq. (7.9) and $\rho(g_i, n_i)$ is the correlation between bins g_i and n_i .

The $\langle N_{\rm jets} \rangle$ distribution is also unfolded in two dimensions where the $(N_{\rm jet})$ distribution is plotted on the vertical axis against either $m_{\rm jj}$ or $|\Delta y|$ on the x-axis. In each bin, x, of $|\Delta y|$ or $m_{\rm jj}$ we loop over all bins of the $N_{\rm jet}$ distribution on the y-axis and calculate $\langle N_{\rm iets} \rangle$ as,

$$\langle N_{\text{jets}} \rangle |_{x} = \frac{\sum_{y} N_{y}^{\text{jets}} n_{y}}{\sum_{y} n_{y}} \Big|_{x} \equiv \frac{N^{j}}{T} \Big|_{x},$$
 (7.11)

where N_y^{jets} labels the number of jets between the leading two jets in bin y of the distribution, and n_y is the number events with that many jets.

The uncertainty on each bin of the $\langle N_{\text{jets}} \rangle$ distribution is calculated in the same way as for the efficiency distributions, but with more correlation terms included to reflect that the second-dimension has more than two bins,

$$\sigma_{\langle N_{
m jets} \rangle}^2 = \sum_i \sum_j \left[\frac{N_i^{
m jets}}{T} - \frac{N^j}{T^2} \right] \left[\frac{N_j^{
m jets}}{T} - \frac{N^j}{T^2} \right] \sigma_{n_i} \sigma_{n_j} \,
ho(n_i, n_j) \; ,$$

where the summations run over the bins in the horizontal and vertical axis of the two-dimensional distributions, and the other terms are defined in Eq. (7.10).

7.5.8.3 Correlations Between Differential Distributions

Statistical correlations between differential distributions were calculated using the *bootstrap* method. Poisson fluctuations were applied to each event in data and a series of N replica histograms were filled each with a weight randomly chosen from a Poisson distribution with a mean of one. Once the histograms have been filled for all events, with different bootstrap weights generated for each event, we are left with N replicas of the data. These can be interpreted as being representations of how the data might have looked if the measurement was repeated N times.

Using these replicas it is possible to calculate the statistical correlation between different variables using the standard formula,

$$\rho_{(i,j)}^{x,y} = \frac{\frac{1}{N} \sum_{N} (x_n^i - \mu_x) * (y_n^j - \mu_y)}{\sigma_x \sigma_y} . \tag{7.12}$$

The bootstrap weights generated can also be used to calculate the correlations between current measurements and any future measurement of the same data, providing they are generated in a consistent way.

Examples of the correlations between bins of different distributions are shown in Fig. 7.9. The published correlation information allows the quantitative comparison of all distributions simultaneously.

7.5.9 Luminosity, Trigger and Lepton-Based Systematics

As the unfolded distributions are normalised to a fiducial cross section, the important issue is whether a given source of systematic uncertainty results in a shape change in the distribution of interest. The uncertainty in the luminosity is, by definition, a flat uncertainty as a function of any given variable and does not change the shapes of our distributions. It is therefore neglected as a possible source of uncertainty in the unfolded distributions.

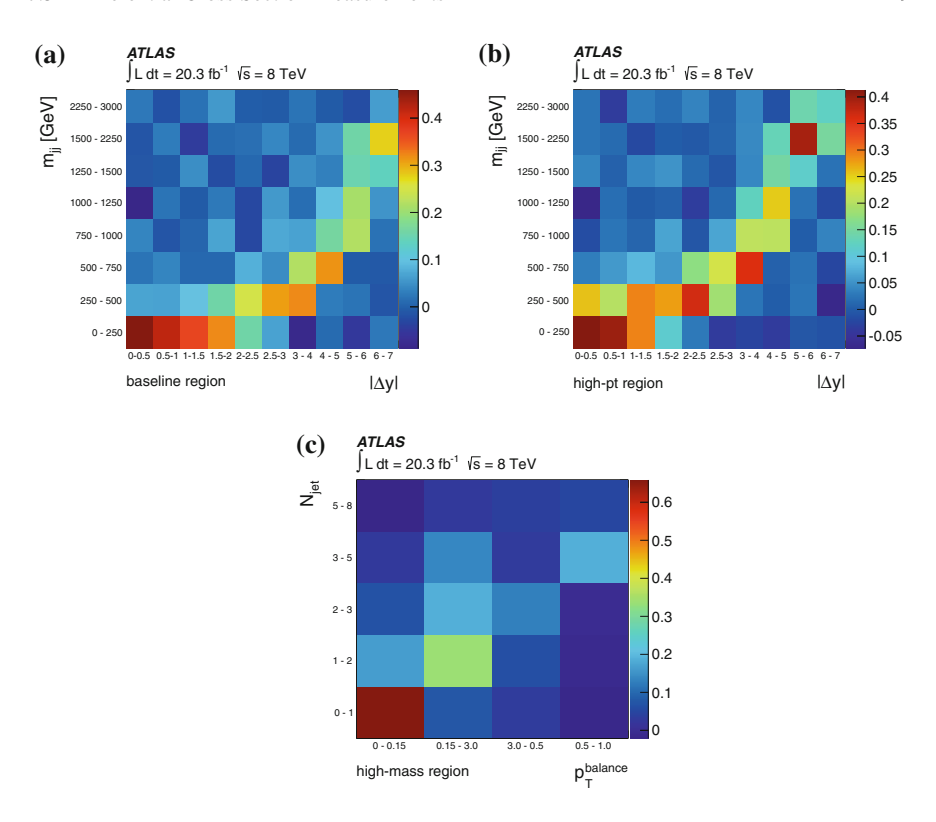


Fig. 7.9 Statistical correlations, evaluated using the Bootstrap technique (cf. Sect. 7.5.8.3), between **a** the differential cross section as a function of $|\Delta y|$ and differential cross section as a function of m_{jj} in the *baseline* region, **b** the differential cross section as a function of $|\Delta y|$ and differential cross section as a function of m_{jj} in the *high*-p_T region and **c** the differential cross section as a function of p_T^{balance} and differential cross section as a function of N_{jet} distributions in the *high-mass* region

The systematic uncertainties associated with the trigger and lepton reconstruction efficiency and momentum resolution were assessed by comparing the nominal reconstruction-level distributions to those obtained after shifting the parameters that control the amount of smearing and scaling applied to the simulated events (cf. Sect. 7.4). The effect of these systematic uncertainties is to change the number of events entering the fiducial region of interest. However the effect is flat as a function of any given variable and the lepton-based systematic uncertainties have a negligible impact on the shape of the distributions. Therefore all lepton-based uncertainties are neglected when calculating the total experimental uncertainty on the unfolded results.

7.5.10 Jet Energy-Based Systematic Uncertainties

Uncertainties affecting the jets used in the analysis will result in changes in the shapes of the measured distributions, and must therefore be evaluated in detail.

Jet energy scale uncertainties take into account effects such as the η -dependence of the jet energy calibration, the uncertainty in the pile-up offset correction, the uncertainty due to the unknown flavour of the jets and the discrepancy observed between data and MC after the full jet calibration procedure has been applied. The effect of each source of uncertainty is estimated by shifting the energy of each jet before any selection cuts are applied. The full unfolding procedure is then repeated after constructing a new response matrix from the energy-shifted MC samples, and the uncertainty is defined by comparing the new distribution to the nominal unfolded result. To reduce the effect of statistical fluctuations and determine the change in shape induced by each source of systematic uncertainty, the unfolded distributions are fitted and the systematic uncertainty is taken to be the ratio of the systematicallyshifted and nominal fits. As the majority of the distributions are steeply falling, the distributions are transformed onto a logarithmic y-scale (i.e. for each bin i, the transform is $y[i] \to \log(y[i])$). A polynomial of order two or three is then used to fit each distribution and a reasonable χ^2/N_{dof} is observed for each fit.³ Figure 7.10 shows the fit to the transformed $\frac{1}{\sigma} \cdot \frac{d\sigma}{dm_{jj}}$ distribution in the *search* phase space, for nominal and shifted jet energies associated with the η -intercalibration modelling component of the jet energy scale uncertainty. The fit functions are then used to construct bin-by-bin jet energy scale uncertainties on each distribution. The impact of this fitting procedure is discussed below.

Effects of a worsened jet energy resolution are estimated by smearing the energy of each jet by a random number drawn from a Gaussian distribution with mean set to the jet energy and width equal to the resolution uncertainty. As with the jet energy scale uncertainties new response matrices are then created using the smeared MC events and the full unfolding procedure is repeated.

The individual effects of all components of the JES on the differential cross section as a function of $|\Delta y|$ and differential cross section as a function of m_{jj} in the *baseline* phase space, after applying the smoothing procedure described above, are shown in Fig. 7.11. The total uncertainty is estimated by taking the sum in quadrature of the individual components.

³Apart from the differential cross section as a function of $|\Delta y|$ in the *search* and *control* phase spaces, all distributions are fit across their entire range. The differential cross section as a function of $|\Delta y|$ in these phase spaces has an unusual shape and is difficult to fit. Therefore the fit is performed in the steeply-falling region $3 < |\Delta y| < 8$, where statistics are lower and the smoothing procedure becomes more important.

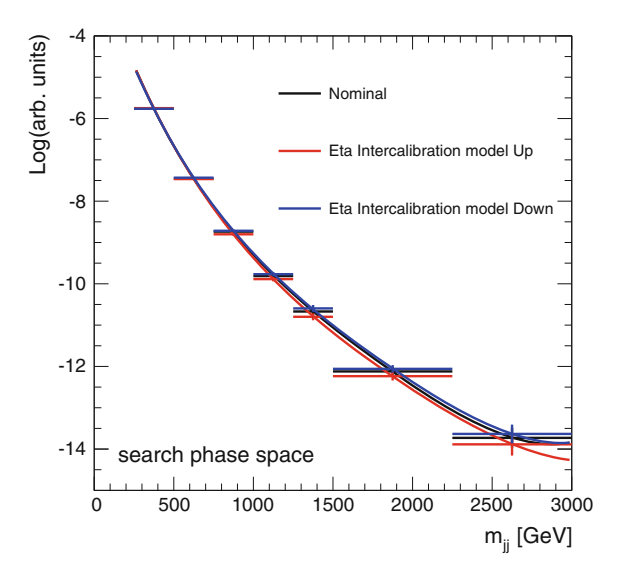


Fig. 7.10 Example fits to the nominal and η -intercalibration systematic-shifted $\frac{1}{\sigma} \cdot \frac{d\sigma}{dm_{\rm ij}}$ distribution in the *search* region. The values in each bin of the nominal and systematic-shifted distributions have been transformed onto a logarithmic scale before fitting with a polynomial of order three. After transforming back to a linear scale, the ratio of systematic-shifted to nominal fit results are then used to determine the relative JES uncertainty due to this JES uncertainty component

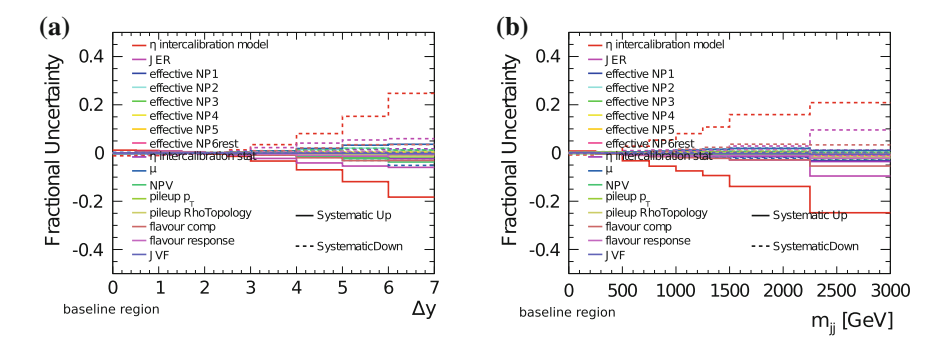


Fig. 7.11 The individual effects of all components of the JES on **a** the differential cross section as a function of $|\Delta y|$ and **b** the differential cross section as a function of m_{ij} in the *baseline* region

7.5.11 Pile-up and JVF Modelling Uncertainty

An uncertainty associated with the mismodelling of the jet vertex fraction is estimated by varying the JVF cut in the MC, repeating the analysis and unfolding, and comparing the resulting distributions. The JVF cut removes some fraction of the signal jets in additional to those originating from pileup, therefore any mismodelling

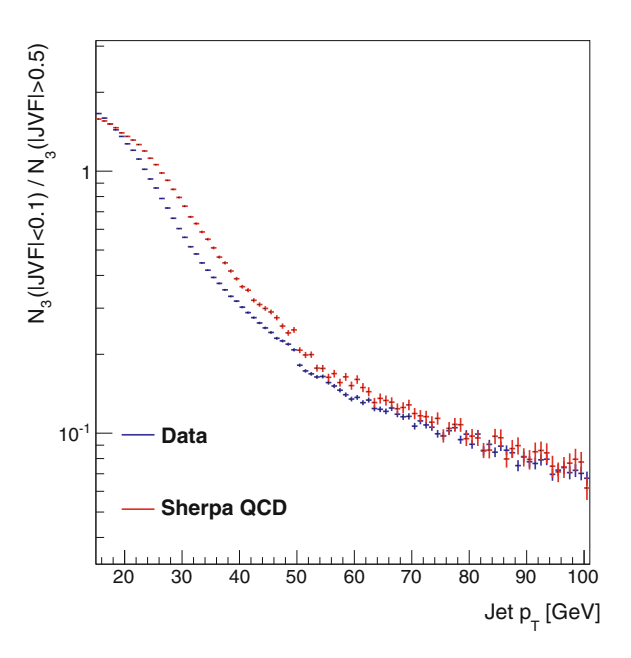
of the JVF distribution could introduce a bias to the shape and normalisation of measured distributions.

The uncertainty due to the number of residual pile-up jets that remain after the application of the JVF cut is estimated using a similar technique to that presented in Sect. 5.8.2. The analysis is repeated after removing all reconstruction-level jets that do not satisfy ΔR (particle jet, reco jet) <0.3. The difference between the particle-level-matched and nominal distributions reflects the impact of pile-up on the distributions in question. However taking the full difference between the two distributions would imply that there was a 100 % uncertainty in the amount of residual pile-up. Figure 7.12 shows the ratio of p_T spectra for jets with |JVF|<0.1 to jets with |JVF|>0.5. I.e. the ratio compares the shapes of a sample of predominantly pile-up jets with a sample of signal jets. In the region 25 GeV < $p_T<40$ GeV the ratio is approximately 30 % higher for MC events compared to data. This implies that there are up to 30 % more pile-up jets in the MC.

This estimate is only valid for central jets, since the calculation of the JVF relies on information obtained by the tracking detectors. For jets in more forward regions the result of the ATLAS measurement of forward transverse energy flow [32] is used to estimate any possible pile-up mismodelling. This analysis found that default MC tunes tended to differ from data in their description of the mean $\sum E_T$ distribution by an extra 15% in the forward regions.

The total pile-up modelling uncertainty is therefore taken to be 35 % of the difference between the particle-level-matched and nominal distributions.

Fig. 7.12 The ratio of jet p_T distributions for jets with |JVF| < 0.1 to jets with |JVF| > 0.5. The distributions were constructed for events containing a Z-boson candidate and jets with $|\eta| < 0.8$



7.5.12 Modelling Uncertainties and Unfolding Closure

An unfolding closure uncertainty is estimated by following the procedure outlined in [33]. Taking the differential cross section as a function of $|\Delta y|$ as an example, the reconstruction-level differential cross section as a function of $|\Delta y|$ is compared to data, and a reweighting function is constructed by fitting the ratio. The particle-level MC is then reweighted and the unfolding is repeated using the reweighted MC to populate the response matrix. The data unfolded using the reweighted MC are then compared to the unfolded distributions obtained using the nominal MC. The difference between the two is taken as an uncertainty, and estimates to what extent the unfolding is dependent on the shape of the original MC in the variable being unfolded. This is referred to the *unfolding closure*.

To estimate how modelling of the other kinematic distributions affect the unfolding of a given distribution, all other distributions which are unfolded, as well as jet p_T distributions, are reweighted (separately) to more closely resemble the data. The Bayesian unfolding procedure is then repeated using the reweighted MC and the results compared to the those obtained from unfolding with the nominal MC. The *theory modelling uncertainty* is taken to be the sum in quadrature of the difference between the default unfolded curve and the unfolded results obtained after reweighting the other, orthogonal distributions. The theory modelling uncertainties are shown in the summaries of systematic uncertainties in Sect. 7.5.13.

7.5.13 Summaries of Systematic and Statistical Uncertainties

Breakdowns of the systematic uncertainties presented in this section are shown in Figs. 7.13, 7.14, 7.15, 7.16, 7.17, 7.18 and 7.19. The total systematic uncertainty is defined as the sum-in-quadrature of the individual sources of experimental and theoretical uncertainty.

For the differential cross sections (Figs. 7.13, 7.14 and 7.15) it is the jet energy-based uncertainties (red dashed) that dominate the overall experimental uncertainty. Theory modelling uncertainties (blue dashed) are generally small, except in regions of phase space that have least sensitivty to the electroweak component of the Z_{jj} cross section (baseline and control regions) and at large values of $|\Delta y|$ and m_{jj} . The uncertainty due to limited statistics in the data also becomes large at very high values of $|\Delta y|$ and m_{jj} . The uncertainty on the efficiency-type distributions (Figs. 7.16, 7.17, 7.18 and 7.19) is in general smaller than for the differential cross sections. Because of the way in which the efficiency-type distributions are constructed, experimental systematic uncertainties can cancel between the numerator and denominator. As for the differential cross sections, it is the jet energy-based uncertainties which are often largest.

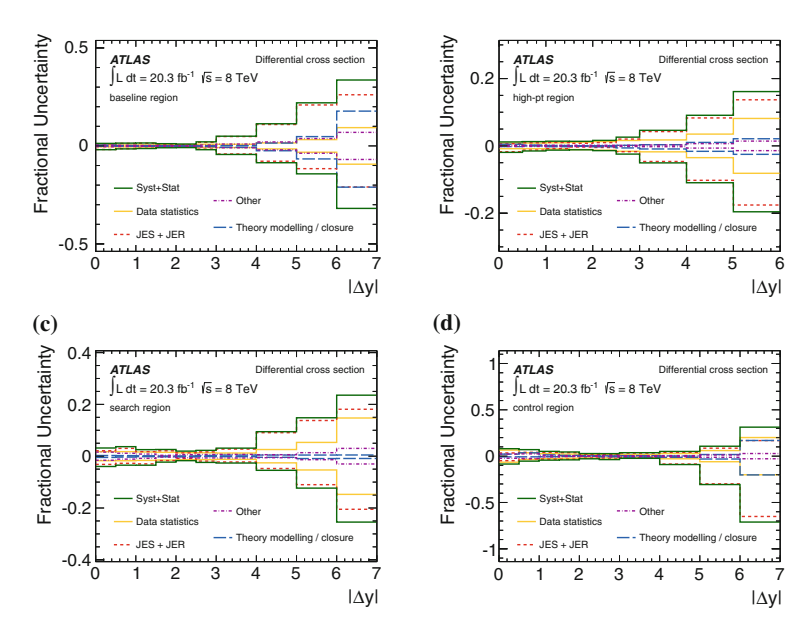


Fig. 7.13 Breakdown of systematic uncertainties on the $\frac{1}{\sigma} \cdot \frac{d\sigma}{d|\Delta y|}$ distribution in the **a** *baseline*, **b** *high*-p_T, **c** *search* and **d** *control* regions. The effect of MC statistics, pile-up modelling and JVF modelling have been combined into one uncertainty labelled 'other'

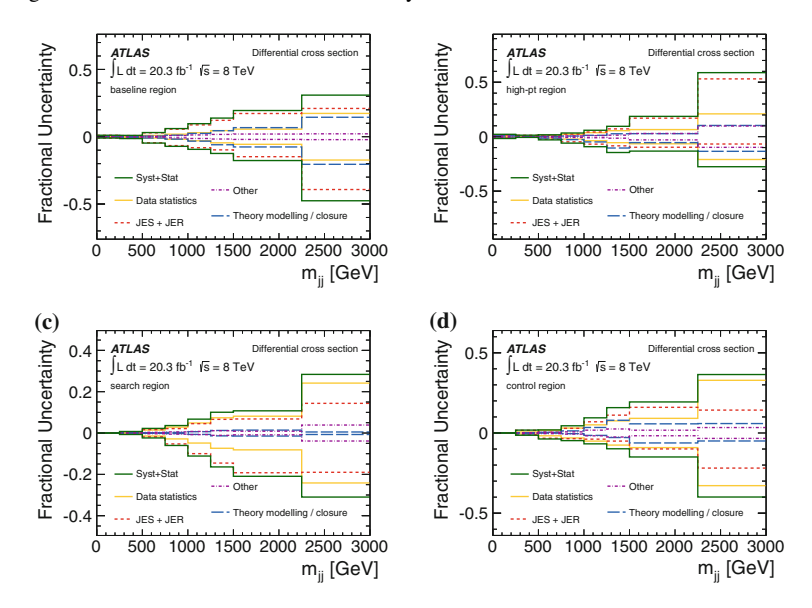


Fig. 7.14 Breakdown of systematic uncertainties on the $\frac{1}{\sigma} \cdot \frac{d\sigma}{dm_{jj}}$ distribution in the **a** *baseline*, **b** *high*-p_T, **c** *search* and **d** *control* regions. The effect of MC statistics, pile-up modelling and JVF modelling have been combined into one uncertainty labelled 'other'

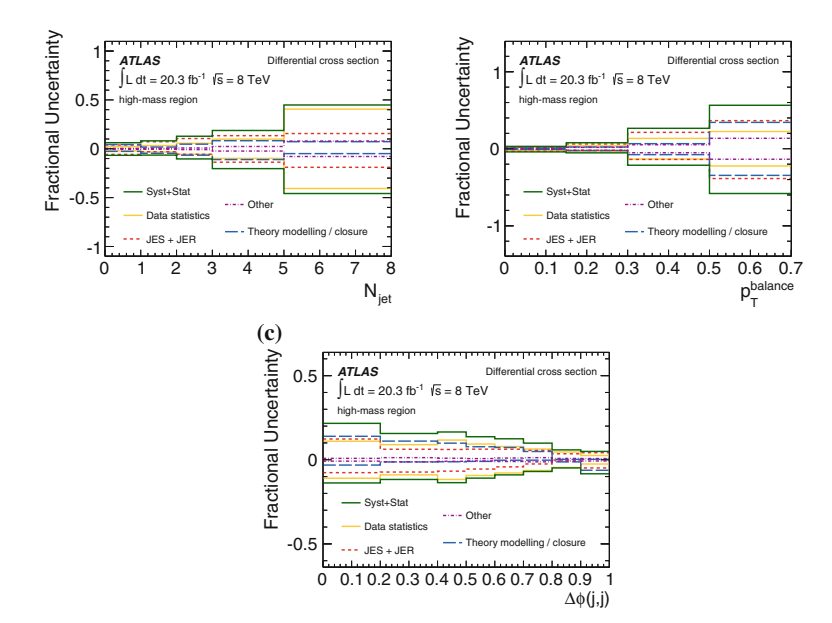


Fig. 7.15 Breakdown of systematic uncertainties on the \mathbf{a} $\frac{1}{\sigma} \cdot \frac{\mathrm{d}\sigma}{\mathrm{d}N_{\mathrm{jet}}}$, \mathbf{b} $\frac{1}{\sigma} \cdot \frac{\mathrm{d}\sigma}{\mathrm{d}p_{\mathrm{T}}^{\mathrm{balance}}}$ and \mathbf{c} $\frac{1}{\sigma} \cdot \frac{\mathrm{d}\sigma}{\mathrm{d}[\Delta\phi(j,j)]}$ distributions in the *high-mass* region. The effect of MC statistics, pile-up modelling and JVF modelling have been combined into one uncertainty labelled 'other'

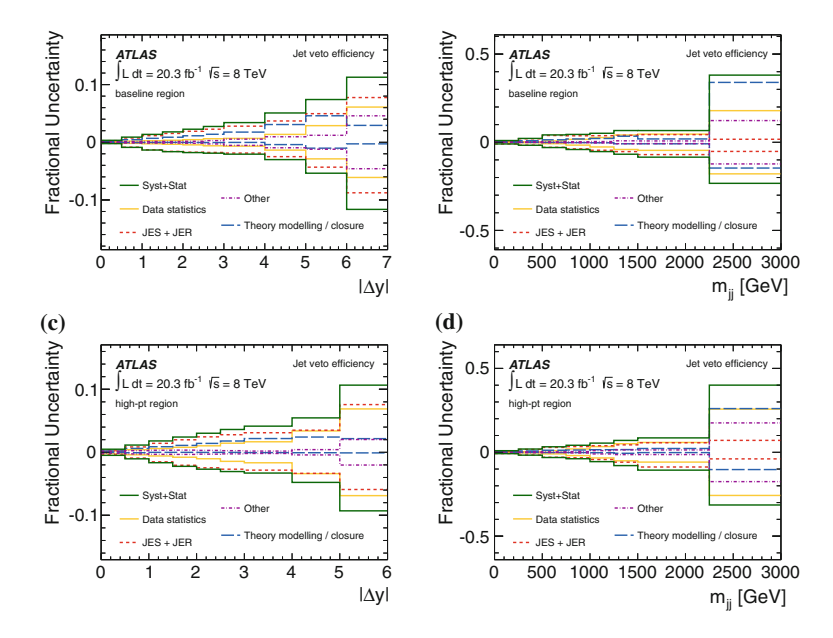


Fig. 7.16 Breakdown of systematic uncertainties on the jet veto efficiency versus $|\Delta y|$ (**a**, **c**) and m_{jj} (**b**, **d**) in the *baseline* (**a**, **b**) and *high*-p_T (**c**, **d**) regions. The effect of MC statistics, pile-up modelling and JVF modelling have been combined into one uncertainty labelled 'other'

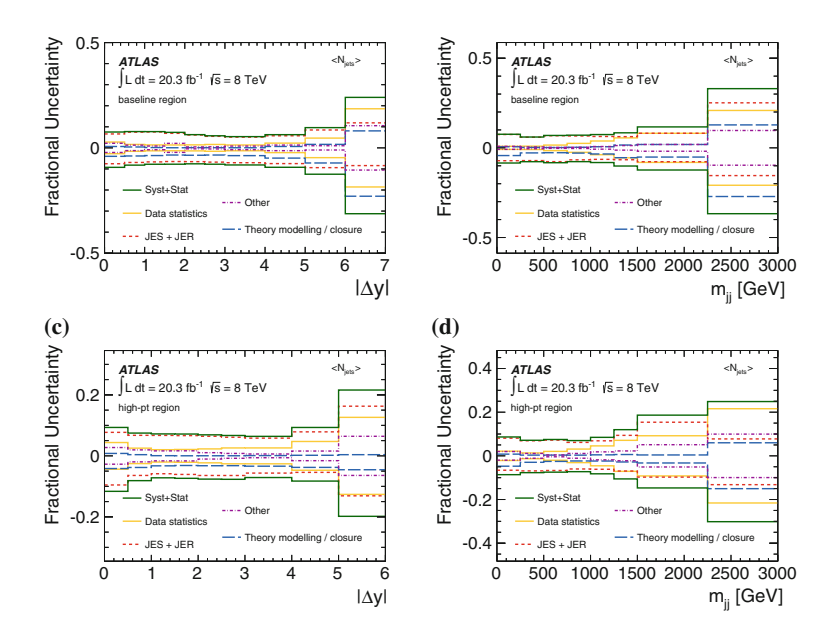


Fig. 7.17 Breakdown of systematic uncertainties on the $\langle N_{\text{jets}} \rangle$ versus $|\Delta y|$ (**a**, **c**) and m_{jj} (**b**, **d**) in the *baseline* (**a**, **b**) and *high*-p_T (**c**, **d**) regions. The effect of MC statistics, pile-up modelling and JVF modelling have been combined into one uncertainty labelled 'other'

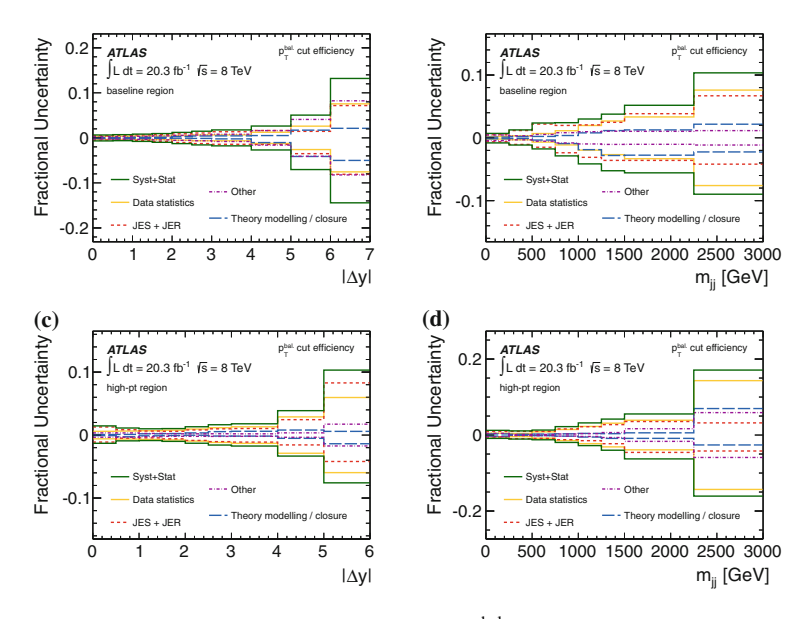


Fig. 7.18 Breakdown of systematic uncertainties on the $p_T^{balance}$ *cut efficiency* versus $|\Delta y|$ (**a**, **c**) and m_{ij} (**b**, **d**) in the *baseline* (**a**, **b**) and *high*-p_T (**c**, **d**) regions. The effect of MC statistics, pile-up modelling and JVF modelling have been combined into one uncertainty labelled 'other'

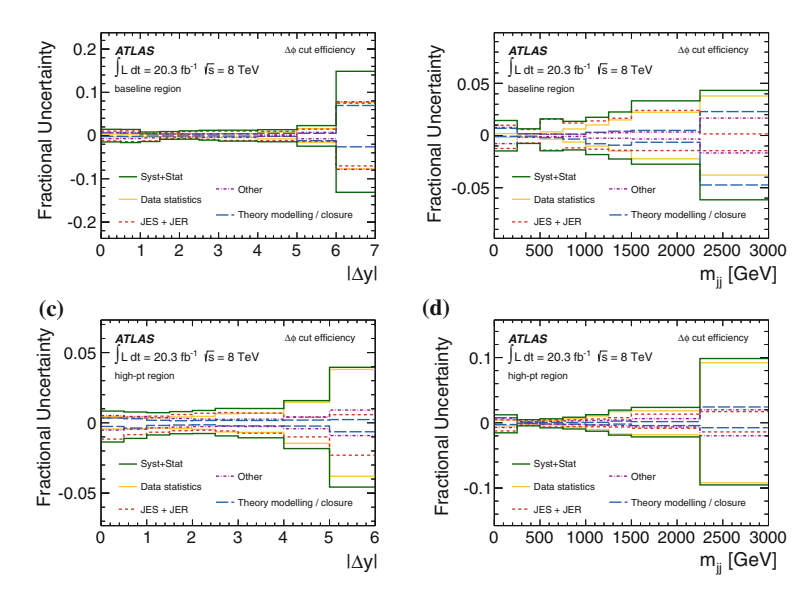


Fig. 7.19 Breakdown of systematic uncertainties on the $\Delta\phi(j,j)$ *cut efficiency* versus $|\Delta y|$ (**a**, **c**) and m_{jj} (**b**, **d**) in the *baseline* (**a**, **b**) and *high*-p_T (**c**, **d**) regions. The effect of MC statistics, pile-up modelling and JVF modelling have been combined into one uncertainty labelled 'other'

7.5.14 Unfolded Differential Cross Sections

The unfolded data are compared to predictions from SHERPA and POWHEG in Figs. 7.20, 7.21, 7.22, 7.23, 7.24, 7.25, 7.26.

The unfolded $\frac{1}{\sigma} \cdot \frac{d\sigma}{d|\Delta y|}$ distribution is shown in Fig. 7.20, for the *baseline* (a), high-p_T (b), search (c) and control (d) fiducial regions. This distribution is sensitive to the differences between the strong and electroweak Zii production. In the electroweak case the recoil of the two quarks against the W-bosons causes the resulting jets to be produce at large rapidities and with a large invariant mass compared to dijet systems produced in the strong Z_{ii} case. In the baseline region there is little difference between the QCD-only and QCD+EW predictions, until very large values of $|\Delta y|$ where the contribution from electroweak production is expected to be enhanced. At large $|\Delta y|$, POWHEG provides a better description of the data than SHERPA, a result which is consistent with previous Z + jets measurements at $\sqrt{s} = 7 \text{ TeV } [1, 2]$. In the high-p_T region the difference between the QCD-only and QCD+EW predictions at large $|\Delta y|$ becomes more pronounced. In this region, both SHERPA and POWHEG QCD+EW predictions give reasonable descriptions of the data. The $\frac{1}{\sigma} \cdot \frac{d\sigma}{d|\Delta v|}$ distribution in the search region again shows POWHEG providing a better description of the data. At large $|\Delta y|$ there is a significant difference between the QCD-only and QCD+EW predictions, with the EW component of the cross-section being required to correctly describe the shape of the distribution in data. In the control region there is almost no difference between the QCD-only and QCD+EW predictions, as expected. Both

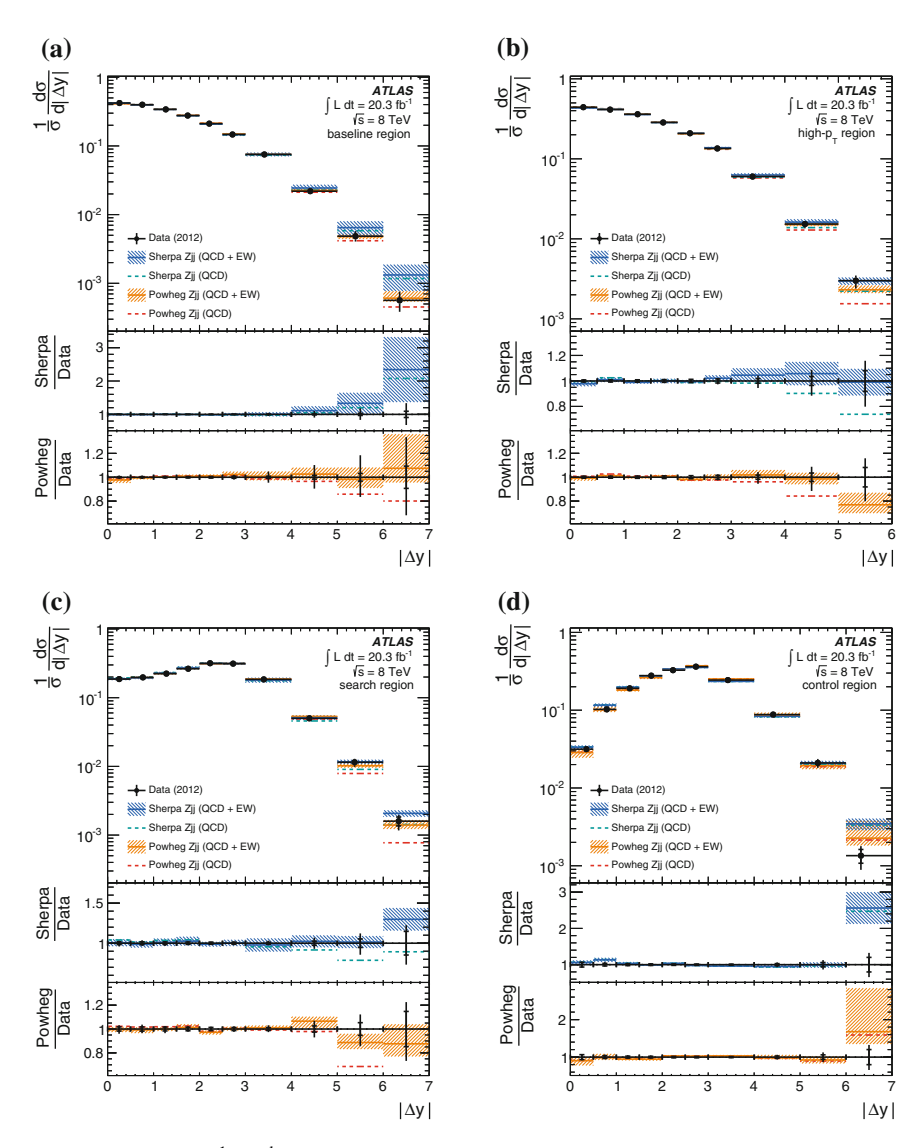


Fig. 7.20 Unfolded $\frac{1}{\sigma} \cdot \frac{d\sigma}{d|\Delta y|}$ distribution in the **a** baseline, **b** high-p_T, **c** search and **d** control regions. The data are shown as closed (black) circles. The vertical error bars show the size of the total uncertainty on the measurement, with tick marks used to reflect the size of the statistical uncertainty only. Particle-level predictions from SHERPA and POWHEG are shown for combined strong and electroweak Z_{jj} production (labelled as QCD+EW) by hatched bands, denoting the model uncertainty, around the central prediction, which is shown as a solid line. The predictions from SHERPA and POWHEG for strong Z_{jj} production (labelled QCD) are shown as dashed lines

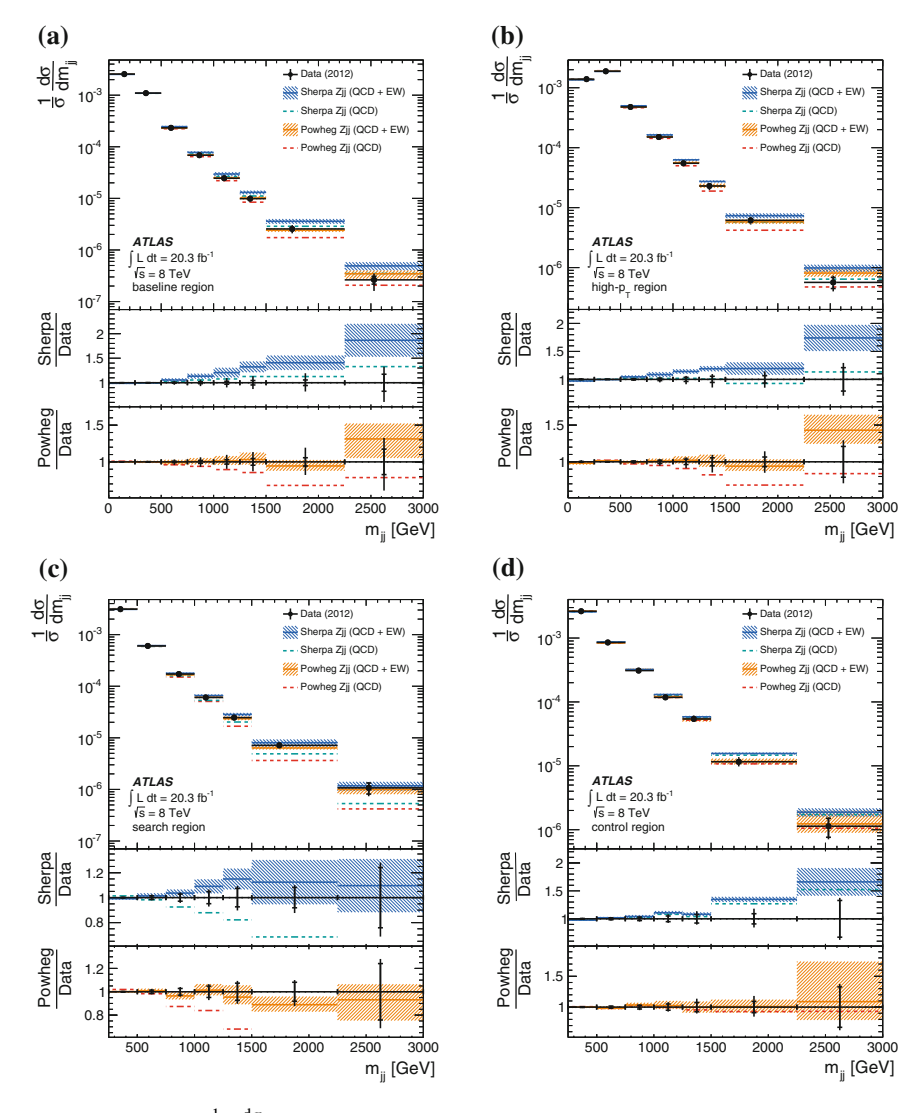


Fig. 7.21 Unfolded $\frac{1}{\sigma} \cdot \frac{d\sigma}{dm_{jj}}$ distribution in the **a** *baseline*, **b** *high*-p_T, **c** *search* and **d** *control* regions. The data and theoretical predictions are presented in the same way as in Fig. 7.20

SHERPA and POWHEG provide good descriptions of the data across the entire range, apart from the last bin which is likely a statistical fluctuation in the data.

Comparisons of the unfolded $\frac{1}{\sigma} \cdot \frac{d\sigma}{dm_{jj}}$ distribution in the four phase space regions are shown in Figs. 7.21a–d. The results are qualitatively the same as for the $|\Delta y|$ distribution, which is expected because m_{jj} and $|\Delta y|$ are correlated variables. The POWHEG QCD+EW prediction does a reasonably good jobs of describing the data in

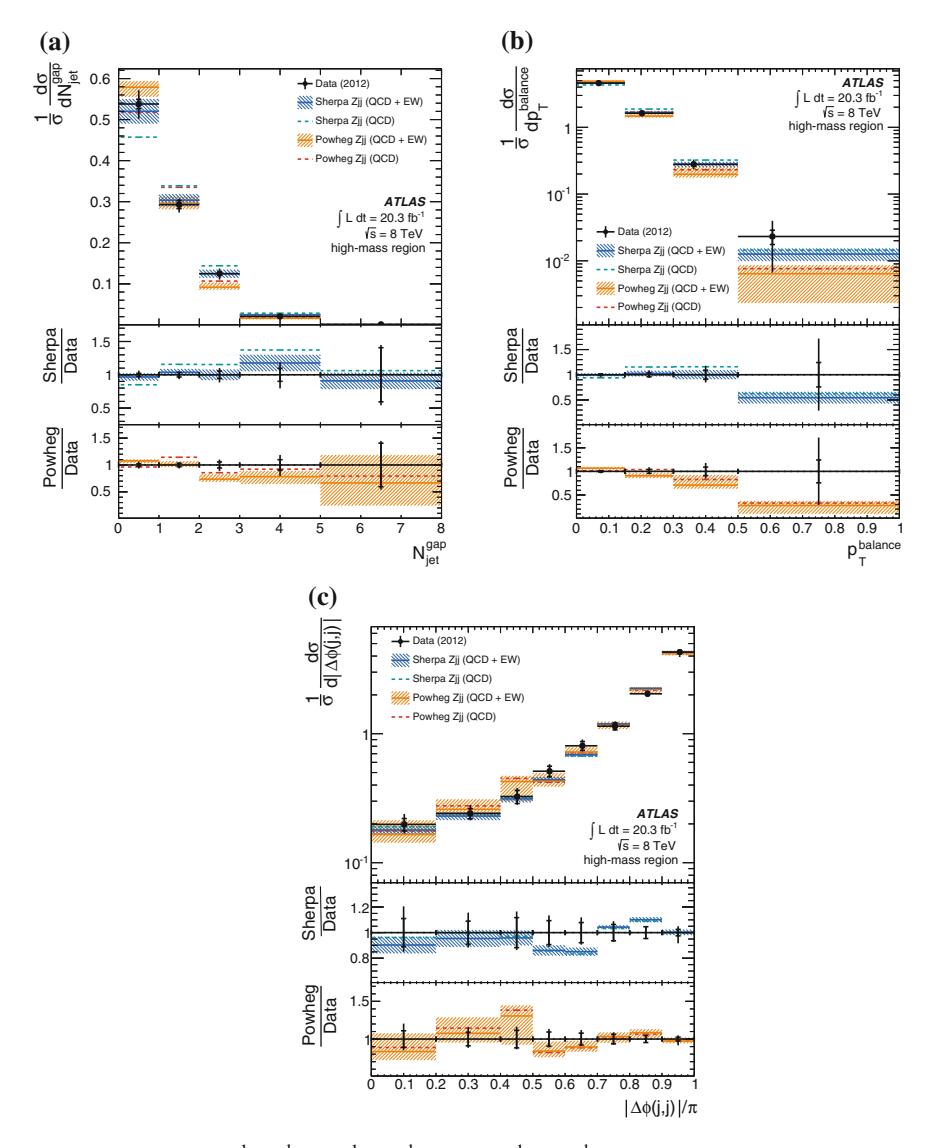


Fig. 7.22 Unfolded **a** $\frac{1}{\sigma} \cdot \frac{d\sigma}{dN_{\rm jet}}$, **b** $\frac{1}{\sigma} \cdot \frac{d\sigma}{dp_{\rm p}^{\rm balance}}$ and **c** $\frac{1}{\sigma} \cdot \frac{d\sigma}{d|\Delta\phi(j,j)|}$ distributions in the *high-mass* region. The data and theoretical predictions are presented in the same way as in Fig. 7.20

all fiducial regions. The Sherpa QCD+EW predictions do not describe the data well in the *baseline* and *high*-p_T regions. Given that POWHEG provides QCD+EW predictions of the differential cross sections in the *baseline* and *high*-p_T regions at next-to-leading order in QCD, this difference in performance is expected. The difference between the QCD-only and QCD+EW predictions in the *search* region is very pronounced

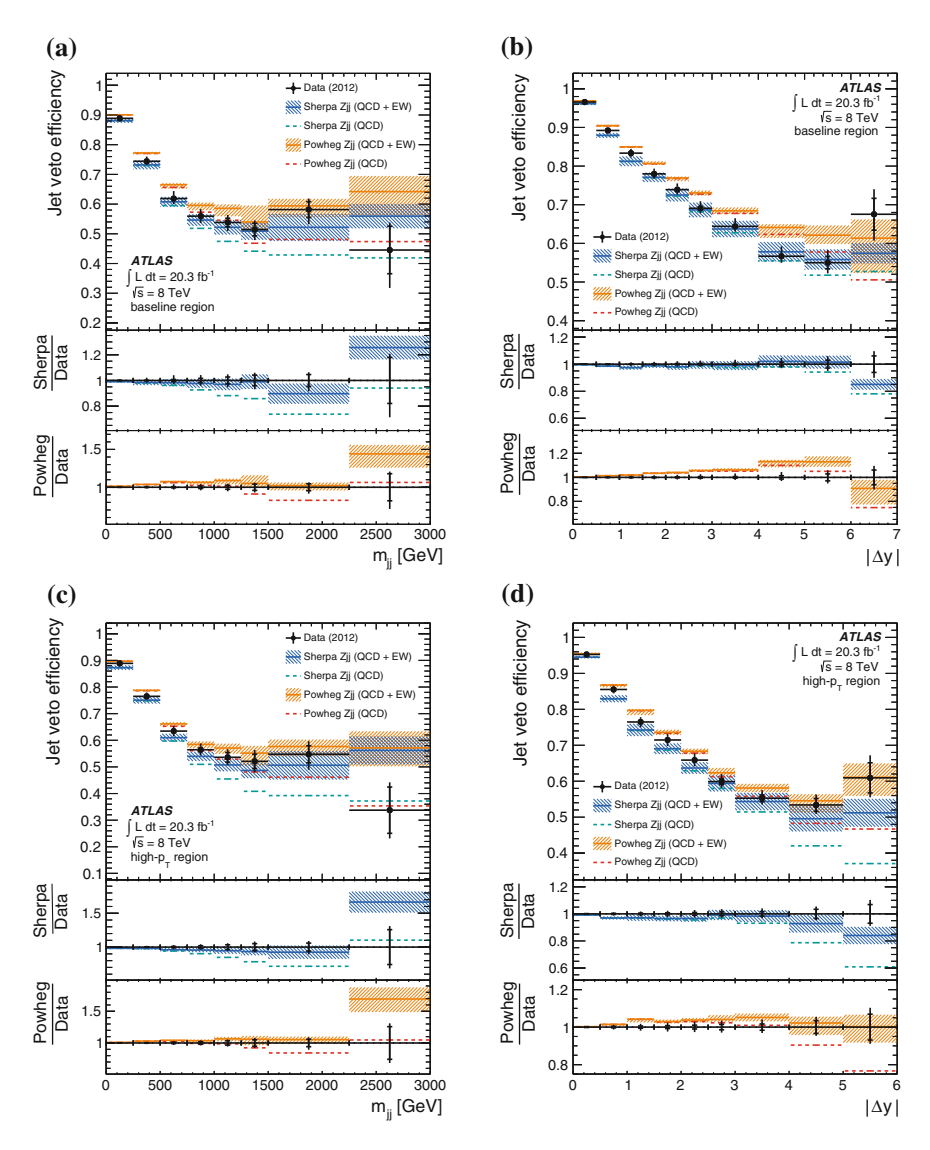


Fig. 7.23 Unfolded jet veto efficiency versus $m_{jj}(\mathbf{a}, \mathbf{c})$ and $|\Delta y|(\mathbf{b}, \mathbf{d})$ in the *baseline* (\mathbf{a}, \mathbf{b}) and high-p_T (\mathbf{c}, \mathbf{d}) regions. The data and theoretical predictions are presented in the same way as in Fig. 7.20

at large m_{jj} . POWHEG and SHERPA give equally good descriptions of the data and it is clear that for values of m_{jj} larger than 1 TeV the electroweak component of the cross section is crucial for correctly describing the shape of distribution in data. The m_{jj} distribution is therefore an obvious candidate for extracting the electroweak component of the cross section, as described in Sect. 7.6. Finally, in the *control* region

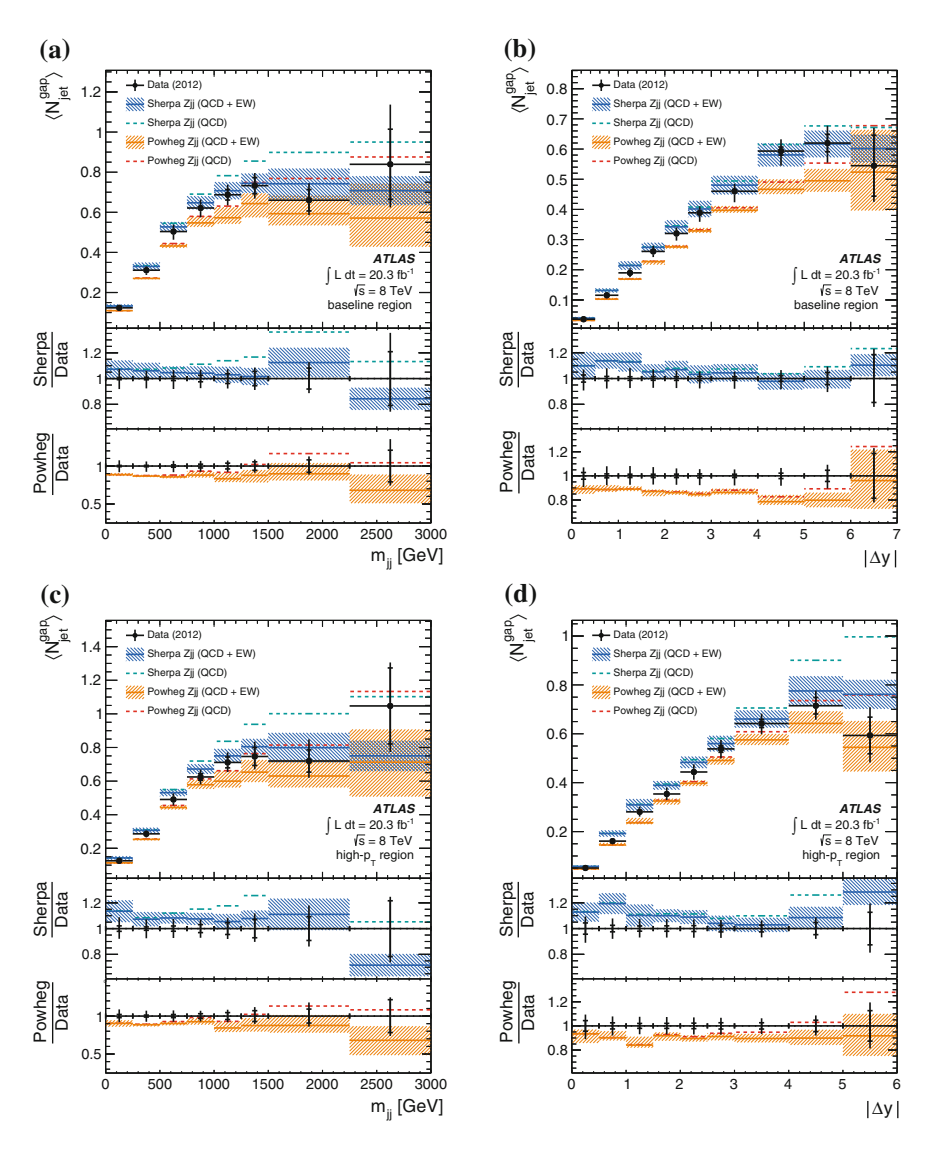


Fig. 7.24 Unfolded $\langle N_{\rm jets} \rangle$ distribution versus $m_{\rm jj}$ (**a**, **c**) and $|\Delta y|$ (**b**, **d**) in the *baseline* (**a**, **b**) and *high*-p_T (**c**, **d**) regions. The data and theoretical predictions are presented in the same way as in Fig. 7.20

there is again little difference between the QCD-only and QCD+EW predictions. POWHEG gives a good description of the data across the full range, while SHERPA shows some deviation from unfolded result for $m_{ij} > 1.5$ TeV.

The unfolded $\frac{1}{\sigma} \cdot \frac{\mathrm{d}\sigma}{\mathrm{d}N_{\mathrm{jet}}}$, $\frac{1}{\sigma} \cdot \frac{\mathrm{d}\sigma}{\mathrm{dp}_{\mathrm{p}}^{\mathrm{balance}}}$ and $\frac{1}{\sigma} \cdot \frac{\mathrm{d}\sigma}{\mathrm{d}|\Delta\phi(j,j)|}$ distributions in the *high-mass* region are shown in Fig. 7.22. The electroweak production process does not involve

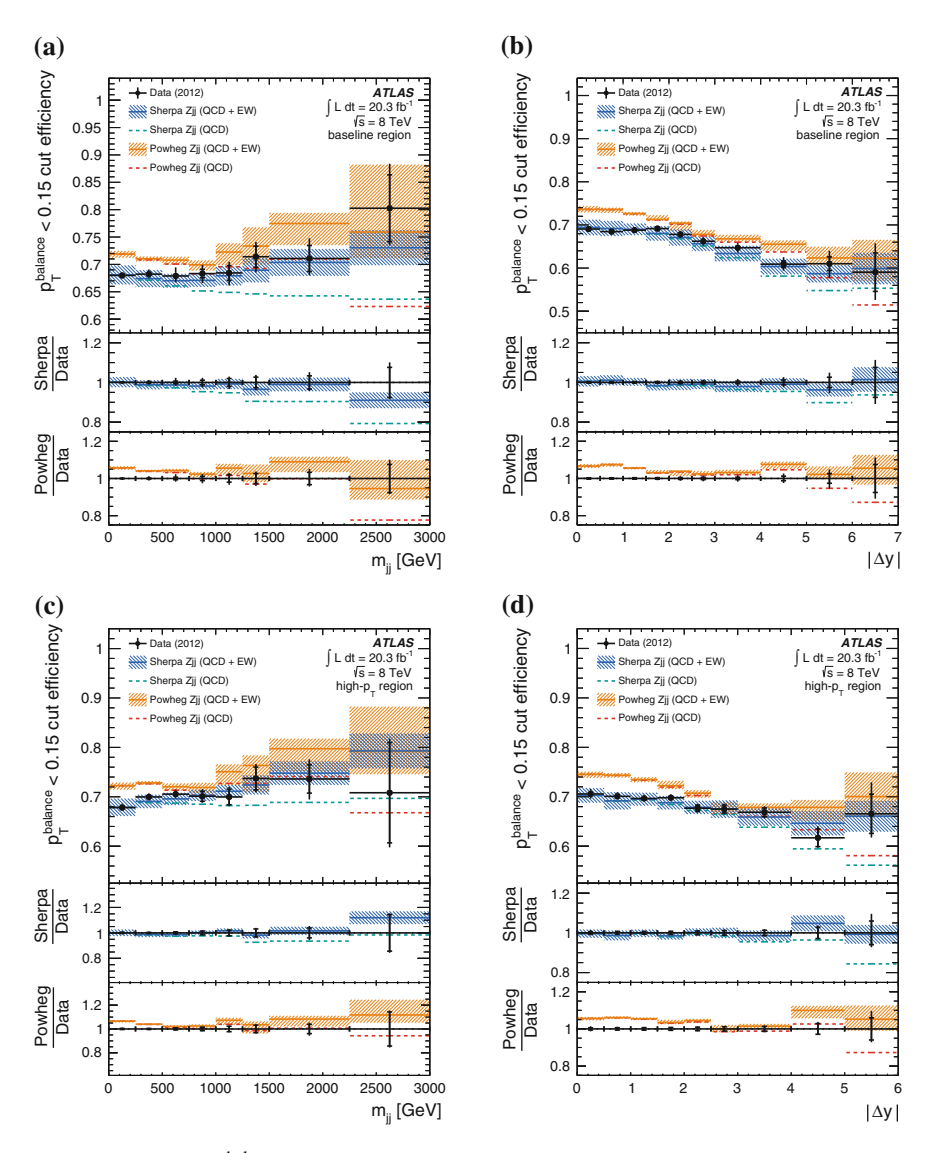


Fig. 7.25 Unfolded $p_T^{balance}$ cut efficiency versus m_{jj} (**a**, **c**) and $|\Delta y|$ (**b**, **d**) in the baseline (**a**, **b**) and high-p_T (**c**, **b**) regions. The data and theoretical predictions are presented in the same way as in Fig. 7.20

the exchange of any coloured particles in the t-channel, and therefore it is expected that little inter-jet radiation will be present in the production of electroweak Z_{jj} events. The lack of radiation between the two boundary jets in the events manifests itself as a more sharply peaked $N_{\rm jet}$ distribution and can be seen clearly in the first bin of Fig. 7.22a. This strengthens the argument that jet veto can be used to distinguish

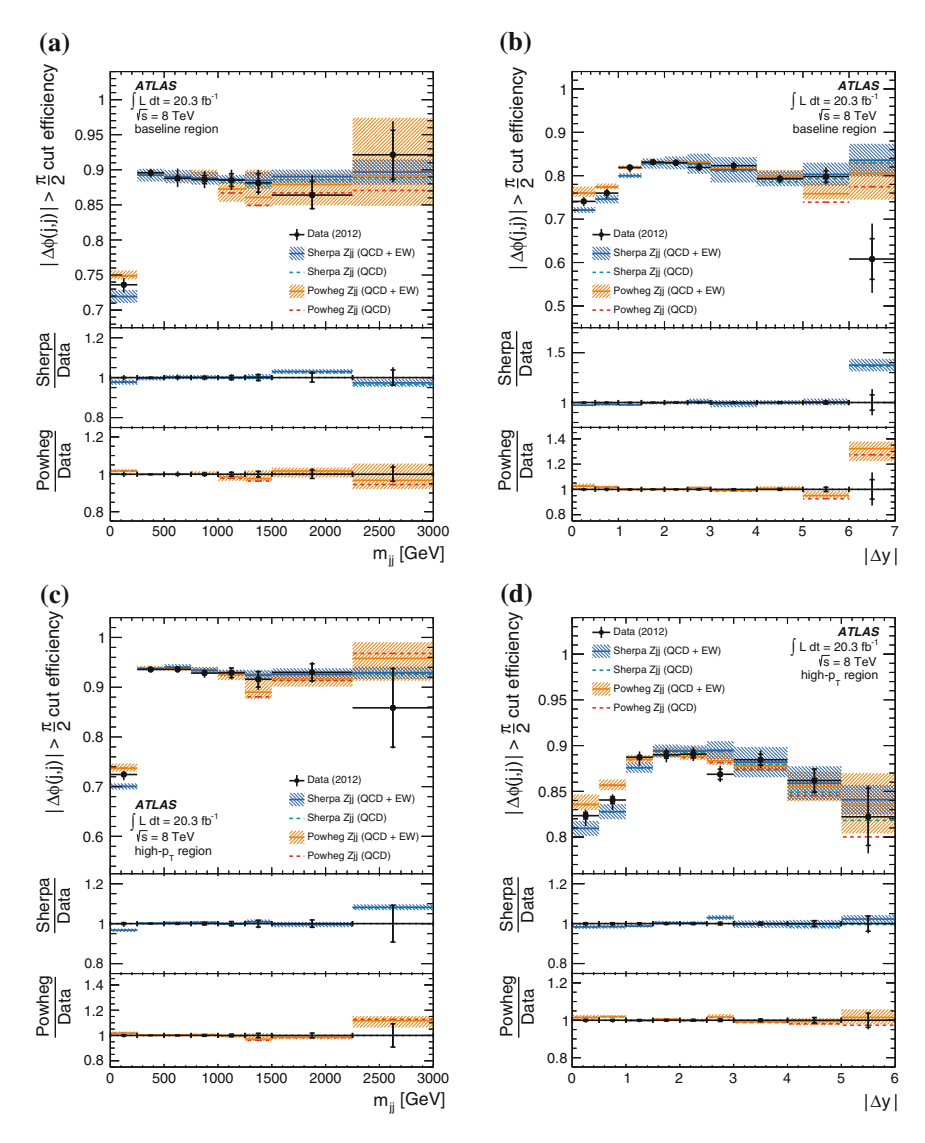


Fig. 7.26 Unfolded $\Delta \phi(j,j)$ cut efficiency versus m_{jj} (**a**, **c**) and $|\Delta y|$ (**b**, **d**) in the baseline (**a**, **b**) and high-p_T (**c**, **d**) regions. The data and theoretical predictions are presented in the same way as in Fig. 7.20

between the QCD and electroweak production mechanisms, as used in the definition of the *search* region. In general both SHERPA and POWHEG give good descriptions of the distributions measured in the *high-mass* region.

The unfolded jet veto efficiency and $\langle N_{\rm jets} \rangle$ as a function of $|\Delta y|$ and $m_{\rm jj}$ are shown in Figs. 7.23 and 7.24. As discussed previously, the lack of colour flow in the

electroweak production process means that little radiation should be produced in the region of rapidity between the two boundary jets. This is clear when comparing the QCD-only and QCD+EW predictions for both distributions in both regions of phase space. In Fig. 7.23 the jet veto efficiency from the QCD+EW prediction is closer to one at large values of $|\Delta y|$ and $m_{\rm jj}$, implying that fewer jets are being produced between the two boundary jets. Similarly in the $\langle N_{\rm jets} \rangle$ distribution the QCD-only predictions are noticeably higher than the QCD+EW ones. In general SHERPA and POWHEG give reasonable descriptions of the data, although it is SHERPA that gives a better prediction across the different phase space regions, and POWHEG is seen to systematically predict too little additional jet activity into the rapidity interval between the two boundary jets.

Finally the $p_T^{balance}$ *cut efficiency* and $\Delta\phi(j,j)$ *cut efficiency* distributions are shown as a function of $|\Delta y|$ and m_{jj} in Figs. 7.25 and 7.26. The separation between the QCD-only and QCD+EW predictions is obvious in the $p_T^{balance}$ *cut efficiency* distribution. The lack of inter-jet radiation in the electroweak production process leads to a higher proportion of events being produced in which the Z-boson is well-balanced against the dijet system. At large values of $|\Delta y|$ and m_{jj} the $p_T^{balance}$ in data is clearly better represented by the QCD+EW prediction. It is SHERPA that does a better job of describing the $p_T^{balance}$ *cut efficiency* in data, while both generators give a good description of the data in the $\Delta\phi(j,j)$ *cut efficiency*.

In general neither SHERPA or POWHEG can fully describe the data in all regions of phase space. For the differential distributions sensitive to the two leading jets it is POWHEG that performs better than SHERPA and more accurately describes the data at large $|\Delta y|$ and m_{jj} . This is expected because POWHEG produces Z_{jj} predictions at NLO in the *baseline* and *high*-pT regions. However, it is SHERPA that gives a better prediction for distributions that are sensitive to the amount of additional radiation produced in the events. POWHEG typically produces too little radiation into the interjet region. This difference is interesting due to the fact that both SHERPA and POWHEG are producing predictions that are leading order in the first extra emission. SHERPA is also leading order in emissions higher than the first, so in cases where the first additional jet falls outside the rapidity interval bounded by the two leading jets then SHERPA should be expected to perform slightly better. By making comparisons such as this we can probe the different approaches to generating events and constrain the uncertainties associated with modelling such topologies in these extreme regions of phase space.

7.6 Electroweak Zii Signal Extraction and Cross Section

As discussed in Sect. 7.5.1 the electroweak contribution to the Z_{jj} cross section is expected to be enhanced in certain regions of phase space. In this section the extraction of the electroweak Z_{jj} cross section will be discussed. This analysis was performed by a larger analysis team of four, therefore a brief description of the analysis method will be presented and detailed focus will be given to the parts of the analysis

sis in which the author played a primary role. Namely, the systematic uncertainties associated with the signal and background modelling, and the determination of limits on anomalous triple gauge couplings.

7.6.1 Extraction Technique

The electroweak component of the Z_{ij} cross section is extracted by performing a fit to the dijet invariant mass spectrum in the search region. As already seen in Fig. 7.21 the invariant mass spectrum is sensitive to the electroweak production process at large values of m_{ii} . The fit is performed using signal and background templates derived from MC. The signal template is made up of SHERPA electroweak Zii events. The background template is constructed from SHERPA QCD Zij events, as well as contributions from the tt and diboson backgrounds. Accurately and precisely describing the shape of the background is crucial for enabling the extraction of the electroweak cross section. Therefore the shape of the background template is constrained using the following data-driven method. A comparison is made between the data and MC m_{ii} spectra in the *control* region. The ratio of data to MC is fitted with a second order polynomial and the fitted function is then used to reweight background m_{ii} template in the search region. Using this technique the experimental and theoretical uncertainties associated with the background template are minimised, and the description of the Z_{ii} events provided by the MC generator is used only to extrapolate between the control and search regions.

After the number of expected electroweak events ($N_{\rm EW}$) has been extracted from the fit, it is converted into a fiducial cross section through the use of a correction factor that accounts for differences in the numbers of selected events at reconstruction and particle level due to detector inefficiencies and resolutions.

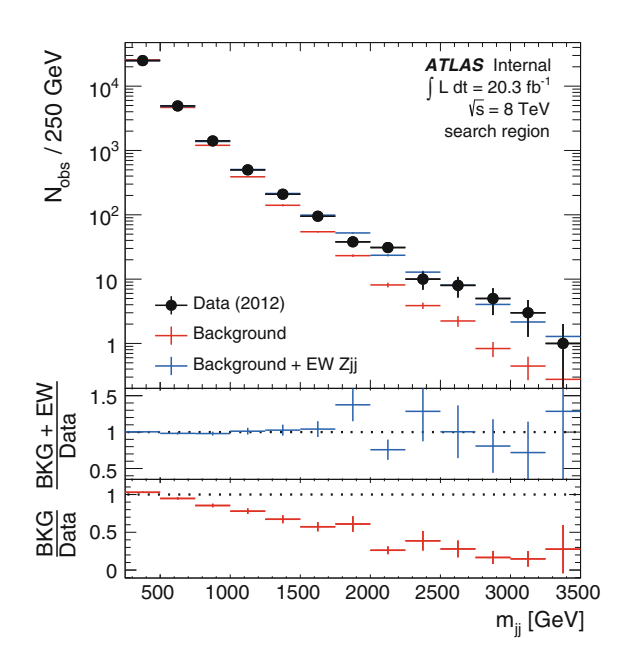
An example fit result is shown in Fig. 7.27, and Table 7.4 summarises the MC predictions and fit results in the electron and muon channels.

	Electron	Muon
Data	14,248	17,938
MC predicted N _{bkg}	$13700 \pm 1200^{+1400}_{-1700}$	$18600 \pm 1500^{+1900}_{-2300}$
MC predicted N _{EW}	$602 \pm 27^{+18}_{-18}$	$731 \pm 29^{+22}_{-22}$
Fitted N _{bkg}	$13351 \pm 144 \pm 29$	$17201 \pm 161 \pm 31$
Fitted N _{EW}	$897 \pm 92 \pm 27$	$737 \pm 98 \pm 28$

Table 7.4 From [7]. The number of fitted strong and electroweak Z_{ij} events

The statistical uncertainties on the fit results due to data and simulation are shown as the first and second uncertainties, respectively. The number of events in data is also presented, in addition to the predictions from the MC simulation for strong and electroweak Z_{jj} production. The first and second uncertainties in the MC prediction represent the experimental and theoretical systematic uncertainties, respectively.

Fig. 7.27 From [7]. The dijet invariant mass distribution in the *search* region. The signal and constrained background templates are scaled to match the number of events obtained in the fit



7.6.2 Experimental Systematic Uncertainties

The systematic uncertainty on $N_{\rm EW}$ has contributions from the uncertainty in the function used to reweight the background template, and standard experimental systematic uncertainties such as the jet energy scale, jet energy resolution and pile-up modelling. Details of the studies used to estimated the size of the uncertainty on the reweighting function and the various sources of experimental uncertainty can be found in [7, 31], and a summary of the sizes of these systematic uncertainties is given in Table 7.5.

7.6.3 Theoretical Modelling of the Signal and Background

The theoretical uncertainties on the signal and background templates are estimated using dedicated MC samples generated to assess the uncertainties on the particle-level differential distributions. As described in 7.3, Monte Carlo samples were generated with varied renormalisation and factorisation scales, a different value of the CKKW matching parameter and variations to the parameters that control the multiple parton interaction model. To ensure that the effects of limited MC statistics are not accounted for several times, the associated uncertainty on $N_{\rm EW}$ is estimated using toy experiments. The procedure differs slightly depending on whether the systematic is affecting the signal or background template. In the case of the signal template, for

Source	ΔN_{EW}		$\Delta \mathcal{C}_{ ext{EW}}$		
	Electrons (%)	Muons (%)	Electrons (%)	Muons (%)	
Lepton systematics	_	_	±3.2	±2.5	
Control region statistics	±8.9	±11.2	_	_	
JES	±5.6		+2.7 -3.4		
JER	±0.4		±0.8	±0.8	
Pileup jet modelling	±0.3		±0.3		
JVF	±1.1		+0.4 -1.0		
Signal modelling	±8.9		+0.6 -1.0		
Background modelling	±7.5		_		
Signal/background interference	±6.2		-		
PDF	+1.5 -3.9		±0.1		

Table 7.5 From [7]. Systematic uncertainties, expressed in percentages, on (i) the number of fitted signal events in the *search* region, N_{EW} , and (ii) the correction factor to the particle-level, C_{EW}

The uncertainties are anti-correlated between $N_{\rm EW}$ and $C_{\rm EW}$.

each source of uncertainty the corresponding systematically shifted $\frac{1}{\sigma} \cdot \frac{d\sigma}{dm_{jj}}$ distribution in the *search* region is Gaussian fluctuated in every bin. The width of the Gaussian distribution used is set to the MC statistical uncertainty in each bin. The fluctuated, shifted distribution is then compared to the nominal $\frac{1}{\sigma} \cdot \frac{d\sigma}{dm_{jj}}$ distribution and the shifted-to-nominal-ratio is fitted with a second order polynomial. The polynomial is then used to reweight the signal template in the *search* region directly and the fit for the number of electroweak events is repeated using the new signal template.

For the background template it is the *control*-to-*search* region extrapolation which is important to assess. The shifted $\frac{1}{\sigma} \cdot \frac{d\sigma}{dm_{jj}}$ distributions in both the *control* and *search* regions are Gaussian fluctuated and their ratio is taken. The *search/control* ratio using the systematically shifted distributions is compared to the *search/control* using the nominal MC. This double ratio is fitted with a first order polynomial, which is then used to reweight the background template in the *search* region. The fit for the $N_{\rm EW}$ is then repeated.

1000 toy experiments were performed and the resulting distribution of $N_{\rm EW}$ was fitted with a Gaussian distribution in order to find its mean, $\mu_{\rm toy}$, and width, $\sigma_{\rm toy}$. The difference between $N_{\rm EW}$ and $\mu_{\rm toy} \pm \sigma_{\rm toy}$ is taken as a symmetrised systematic uncertainty. The total theoretical uncertainty is found by taking the envelope of the various generator-level variations.

 $^{^4\}sigma_{\rm toy}$ is either added or taken away from $\mu_{\rm toy}$ to produce the largest difference with respect to the nominal $N_{\rm FW}$.

7.6.4 Uncertainty Due to Signal and Background Interference

The strong and electroweak Monte Carlo samples were generated and used independently throughout the measurements of the differential cross sections and extraction of the electroweak component of the cross section. However, there exists the possibility of interference between the strong and electroweak production mechanisms. The interference between the strong and electroweak production of a Higgs boson in association with dijets (H_{ii}) has been calculated and found to be negligible [34–37]. No similar calculations have been performed for the case of Z_{ii} production, however the source of the interference is expected to be the same as in the H_{ii} case and so typically the assumption is made that the interference between the strong and electroweak Z_{ii} production is also small. The systematic uncertainty associated with the possible interference between the electroweak and QCD production was estimated by generating dedicated SHERPA samples in which the interference was included. In the default SHERPA samples, in which the QCD and electroweak processes are generated separately, the MC is set up by providing the incoming and outgoing partons for the process of interest, and the number of QCD or EW vertices the process must contain. For example, the default QCD Zii samples can be generated by specifying the following lines

```
Process 93 93 -> 13 -13 93{4} Order_EW 2
```

where 93 is a shorthand for gluons and light quarks, 93 {x} requests *up to* x additional partons of type 93, and Order_EW 2 specifies that all Feynman diagrams must have two electroweak couplings, e.g. the production and decay of a Z-boson. Events comprising the electroweak processes are generated by setting

```
Process 93 93 -> 13 -13 93 93 93 {1} Order_EW 4 Min_N_TChannels 1.
```

The reduced number of additional partons in the final state speeds up the calculations of the matrix elements and generation of the events, four electroweak couplings are requested and $\texttt{Min_N_TChannels}\ 1$ forces there to be at least one exchange of an electroweak gauge boson thereby removing contributions from diboson-initiated Z_{ij} events such as the example given in Fig. 7.2c.

A sample of events made up of both QCD and electroweak processes can be generated by setting

```
Process 93 93 -> 13 -13 93 93 Max_Order_EW 4
```

where Max_Order_EW 4 specifies that diagrams with up to four electroweak couplings should be generated. The reason for reverting to the core Z_{jj} process, and foregoing any matching of the matrix elements to the parton shower, was to avoid the problem of the SHERPA automatic scale setter not coping well with the case of diagrams with different orders of the electroweak coupling [38]. Using these settings both the QCD and electroweak matrix elements are included at the amplitude level,

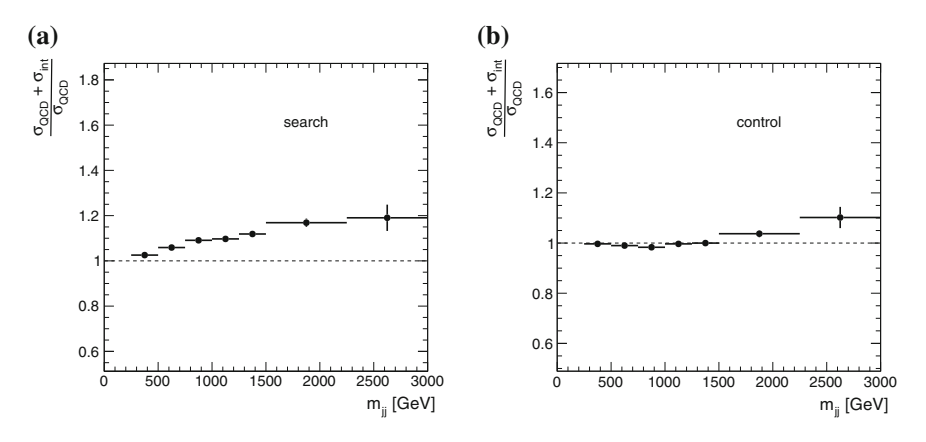


Fig. 7.28 The effect of interference on the QCD-only m_{jj} distribution in the **a** search, and **b** control regions

and therefore the interference between them will also be calculated. These events will be referred to as the *Both* sample. New samples of QCD-only and EW-only events were also generated using just the core $2 \rightarrow 4$ configuration to ensure fair comparisons.

The change in shape of the m_{jj} distribution due to the interference terms was estimated by subtracting the m_{jj} distribution in the QCD-only and EW-only samples from the Both sample, i.e. $m_{jj}^{int.} = m_{jj}^{Both-QCD-EW}$, after normalising each to their respective fiducial cross sections. To estimate how this interference might affect the fit for N_{EW} , $m_{ij}^{int.}$ is added to m_{jj}^{QCD} (Fig. 7.28) and used to derive a reweighting function. This function is then used to reweight the background template in the *search* or *control* regions only, where the assumption is made that the interference affects only one of the regions and therefore provides a conservative estimate of the uncertainty by maximising the effect on the measurement.

When reweighting the background template in the *search* region the value of $N_{\rm EW}$ was reduced by 6.2%. Reweighting the background template in the *control* region resulted in the extracted value of $N_{\rm EW}$ increasing by 6.2%. Therefore an additional, conservative, systematic uncertainty of $\pm 6.2\%$ was assigned to the final measurement.

The effect of the interference on the unfolded differential distributions was estimated using the same set of dedicated MC samples, and found to be negligible.

7.6.5 Electroweak Fiducial Cross Section Results

The measured fiducial cross sections in the electron and muon channels were

$$\sigma^{ee}_{\rm EW} = 67.2 \pm 6.9 \, ({\rm stat})^{+12.7}_{-13.4} \, ({\rm syst}) \, \pm 1.9 \, ({\rm lumi}) \, {\rm fb}$$
 and $\sigma^{\mu\mu}_{\rm EW} = 45.6 \, \pm 6.1 \, ({\rm stat})^{+9.6}_{-9.6} \, ({\rm syst}) \, \pm 1.3 \, ({\rm lumi}) \, {\rm fb}.$

The measurements in the two channels are consistent to within 1.7σ when taking into account the systematic uncertainties that are uncorrelated between the channels. The two results are then combined using a weighted average, where the weight for each channel is taken to be the inverse of the square of the uncorrelated uncertainty.

The combined fiducial cross section is

$$\sigma_{\rm EW} = 54.7 \pm 4.6 \, ({\rm stat})^{+9.8}_{-10.4} \, ({\rm syst}) \pm 1.5 \, ({\rm lumi}) \, {\rm fb},$$

and the theoretical prediction from POWHEG for the electroweak Z_{jj} cross section is $46.1 \pm 0.2 \, (\text{stat})^{+0.3}_{-0.2} \, (\text{scale}) \, \pm 0.8 \, (\text{PDF}) \, \pm 0.5 \, (\text{model})$ fb, which is in good agreement with the data. The significance of the extracted signal is estimated using pseudoexperiments and the background-only hypothesis was rejected at greater than 5σ significance.

The fiducial cross section for electroweak Z_{jj} production was also extracted using events in the *search* region that also have $m_{jj} > 1$ TeV, by simply integrating the fitted signal template. This extreme region of phase space has the most sensitivity to the electroweak component of the Z_{jj} cross section, and therefore the least sensitivity to the normalisation of the background. The measured value of the fiducial cross section in this region was

$$\sigma_{\rm EW} (m_{\rm jj} > 1 \,{\rm TeV}) = 10.7 \pm 0.9 \,({\rm stat}) \,\pm 1.9 \,({\rm syst}) \,\pm 0.3 \,({\rm lumi}) \,{\rm fb},$$

which, once more, is in good agreement with the prediction of the fiducial Z_{jj} cross section from POWHEG, of

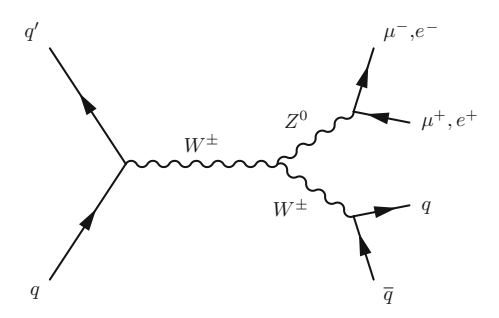
$$9.38 \pm 0.05 \, (\text{stat})^{+0.15}_{-0.24} \, (\text{scale}) \, \pm 0.24 \, (\text{PDF}) \, \pm 0.09 \, (\text{model}) \, \text{fb}$$

7.7 Limits on Anomalous Triple Gauge Couplings

The observation of electroweak Z_{jj} production enables limits to be placed on anomalous triple gauge couplings (aTGCs). Typically aTGC limits have been set by measuring vector boson pair production (Fig. 7.29), wherein all three bosons entering the WWZ vertex have time-like momentum.

In the VBF production process (cf. Fig. 7.1b) however, two of the gauge bosons have space-like momentum transfer. Therefore electroweak Z_{jj} can be used to provide a complimentary test of aTGCs. Indeed, it has been emphasised that complete information about triple gauge couplings can only be obtained if VBF production is measured in addition to vector boson pair production [39].

Fig. 7.29 An example Feynman diagram showing vector boson pair production



The effective Lagrangian, \mathcal{L} , for aTGCs can be written as

$$\frac{\mathcal{L}}{i \cdot g_{WWZ}} = g_{1,Z} \left(W_{\mu\nu}^{\dagger} W^{\mu} Z^{\nu} - W_{\mu\nu} W^{\dagger\mu} Z^{\nu} \right)
+ \kappa_Z W_{\mu}^{\dagger} W_{\nu} Z^{\mu\nu} + \frac{\lambda_Z}{m_W^2} W_{\rho\mu}^{\dagger} W_{\nu}^{\mu} Z^{\nu\rho}$$
(7.13)

if only terms that conserve charge conjugation and parity are retained from the general expression [40]. Here we have $g_{WWZ}=-e\cot(\theta_W), e$ is the electric charge, θ_W is the weak mixing angle, W^μ and Z^μ are the W-boson and Z-boson fields, $X_{\mu\nu}=\partial_\mu X_\nu-\partial_\nu X_\mu$ with X=W or Z and $g_{1,Z}$, κ_Z and λ_Z are dimensionless couplings. The SM values of these couplings are $g_{1,Z}^{\rm SM}=1, \kappa_Z^{\rm SM}=1$ and $\lambda_Z=0$.

When using this effective Lagrangian the tree-level *S*-matrix violates unitarity at large energy scales, which is preserved in the full theory by form factor effects, i.e. the couplings can be modified by a dipole form factor

$$a(\hat{s}) = \frac{a_0}{(1 + \hat{s}/\Lambda^2)^2}$$

where a_0 is the bare coupling, \hat{s} is the partonic centre-of-mass energy and Λ is a unitarisation scale. In this measurement two choices of unitarisation scale are made, $\Lambda = 6$ TeV and $\Lambda = \infty$.

Limits on the aTGCs are set by counting the number of events that enter the search region and also have $m_{jj} > 1$ TeV. There are 900 such events in data. 291 signal events are estimated using the SHERPA electroweak Z_{jj} samples and 592 background events are expected after fitting the m_{jj} spectrum with signal and background templates. The change in number of signal events for a given aTGC form factor and set of parameter variations is estimated by varying the corresponding parameters in SHERPA and generating a new sample of events. For a given aTGC parameter, the predicted number of signal events at detector level, $N_{\rm det}^{\rm aTGC}$, is estimated by

$$\frac{N_{\rm det}^{\rm aTGC}}{N_{\rm det}^{\rm SM}} = \frac{\sigma^{\rm aTGC}}{\sigma^{\rm SM}} , \qquad (7.14)$$

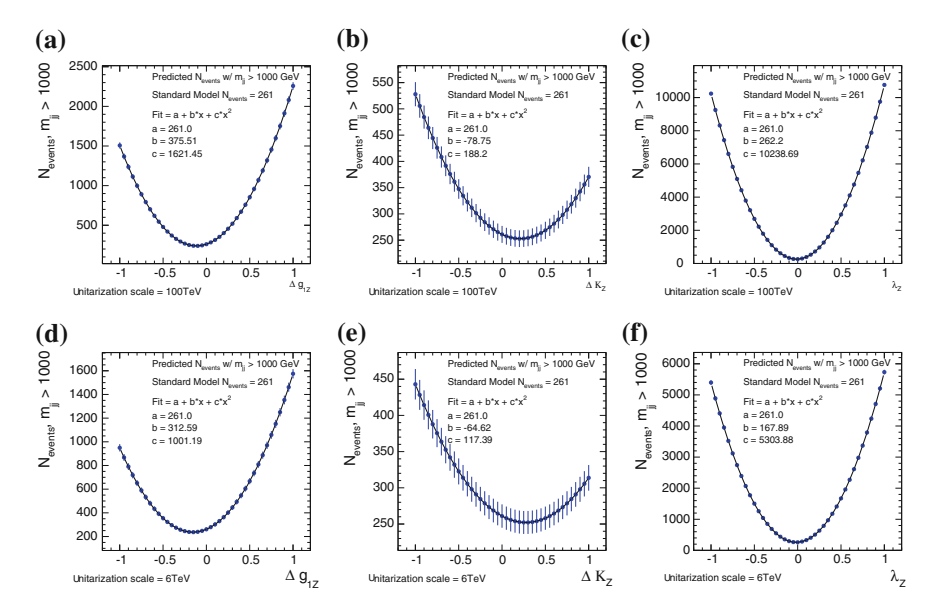


Fig. 7.30 The expected number of signal events with $m_{\rm jj} > 1$ TeV in the *search* region as a function of **a** $\Delta g_{1,Z}$, **b** $\Delta \kappa_Z$ and **c** λ_Z , for a unitarisation scale of 100 TeV. Figures (**c**-**f**) show the same plots but for a unitarisation scale of 6 TeV. In each of these plots, one parameter is varied whilst the other parameters are fixed to the SM values

where $N_{\rm det}^{\rm SM}=261$ is the predicted number of events for the SM coupling, $\sigma^{\rm aTGC}$ is the electroweak aTGC cross section in the fiducial region (*search* region plus $m_{\rm jj}>1\,{\rm TeV}$) and $\sigma^{\rm SM}$ is the electroweak SM cross section in the same fiducial region.

Figure 7.30 shows the predicted number of signal events when varying a given aTGC parameter and keeping the others fixed to their SM values. Changing the aTGC parameters in the Lagrangian in Eq. (7.13) corresponds to altering the matrix elements ultimately used to calculate the cross section. Since cross sections are proportional to squared matrix elements, altering the aTGC parameters leads to changes in the cross section that can be fit with the quadratic functions shown in Fig. 7.30. There is a large increase in the number of events for large values of $\Delta g_{1,Z}$ and $\Delta \lambda_Z$, implying that this analysis will be most sensitive to those coupling parameters.

The expected number of signal events are used, along with the estimated number of background events and information about the size of systematic uncertainties, as input to the ATLAS Standard Model groups fitting code, in which a profile likelihood test [41] is used to set frequentist confidence intervals. Full details can be found in [31, 42].

Table 7.6 shows the 95 % confidence intervals obtained on the anomalous coupling parameters $\Delta g_{1,Z}$ and λ_Z . The limits are not as powerful as the ones which have been set in a previous ATLAS measurement of WZ production [43], however they are the first ever limits set on aTGCs using the vector boson fusion production channel.

the number of events with $m_{\parallel} > 1$ for in the search region					
aTGC	$\Lambda = 6 \text{TeV (obs)}$	$\Lambda = 6 \text{TeV (exp)}$	$\Lambda = \infty \text{ (obs)}$	$\Lambda = \infty \text{ (exp)}$	
$\Delta g_{1,Z}$	[-0.65, 0.33]	[-0.58, 0.27]	[-0.50, 0.26]	[-0.45, 0.22]	
λ_Z	[-0.22, 0.19]	[-0.19, 0.16]	[-0.15, 0.13]	[-0.14, 0.11]	

Table 7.6 From [7]. The 95 % confidence intervals obtained on the aTGC parameters from counting the number of events with $m_{ii} > 1$ TeV in the *search* region

Observed and expected intervals, labelled 'obs' and 'exp' respectively, are presented for unitarisation scales of $\Lambda=6$ TeV and $\Lambda=\infty$

References

- 1. ATLAS Collaboration, (2012). Measurement of the production cross section for Z/gamma* in association with jets in pp collisions at $\sqrt{s} = 7$ TeV with the ATLAS detector. *Physical Review*, D85, 032009.
- 2. ATLAS Collaboration, (2013). Measurement of the production cross section of jets in association with a Z boson in pp collisions at $\sqrt{s} = 7$ TeV with the ATLAS detector. *JHEP*, 07, 032.
- 3. Chatrchyan, S., et al. (2012). Jet production rates in association with W and Z Bosons in pp collisions at $\sqrt{s} = 7$ TeV. *JHEP*, 1201, 010.
- Khachatryan, V., et al. (2014). Measurements of jet multiplicity and differential production cross sections of Z+jets events in proton-proton collisions at sqrt(s) = 7 TeV. arXiv: 1408.3104 [hep-ex].
- Arnold, K., Bellm, J., Bozzi, G., Brieg, M., Campanario, F. et al., (2001). VBFNLO: A Parton Level Monte Carlo for processes with electroweak Bosons - manual for version 2.5.0. arXiv: 1107.4038 [hep-ph].
- Oleari, C., & Zeppenfeld, D. (2004). QCD corrections to electroweak nu(l) j j and l+ l- j j production. *Physical Review D*, 69, 093004.
- 7. ATLAS Collaboration, (2014). Measurement of the electroweak production of dijets in association with a Z-boson and distributions sensitive to vector boson fusion in proton-proton collisions at $\sqrt{s} = 8$ TeV using the ATLAS detector. *JHEP*, 1404, 031.
- ATLAS Muon Combined Performance Guidelines for Analyses of 2012 Data. Retrieved 31 July 2014, from https://twiki.cern.ch/twiki/bin/viewauth/AtlasProtected/ MCPAnalysisGuidelinesData2012.
- 9. Gleisberg, T., Hoeche, S., Krauss, F., Schonherr, M., Schumann, S., et al. (2009). Event generation with SHERPA 1.1. *JHEP*, 0902, 007.
- Nason, P. (2004). A new method for combining NLO QCD with shower Monte Carlo algorithms. JHEP, 0411, 040.
- 11. Frixione, S., Nason, P., & Oleari, C. (2007). Matching NLO QCD computations with Parton Shower simulations: The POWHEG method. *JHEP*, 0711, 070.
- 12. Alioli, S., Nason, P., Oleari, C., & Re, E. (2010). A general framework for implementing NLO calculations in shower Monte Carlo programs: The POWHEG BOX. *JHEP*, 1006, 043.
- 13. Catani, S., Krauss, F., Kuhn, R., & Webber, B. (2001). QCD matrix elements + parton showers. *JHEP*, 0111, 063.
- 14. Campbell, J. M., Ellis, R. K., Nason, P., & Zanderighi, G. (2013). W and Z bosons in association with two jets using the POWHEG method. *JHEP*, *1308*, 005.
- Jager, B., Schneider, S., & Zanderighi, G. (2012). Next-to-leading order QCD corrections to electroweak Zjj production in the POWHEG BOX. *JHEP*, 1209, 083.
- Hamilton, K., Nason, P., & Zanderighi, G. (2012). MINLO: Multi-scale improved NLO. JHEP, 1210, 155.
- 17. Hoeche, S., Schumann, S., & Siegert, F. (2010). Hard photon production and matrix-element parton-shower merging. *Physical Review D*, 81, 034026.

References 175

 Schumann, S., & Krauss, F. (2008). A Parton shower algorithm based on Catani-Seymour dipole factorisation. JHEP, 0803, 038.

- 19. Hoeche, S., & Schonherr, M. (2012). Uncertainties in next-to-leading order plus parton shower matched simulations of inclusive jet and dijet production. *Physical Review D*, 86, 094042.
- Skands, P. Z. (2010). Tuning Monte Carlo generators: The Perugia tunes. *Physical Review D*, 82, 074018.
- Agostinelli, S. et al., (2003). Geant4-a simulation toolkit. Nuclear Instruments and Methods in Physics Research Section A: Accelerators, Spectrometers, Detectors and Associated Equipment, 506, 250–303. issn: 0168–9002.
- Allison, J., et al. (2006). Geant4 developments and applications. *IEEE Transactions on Nuclear Science*, 53, 270–278. issn: 0018–9499.
- ATLAS Collaboration, (2011). Further ATLAS tunes of PYTHIA6 and Pythia 8 tech. rep. ATL-PHYS-PUB-2011-014 (CERN, Geneva).
- 24. Martin, A., Stirling, W., Thorne, R., & Watt, G. (2009). Parton distributions for the LHC. *European Physical Journal C*, 63, 189–285.
- Mangano, M. L., Moretti, M., Piccinini, F., Pittau, R., & Polosa, A. D. (2003). ALPGEN, a generator for hard multiparton processes in hadronic collisions. *JHEP*, 0307, 001.
- ATLAS Collaboration, (2011). New ATLAS event generator tunes to 2010 data tech. rep. ATL-PHYS-PUB-2011-008 (CERN, Geneva).
- Frixione, S., & Webber, B. R. (2002). Matching NLO QCD computations and parton shower simulations. JHEP, 0206, 029.
- 28. Czakon, M. & Mitov, A. (2011). Top++: A program for the calculation of the top-pair cross-section at Hadron colliders. arXiv: 1112.5675 [hep-ph].
- 29. D'Agostini, G. (2010). Improved iterative Bayesian unfolding. ArXiv e-prints. arXiv: 1010.0632 [physics.data-an].
- 30. D'Agostini, G. (2010). Improved iterative Bayesian unfolding. arXiv:1010.0632 [hep-ph].
- 31. Gutschow, C., Jones, G., Joshi, K., Nurse, E., & Pilkington, A. D. (2013) Measurement of the electroweak Z-boson plus dijet production cross section and distributions sensitive to the vector boson fusion production process in pp collisions at sqrts = 8 TeV with the ATLAS detector tech. rep. ATL-COM-PHYS-2013-331 (CERN, Geneva).
- 32. ATLAS Collaboration, (2012). Measurements of the pseudorapidity dependence of the total transverse energy in proton-proton collisions at $\sqrt{s} = 7$ TeV with ATLAS. *JHEP*, 1211, 033.
- 33. ATLAS Standard Model Working Group unfolding recommendations. Retrieved June 13, 2014, from https://twiki.cern.ch/twiki/bin/view/AtlasProtected/StandardModelUnfolding_# How should systematic uncertaint.
- 34. Andersen, J. R., & Smillie, J. M. (2007). QCD and electroweak interference in Higgs production by gauge boson fusion. *Physical Review D*, 75, 037301.
- 35. Ciccolini, M., Denner, A., & Dittmaier, S. (2008). Electroweak and QCD corrections to Higgs production via vector-boson fusion at the LHC. *Physical Review D*, 77, 013002.
- 36. Andersen, J., Binoth, T., Heinrich, G., & Smillie, J. (2008). Loop induced interference effects in Higgs Boson plus two jet production at the LHC. *JHEP*, 0802, 057.
- 37. Bredenstein, A., Hagiwara, K., & Jager, B. (2008). Mixed QCD-electroweak contributions to Higgs-plus-dijet production at the LHC. *Physical Review D*, 77, 073004.
- 38. Siegert, F. (2013). Private communication. Nov., 1,
- 39. Baur, U. & Zeppenfeld, D. (1993). Measuring three vector boson couplings in $qq \rightarrow qqW$ at the SSC. arXiv:hep-ph/9309227 [hep-ph].
- 40. Hagiwara, K., Peccei, R., Zeppenfeld, D., & Hikasa, K. (1987). Probing the Weak Boson sector in e⁺e⁻ → W⁺W⁻. Nuclear Physics, B282, 253.
- 41. Cowan, G., Cranmer, K., Gross, E., & Vitells, O. (2011). Asymptotic formulae for likelihood-based tests of new physics. *European Physical Journal C*, 71, 1554.
- 42. Blazey, G. et al., (2012). A measurement of WZ production in proton-proton collisions at sqrt(s) = 7 TeV with the ATLAS Detector tech. rep. ATL-COM-PHYS-2012-488 (CERN, Geneva).
- 43. ATLAS Collaboration. Measurement of WZ production in proton-proton collisions at $\sqrt{s} = 7$ TeV with the ATLAS detector. ATLAS Collaboration.

Chapter 8 Conclusions

The QCD description of quark and gluon radiation is important for a wide range of ATLAS analyses, since uncertainties associated with the QCD modelling can be large. Studies have been performed to precisely measure properties of the quark and gluon radiation in top-antitop and Z+ jets final states. Those properties have also been exploited to determine characteristics of the underlying physical processes in which the radiation was observed.

A measurement of $t\bar{t}$ production with a veto on additional central jet activity was performed using $2.05\,\mathrm{fb^{-1}}$ of proton-proton collision data collected by ATLAS at $\sqrt{s}=7\,\mathrm{TeV}$. A precise measurement of the jet veto efficiency performed for the first time in $t\bar{t}$ events showed generally good agreement between the data and predictions produced with next-to-leading order and multi-leg leading order Monte Carlo generators. However in some regions of phase space the precision of the measurement allowed some slight deviations to be observed. For example the MC@NLO generator was found to underestimate the amount of additional radiation produced in very central regions of the detector, |y|<0.8. The results were used to constrain the uncertainty associated with the QCD modelling of quark and gluon radiation in $t\bar{t}$ events. The uncertainty was reduced by approximately a factor of two and lead to reduced uncertainties for all subsequent measurements sensitive to $t\bar{t}$ final states.

Two phenomenology studies of the additional quark and gluon radiation in boosted $t\bar{t}$ events were also performed. In the first, dedicated algorithms were used to tag hadronically decaying boosted top jets, produced in the decay of a new heavy resonance. The remaining soft radiation was analysed, and it was determined that the jet veto efficiency can be used as a tool to identify the colour structure—colour singlet or colour octet—of a new heavy particle decaying to $t\bar{t}$. A detailed feasibility study showed that if a heavy resonance was observed at the LHC, its colour could be reliably extracted with around $10\,{\rm fb}^{-1}$ of data recorded at $\sqrt{s}=14\,{\rm TeV}$.

During the first phenomenology study an unexpected difference was observed in the efficiency to tag top-jets originating from either the colour singlet or colour octet resonance. This was investigated further in a follow-up study. Detailed investigations using four widely-used top-tagging algorithms confirmed that the colour structure of an event can have a large impact on the efficiency of tagging top-jets. The difference 178 8 Conclusions

was found to be due to the different patterns of quark and gluon radiation produced in association with the tt system. A heavy colour singlet s-channel resonance produces more additional radiation than a heavy colour octet. This is in stark contrast to the exchange of a t-channel colour singlet, such as the vector boson fusion system studied later. The flow of colour from initial to final state in that case results in reduced amounts of additional quark and gluon radiation. The additional soft radiation produced in association with the heavy resonances and tt systems contaminates the jets used as inputs to the top-tagging algorithms and worsens their performance. The results have consequences for experimental searches; the algorithm used should be considered carefully, and the algorithm parameters optimised to minimise the efficiency differences. In particular, jets used as input to the algorithms should be defined using a radius parameter that is as small as is feasible, and attention must be paid to the tightness of cuts since efficiency differences increase as background mis-tag probabilities are reduced.

Finally, measurements of the electroweak production of a dijets in association with a Z-boson and distributions sensitive to vector boson fusion were performed using pp collision data recorded by ATLAS at $\sqrt{s}=8$ TeV. Five regions of phase space were defined with varying sensitivity to the electroweak component of the Z_{jj} cross section, and several distributions were measured in each region of phase space. For example differential cross sections as a function of various kinematic properties of the dijet system and distributions sensitive to the additional radiation produced in the events, such as the jet veto efficiency. An iterative Bayesian unfolding procedure was used to correct the measured data for detector acceptance and resolution effects. Data were then compared to predictions from next-to-leading order and multi-leg leading order Monte Carlo generators, which were able to describe the data with varying degrees of success. The electroweak contribution to the Z_{jj} cross section was extracted using a two-component template fit to the dijet invariant mass distribution in a *search* region of phase space in which the electroweak component was expected to be enhanced. A fiducial cross section of

$$54.7 \pm 4.6 \, (stat)^{+9.8}_{-10.4} \, (syst) \, \pm 1.5 \, (lumi) \, fb$$

was measured and found to be in good agreement with the next-to-leading order theory prediction of

$$46.1 \pm 0.2 \, (\text{stat})^{+0.3}_{-0.2} \, (\text{scale}) \, \pm 0.8 \, (\text{PDF}) \, \pm 0.5 \, (\text{model}) \, \text{fb}.$$

An estimate of the measurement significance showed that the background-only hypothesis was excluded at greater than the 5σ level.